

1

2

3

4

5

# Simultaneous Measurement of Oscillation Parameters in Beam and Atmospheric Neutrino Data from Tokai-to-Kamioka and Super-Kamiokande Experiments

6

Daniel Robert Clement Barrow

7

8

Magdalen College,  
Oxford University

9

Version 1.1

10

A Dissertation Submitted to Oxford University  
11 for the Degree of Doctor of Philosophy

13                   **Simultaneous Measurement of**

14                   **Oscillation Parameters in Beam and**

15                   **Atmospheric Neutrino Data from**

16                   **Tokai-to-Kamioka and**

17                   **Super-Kamiokande Experiments**

18                   *Abstract*

19                   Lorem ipsum dolor sit amet, consectetur adipiscing elit, sed do eiusmod tempor incididunt ut labore et dolore magna aliqua. Nulla aliquet porttitor lacus luctus accumsan tortor posuere. Pulvinar neque laoreet suspendisse interdum. Sem viverra aliquet eget sit. Nunc sed velit dignissim sodales ut eu sem integer vitae. At erat pellentesque adipiscing commodo elit at imperdiet dui accumsan. Fames ac turpis egestas integer eget aliquet nibh. Scelerisque eu ultrices vitae auctor eu augue. Purus non enim praesent elementum facilisis leo vel. Sollicitudin nibh sit amet commodo. Vitae auctor eu augue ut. Vel quam elementum pulvinar etiam. A condimentum vitae sapien pellentesque habitant morbi tristique senectus. Viverra accumsan in nisl nisi scelerisque eu ultrices. Sed viverra ipsum nunc aliquet bibendum enim.

## 32 Declaration

33 This dissertation is the result of my own work, except where ex-  
34 plicit reference is made to the work of others, and has not been sub-  
35 mitted for another qualification to this or any other university. This  
36 dissertation does not exceed the word limit for the respective Degree  
37 Committee.

38 Daniel Robert Clement Barrow

39 ©The copyright of this thesis rests with the author and is made available under a Creative  
40 Commons Attribution Non-Commercial No Derivatives licence. Researchers are free to copy,  
41 distribute or transmit the thesis on the condition that they attribute it, that they do not use  
42 it for commercial purposes and that they do not alter, transform or build upon it. For any  
43 reuse or redistribution, researchers must make clear to others the licence terms of this work.

44

## Acknowledgements

45 at pretium nibh ipsum. Eget nunc scelerisque viverra mauris in aliquam. Arcu vitae  
46 elementum curabitur vitae nunc sed velit dignissim. Sed arcu non odio euismod lacinia  
47 at quis risus sed. Vitae tempus quam pellentesque nec nam aliquam sem et tortor.  
48 Viverra aliquet eget sit amet tellus cras adipiscing. Purus sit amet luctus venenatis  
49 lectus magna. In aliquam sem fringilla ut morbi tincidunt augue. Fermentum dui  
50 faucibus in ornare. Aliquam malesuada bibendum arcu vitae elementum curabitur  
51 vitae nunc sed.

52 Ultricies leo integer malesuada nunc vel risus commodo. Tellus cras adipiscing  
53 enim eu turpis egestas pretium. Dictumst quisque sagittis purus sit amet volutpat  
54 consequat mauris nunc. Vitae congue mauris rhoncus aenean vel elit scelerisque  
55 mauris pellentesque. Vel facilisis volutpat est velit egestas dui id ornare. Suscipit  
56 adipiscing bibendum est ultricies. At in tellus integer feugiat scelerisque varius  
57 morbi enim. Cras semper auctor neque vitae tempus. Commodo sed egestas egestas  
58 fringilla phasellus faucibus. Cras pulvinar mattis nunc sed blandit. Pretium viverra  
59 suspendisse potenti nullam ac tortor vitae. Purus sit amet volutpat consequat. Orci  
60 sagittis eu volutpat odio facilisis mauris. Sit amet massa vitae tortor condimentum  
61 lacinia quis. Commodo sed egestas egestas fringilla phasellus. Sed libero enim sed  
62 faucibus turpis. Vitae tempus quam pellentesque nec.

63 Blandit massa enim nec dui. Viverra tellus in hac habitasse platea dictumst vestibulu-  
64 lum. Bibendum enim facilisis gravida neque convallis. Sagittis nisl rhoncus mattis  
65 rhoncus urna neque. Nisl rhoncus mattis rhoncus urna neque. Ac tortor vitae purus  
66 faucibus ornare. Aenean sed adipiscing diam donec adipiscing tristique risus. Sapien  
67 nec sagittis aliquam malesuada bibendum. Et leo duis ut diam quam nulla. Tellus  
68 rutrum tellus pellentesque eu tincidunt tortor aliquam nulla facilisi.

# **Contents**

<b>1</b>	<b>Introduction</b>	<b>1</b>
<b>2</b>	<b>Neutrino Oscillation Physics</b>	<b>2</b>
2.1	Discovery of Neutrinos . . . . .	2
2.2	Theory of Neutrino Oscillation . . . . .	4
2.2.1	Three Flavour Oscillations . . . . .	4
2.2.2	The MSW Effect . . . . .	8
2.3	Neutrino Oscillation Measurements . . . . .	9
2.3.1	Solar Neutrinos . . . . .	11
2.3.2	Atmospheric Neutrinos . . . . .	13
2.3.3	Accelerator Neutrinos . . . . .	16
2.3.4	Reactor Neutrinos . . . . .	18
2.4	Summary . . . . .	20
<b>3</b>	<b>T2K and SK Experiment Overview</b>	<b>23</b>
3.1	The Super-Kamiokande Experiment . . . . .	23
3.1.1	The SK Detector . . . . .	24
3.1.2	Calibration . . . . .	28
3.1.3	Data Acquisition and Triggering . . . . .	31
3.1.4	Cherenkov Radiation . . . . .	33
3.2	The Tokai to Kamioka Experiment . . . . .	35
3.2.1	The Neutrino Beam . . . . .	37
3.2.2	The Near Detector at 280m . . . . .	40
3.2.2.1	Fine Grained Detectors . . . . .	43
3.2.2.2	Time Projection Chambers . . . . .	44

93	3.2.2.3	$\pi^0$ Detector . . . . .	46
94	3.2.2.4	Electromagnetic Calorimeter . . . . .	46
95	3.2.2.5	Side Muon Range Detector . . . . .	48
96	3.2.3	The Interactive Neutrino GRID . . . . .	48
97	<b>4</b>	<b>Bayesian Statistics and Markov Chain Monte Carlo Techniques</b>	50
98	4.1	Bayesian Statistics . . . . .	51
99	4.2	Monte Carlo Simulation . . . . .	52
100	4.2.1	Markov Chain Monte Carlo . . . . .	53
101	4.2.2	Metropolis-Hastings Algorithm . . . . .	56
102	4.2.3	MCMC Optimisation . . . . .	58
103	4.3	Understanding the MCMC Results . . . . .	61
104	4.3.1	Marginalisation . . . . .	62
105	4.3.2	Parameter Estimation and Credible Intervals . . . . .	63
106	4.3.3	Bayesian Model Comparisons . . . . .	65
107	4.3.4	Comparison of MCMC Output to Expectation . . . . .	66
108	<b>5</b>	<b>Simulation, Reconstruction, and Event Reduction</b>	68
109	5.1	Simulation . . . . .	68
110	5.2	Event Reconstruction at SK . . . . .	73
111	5.3	Event Reduction at SK . . . . .	84
112	<b>6</b>	<b>Sample Selections and Systematics</b>	90
113	6.1	Sample Selection . . . . .	90
114	6.1.1	Atmospheric Samples . . . . .	90
115	6.1.2	Near Detector Beam Samples . . . . .	97
116	6.1.3	Far Detector Beam Samples . . . . .	98
117	6.2	Systematic Uncertainties . . . . .	103
118	6.2.1	Beam Flux . . . . .	103

119	6.2.2 Atmospheric Flux . . . . .	105
120	6.2.3 Neutrino Interaction . . . . .	106
121	6.2.4 Near Detector . . . . .	112
122	6.2.5 Far Detector . . . . .	114
123	6.2.5.1 Beam Samples . . . . .	115
124	6.2.5.2 Atmospheric Samples . . . . .	118
125	6.2.5.3 Correlated Detector Model . . . . .	120
126	<b>7 Oscillation Probability Calculation</b>	<b>127</b>
127	7.1 Overview . . . . .	128
128	7.2 Treatment of Fast Oscillations . . . . .	136
129	7.3 Calculation Engine . . . . .	142
130	7.4 Matter Density Profile . . . . .	145
131	7.5 Production Height Averaging . . . . .	151
132	<b>Bibliography</b>	<b>155</b>
133	<b>List of Figures</b>	<b>167</b>
134	<b>List of Tables</b>	<b>177</b>



<sup>136</sup> Chapter 1

<sup>137</sup> Introduction

<sup>138</sup> **Chapter 2**

<sup>139</sup> **Neutrino Oscillation Physics**

<sup>140</sup> When first proposed, neutrinos were expected to be massless fermions that only in-  
<sup>141</sup> teract through weak and gravitational forces. This meant they were very difficult to  
<sup>142</sup> detect as they can pass through significant amounts of matter without interacting. De-  
<sup>143</sup> spite this, experimental neutrino physics has developed with many different detection  
<sup>144</sup> techniques and neutrino sources being used today. In direct tension with standard  
<sup>145</sup> model physics, neutrinos have been determined to oscillate between different lepton  
<sup>146</sup> flavours, requiring them to have mass.

<sup>147</sup> The observation techniques which lead to the discovery of the neutrino are doc-  
<sup>148</sup> umented in section 2.1. The theory underpinning neutrino oscillation is described  
<sup>149</sup> in section 2.2 and includes the approximations which can be made to simplify the  
<sup>150</sup> understanding of neutrino oscillation in the two-flavour approximation. Past, current,  
<sup>151</sup> and future neutrino experiments are detailed in section 2.3, including the reactor,  
<sup>152</sup> atmospheric, and long-baseline accelerator neutrino sources that have been used to  
<sup>153</sup> successfully constrain oscillation parameters. Finally, the current state of oscillation  
<sup>154</sup> parameter measurements are summarised in section 2.4.

<sup>155</sup> **2.1 Discovery of Neutrinos**

<sup>156</sup> At the start of the 20<sup>th</sup> century, the electrons emitted from the  $\beta$ -decay of the nucleus  
<sup>157</sup> were found to have a continuous energy spectrum [1,2]. This observation seemingly  
<sup>158</sup> broke the energy conservation invoked within that period's nuclear models. Postulated

159 in 1930 by Pauli as the solution to this problem, the neutrino (originally termed  
160 “neutron”) was theorized to be an electrically neutral spin-1/2 fermion with a mass of  
161 the same order of magnitude as the electron [3]. This neutrino was to be emitted with  
162 the electron in  $\beta$ -decay to alleviate the apparent breaking of energy conservation. As a  
163 predecessor of today’s weak interaction model, Fermi’s theory of  $\beta$ -decay developed  
164 the understanding by coupling the four constituent particles; electron, proton, neutron,  
165 and neutrino, into a consistent model [4].

166 Whilst Pauli was not convinced of the ability to detect neutrinos, the first observa-  
167 tions of the particle were made in the mid-1950s when neutrinos from a reactor were  
168 observed via the inverse  $\beta$ -decay (IBD) process,  $\bar{\nu}_e + p \rightarrow n + e^+$  [5, 6]. The detector  
169 consisted of two parts: a neutrino interaction medium and a liquid scintillator. The  
170 interaction medium was built from two water tanks. These were loaded with cadmium  
171 chloride to allow increased efficiency of neutron capture. The positron emitted from  
172 IBD annihilates,  $e^+ + e^- \rightarrow 2\gamma$ , generating a prompt signal and the neutron is captured  
173 on the cadmium via  $n + {}^{108}Cd \rightarrow {}^{109*}Cd \rightarrow {}^{109}Cd + \gamma$ , producing a delayed signal. An  
174 increase in the coincidence rate was observed when the reactor was operating which  
175 was interpreted as interactions from neutrinos generated in the reactor.

176 After the discovery of the  $\nu_e$ , the natural question of how many flavours of neutrino  
177 exist was asked. In 1962, a measurement of the  $\nu_\mu$  was conducted at the Brookhaven  
178 National Laboratory [7]. A proton beam was directed at a beryllium target, gener-  
179 ating a  $\pi$ -dominated beam which then decayed via  $\pi^\pm \rightarrow \mu^\pm + (\nu_\mu, \bar{\nu}_\mu)$ , and the  
180 subsequent interactions of the  $\nu_\mu$  were observed. As the subsequent interaction of  
181 the neutrino generates muons rather than electrons, it was determined the  $\nu_\mu$  was  
182 fundamentally different from  $\nu_e$ . The final observation to be made was that of the  $\nu_\tau$   
183 from the DONUT experiment [8]. Three neutrinos seem the obvious solution as it  
184 mirrors the known number of charged lepton (as they form weak isospin doublets) but

185 there could be evidence of more. Several neutrino experiments have found anomalous  
186 results [9, 10] which could be attributed to sterile neutrinos. However, cosmological  
187 observations indicate the number of neutrino species  $N_{eff} = 2.99 \pm 0.17$  [11], as mea-  
188 sured from the cosmic microwave background power spectrum, and Stanford Linear  
189 Accelerator found the number of active neutrino flavours to be  $N_\nu 2.9840 \pm 0.0082$  [12]  
190 from measurements of the Z-decay width.

## 191 2.2 Theory of Neutrino Oscillation

192 As direct evidence of beyond Standard Model physics, a neutrino generated with  
193 lepton flavour  $\alpha$  can change into a different lepton flavour  $\beta$  after propagating some  
194 distance. This phenomenon is called neutrino oscillation and requires that neutrinos  
195 must have a non-zero mass (as seen in subsection 2.2.1). This observation is direct  
196 evidence of beyond standard model physics. This behaviour has been characterised  
197 by the Pontecorvo-Maki-Nakagawa-Sakata (PMNS) [13–15] mixing matrix which  
198 describes how the flavour and mass of neutrinos are associated. This is analogous to  
199 the Cabibbo-Kobayashi-Maskawa (CKM) [16] matrix measured in quark physics.

### 200 2.2.1 Three Flavour Oscillations

201 The PMNS parameterisation defines three flavour eigenstates,  $\nu_e$ ,  $\nu_\mu$  and  $\nu_\tau$  (indexed  
202  $\nu_\alpha$ ), which are eigenstates of the weak interaction and three mass eigenstates,  $\nu_1$ ,  $\nu_2$  and  
203  $\nu_3$  (indexed  $\nu_i$ ). Each mass eigenstate is the superposition of all three flavour states,

$$|\nu_i\rangle = \sum_\alpha U_{\alpha i} |\nu_\alpha\rangle. \quad (2.1)$$

204 Where  $U$  is the PMNS matrix which is unitary and connects the mass and flavour

205 eigenstates.

206 The weak interaction couples to flavour eigenstates so neutrinos interact with

207 leptons of the same flavour. The propagation of a neutrino flavour eigenstate, in a

208 vacuum, can be re-written as a plane-wave solution to the time-dependent Schrödinger

209 equation,

$$|\nu_\alpha(t)\rangle = \sum_i U_{\alpha i}^* |\nu_i\rangle e^{-i\phi_i}. \quad (2.2)$$

210 The probability of observing a neutrino of flavour eigenstate  $\beta$  from one which

211 originated as flavour  $\alpha$  can be calculated as,

$$P(\nu_\alpha \rightarrow \nu_\beta) = |\langle \nu_\beta | \nu_\alpha(t) \rangle|^2 = \sum_{i,j} U_{\alpha i}^* U_{\beta i} U_{\alpha j} U_{\beta j}^* e^{-i(\phi_j - \phi_i)} \quad (2.3)$$

212 The  $\phi_i$  term can be expressed in terms of the energy,  $E_i$ , and magnitude of the

213 three momenta,  $p_i$ , of the neutrino,  $\phi_i = E_i t - p_i x$  ( $t$  and  $x$  being time and position

214 coordinates). Therefore,

$$\phi_j - \phi_i = E_j t - E_i t - p_j x + p_i x. \quad (2.4)$$

215 For a relativistic particle,  $E_i \gg m_i$ ,

$$p_i = \sqrt{E_i^2 - m_i^2} \approx E_i - \frac{m_i^2}{2E_i}. \quad (2.5)$$

216 Making the approximations that neutrinos are relativistic, the mass eigenstates  
217 were created with the same energy and that  $x = L$ , where  $L$  is the distance traveled by  
218 the neutrino, Equation 2.4 then becomes

$$\phi_j - \phi_i = \frac{\Delta m_{ij}^2 L}{2E}, \quad (2.6)$$

219 where  $\Delta m_{ij}^2 = m_j^2 - m_i^2$ . This, combined with further use of unitarity relations  
220 results in Equation 2.3 becoming

$$P(\nu_\alpha \rightarrow \nu_\beta) = \delta_{\alpha\beta} - 4 \sum_{i>j} \Re \left( U_{\alpha i}^* U_{\beta i} U_{\alpha j} U_{\beta j}^* \right) \sin^2 \left( \frac{\Delta m_{ij}^2 L}{4E} \right) + (-) 2 \sum_{i>j} \Im \left( U_{\alpha i}^* U_{\beta i} U_{\alpha j} U_{\beta j}^* \right) \sin \left( \frac{\Delta m_{ij}^2 L}{2E} \right). \quad (2.7)$$

221 Where  $\delta_{\alpha\beta}$  is the Kronecker delta function and the negative sign on the last term is  
222 included for the oscillation probability of antineutrinos.

223 Typically, the PMNS matrix is parameterised into three mixing angles, a charge  
224 parity (CP) violating phase  $\delta_{CP}$ , and two Majorana phases  $\alpha_{1,2}$ ,

$$U = \underbrace{\begin{pmatrix} 1 & 0 & 0 \\ 0 & c_{23} & s_{23} \\ 0 & -s_{23} & c_{23} \end{pmatrix}}_{\text{Atmospheric, Accelerator}} \underbrace{\begin{pmatrix} c_{13} & 0 & s_{13}e^{-i\delta_{CP}} \\ 0 & 1 & 0 \\ -s_{13}e^{-i\delta_{CP}} & 0 & c_{13} \end{pmatrix}}_{\text{Reactor, Accelerator}} \underbrace{\begin{pmatrix} c_{12} & s_{12} & 0 \\ -s_{12} & c_{12} & 0 \\ 0 & 0 & 1 \end{pmatrix}}_{\text{Reactor, Solar}} \underbrace{\begin{pmatrix} e^{i\alpha_1/2} & 0 & 0 \\ 0 & e^{i\alpha_2/2} & 0 \\ 0 & 0 & 1 \end{pmatrix}}_{\text{Majorana}}. \quad (2.8)$$

225 Where  $s_{ij} = \sin(\theta_{ij})$  and  $c_{ij} = \cos(\theta_{ij})$ . The oscillation parameters are often  
 226 grouped; (1,2) as “solar”, (2,3) as “atmospheric” and (1,3) as “reactor”. Many  
 227 neutrino experiments aim to measure the PMNS parameters from a wide array of  
 228 origins, as is the purpose of this thesis.

229 The Majorana phase,  $\alpha_{1,2}$ , included within the fourth matrix in Equation 2.8 is only  
 230 included for completeness. For an oscillation analysis experiment, any terms contain-  
 231 ing this phase disappear due to taking the expectation value of the PMNS matrix.  
 232 Measurements of these phases are typically performed by experiments searching for  
 233 neutrino-less double  $\beta$ -decay [17].

234 A two flavour approximation can be obtained when one assumes the third mass  
 235 eigenstate is degenerate with another. As discussed in section 2.3, it is found that  
 236  $\Delta m_{21}^2 \ll |\Delta m_{31}^2|$ . This results in the two flavour approximation being reasonable for  
 237 understanding the features of the oscillation. In this two flavour case, the mixing  
 238 matrix becomes,

$$U_{2 \text{ Flav.}} = \begin{pmatrix} \cos(\theta) & \sin(\theta) \\ -\sin(\theta) & \cos(\theta) \end{pmatrix}. \quad (2.9)$$

<sup>239</sup> This culminates in the oscillation probability,

$$\begin{aligned} P(\nu_\alpha \rightarrow \nu_\alpha) &= 1 - \sin^2(2\theta) \sin^2\left(\frac{\Delta m^2 L}{4E}\right), \\ P(\nu_\alpha \rightarrow \nu_\beta) &= \sin^2(2\theta) \sin^2\left(\frac{\Delta m^2 L}{4E}\right). \end{aligned} \quad (2.10)$$

<sup>240</sup> Where  $\alpha \neq \beta$ . For a fixed neutrino energy, the oscillation probability is a sinusoidal  
<sup>241</sup> function depending upon the distance over which the neutrino propagates. The  
<sup>242</sup> frequency and amplitude of oscillation are dependent upon  $\Delta m^2/4E$  and  $\sin^2 2\theta$ ,  
<sup>243</sup> respectively. The oscillation probabilities presented thus far assume  $c = 1$ , where  
<sup>244</sup>  $c$  is the speed of light in vacuum. In more familiar units, the maximum oscillation  
<sup>245</sup> probability for a fixed value of  $\theta$  is given at  $L[km]/E[GeV] \sim 1.27/\Delta m^2$ . It is this  
<sup>246</sup> calculation that determines the best  $L/E$  value for a given experiment to be designed  
<sup>247</sup> around for measurements of a specific value of  $\Delta m^2$ .

### <sup>248</sup> 2.2.2 The MSW Effect

<sup>249</sup> The theory of neutrino oscillation in a vacuum has been described in subsection 2.2.1.  
<sup>250</sup> However, the beam neutrinos and atmospheric neutrinos originating from below the  
<sup>251</sup> horizon propagate through matter in the Earth. The coherent scattering of neutrinos  
<sup>252</sup> from a material target modifies the Hamiltonian of the system. This results in a change  
<sup>253</sup> in the oscillation probability. Notably, charged current scattering ( $\nu_e + e^- \rightarrow \nu_e + e^-$ ,  
<sup>254</sup> propagated by a  $W$  boson) only affects electron neutrinos whereas the neutral current  
<sup>255</sup> scattering ( $\nu_l + l^- \rightarrow \nu_l + l^-$ , propagated by a  $Z^0$  boson) interacts through all neutrino  
<sup>256</sup> flavours equally. In the two-flavour approximation, the effective mixing parameter  
<sup>257</sup> becomes

$$\sin^2(2\theta) \rightarrow \sin^2(2\theta_m) = \frac{\sin^2(2\theta)}{(A/\Delta m^2 - \cos(2\theta))^2 + \sin^2(2\theta)}, \quad (2.11)$$

where  $A = 2\sqrt{2}G_F N_e E$ ,  $N_e$  is the electron density of the medium and  $G_F$  is Fermi's constant. It is clear to see that there exists a value of  $A = \Delta m^2 \cos(2\theta)$  for  $\Delta m^2 > 0$  which results in a divergent mixing parameter. This resonance is termed the Mikheyev-Smirnov-Wolfenstein (MSW) effect (or more colloquially, the matter resonance) which regenerates the electron neutrino component of the neutrino flux [18–20]. The density at which the resonance occurs is given by

$$N_e = \frac{\Delta m^2 \cos(2\theta)}{2\sqrt{2}G_F E}. \quad (2.12)$$

At densities lower than this critical value, the oscillation probability will be much closer to that of vacuum oscillation. For antineutrinos,  $N_e \rightarrow -N_e$  [21]. The resonance occurring from the MSW effect depends on the sign of  $\Delta m^2$ . Therefore, any neutrino oscillation experiment which observes neutrinos and antineutrinos which have propagated through matter can have some sensitivity to the ordering of the neutrino mass eigenstates.

## 2.3 Neutrino Oscillation Measurements

As evidence of beyond standard model physics, the 2015 Nobel Prize in Physics was awarded to the Super-Kamiokande (SK) [22] and Sudbury Neutrino Observatory (SNO) [23] collaborations for the first definitive observation of solar and atmospheric

<sup>274</sup> neutrino oscillation [24]. Since then, the field has seen a wide array of oscillation  
<sup>275</sup> measurements from a variety of neutrino sources. As seen in subsection 2.2.1, the  
<sup>276</sup> neutrino oscillation probability is dependent on the ratio of the propagation baseline,  $L$ ,  
<sup>277</sup> to the neutrino energy,  $E$ . It is this ratio that determines the type of neutrino oscillation  
<sup>278</sup> a particular experiment is sensitive to.

<sup>279</sup> As illustrated in Figure 2.1, there are many neutrino sources that span a wide  
<sup>280</sup> range of energies. The least energetic neutrinos are from diffuse supernovae and  
<sup>281</sup> terrestrial neutrinos at  $O(1)$  MeV whereas the most energetic neutrinos originate from  
<sup>282</sup> atmospheric and galactic neutrinos of  $> O(1)$  TeV.

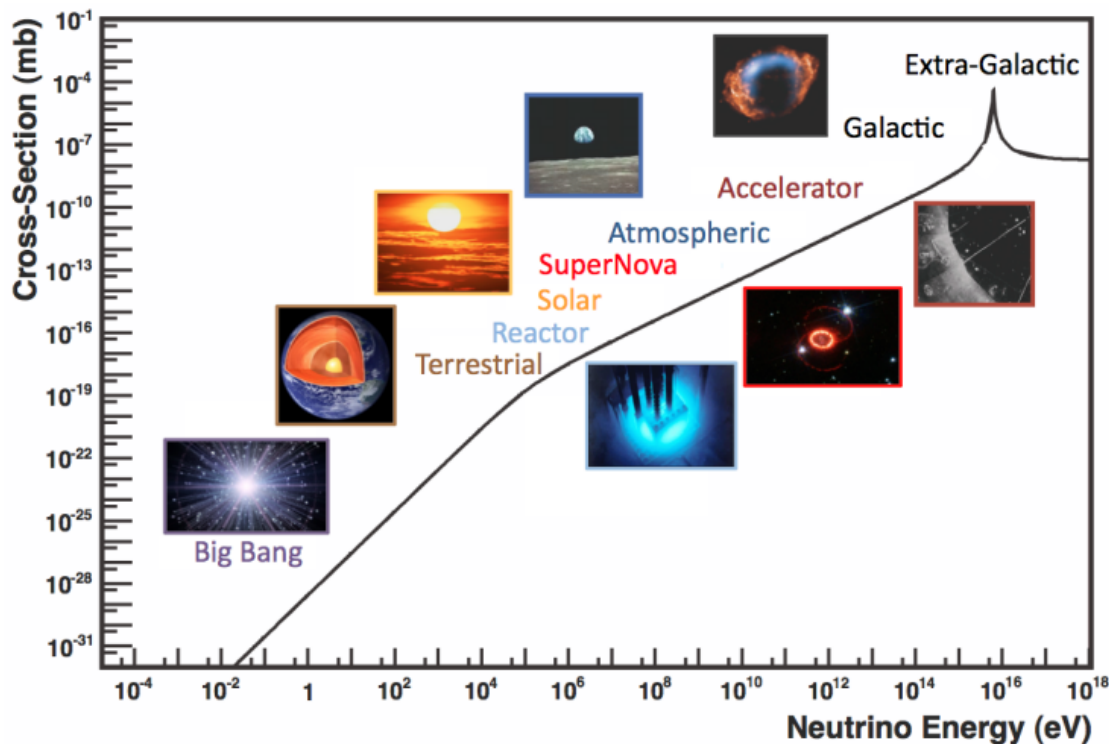


**Figure 2.1:** The cross-section of neutrinos from various natural and man-made sources as a function of neutrino energy. Taken from [25]

### <sup>283</sup> 2.3.1 Solar Neutrinos

<sup>284</sup> Solar neutrinos are emitted from fusion reaction chains at the center of the Sun. The  
<sup>285</sup> solar neutrino flux, given as a function of neutrino energy for different fusion and  
<sup>286</sup> decay chains, is illustrated in Figure 2.2. Whilst proton-proton fusion generates the  
<sup>287</sup> largest flux of neutrinos, the neutrinos are of low energy and are difficult to reconstruct  
<sup>288</sup> due to the IBD interaction threshold of 1.8MeV. Consequently, most experiments focus  
<sup>289</sup> on the neutrinos from the decay of  $^8B$  (via  $^8B \rightarrow ^8Be^* + e^+ + \nu_e$ ), which are higher  
<sup>290</sup> energy.

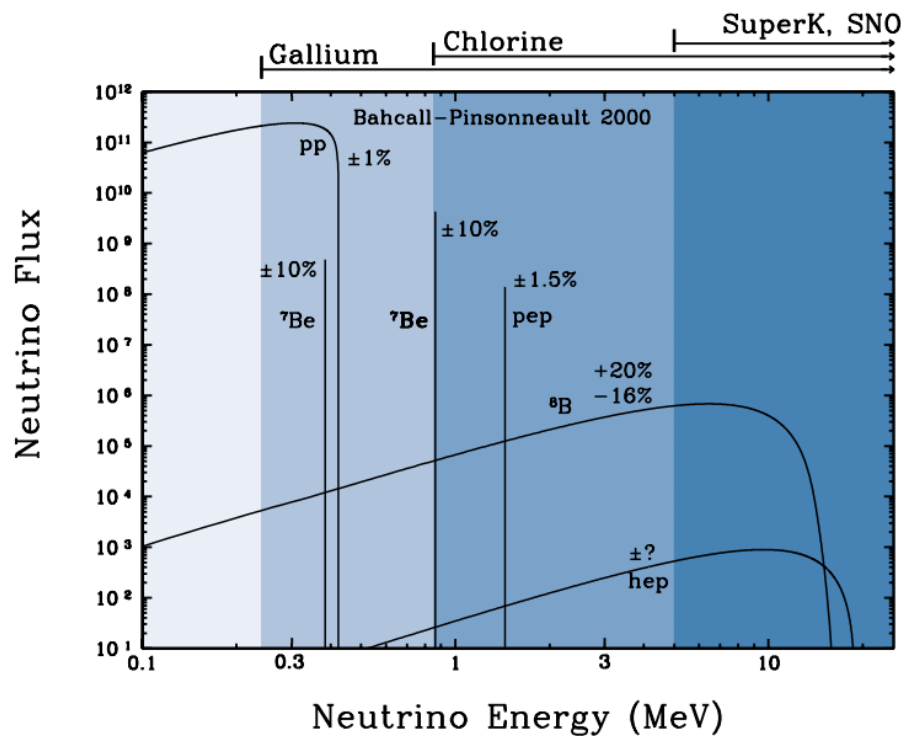


**Figure 2.2:** The solar neutrino flux as a function of neutrino energy for various fusion reactions and decay chains as predicted by the Standard Solar Model. Taken from [26].

<sup>291</sup> The first measurements of solar neutrinos observed a significant reduction in the  
<sup>292</sup> event rate compared to predictions from the Standard Solar Model [27, 28]. The  
<sup>293</sup> proposed solution to this “solar neutrino problem” was  $\nu_e \leftrightarrow \nu_\mu$  oscillations in a

<sup>294</sup> precursory version of the PMNS model [29]. The Kamiokande [30], Gallex [31] and  
<sup>295</sup> Sage [32] experiments confirmed the  $\sim 0.5$  factor deficit of solar neutrinos.

<sup>296</sup> The conclusive solution to this problem was determined by the SNO collaboration  
<sup>297</sup> [33]. Using a deuterium water target to observe  ${}^8B$  neutrinos, the event rate of charged  
<sup>298</sup> current (CC), neutral current (NC), and elastic scattering (ES) interactions (Given in  
<sup>299</sup> Equation 2.13) was simultaneously measured. CC events can only occur for electron  
<sup>300</sup> neutrinos, whereas the NC channel is agnostic to neutrino flavour, and the ES reaction  
<sup>301</sup> has a slight excess sensitivity to electron neutrino interactions. This meant that there  
<sup>302</sup> were direct measurements of the  $\nu_e$  and  $\nu_x$  neutrino flux. It was concluded that the  
<sup>303</sup> CC and ES interaction rates were consistent with the deficit previously observed.  
<sup>304</sup> Most importantly, the NC reaction rate was only consistent with the others under the  
<sup>305</sup> hypothesis of flavour transformation.



<sup>306</sup> Many experiments have since measured the neutrino flux of different interaction  
<sup>307</sup> chains within the sun [34–36]. The most recent measurement was that of CNO neutrinos  
<sup>308</sup> which were recently observed with  $5\sigma$  significance by the Borexino collaboration.  
<sup>309</sup> Future neutrino experiments aim to further these spectroscopic measurements of  
<sup>310</sup> different fusion chains within the Sun [37–39]. Solar neutrinos act as an irreducible  
<sup>311</sup> background for dark matter experiments like DARWIN but oscillation parameter  
<sup>312</sup> measurements can be made [40].

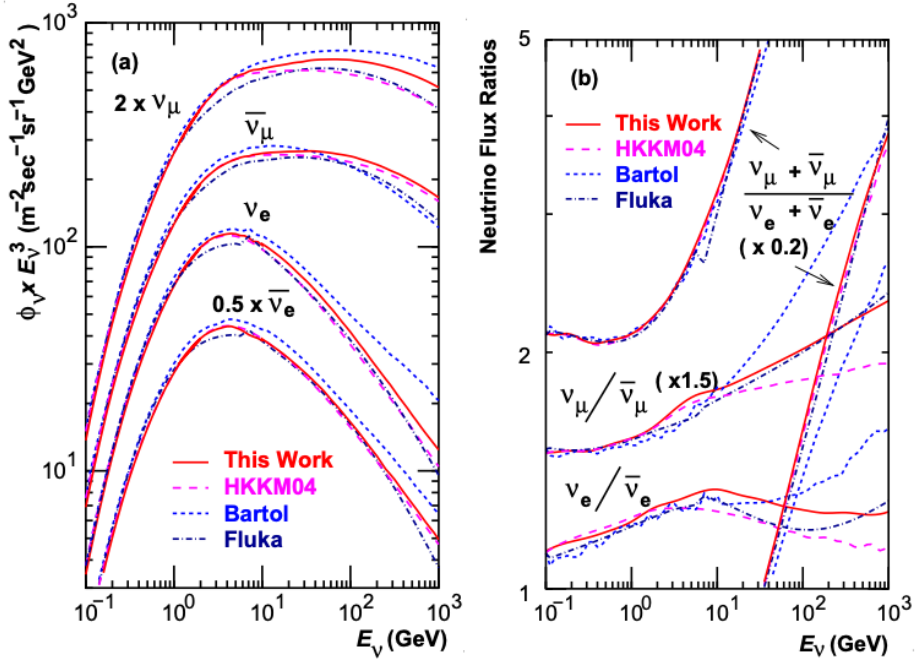
### <sup>313</sup> 2.3.2 Atmospheric Neutrinos

- <sup>314</sup> The interactions of primary cosmic ray protons in Earth's upper atmosphere generate  
<sup>315</sup> showers of energetic hadrons. These are mostly pions and kaons which when they  
<sup>316</sup> decay produce a natural source of neutrinos spanning energies of MeV to TeV [41].  
<sup>317</sup> The main decay is via

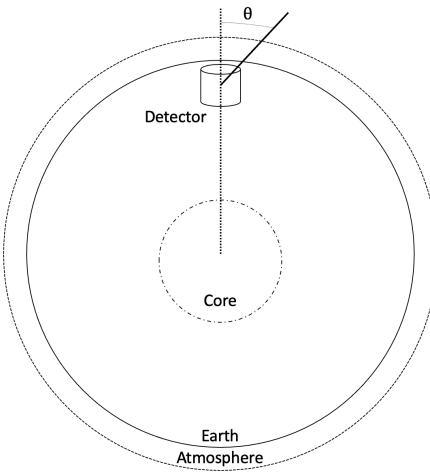
$$\begin{aligned} \pi^\pm &\rightarrow \mu^\pm + (\nu_\mu, \bar{\nu}_\mu) \\ \mu^\pm &\rightarrow e^\pm + (\nu_e, \bar{\nu}_e) + (\nu_\mu, \bar{\nu}_\mu) \end{aligned} \tag{2.14}$$

<sup>318</sup> such that for a single pion decay, three neutrinos are typically produced. The  
<sup>319</sup> atmospheric neutrino flux energy spectra as predicted by the Bartol [42], Honda  
<sup>320</sup> [43–45], and FLUKA [46] models are illustrated in Figure 2.3. The flux distribution  
<sup>321</sup> peaks at an energy of  $O(10)\text{GeV}$ . The uncertainties associated with these models  
<sup>322</sup> are dominated by the hadronic production of kaon and pions as well as the primary  
<sup>323</sup> cosmic flux.

<sup>324</sup> Unlike long-baseline experiments which have a fixed baseline, the distance at-  
<sup>325</sup> mospheric neutrinos propagate is dependent upon the zenith angle at which they  
<sup>326</sup> interact. This is illustrated in Figure 2.4. Neutrinos that are generated directly above  
<sup>327</sup> the detector ( $\cos(\theta) = 1.0$ ) have a baseline equivalent to the height of the atmosphere  
<sup>328</sup> whereas neutrinos that interact directly below the detector ( $\cos(\theta) = -1.0$ ) have to  
<sup>329</sup> travel a length equal to the diameter of the Earth. This means atmospheric neutrinos  
<sup>330</sup> have a baseline that varies from  $O(20)\text{km}$  to  $O(6 \times 10^3)\text{km}$ . Any neutrino generated  
<sup>331</sup> at or below the horizon will be subject to matter effects as they propagate through the  
<sup>332</sup> Earth.



**Figure 2.3:** Left panel: The atmospheric neutrino flux for different neutrino flavours as a function of neutrino energy as predicted by the 2007 Honda model (“This work”) [43], the 2004 Honda model (“HKKM04”) [44], the Bartol model [42] and the FLUKA model [46]. Right panel: The ratio of the muon to electron neutrino flux as predicted by all the quoted models. Both figures taken from [43].



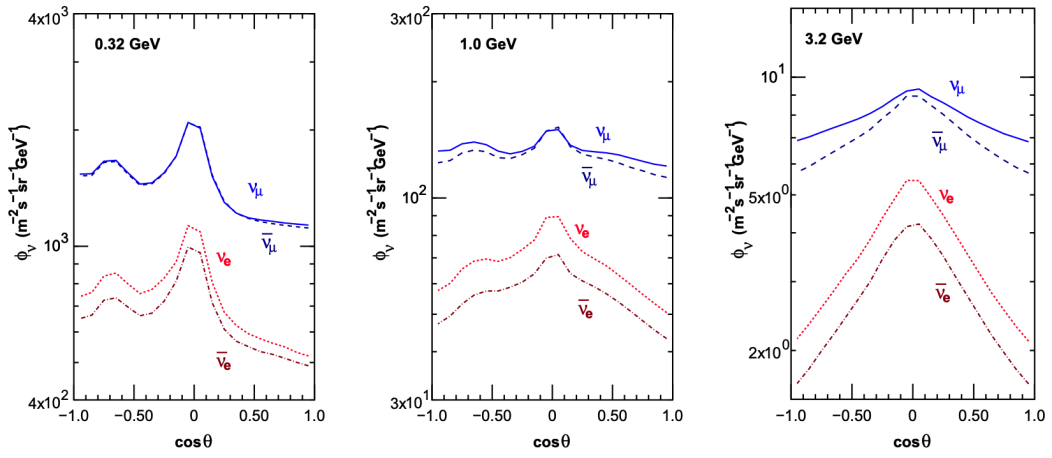
**Figure 2.4:** A diagram illustrating the definition of zenith angle as used in the Super Kamiokande experiment [47].

Figure 2.5 highlights the neutrino flux as a function of the zenith angle for different

slices of neutrino energy. For medium to high-energy neutrinos (and to a lesser degree

for low-energy neutrinos), the flux is approximately symmetric around  $\cos(\theta) = 0$ .

To the accuracy of this approximation, the systematic uncertainties associated with atmospheric flux for comparing upward-going and down-going neutrino cancels. This allows the down-going events, which are mostly insensitive to oscillation probabilities, to act as an unoscillated prediction (similar to a near detector in an accelerator neutrino experiment).



**Figure 2.5:** Prediction of  $\nu_e, \bar{\nu}_e, \nu_\mu, \bar{\nu}_\mu$  fluxes as a function of zenith angle as calculated by the HKKM model [45]. The left, middle and right panels represent three values of neutrino energy, 0.32GeV, 1.0GeV and 3.2GeV respectively. Predictions for other models including Bartol [42], Honda [43] and FLUKA [46] are given in [47].

Precursory hints of atmospheric neutrinos were observed in the mid-1960s searching for  $\nu_\mu + X \xrightarrow{(-)} X^* + \mu^\pm$  [48], although it was called an anomaly at the time of measurement. This was succeeded with the IMB-3 [49] and Kamiokande [50] experiments which measured the ratio of muon neutrinos compared to electron neutrinos  $R(\nu_\mu/\nu_e)$ . Both experiments were found to have a consistent deficit of muon neutrinos, with  $R(\nu_\mu/\nu_e) = 0.67 \pm 0.17$  and  $R(\nu_\mu/\nu_e) = 0.60^{+0.07}_{-0.06} \pm 0.05$ . Super-Kamiokande (SK) [47] extended this analysis by fitting oscillation parameters in  $P(\nu_\mu \rightarrow \nu_\tau)$  which found best fit parameters  $\sin^2(2\theta) > 0.92$  and  $1.5 \times 10^{-3} < \Delta m^2 < 3.4 \times 10^{-3}$ eV $^2$ .

Since then, atmospheric neutrino experiments have been making precision measurements of the  $\sin^2(\theta_{23})$  and  $\Delta m^2_{32}$  oscillation parameters. Atmospheric neutrino oscillation is dominated by  $P(\nu_\mu \rightarrow \nu_\tau)$ , where SK observed a  $4.6\sigma$  discovery of  $\nu_\tau$

<sup>352</sup> appearance [51]. Figure 2.6 illustrates the current estimates on the atmospheric mixing  
<sup>353</sup> parameters from a wide range of atmospheric and accelerator neutrino observatories.

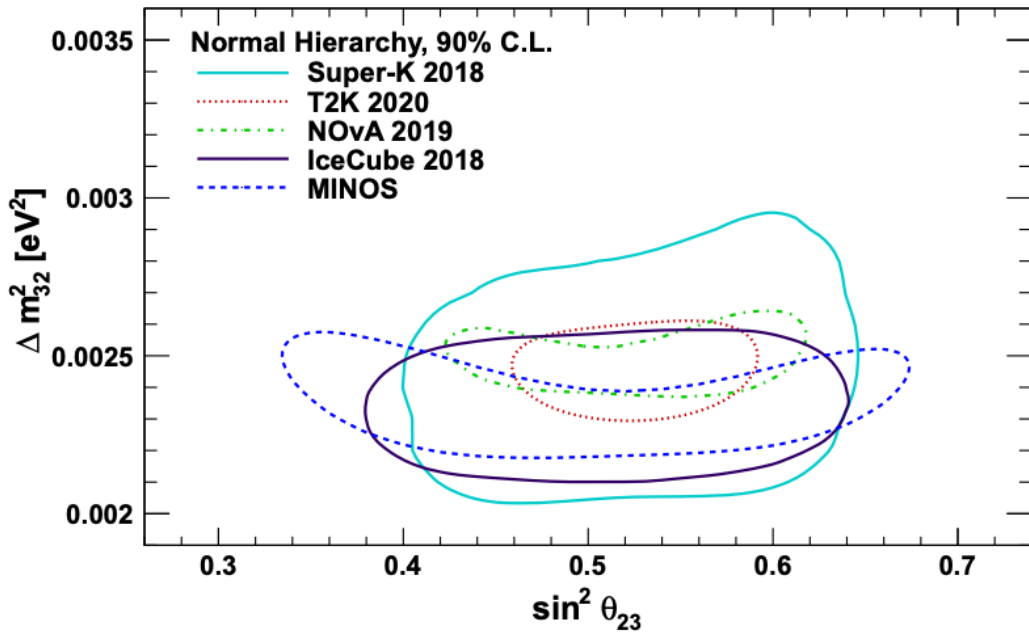


**Figure 2.6:** Constraints on the atmospheric oscillation parameters,  $\sin^2(\theta_{23})$  and  $\Delta m_{32}^2$ , from atmospheric and long baseline experiments: SK [52], T2K [53], NOvA [54], IceCube [55] and MINOS [56]. Figure taken from [57].

### <sup>354</sup> 2.3.3 Accelerator Neutrinos

<sup>355</sup> The concept of using a man-made “neutrino beam” was first realised in 1962 [58].  
<sup>356</sup> Since then, many experiments have followed which all use the same fundamental  
<sup>357</sup> concepts. Typically, a proton beam is aimed at a target producing charged mesons that  
<sup>358</sup> decay to neutrinos. The mesons can be sign-selected by the use of magnetic focusing  
<sup>359</sup> horns to generate a neutrino or antineutrino beam. Pions are the primary meson that  
<sup>360</sup> decay and depending on the orientation of the magnetic field, a muon (anti-)neutrino  
<sup>361</sup> beam is generated via  $\pi^+ \rightarrow \mu^+ + \nu_\mu$  or  $\pi^- \rightarrow \mu^- + \bar{\nu}_\mu$ . The decay of muons and  
<sup>362</sup> kaons does result in an irreducible intrinsic electron neutrino background. In T2K,  
<sup>363</sup> this background contamination is  $O(< 1\%)$  [59]. There is also an approximately  $\sim 5\%$

<sup>364</sup> “wrong-sign” neutrino background of  $\bar{\nu}_\mu$  generated via the same decays. As the beam is  
<sup>365</sup> generated by proton interactions (rather than anti-proton interactions), the wrong-sign  
<sup>366</sup> component in the antineutrino beam is larger when operating in neutrino mode.

<sup>367</sup> Tuning the proton energy in the beam and using beam focusing techniques allows  
<sup>368</sup> the neutrino energy to be set to a value that maximises the disappearance oscillation  
<sup>369</sup> probability in the  $L/E$  term in Equation 2.10. This means that accelerator experiments  
<sup>370</sup> are typically more sensitive to the mixing parameters as compared to a natural neutrino  
<sup>371</sup> source. However, the disadvantage compared to atmospheric neutrino experiments is  
<sup>372</sup> that the baseline has to be shorter due to the lower flux. Consequently, there is typically  
<sup>373</sup> less sensitivity to matter effects and the ordering of the neutrino mass eigenstates.

<sup>374</sup> A neutrino experiment measures

$$R(\vec{x}) = \Phi(E_\nu) \times \sigma(E_\nu) \times \epsilon(\vec{x}) \times P(\nu_\alpha \rightarrow \nu_\beta), \quad (2.15)$$

<sup>375</sup> where  $R(\vec{x})$  is the event rate of neutrinos at position  $\vec{x}$ ,  $\Phi(E_\nu)$  is the flux of neutrinos  
<sup>376</sup> with energy  $E_\nu$ ,  $\sigma(E_\nu)$  is the cross-section of the neutrino interaction and  $\epsilon(\vec{x})$  is the  
<sup>377</sup> efficiency and resolution of the detector. In order to leverage the most out of an  
<sup>378</sup> accelerator neutrino experiment, the flux and cross-section systematics need to be  
<sup>379</sup> constrained. This is typically done via the use of a “near detector”, situated at a baseline  
<sup>380</sup> of  $O(1)$ km. This detector observes the unoscillated neutrino flux and constrains the  
<sup>381</sup> parameters used within the flux and cross-section model.

<sup>382</sup> The first accelerator experiments to precisely measure oscillation parameters were  
<sup>383</sup> MINOS [60] and K2K [61]. These experiments confirmed the  $\nu_\mu$  disappearance seen in  
<sup>384</sup> atmospheric neutrino experiments by finding consistent parameter values for  $\sin^2(\theta_{23})$   
<sup>385</sup> and  $\Delta m_{23}^2$ . The current generation of accelerator neutrino experiments, T2K and NO $\nu$ A

<sup>386</sup> extended this field by observing  $\bar{\nu}_\mu \rightarrow \bar{\nu}_e$  and lead the sensitivity to atmospheric mix-  
<sup>387</sup> ing parameters as seen in Figure 2.6 [62]. The two experiments differ in their peak  
<sup>388</sup> neutrino energy, baseline, and detection technique. The NO $\nu$ A experiment is situated  
<sup>389</sup> at a baseline of 810km from the NuMI beamline which delivers 2GeV neutrinos. The  
<sup>390</sup> T2K neutrino beam is peaked around 0.6GeV and propagates 295km. The NO $\nu$ A  
<sup>391</sup> experiment also uses functionally identical detectors (near and far) which allow the  
<sup>392</sup> approximate cancellation of detector systematics whereas T2K uses a plastic scintil-  
<sup>393</sup> lator technique at the near detector and a water Cherenkov far detector. The future  
<sup>394</sup> generation experiments DUNE [63] and Hyper-Kamiokande [64] will succeed these  
<sup>395</sup> experiments as the high-precision era of neutrino oscillation parameter measurements  
<sup>396</sup> develops.

<sup>397</sup> Several anomalous results have been observed in the LSND [9] and MiniBooNE [10]  
<sup>398</sup> detectors which were designed with purposefully short baselines. Parts of the neu-  
<sup>399</sup> trino community attributed these results to oscillations induced by a fourth “sterile”  
<sup>400</sup> neutrino [65] but several searches in other experiments, MicroBooNE [66] and KAR-  
<sup>401</sup> MEN [67], found no hints of additional neutrino species. The solution to the anomalous  
<sup>402</sup> results is still being determined.

#### <sup>403</sup> 2.3.4 Reactor Neutrinos

<sup>404</sup> As illustrated in the first discovery of neutrinos (section 2.1), nuclear reactors are a very  
<sup>405</sup> useful man-made source of electron antineutrinos. For reactors that use low-enriched  
<sup>406</sup> uranium  $^{235}\text{U}$  as fuel, the antineutrino flux is dominated by the  $\beta$ -decay fission of  $^{235}\text{U}$ ,  
<sup>407</sup>  $^{238}\text{U}$ ,  $^{239}\text{Pu}$  and  $^{241}\text{Pu}$  [68] as illustrated in Figure 2.7.

<sup>408</sup> Due to their low energy, reactor electron antineutrinos predominantly interact  
<sup>409</sup> via the inverse  $\beta$ -decay (IBD) interaction. The typical signature contains two signals

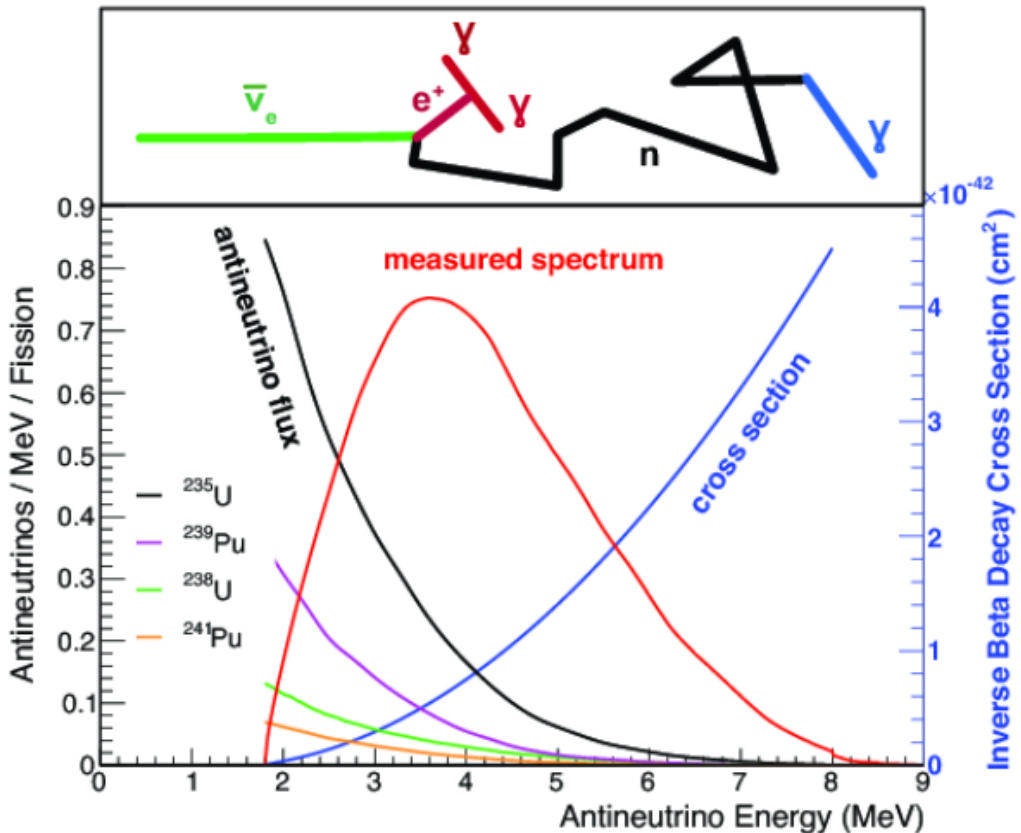


**Figure 2.7:** Reactor electron antineutrino fluxes for  $^{235}\text{U}$  (Black),  $^{238}\text{U}$  (Green),  $^{239}\text{Pu}$  (Purple), and  $^{241}\text{Pu}$  (Orange) isotopes. The inverse  $\beta$ -decay cross-section (Blue) and corresponding measurable neutrino spectrum (Red) are also given. Top panel: Schematic of Inverse  $\beta$ -decay interaction including the eventual capture of the emitted neutron. This capture emits a  $\gamma$ -ray which provides a second signal of the event. Taken from [69].

delayed by  $O(200)\mu\text{s}$ ; firstly the prompt photons from positron annihilation, and secondly the photons emitted ( $E_{tot}^\gamma = 2.2\text{MeV}$ ) from de-excitation after neutron capture on hydrogen. Searching for both signals improves the detector's ability to distinguish between background and signal events [70]. Recently, SK included gadolinium dopants into the ultra-pure water to increase the energy released from the photon cascade to  $\sim 8\text{MeV}$  and reduce the time of the delayed signal to  $\sim 28\mu\text{s}$ .

There are many short baseline experiments ( $L \sim O(1)\text{km}$ ) that have measured the  $\sin^2(\theta_{13})$  and  $\Delta m_{23}^2$  oscillation parameters. Daya Bay [71], RENO [72] and Double Chooz [73] have all provided precise measurements, with the first discovery of a

419 non-zero  $\theta_{13}$  made by Daya Bay and RENO (and complemented by T2K [73]). The  
420 constraints on  $\sin^2(\theta_{13})$  by the reactor experiments lead the field and are often used as  
421 external inputs to accelerator neutrino experiments to improve their sensitivity to  $\delta_{CP}$   
422 and mass hierarchy determination. JUNO-TAO [74], a small collaboration within the  
423 larger JUNO experiment, is a next-generation reactor experiment that aims to precisely  
424 measure the isotopic antineutrino yields from the different fission chains. Alongside  
425 this, it aims to explain the ‘5MeV excess’ [75–77] by conducting a search for sterile  
426 neutrinos with a mass scale of around 1eV.

427 Kamland [78] is the only experiment to have observed reactor neutrinos using a  
428 long baseline (flux weighted averaged baseline of  $L \sim 180\text{km}$ ) which allows it to have  
429 sensitivity to  $\Delta m_{12}^2$ . Combined with the SK solar neutrino experiment, the combined  
430 analysis puts the most stringent constraint on  $\Delta m_{12}^2$  [79].

## 431 2.4 Summary

432 Since observing the first evidence of neutrino oscillations in the late 1990’s, numerous  
433 measurements of the mixing parameters have been made. Many experiments use  
434 neutrinos as a tool for discovery of new physics (diffuse supernova background,  
435 neutrinoless double beta decay and others) so the PMNS parameters are summarised  
436 in the Particle Data Group (PDG) review tables. The analysis presented in this thesis  
437 focuses on the 2020 T2K oscillation analysis presented in [80] where the 2018 PDG  
438 constraints [81] were used. These constraints are outlined in Table 2.1.

439 The  $\sin^2(\theta_{13})$  measurement stems from the electron antineutrino disappearance,  
440  $P(\bar{\nu}_e \rightarrow \bar{\nu}_e)$ , and is take as the average best-fit from the combination of Daya Bay,  
441 Reno and Double Chooz. It is often used as a prior uncertainty within other neu-  
442 trino oscillation experiments, typically termed the reactor constraint. The  $\sin^2(\theta_{12})$

Parameter	2018 Constraint
$\sin^2(\theta_{12})$	$0.307 \pm 0.013$
$\Delta m_{21}^2$	$(7.53 \pm 0.18) \times 10^{-5} \text{ eV}^2$
$\sin^2(\theta_{13})$	$(2.12 \pm 0.08) \times 10^{-2}$
$\sin^2(\theta_{23})$ (I.H., Q1)	$0.421^{+0.033}_{-0.025}$
$\sin^2(\theta_{23})$ (I.H., Q2)	$0.592^{+0.023}_{-0.030}$
$\sin^2(\theta_{23})$ (N.H., Q1)	$0.417^{+0.025}_{-0.028}$
$\sin^2(\theta_{23})$ (N.H., Q2)	$0.597^{+0.024}_{-0.030}$
$\Delta m_{32}^2$ (I.H.)	$(-2.56 \pm 0.04) \times 10^{-3} \text{ eV}^2$
$\Delta m_{32}^2$ (N.H.)	$(2.51 \pm 0.05) \times 10^{-3} \text{ eV}^2$

**Table 2.1:** The 2018 Particle Data Group constraints of the oscillation parameters taken from [81]. The value of  $\Delta m_{23}^2$  is given for both normal hierarchy (N.H.) and inverted hierarchy (I.H.) and  $\sin^2(\theta_{23})$  is broken down by whether its value is below (Q1) or above (Q2) 0.5.

parameter is predominantly measured through electron neutrino disappearance,  $P(\nu_e \rightarrow \nu_{\mu,\tau})$ , in solar neutrino experiments. The long-baseline reactor neutrino experiment Kamland also has sensitivity to this parameter and is used in a joint fit to solar data from SNO and SK, using the reactor constraint. Measurements of  $\sin^2(\theta_{23})$  are made by long-baseline and atmospheric neutrino experiments. The PDG value is a joint fit of T2K, NOvA, MINOS and IceCube DeepCore experiments. The latest T2K-only measurement, provided at Neutrino2020 and is the basis of this thesis, is given as  $\sin^2(\theta_{23}) = 0.546^{+0.024}_{-0.046}$  [80]. The PDG constraint on  $\Delta m_{12}^2$  is provided by the KamLAND experiment using solar and geoneutrino data. This measurement utilised a  $\sin^2(\theta_{13})$  constraint from accelerator (T2K, MINOS) and reactor neutrino (Daya Bay, RENO, Double Chooz) experiments. Accelerator measurements make some of the most stringent constraints on  $\Delta m_{23}^2$  although atmospheric experiments have more sensitivity to the mass hierarchy determination. The PDG performs a joint fit of accelerator and atmospheric data, in both normal and inverted hierarchy separately. The latest T2K-only result is  $\Delta m_{32}^2 = 2.49^{+0.058}_{-0.082} \times 10^{-3} \text{ eV}^2$  favouring normal hierarchy [80]. The value of  $\delta_{CP}$  is largely undetermined. CP-conserving values of 0 and  $\pi$  were

<sup>459</sup> rejected with  $\sim 2\sigma$  intervals, as published in Nature, although more recent analysis  
<sup>460</sup> have reduced the rejection intervals to 90%. Since the 2018 PDG publication, there has  
<sup>461</sup> been a new measurement of  $\sin^2(\theta_{13}) = (2.20 \pm 0.07) \times 10^{-2}$  [82], alongside updated  
<sup>462</sup>  $\Delta m_{23}^2$  and  $\sin^2(\theta_{23})$  measurements.

<sup>463</sup> Throughout this thesis, several sample spectra predictions and contours are pre-  
<sup>464</sup> sented which require oscillation parameters to be assumed. Table 2.2 defines two sets  
<sup>465</sup> of oscillation parameters, with “Asimov A” set being close to the preferred values  
<sup>466</sup> from a previous T2K-only fit [83] and “Asimov B” being CP-conserving and further  
<sup>467</sup> from maximal  $\theta_{23}$  mixing.

Parameter	Asimov A	Asimov B
$\Delta m_{12}^2$	$7.53 \times 10^{-5} \text{ eV}^2$	
$\Delta m_{32}^2$	$2.509 \times 10^{-3} \text{ eV}^2$	
$\sin^2(\theta_{12})$	0.304	
$\sin^2(\theta_{13})$	0.0219	
$\sin^2(\theta_{23})$	0.528	0.45
$\delta_{CP}$	-1.601	0.0

**Table 2.2:** Reference values of the neutrino oscillation parameters for two different oscillation parameter sets.

<sup>468</sup> **Chapter 3**

<sup>469</sup> **T2K and SK Experiment Overview**

<sup>470</sup> As the successor of the Kamiokande experiment, the Super-Kamiokande (SK) collaboration has been leading atmospheric neutrino oscillation analyses for over two decades.  
<sup>471</sup> The detector has provided some of the strongest constraints on proton decay and the  
<sup>472</sup> first precise measurements of the  $\Delta m_{23}^2$  and  $\sin^2(\theta_{23})$  neutrino oscillation parameters.  
<sup>473</sup> The ability of the detector to low-energy neutrino events has been significantly im-  
<sup>474</sup> proved with the recent gadolinium doping of the ultra-pure water target. The history,  
<sup>475</sup> detection technique, and operation of the SK detector is described in section 3.1.  
<sup>476</sup>

<sup>477</sup> The Tokai-to-Kamioka (T2K) experiment was one of the first long-baseline ex-  
<sup>478</sup> periments to use both neutrino and antineutrino beams to precisely measure the  
<sup>479</sup> charge parity violation within the neutrino sector. With the SK detector observing  
<sup>480</sup> the oscillated neutrino flux, the T2K experiment observed the first hints of a non-zero  
<sup>481</sup>  $\sin^2(\theta_{13})$  measurement and continues to lead the field with the constraints it provides  
<sup>482</sup> on  $\sin^2(\theta_{13})$ ,  $\sin^2(\theta_{23})$ ,  $\Delta m_{23}^2$  and  $\delta_{CP}$ . The techniques which T2K uses in gener-  
<sup>483</sup> ating its neutrino beam as well as the near-detector used to constrain the flux and  
<sup>484</sup> cross-section parameters used in this analysis are documented in section 3.2.

<sup>485</sup> **3.1 The Super-Kamiokande Experiment**

<sup>486</sup> The SK experiment began taking data in 1996 [84] and has had many modifications  
<sup>487</sup> throughout its lifespan. There have been seven defined periods of data taking as  
<sup>488</sup> noted in Table 3.1. Data taking began in SK-I which ran for five years. Between the

489 SK-I and SK-II periods, a significant proportion of the PMTs were damaged during  
 490 maintenance. Those that survived were equally distributed throughout the detector  
 491 in the SK-II era, which resulted in a reduced photo-coverage. From SK-III onwards,  
 492 repairs to the detector meant the full suite of PMTs was operational. Before the  
 493 start of SK-IV, the data acquisition and electronic systems were upgraded. Between  
 494 SK-IV and SK-V, a significant effort was placed into tank open maintenance and  
 495 repair/replacement of defective PMTs, a task for which the author of this thesis was  
 496 required. Consequently, the detector conditions were significantly different between  
 497 the two operational periods. SK-VI saw the start of the 0.01% gadolinium doped water.  
 498 SK-VII, which started during the writing of this thesis, has increased the gadolinium  
 499 concentration to 0.03% for continued operation [85].

Period	Start Date	End Date	Live-time (days)
I	April 1996	July 2001	1489.19
II	October 2002	October 2005	798.59
III	July 2006	September 2008	518.08
IV	September 2008	May 2018	3244.4
V	January 2019	July 2020	461.02
VI	July 2020	May 2022	583.3
VII	May 2022	Ongoing	N/A

**Table 3.1:** The various SK periods and respective live-time. The SK-VI live-time is calculated until 1<sup>st</sup> April 2022. SK-VII started during the writing of this thesis.

### 500 3.1.1 The SK Detector

501 The basic structure of the Super-Kamiokande (SK) detector is a cylindrical tank with a  
 502 diameter 39.3m and height 41.1m filled with ultrapure water [86]. A diagram of the  
 503 significant components of the SK detector is given in Figure 3.1. The SK detector is  
 504 situated in the Kamioka mine in Gifu, Japan. The mine is underground with roughly  
 505 1km rock overburden (2.7km water equivalent overburden) [87]. At this depth, the

506 rate of cosmic ray muons is significantly decreased to a value of  $\sim 2\text{Hz}$ . The top of  
 507 the tank is covered with stainless steel which is designed as a working platform for  
 508 maintenance, calibration, and location for high voltage and data acquisition electronics.

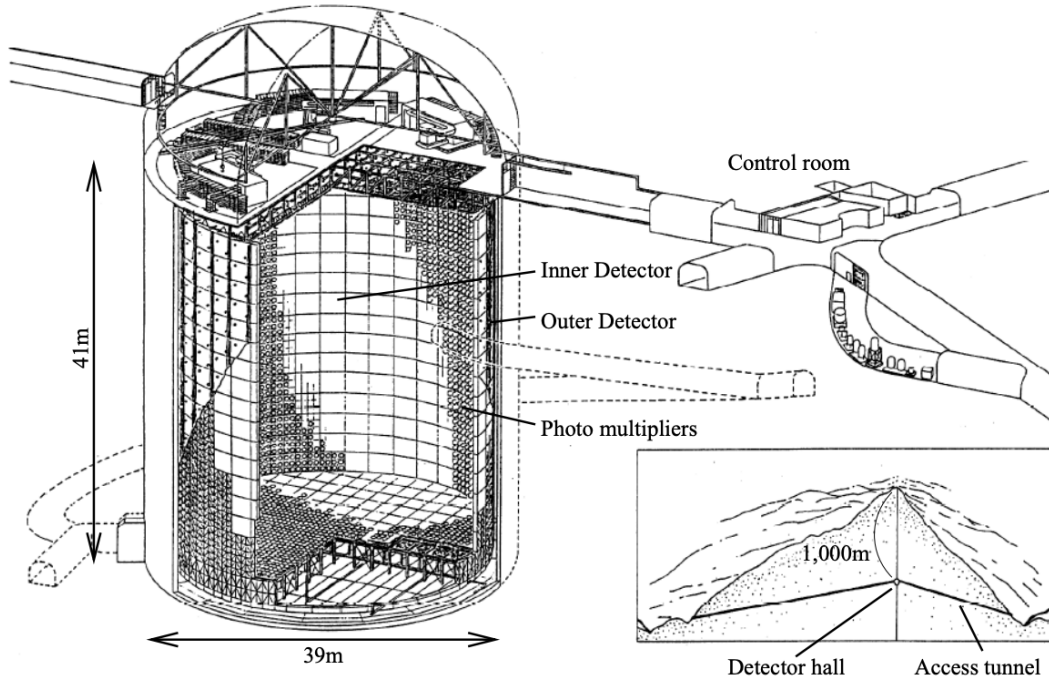


**Figure 3.1:** A schematic diagram of the Super-Kamiokande Detector. Taken from [88].

509 A smaller cylindrical structure (36.2m diameter, 33.8m height) is situated inside the  
 510 tank, with an approximate 2m gap between this structure and the outer tank wall. The  
 511 purpose of this structure is to support the photomultiplier tubes (PMTs). The volume  
 512 inside and outside the support structure is referred to as the inner detector (ID) and  
 513 outer detector (OD), respectively. In the SK-IV era, the ID and OD are instrumented  
 514 by 11,129 50cm and 1,885 20cm PMTs respectively [86]. The ID contains a 32kton  
 515 mass of water. Many analyses performed at SK use a “fiducial volume” defined by the  
 516 volume of water inside the ID excluding some distance to the ID wall. This reduces the  
 517 volume of the detector which is sensitive to neutrino events but reduces radioactive  
 518 backgrounds and allows for better reconstruction performance. The nominal fiducial

519 volume is defined as the area contained inside 2m from the ID wall for a total of  
520 22.5kton water [89].

521 The two regions of the detector (ID and OD) are optically separated with opaque  
522 black plastic. The purpose of this is to determine whether a track entered or exited  
523 the ID. This allows cosmic ray muons and partially contained events to be tagged and  
524 separated from neutrino events entirely contained within the ID. This black plastic is  
525 also used to cover the area between the ID PMTs to reduce photon reflection from the  
526 ID walls. Opposite to this, the OD is lined with a reflective material to allow photons to  
527 reflect around inside the OD until collected by one of the PMTs. Furthermore, each OD  
528 PMT is backed with  $50 \times 50\text{cm}$  plates of wavelength shifting acrylic which increases  
529 the efficiency of light collection [87].

530 In the SK-IV data-taking period, the photocathode coverage of the detector, or the  
531 fraction of the ID wall instrumented with PMTs, is  $\sim 40\%$  [87]. The PMTs have a  
532 quantum efficiency (the ratio of detected electrons to incident photons) of  $\sim 21\%$  for  
533 photons with wavelengths of  $360\text{nm} < \lambda < 390\text{nm}$ . The proportion of photoelectrons  
534 that produce a signal in the dynode of a PMT, termed the collection efficiency, is  
535  $> 70\%$  [87]. The PMTs used within SK are most sensitive to photons with wavelength  
536  $300\text{nm} \leq \lambda \leq 600\text{nm}$  [87]. One disadvantage of using PMTs as the detection media  
537 is that the Earth's geomagnetic field can modify its response. Therefore, a set of  
538 compensation coils is built around the inner surface of the detector to mitigate this  
539 effect [90].

540 As mentioned, the SK detector is filled with ultrapure water, which in a perfect  
541 world would contain no impurities. However, bacteria and organic compounds can  
542 significantly degrade the water quality. This decreases the attenuation length, which  
543 reduces the total number of photons that hit a PMT. To combat this, a sophisticated  
544 water treatment system has been developed [87, 91]. UV lights, mechanical filters,

545 and membrane degasifiers are used to reduce the bacteria, suspended particulates,  
546 and radioactive materials from the water. The flow of water within the tank is also  
547 critical as it can remove stagnant bacterial growth or build-up of dust on the surfaces  
548 within the tank. Gravity drifts impurities in the water towards the bottom of the  
549 tank which, if left uncontrolled, can create asymmetric water conditions between  
550 the top and bottom of the tank. Typically, the water entering the tank is cooled  
551 below the ambient temperature of the tank to control convection and inhibit bacteria  
552 growth. Furthermore, the rate of dark noise hits within PMTs is sensitive to the PMT  
553 temperature [92] so controlling the temperature gradients within the tank is beneficial  
554 for stable measurements.

555 SK-VI is the first phase of the SK experiment to use gadolinium dopants within  
556 the ultrapure water [85]. As such, the SK water system had to be replaced to avoid  
557 removing the gadolinium concentrate from the ultrapure water [93]. For an inverse  
558  $\beta$ -decay (IBD) interaction in a water target, the emitted neutron is thermally captured  
559 on hydrogen. This process releases 2.2MeV  $\gamma$  rays which are difficult to detect as  
560 the resulting Compton scattered electrons are very close to the Cherenkov threshold,  
561 limiting the number of photons produced. Thermal capture of neutrons on gadolin-  
562 ium generates  $\gamma$  rays with higher energy (8MeV [70]) meaning they are more easily  
563 detected. SK-VI has 0.01% Gd loading (0.02% gadolinium sulphate by mass) which  
564 causes  $\approx$  50% of neutrons emitted by IBD to be captured on gadolinium [94, 95].  
565 Whilst predominantly useful for low energy analyses, Gd loading allows better  $\nu/\bar{\nu}$   
566 separation for atmospheric neutrino event selections [96]. Efforts are currently in place  
567 to increase the gadolinium concentrate to 0.03% for  $\approx$  75% neutron capture efficiency  
568 on gadolinium [97]. The final stage of loading targets 0.1% concentrate.

### **569 3.1.2 Calibration**

570 The calibration of the SK detector is documented in [86] and summarised below. The  
571 analysis presented within this thesis is dependent upon ‘high energy events’ (Charged  
572 particles with  $O(> 100)\text{MeV}$  momenta). These are events that are expected to generate  
573 a larger number of photons such that each PMT will be hit with multiple photons.  
574 The reconstruction of these events depends upon the charge deposited within each  
575 PMT and the timing response of each individual PMT. Therefore, the most relevant  
576 calibration techniques to this thesis are outlined.

577 Before installation, 420 PMTs were calibrated to have identical charge responses  
578 and then distributed throughout the tank in a cross-shape pattern (As illustrated by  
579 Figure 3.2). These are used as a standardised measure for the rest of the PMTs installed  
580 at similar geometric positions within SK to be calibrated against. To perform this  
581 calibration, a xenon lamp is located at the center of the SK tank which flashes uniform  
582 light at 1Hz. This allows for geometrical effects, water quality variation, and timing  
583 effects to be measured in-situ throughout normal data-taking periods.

584 When specifically performing calibration of the detector (in out-of-data taking  
585 mode), the water in the tank was circulated to avoid top/bottom asymmetric water  
586 quality. Any non-uniformity within the tank significantly affects the PMT hit proba-  
587 bility through scattering or absorption. This becomes a dominant effect for the very  
588 low-intensity light sources discussed later which are designed such that only one  
589 photon is incident upon a given PMT.

590 The “gain” of a PMT is defined as the ratio of the total charge of the signal produced  
591 compared to the charge of photoelectrons emitted by the photocathodes within the  
592 PMT. To calibrate the signal of each PMT, the “relative” and “absolute” gain values are

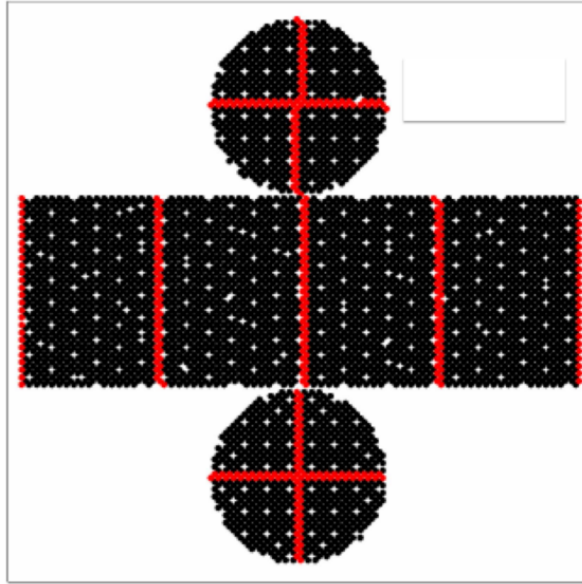


**Figure 3.2:** The location of “standard PMTs” (red) inside the SK detector. Taken from [86].

593 measured. The relative gain is the variation of gain among each of the PMTs whereas  
 594 the absolute gain is the average gain of all PMTs.

595       The relative gain is calibrated as follows. A laser is used to generate two measure-  
 596       ments: a high-intensity flash that illuminates every PMT with a sufficient number of  
 597       photons, and a low-intensity flash in which only a small number of PMTs collect light.  
 598       The first measurement creates an average charge,  $Q_{obs}(i)$  on PMT  $i$ , whereas the second  
 599       measurement ensures that each hit PMT only generates a single photoelectron. For the  
 600       low-intensity measurement, the number of times each PMT records a charge larger  
 601       than 1/4 photoelectrons,  $N_{obs}(i)$ , is counted. The values measured can be expressed as

$$\begin{aligned} Q_{obs}(i) &\propto I_H \times f(i) \times \epsilon(i) \times G(i), \\ N_{obs}(i) &\propto I_L \times f(i) \times \epsilon(i), \end{aligned} \tag{3.1}$$

602       Where  $I_H$  and  $I_L$  is the intensity of the high and low flashes,  $f(i)$  is the acceptance  
 603       efficiency of the  $i^{\text{th}}$  PMT,  $\epsilon(i)$  is the product of the quantum and collection efficiency

604 of the  $i^{\text{th}}$  PMT and  $G(i)$  is the gain of the  $i^{\text{th}}$  PMT. The relative gain for each PMT can  
 605 determined by taking the ratio of these quantities.

606 The absolute gain calibration is performed by observing fixed energy  $\gamma$ -rays of  
 607  $E_{\gamma} \sim 9\text{MeV}$  emitted isotropically from neutron capture on a NiCf source situated at  
 608 the center of the detector. This generates a photon yield of about 0.004 photoelec-  
 609 trons/PMT/event, meaning that  $> 99\%$  of PMT signals are generated from single  
 610 photoelectrons. A charge distribution is generated by performing this calibration over  
 611 all PMTs, and the average value of this distribution is taken to be the absolute gain  
 612 value.

613 As mentioned in subsection 3.1.1, the average quantum and collection efficiency  
 614 for the SK detector is  $\sim 21\%$  and  $> 70\%$  respectively. However, these values do differ  
 615 between each PMT and need to be calibrated accordingly. Consequently, the NiCf  
 616 source is also used to calibrate the “quantum  $\times$  collection” efficiency (denoted “QE”)  
 617 value of each PMT. The NiCf low-intensity source is used as the PMT hit probability  
 618 is proportional to the QE ( $N_{\text{obs}}(i) \propto \epsilon(i)$  in Equation 3.1). A Monte Carlo prediction  
 619 which includes photon absorption, scattering, and reflection is made to estimate the  
 620 number of photons incident on each PMT and the ratio of the number of predicted  
 621 to observed hits is calculated. The difference is attributed to the QE efficiency of that  
 622 PMT. This technique is extended to calculate the relative QE efficiency by normalizing  
 623 the average of all PMTs which removes the dependence on the light intensity.

624 Due to differing cable lengths and readout electronics, the timing response between  
 625 a photon hitting the PMT and the signal being captured by the data acquisition can be  
 626 different between each PMT. Due to threshold triggers (Described in subsection 3.1.3),  
 627 the time at which a pulse reaches a threshold is dependent upon the size of the pulse.  
 628 This is known as the ‘time-walk’ effect and also needs to be accounted for in each PMT.  
 629 To calibrate the timing response, a pulse of light with width 0.2ns is emitted into the

630 detector through a diffuser. Two-dimensional distributions of time and pulse height  
631 (or charge) are made for each PMT and are used to calibrate the timing response. This  
632 is performed in-situ during data taking with the light source pulsing at 0.03Hz.

633 The top/bottom water quality asymmetry is measured using the NiCf calibration  
634 data and cross-referencing these results to the “standard PMTs”. The water attenuation  
635 length is continuously measured by the rate of vertically-downgoing cosmic-ray  
636 muons which enter via the top of the tank.

637 Dark noise is the phenomenon where a PMT registers a pulse that is consistent  
638 with a single photoelectron emitted from photon detection despite the PMT being in  
639 complete darkness. This is predominately caused by two processes. Firstly there is  
640 intrinsic dark noise which is where photoelectrons gain enough thermal energy to be  
641 emitted from the photocathode, and secondly, the radioactive decay of contaminants  
642 inside the structure of the PMT. Typical dark noise rate for PMTs used within SK are  
643  $O(3)$ kHz [87]. This is lower than the expected number of photons generated for a ‘high  
644 energy event’ (As described in subsection 3.1.4) but instability in this value can cause  
645 biases in reconstruction. Dark noise is related to the gain of a PMT and is calibrated  
646 using hits inside a time window recorded before an event trigger [98].

### 647 3.1.3 Data Acquisition and Triggering

648 The analysis presented in this thesis only uses the SK-IV period of the SK experiment  
649 so this subsection focuses on the relevant points of the data acquisition and triggering  
650 systems to that SK period. The earlier data acquisition and triggering systems are  
651 documented in [99, 100].

652 Before the SK-IV period started, the existing front-end electronics were replaced  
653 with “QTC-Based Electrons with Ethernet, QBEE” systems [101]. When the QBEE

observes a signal above a 1/4 photoelectron threshold, the charge-to-time (QTC) converter generates a rectangular pulse. The start of the rectangular pulse indicates the time at which the analog photoelectron signal was received and the width of the pulse indicates the total charge integrated throughout the signal. This is then digitized by time-to-digital converters and sent to the “front-end” PCs. The digitized signal from every QBEE is then chronologically ordered and sent to the “merger” PCs. It is the merger PCs that apply the software trigger. Any triggered events are passed to the “organizer” PC. This sorts the data stream of multiple merger PCs into chronologically ordered events which are then saved to disk. The schematic of data flow from PMTs to disk is illustrated in Figure 3.3.

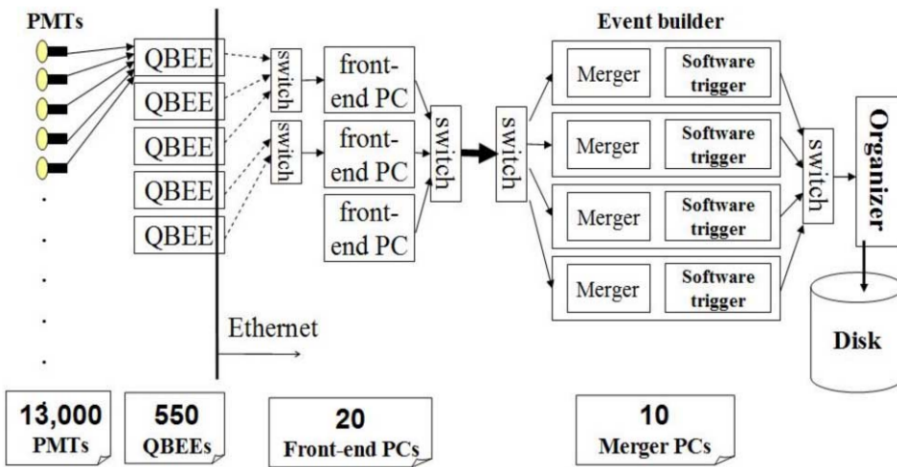


**Figure 3.3:** Schematic view of the data flow through the data acquisition and online system. Taken from [102].

The software trigger (described in [103]) operates by determining the number of PMT hits within a 200ns sliding window,  $N_{200}$ . This window coincides with the maximum time that a Cherenkov photon would take to traverse the length of the SK tank [100]. For lower energy events that generate fewer photons, this technique is useful for eliminating background processes like dark noise and radioactive decay which would be expected to separate in time. When the value of  $N_{200}$  exceeds some threshold, a software trigger is issued. There are several trigger thresholds used within

the SK-IV period which are detailed in Table 3.2. If one of these thresholds is met, the PMT hits within an extended time window are also read out and saved to disk. In the special case of an event that exceeds the SHE trigger but does not exceed the OD trigger, the AFT trigger looks for delayed coincidences of 2.2MeV gamma rays emitted from neutron capture in a  $535\mu\text{s}$  window after the SHE trigger. A similar but more complex “Wideband Intelligent Trigger (WIT)” has been deployed and is described in [104].

Trigger	Acronym	Condition	Extended time window ( $\mu\text{s}$ )
Super Low Energy	SLE	>34/31 hits	1.3
Low Energy	LE	>47 hits	40
High Energy	HE	>50 hits	40
Super High Energy	SHE	>70/58 hits	40
Outer Detector	OD	>22 hits in OD	N/A

**Table 3.2:** The trigger thresholds and extended time windows saved around an event which were utilised throughout the SK-IV period. The exact thresholds can change and the values listed here represent the thresholds at the start and end of the SK-IV period.

### 3.1.4 Cherenkov Radiation

Cherenkov light is emitted from any highly energetic charged particle traveling with relativistic velocity,  $\beta$ , greater than the local speed of light in a medium [105]. Cherenkov light is formed at the surface of a cone with characteristic pitch angle,

$$\cos(\theta) = \frac{1}{\beta n}. \quad (3.2)$$

where  $n$  is the refractive index of the medium. Consequently, the Cherenkov momentum threshold,  $P_{thres}$ , is dependent upon the mass,  $m$ , of the charged particle moving through the medium,

$$P_{thres} = \frac{m}{\sqrt{n^2 - 1}} \quad (3.3)$$

For water, where  $n = 1.33$ , the Cherenkov threshold momentum and energy for various particles are given in Table 3.3. In contrast,  $\gamma$ -rays are detected indirectly via the combination of photons generated by Compton scattering and pair production. The threshold for detection in the SK detector is typically higher than the threshold for photon production. This is due to the fact that the attenuation of photons in the water means that typically  $\sim 75\%$  of Cherenkov photons reach the ID PMTs. Then the collection and quantum efficiencies described in subsection 3.1.1 result in the number of detected photons being lower than the number of photons which reach the PMTs.

Particle	Threshold Momentum (MeV)	Threshold Energy (MeV)
Electron	0.5828	0.7751
Muon	120.5	160.3
Pion	159.2	211.7
Proton	1070.0	1423.1

**Table 3.3:** The threshold momentum and energy for a particle to generate Cherenkov light in ultrapure water, as calculated in Equation 3.2 in ultrapure water which has refractive index  $n = 1.33$ .

The Frank-Tamm equation [106] describes the relationship between the number of Cherenkov photons generated per unit length,  $dN/dx$ , the wavelength of the photons generated,  $\lambda$ , and the relativistic velocity of the charged particle,

$$\frac{d^2N}{dxd\lambda} = 2\pi\alpha \left(1 - \frac{1}{n^2\beta^2}\right) \frac{1}{\lambda^2}. \quad (3.4)$$

696 where  $\alpha$  is the fine structure constant. For a 100MeV momentum electron, approx-  
 697 imately 330 photons will be produced per centimeter in the  $300\text{nm} \leq \lambda \leq 700\text{nm}$   
 698 region which the ID PMTs are most sensitive to [87].

## 699 3.2 The Tokai to Kamioka Experiment

700 The Tokai to Kamioka (T2K) experiment is a long-baseline neutrino oscillation exper-  
 701 iment located in Japan. Proposed in the early 2000s [107, 108] to replace K2K [109],  
 702 T2K was designed to observe electron neutrino appearance whilst precisely measuring  
 703 the oscillation parameters associated with muon neutrino disappearance [110]. The  
 704 experiment consists of a neutrino beam generated at the Japan Proton Accelerator  
 705 Research Complex (J-PARC), a suite of near detectors situated 280m from the beam  
 706 target, and the Super Kamiokande far detector positioned at a 295km baseline. The  
 707 cross-section view of the T2K experiment is drawn in Figure 3.4.

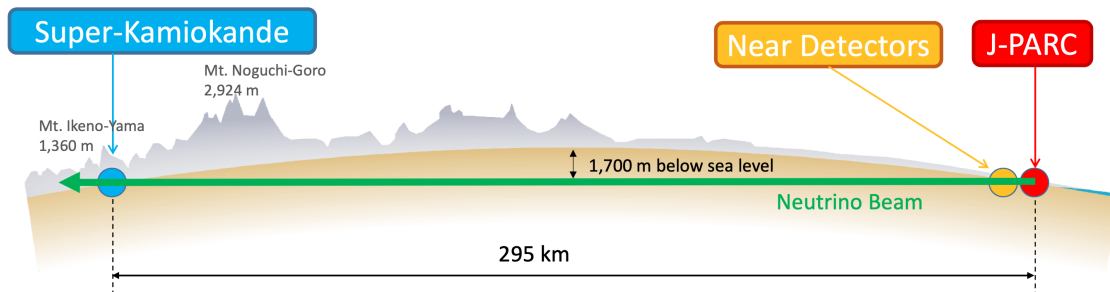


**Figure 3.4:** The cross-section view of the Tokai to Kamioka experiment illustrating the beam generation facility at J-PARC, the near detector situated at a baseline of 280m and the Super Kamiokande far detector situated 295km from the beam target.

The T2K collaboration makes world-leading measurements of the  $\sin^2(\theta_{23})$ ,  $\Delta m_{23}^2$ , and  $\delta_{CP}$  oscillation parameters. Improvements in the precision and accuracy of parameter estimates are still being made by including new data samples and developing the models which describe the neutrino interactions and detector responses [111]. Electron neutrino appearance was first observed at T2K in 2014 [112] with  $7.3\sigma$  significance.

The near detectors provide constraints on the beam flux and cross-section model parameters used within the oscillation analysis by observing the unoscillated neutrino beam. There are a host of detectors situated in the near detector hall (As illustrated in Figure 3.5): ND280 (subsection 3.2.2), INGRID (subsection 3.2.3), NINJA [113], WAGASCI [114], and Baby-MIND [115]. The latter three are not currently used within the oscillation analysis presented within this thesis.

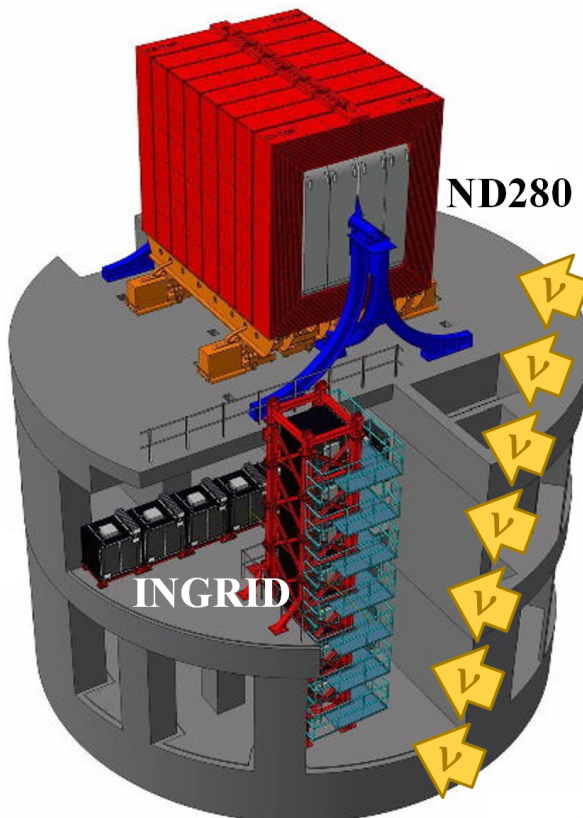


**Figure 3.5:** The near detector suite for the T2K experiment showing the ND280 and INGRID detectors. The distance between the detectors and the beam target is 280m.

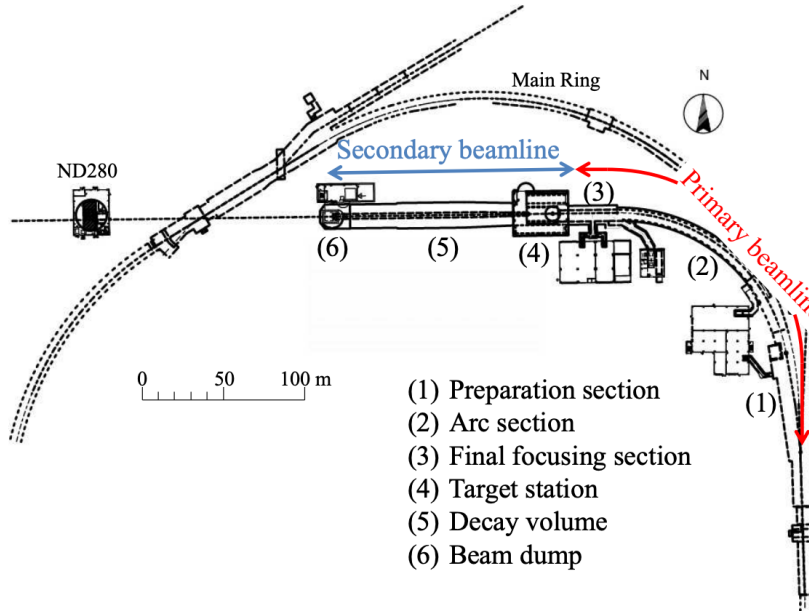
Whilst this thesis presents the ND280 in terms of its purpose for the oscillation analysis, the detector can also make many cross-section measurements at neutrino energies of  $O(1)$ GeV for the different targets within the detector [116, 117]. These measurements are of equal importance as they can lead the way in determining the model parameters used in the interaction models for the future high-precision era of neutrino physics.

DB: Discuss BANFF, PTheta, MaCh3 and covariance

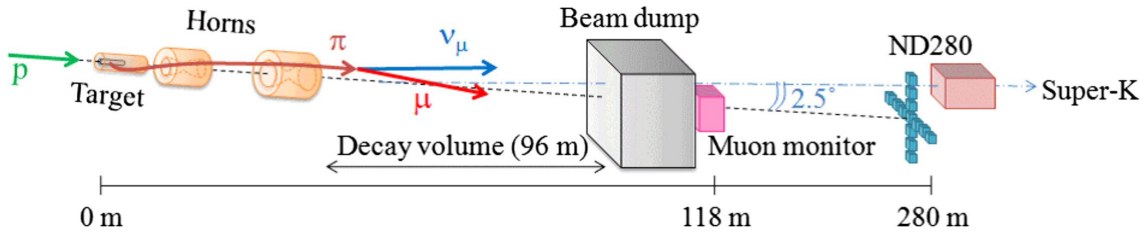
### 3.2.1 The Neutrino Beam

The neutrino beam used within the T2K experiment is described in [59, 118] and summarised below. The accelerating facility at J-PARC is composed of two sections; the primary and secondary beamlines. Figure 3.6 illustrates a schematic of the beamline, focusing mostly on the components of the secondary beamline. The primary beamline has three accelerators that progressively accelerate protons; a linear accelerator, a rapid-cycling synchrotron, and the main-ring (MR) synchrotron. Once fully accelerated by the MR, the protons have a kinetic energy of 30GeV. Eight bunches of these protons, separated by 500ns, are extracted per “spill” from the MR and directed towards a graphite target (a rod of length 91.4cm and diameter 2.6cm). Spills are extracted at 0.5Hz with  $\sim 3 \times 10^{14}$  protons contained per spill.

The secondary beamline consists of three main components: the target station, the decay volume, and the beam dump. The target station is comprised of the target, beam monitors, and three magnetic focusing horns. The proton beam interacts with the graphite target to form a secondary beam of mostly pions and kaons. The secondary beam travels through a 96m long decay volume, generating neutrinos through the following decays [59],



(a) Primary and secondary beamline



(b) Secondary beamline

**Figure 3.6:** Top panel: Bird's eye view of the most relevant part of primary and secondary beamline used within the T2K experiment. The primary beamline is the main-ring proton synchrotron, kicker magnet, and graphite target. The secondary beamline consists of the three focusing horns, decay volume, and beam dump. Figure taken from [118]. Bottom panel: The side-view of the secondary beamline including the focusing horns, beam dump and neutrino detectors. Figure taken from [119].

$$\pi^+ \rightarrow \mu^+ + \nu_\mu$$

$$\pi^- \rightarrow \mu^- + \bar{\nu}_\mu$$

$$K^+ \rightarrow \mu^+ + \nu_\mu$$

$$K^- \rightarrow \mu^- + \bar{\nu}_\mu$$

$$\rightarrow \pi^0 + e^+ + \nu_e$$

$$\rightarrow \pi^0 + e^- + \bar{\nu}_e$$

$$\rightarrow \pi^0 + \mu^+ + \nu_\mu$$

$$\rightarrow \pi^0 + \mu^- + \bar{\nu}_\mu$$

$$K_L^0 \rightarrow \pi^- + e^+ + \nu_e$$

$$K_L^0 \rightarrow \pi^+ + e^- + \bar{\nu}_e$$

$$\rightarrow \pi^- + \mu^+ + \nu_\mu$$

$$\rightarrow \pi^+ + \mu^- + \bar{\nu}_\mu$$

$$\mu^+ \rightarrow e^+ + \bar{\nu}_\mu + \nu_e$$

$$\mu^- \rightarrow e^- + \nu_\mu + \bar{\nu}_e$$

The electrically charged component of the secondary beam is focused towards the far detector by the three magnetic horns. These horns direct charged particles of a particular polarity towards SK whilst defocusing the oppositely charged particles. This allows a mostly neutrino or mostly antineutrino beam to be used within the experiment, denoted as “forward horn current (FHC)” or “reverse horn current (RHC)” respectively.

Figure 3.7 illustrates the different contributions to the FHC and RHC neutrino flux.

The low energy flux is dominated by the decay of pions whereas kaon decay becomes the dominant source of neutrinos for  $E_\nu > 3\text{GeV}$ . The “wrong-sign” component, which is the  $\bar{\nu}_\mu$  background in a  $\nu_\mu$  beam, and the intrinsic irreducible  $\nu_e$  background, are predominantly due to muon decay for  $E_\nu < 2\text{GeV}$ . As the antineutrino production cross-section is smaller than the neutrino cross-section, the wrong-sign component is more dominant in the RHC beam as compared to that in the FHC beam.

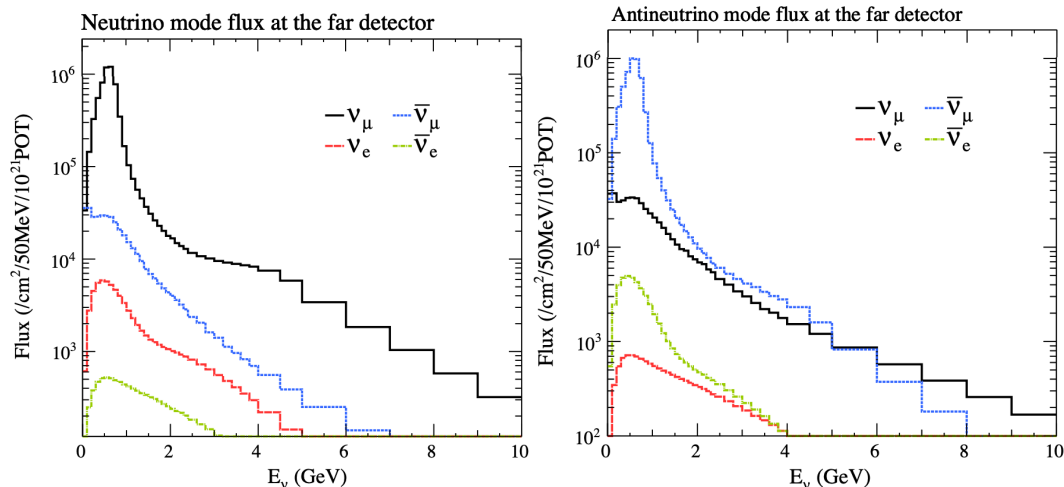


**Figure 3.7:** The Monte Carlo prediction of the energy spectrum for each flavour of neutrino ( $\nu_e$ ,  $\bar{\nu}_e$ ,  $\nu_\mu$  and  $\bar{\nu}_\mu$ ) in the neutrino dominated beam FHC mode (Left) and antineutrino dominated beam RHC mode (Right) expected at SK. Taken from [120].

The beam dump, situated at the end of the decay volume, stops all charged particles other than highly energetic muons ( $p_\mu > 5\text{GeV}$ ). The MuMon detector monitors the

<sup>759</sup> penetrating muons to determine the beam direction and intensity which is used to  
<sup>760</sup> constrain some of the beam flux systematics within the analysis [119, 121].

<sup>761</sup> The T2K experiment uses an off-axis beam to narrow the neutrino energy distribu-  
<sup>762</sup> tion. This was the first implementation of this technique in a long-baseline neutrino  
<sup>763</sup> oscillation experiment after its original proposal [122]. Pion decay,  $\pi \rightarrow \mu + \nu_\mu$ , is a  
<sup>764</sup> two-body decay. Consequently, the neutrino energy,  $E_\nu$ , can be determined based on  
<sup>765</sup> the pion energy,  $E_\pi$ , and the angle at which the neutrino is emitted,  $\theta$ ,

$$E_\nu = \frac{m_\pi^2 - m_\mu^2}{2(E_\pi - p_\pi \cos(\theta))}, \quad (3.5)$$

<sup>766</sup> where  $m_\pi$  and  $m_\mu$  are the mass of the pion and muon respectively. For a fixed  
<sup>767</sup> energy pion, the neutrino energy distribution is dependent upon the angle at which the  
<sup>768</sup> neutrinos are observed from the initial pion beam direction. For the 295km baseline at  
<sup>769</sup> T2K,  $E_\nu = 0.6\text{GeV}$  maximises the electron neutrino appearance probability,  $P(\nu_\mu \rightarrow \nu_e)$ ,  
<sup>770</sup> whilst minimising the muon disappearance probability,  $P(\nu_\mu \rightarrow \nu_\mu)$ . Figure 3.8  
<sup>771</sup> illustrates the neutrino energy distribution for a range of off-axis angles, as well as the  
<sup>772</sup> oscillation probabilities most relevant to T2K.

### <sup>773</sup> 3.2.2 The Near Detector at 280m

<sup>774</sup> Whilst all the near detectors are situated in the same “pit” located at 280m from the  
<sup>775</sup> beamline, the “ND280” detector is the off-axis detector which is situated at the same  
<sup>776</sup> off-axis angle as the Super-Kamiokande far detector. It has two primary functions;  
<sup>777</sup> firstly it measures the neutrino flux and secondly it counts the event rates of different  
<sup>778</sup> types of neutrino interactions. Both of these constrain the flux and cross-section

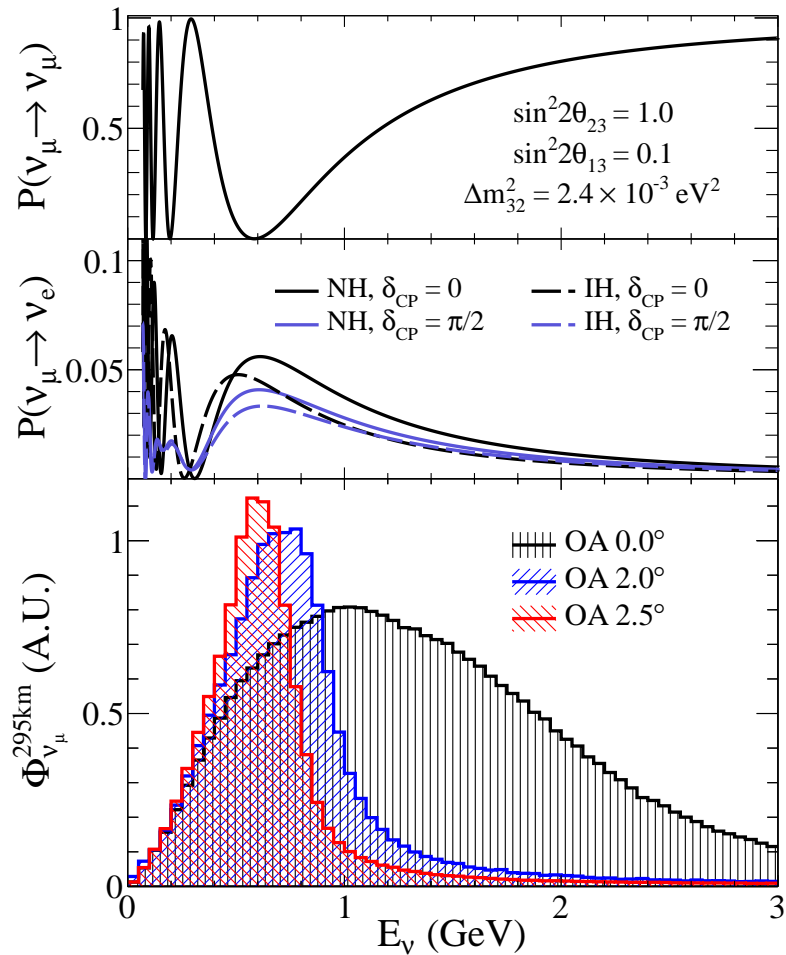


**Figure 3.8:** Top panel: T2K muon neutrino disappearance probability as a function of neutrino energy. Middle panel: T2K electron neutrino appearance probability as a function of neutrino energy. Bottom panel: The neutrino flux distribution for three different off-axis angles (Arbitrary units) as a function of neutrino energy.

systematics invoked within the model for a more accurate prediction of the expected event rate at the far detector.

As illustrated in Figure 3.9, the ND280 detector consists of several sub-detectors. The most important part of the detector for this analysis is the tracker region. This is comprised of two time projection chambers (TPCs) sandwiched between three fine grain detectors (FGDs). The FGDs contain both hydrocarbon plastics and water targets for neutrino interactions and provide track reconstruction near the interaction vertex. The emitted charged particles can then propagate into the TPCs which provide particle identification and momentum reconstruction. The FGDs and TPCs are

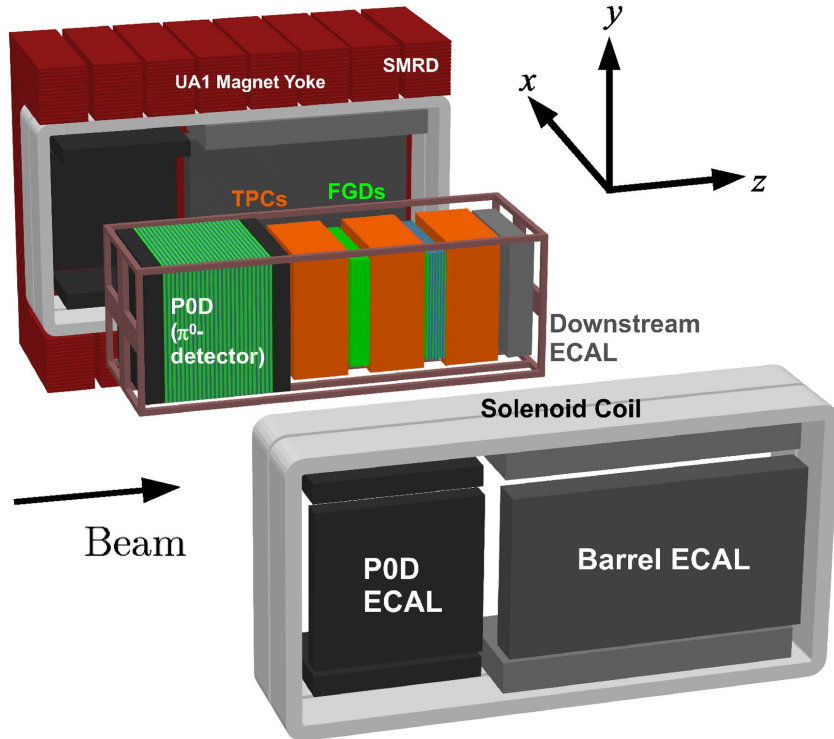


**Figure 3.9:** The components of the ND280 detector. The neutrino beam travels from left to right. Taken from [118].

788 further described in subsubsection 3.2.2.1 and subsubsection 3.2.2.2 respectively. The  
 789 electromagnetic calorimeter (ECAL) encapsulates the tracker region alongside the  $\pi^0$   
 790 detector (P0D). The ECAL measures the deposited energy from photons emitted from  
 791 interactions within the FGD. The P0D constrains the cross-section of neutral current  
 792 interactions which generate neutral pions, which is one of the largest backgrounds in  
 793 the electron neutrino appearance oscillation channel. The P0D and ECAL detectors  
 794 are detailed in subsubsection 3.2.2.3 and subsubsection 3.2.2.4 respectively. The entire  
 795 detector is located within a large yoke magnet which produces a 0.2T magnetic field.  
 796 This design of the magnet also includes a scintillating detector called the side muon  
 797 range detector (SMRD) which is used to track high-angle muons as well as acting as a  
 798 cosmic veto. The SMRD is described in subsubsection 3.2.2.5.

**799 3.2.2.1 Fine Grained Detectors**

800 The T2K tracker region is comprised of two fine grained detectors (FGD) and three  
801 Time Projection Chambers (TPC). A detailed description of the FGD design, construc-  
802 tion, and assembly is found in [123] and summarised below. The FGDs are the primary  
803 target for neutrino interactions with a mass of 1.1 tonnes per FGD. Alongside this,  
804 the FGDs are designed to be able to track short-range particles which do not exit the  
805 FGD. Typically, short-range particles are low momentum and are observed as tracks  
806 that deposit a large amount of energy per unit length. This means the FGD needs  
807 good granularity to resolve these particles. The FGDs have the best timing resolution  
808 ( $\sim 3\text{ns}$ ) of any of the sub-detectors of the ND280 detector. As such, the FGDs are  
809 used for time of flight measurements to distinguish forward going positively charged  
810 particles from backward going negatively charged particles. Finally, any tracks which  
811 pass through multiple sub-detectors are required to be track matched to the FGD.

812 Both FGDs are made from square scintillator planes of side length 186cm and  
813 width 2.02cm. Each plane consists of two layers of 192 scintillator bars in an X or Y  
814 orientation. A wavelength shifting fiber is threaded through the center of each bar and  
815 is read out by a multi-pixel photon counter (MPPC). FGD1 is the most upstream of  
816 the two FGDs and contains 15 planes of carbon plastic scintillator which is a common  
817 target in external neutrino scattering data. As the far detector is a pure water target, 7  
818 of the 15 scintillator planes in FGD2 have been replaced with a hybrid water-scintillator  
819 target. Due to the complexity of the nucleus, nuclear effects can not be extrapolated  
820 between different nuclei. Therefore having the ability to take data on one target which  
821 is the same as external data and another target which is the same as the far detector  
822 target is beneficial for reliable model parameter estimates.

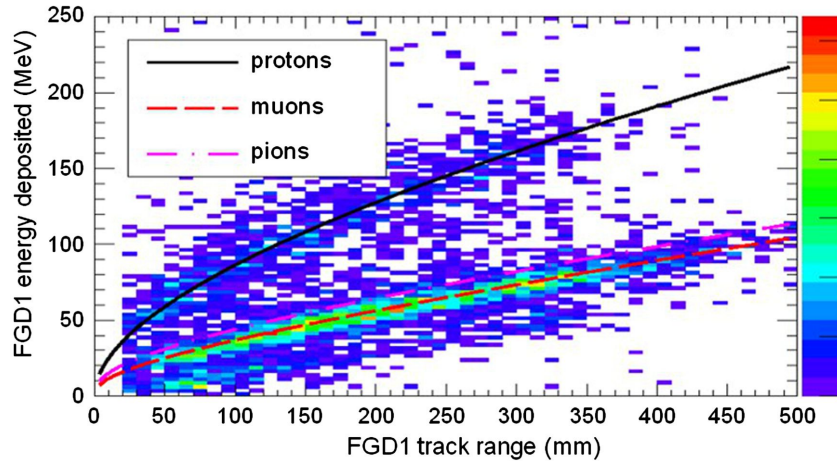


**Figure 3.10:** Comparison of data to Monte Carlo prediction of integrated deposited energy as a function of track length for particles that stopped in FGD1. Taken from [123].

The integrated deposited energy is used for particle identification. The FGD can distinguish protons from other charged particles by comparing the integrated deposited energy from data to Monte Carlo prediction as seen in Figure 3.10.

### 3.2.2.2 Time Projection Chambers

The majority of particle identification and momentum measurements within ND280 are provided by three Time Projection Chambers (TPCs) [124]. The TPCs are located on either side of the FGDs. They are located inside of the magnetic field meaning the momentum of a charged particle can be determined from the bending of the track.

Each TPC module consists of two gas-tight boxes, as shown in Figure 3.11, which are made of non-magnetic material. The outer box is filled with CO<sub>2</sub> which acts as an electrical insulator between the inner box and the ground. The inner box forms the field cage which produces a uniform electric drift field of  $\sim 275\text{V/cm}$  and is filled with an argon gas mixture. Charged particles moving through this gas mixture ionize the gas and the ionised charge is drifted towards micromegas detectors which measure the ionization charge. The time and position information in the readout allows a three-dimensional image of the neutrino interaction.

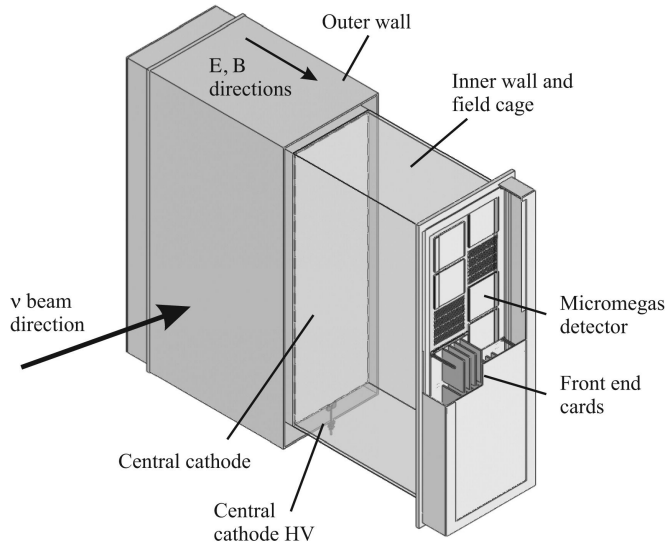


**Figure 3.11:** Schematic design of a Time Projection Chamber detector. Taken from [124].

839     The particle identification of tracks that pass through the TPCs is performed using  
 840     dE/dx measurements. Figure 3.12 illustrates the data to Monte Carlo distributions  
 841     of the energy lost by a charged particle passing through the TPC as a function of the  
 842     reconstructed particle momentum. The resolution is  $7.8 \pm 0.2\%$  meaning that electrons  
 843     and muons can be distinguished. This allows reliable measurements of the intrinsic  $\nu_e$   
 844     component of the beam.

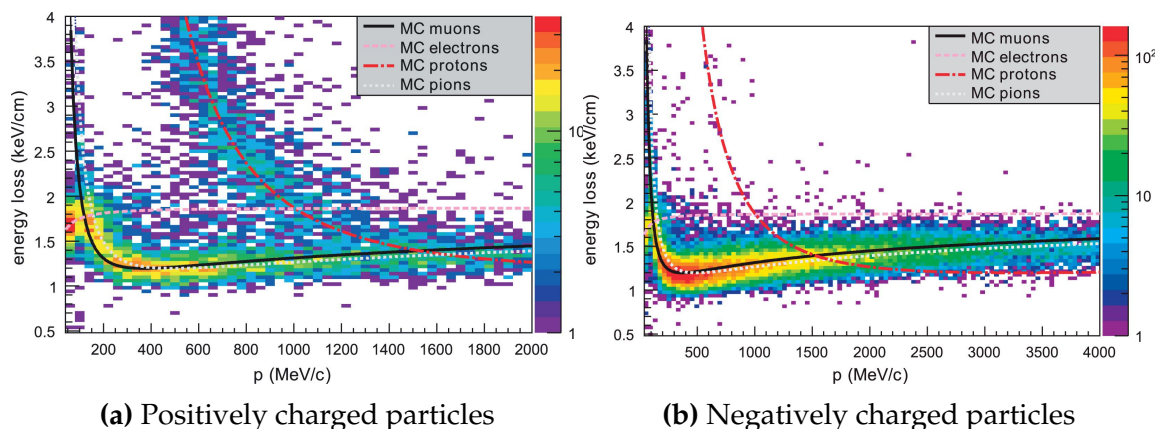


**Figure 3.12:** The distribution of energy loss as a function of reconstructed momentum for charged particles passing through the TPC, comparing data to Monte Carlo prediction. Taken from [124].

**<sup>845</sup> 3.2.2.3  $\pi^0$  Detector**

<sup>846</sup> If one of the  $\gamma$ -rays from a  $\pi^0 \rightarrow 2\gamma$  decay is missed at the far detector, the recon-  
<sup>847</sup> struction will determine that event to be a charge current  $\nu_e$ -like event. This is one of  
<sup>848</sup> the main backgrounds hindering the electron neutrino appearance searches. The  $\pi^0$   
<sup>849</sup> detector (P0D) measures the cross-section of the neutral current induced neutral pion  
<sup>850</sup> production on a water target to constrain this background.

<sup>851</sup> The P0D is a cube of approximately 2.5m length consisting of layers of scintillating  
<sup>852</sup> bars, brass and lead sheets, and water bags as illustrated in Figure 3.13. Two electro-  
<sup>853</sup> magnetic calorimeters are positioned at the most upstream and most downstream  
<sup>854</sup> position in the sub-detector and the water target is situated in between them. The  
<sup>855</sup> scintillator layers are built from two triangular bars orientated in opposite directions  
<sup>856</sup> to form a rectangular layer. Each triangular scintillator bar is threaded with optical  
<sup>857</sup> fiber which is read out by MPPCs. The high-Z brass and lead regions produce electron  
<sup>858</sup> showers from the photons emitted in  $\pi^0$  decay.

<sup>859</sup> The sub-detector can generate measurements of NC1 $\pi^0$  cross-sections on a water  
<sup>860</sup> target by measuring the event rate both with and without the water target, with the  
<sup>861</sup> cross-section on a water target being determined as the difference. The total active  
<sup>862</sup> mass is 16.1 tonnes when filled with water and 13.3 tonnes when empty.

**<sup>863</sup> 3.2.2.4 Electromagnetic Calorimeter**

<sup>864</sup> The electromagnetic calorimeter [126] (ECal) encapsulates the P0D and tracking sub-  
<sup>865</sup> detectors. Its primary purpose is to aid  $\pi^0$  reconstruction from any interaction in  
<sup>866</sup> the tracker. To do this, it measures the energy and direction of photon showers from  
<sup>867</sup>  $\pi^0 \rightarrow 2\gamma$  decay. It can also distinguish pion and muon tracks depending on the shape  
<sup>868</sup> of the photon shower deposited.

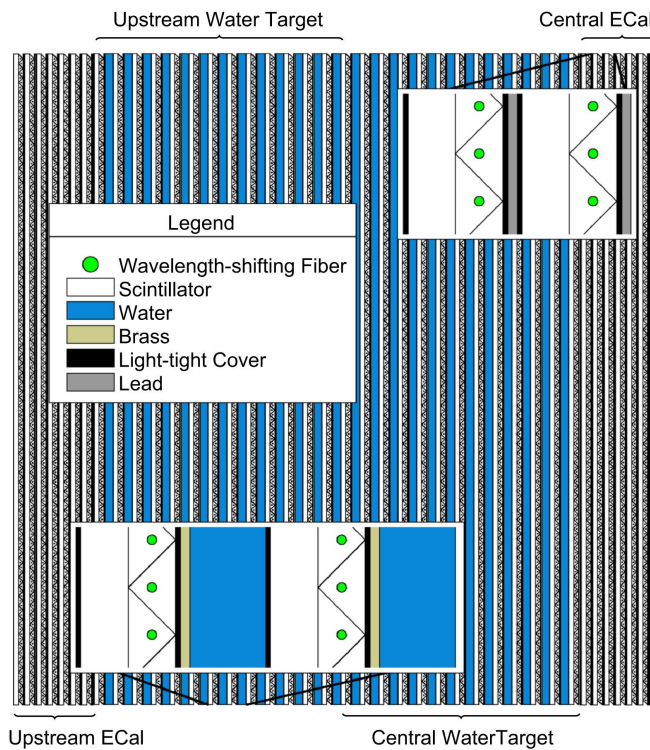


**Figure 3.13:** A schematic of the P0D side-view. Taken from [125].

869        The ECal is comprised of three sections; the P0D ECal which surrounds the P0D,  
 870        the barrel ECal which encompasses the tracking region, and the downstream ECal  
 871        which is situated downstream of the tracker region. The barrel and downstream  
 872        ECals are tracking calorimeters that focus on electromagnetic showers from high-angle  
 873        particles emitted from the tracking sub-detectors. Particularly in the TPC, high-angle  
 874        tracks (those which travel perpendicularly to the beam-axis) can travel along a single  
 875        scintillator bar resulting in very few hits. The width of the barrel and downstream  
 876        ECal corresponds to  $\sim 11$  electron radiation lengths to ensure a significant amount of  
 877        the  $\pi^0$  energy is contained. As the P0D has its own calorimetry which reconstructs  
 878        showers, the P0D ECal determines the energy which escapes the P0D.

879        Each ECal is constructed of multiple layers of scintillating bars sandwiched between  
 880        lead sheets. The scintillating bars are threaded with optical fiber and read out by  
 881        MPPCs. Each sequential layer of the scintillator is orientated perpendicular to the

882 previous which allows a three dimensional event displays. The target mass of the P0D  
883 ECal, barrel ECal, and downstream ECal are 1.50, 4.80 and 6.62 tonnes respectively.

884 **3.2.2.5 Side Muon Range Detector**

885 As illustrated in Figure 3.9, the ECal, FGDs, P0D, and TPCs are enclosed within the  
886 UA1 magnet. Originally designed for the NOMAD [127] experiment and reconditioned  
887 for use in the T2K experiment [128], the UA1 magnet provides a uniform horizontal  
888 magnetic field of 0.2T with an uncertainty of  $2 \times 10^{-4}$ T.

889 Built into the UA1 magnet, the side muon range detector (SMRD) [129] monitors  
890 high-energy muons which leave the tracking region and permeate through the ECal.  
891 It additionally acts as a cosmic muon veto and trigger.

892 **3.2.3 The Interactive Neutrino GRID**

893 The Interactive Neutrino GRID (INGRID) detector is situated within the same “pit” as  
894 the other near detectors. It is aligned with the beam in the “on-axis” position and mea-  
895 sures the beam direction, spread, and intensity. The detector was originally designed  
896 with 16 identical modules [118] (two modules have since been decommissioned) and a  
897 “proton” module. The design of the detector is cross-shaped with length and height  
898 10m × 10m as illustrated in Figure 3.14.

899 Each module is composed of iron sheets interlaced with eleven tracking scintillator  
900 planes for a total target mass of 7.1 tonnes per module. The scintillator design is an X-Y  
901 pattern of 24 bars in both orientations, where each bar contains wave-length shifting  
902 fibers which are connected to multi-pixel photon counters (MPPCs). Each module is  
903 encapsulated inside veto planes to aid the rejection of charged particles entering the  
904 module.

905     The proton module is different from the other modules in that it consists of entirely  
 906   scintillator planes with no iron target. The scintillator bars are also smaller than those  
 907   used in the other modules to increase the granularity of the detector and improve  
 908   tracking capabilities. The module sits in the center of the beamline and is designed to  
 909   give precise measurements of quasi-elastic charged current interactions to evaluate  
 910   the performance of the Monte Carlo simulation of the beamline.

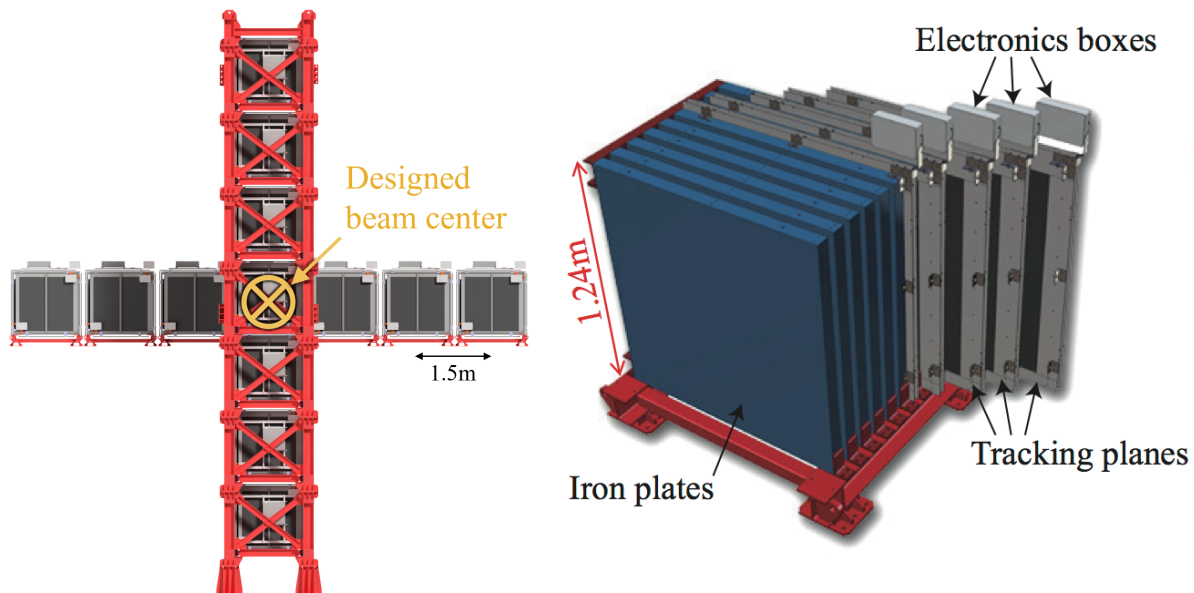


**Figure 3.14:** Left panel: The Interactive Neutrino GRID on-axis Detector. 14 modules are arranged in a cross-shape configuration, with the center modules being directly aligned with the on-axis beam. Right panel: The layout of a single module of the INGRID detector. Both figures are recreated from [118].

911     The INGRID detector can measure the beam direction to an uncertainty of 0.4mrad  
 912   and the beam center within a resolution of 10cm [118]. The beam direction in both the  
 913   vertical and horizontal directions is discussed in [130] and it is found to be in good  
 914   agreement with the MUMON monitor described in subsection 3.2.1.

915 **Chapter 4**

916 **Bayesian Statistics and Markov Chain**  
917 **Monte Carlo Techniques**

918 This thesis presents a Bayesian oscillation analysis. To extract the oscillation parameters,  
919 a Markov Chain Monte Carlo (MCMC) method is used. This chapter explains  
920 the theory of how parameter estimates can be determined using this technique and  
921 condenses the material found in the literature [131–134].

922 The oscillation parameter determination presented within this thesis is built upon  
923 a simultaneous fit to neutrino beam data in the near detector, beam data at SK and  
924 atmospheric data at SK. In total, there are four oscillation parameters of interest  
925 ( $\sin^2(\theta_{23})$ ,  $\sin^2(\theta_{13})$ ,  $\Delta m_{23}^2$ , and  $\delta_{CP}$ ), two oscillation parameters to which this study  
926 will not be sensitive ( $\sin^2(\theta_{12})$ ,  $\Delta m_{12}^2$ ) and many nuisance parameters that control the  
927 systematic uncertainty models invoked within this study.

928 The MCMC technique generates a multi-dimensional probability distribution across  
929 all of the model parameters used in the fit. To determine the parameter estimate of a  
930 single parameter, this multi-dimensional object is integrated over all other parameters.  
931 This process is called Marginalisation and is further described in subsection 4.3.1.  
932 Monte Carlo techniques approximate the probability distribution of each parameter  
933 within the limit of generating infinite samples. As ever, generating a large number of  
934 samples is time and resource-dependent. Therefore, an MCMC technique is utilised  
935 within this analysis to reduce the required number of steps to sufficiently sample the  
936 parameter space. This technique is described in further detail in subsection 4.2.1.

## <sup>937</sup> 4.1 Bayesian Statistics

<sup>938</sup> Bayesian inference treats observable data,  $D$ , and model parameters,  $\vec{\theta}$ , on equal  
<sup>939</sup> footing such that a probability model of both data and parameters is required. This is  
<sup>940</sup> the joint probability distribution  $P(D, \vec{\theta})$  and can be described by the prior distribution  
<sup>941</sup> for model parameters  $P(\vec{\theta})$  and the likelihood of the data given the model parameters  
<sup>942</sup>  $P(D|\vec{\theta})$ ,

$$P(D, \vec{\theta}) = P(D|\vec{\theta})P(\vec{\theta}). \quad (4.1)$$

<sup>943</sup> The prior distribution,  $P(\vec{\theta})$ , describes all previous knowledge about the parameters  
<sup>944</sup> within the model. For example, if the risk of developing health problems is known  
<sup>945</sup> to increase with age, the prior distribution would describe the increase. For the  
<sup>946</sup> purpose of this analysis, the prior distribution is typically the best-fit values taken  
<sup>947</sup> from external data measurements with a Gaussian uncertainty. The prior distribution  
<sup>948</sup> can also contain correlations between model parameters. In an analysis using Monte  
<sup>949</sup> Carlo techniques, the likelihood of measuring some data assuming some set of model  
<sup>950</sup> parameters is calculated by comparing the Monte Carlo prediction generated at that  
<sup>951</sup> particular set of model parameters to the data.

<sup>952</sup> It is parameter estimation that is important for this analysis and as such, we apply  
<sup>953</sup> Bayes' theorem [135] to calculate the probability for each parameter to have a certain  
<sup>954</sup> value given the observed data,  $P(\vec{\theta}|D)$ , which is known as the posterior distribution  
<sup>955</sup> (often termed the posterior). This can be expressed as

$$P(\vec{\theta}|D) = \frac{P(D|\vec{\theta})P(\vec{\theta})}{\int P(D|\vec{\theta})P(\vec{\theta})d\vec{\theta}}. \quad (4.2)$$

956 The denominator in Equation 4.2 is the integral of the joint probability distribution

957 over all values of all parameters used within the fit. For brevity, we say that the  
958 posterior distribution is

$$P(\vec{\theta}|D) \propto P(D|\vec{\theta})P(\vec{\theta}). \quad (4.3)$$

959 In subsection 4.3.1, we see that for the cases used within this analysis, it is reason-  
960 able to know the posterior to some normalisation constant.

## 961 4.2 Monte Carlo Simulation

962 Monte Carlo techniques are used to numerically solve a complex problem that does  
963 not necessarily have an analytical solution. These techniques rely on building a large  
964 ensemble of samples from an unknown distribution and then using the ensemble to  
965 approximate the properties of the distribution.

966 An example that uses Monte Carlo techniques is to calculate the area underneath  
967 a curve. For example, take the problem of calculating the area under a straight line  
968 with gradient  $M = 0.4$  and intercept  $C = 1.0$ . Analytically, one can calculate the area  
969 under the line is equal to 30 units for  $0 \leq x \leq 10$ . Using Monte Carlo techniques,  
970 one can calculate the area under this line by throwing many random values for the  $x$   
971 and  $y$  components of each sample and then calculating whether that point falls below

the line. The area can then be calculated by the ratio of points below the line to the total number of samples thrown multiplied by the total area in which samples were scattered. The study is shown in Figure 4.1 highlights this technique and finds the area under the curve to be 29.9 compared to an analytical solution of 30.0. The deviation of the numerical to analytical solution can be attributed to the number of samples used in the study. The accuracy of the approximation in which the properties of the Monte Carlo samples replicate those of the desired distribution is dependent on the number of samples used. Replicating this study with a differing number of Monte Carlo samples used in each study (As shown in Figure 4.2) highlights how the Monte Carlo techniques are only accurate within the limit of a high number of samples.

Whilst the above example has an analytical solution, these techniques are just as applicable to complex solutions. Clearly, any numerical solution is only as useful as its efficiency. As discussed, the accuracy of the Monte Carlo technique is dependent upon the number of samples generated to approximate the properties of the distribution. Furthermore, if the positions at which the samples are evaluated are not ‘cleverly’ picked, the efficiency of the Monte Carlo technique significantly drops. Given the example in Figure 4.1, if the region in which the samples are scattered significantly extends passed the region of interest, many calculations will be calculated but do not add to the ability of the Monte Carlo technique to achieve the correct result. For instance, any sample evaluated at a  $y \geq 5$  could be removed without affecting the final result. This does bring in an aspect of the ‘chicken and egg’ problem in that to achieve efficient sampling, one needs to know the distribution beforehand.

#### 4.2.1 Markov Chain Monte Carlo

This analysis utilises a multi-dimensional probability distribution, with some dimensions being significantly more constrained than others. This could be from prior

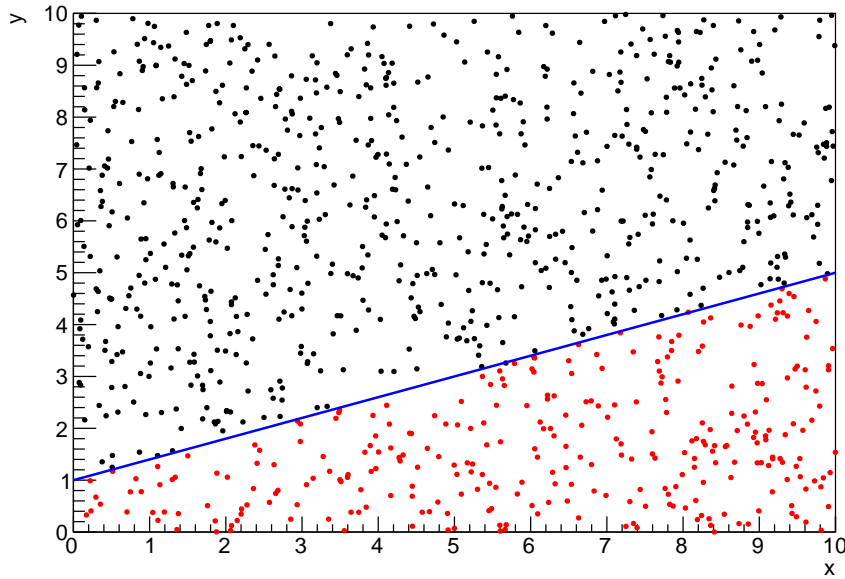


**Figure 4.1:** Example of using Monte Carlo techniques to find the area under the blue line. The gradient and intercept of the line are 0.4 and 1.0 respectively. The area found to be under the curve using one thousand samples is 29.9 units.

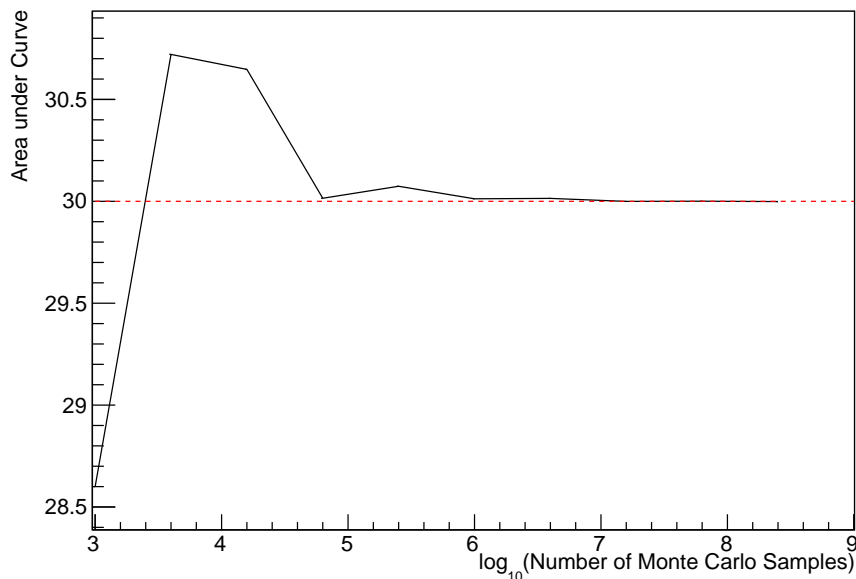


**Figure 4.2:** The area under a line of gradient 0.4 and intercept 1.0 for the range  $0 \leq x \leq 10$  as calculated using Monte Carlo techniques as a function of the number of samples used in each repetition. The analytical solution to the area is 30 units as given by the red line.

knowledge of parameter distributions from external data or un-physical regions in which parameters can not exist. Consequently, the Monte Carlo techniques used need to be as efficient as possible. For this analysis, the Markov Chain Monte Carlo (MCMC) technique is chosen. An MCMC technique is a Monte Carlo technique that uses a Markov chain to select which points at which to sample the parameter distribution. This technique performs a semi-random stochastic walk through the allowable parameter space. This builds a posterior distribution which has the property that the density of sampled points is proportional to the probability density of that parameter. This does mean that the samples produced by this technique are not statistically independent but they will cover the space of the distribution.

A Markov chain functions by selecting the position of step  $\vec{x}_{i+1}$  based on the position of  $\vec{x}_i$ . The space in which the Markov chain selects samples is dependent upon the total number of parameters utilised within the fit, where a discrete point in this space is described by the N-dimensional space  $\vec{x}$ . In a perfectly operating Markov chain, the position of the next step depends solely on the previous step and not on the further history of the chain ( $\vec{x}_0, \vec{x}_1$ , etc.). However, in solving the multi-dimensionality of the fit used within this analysis, each step becomes correlated with several of the steps preceding itself. This behaviour is further explained in subsection 4.2.3. Providing the MCMC chain is well optimised, it will begin to converge towards a unique stationary distribution. The period between the chain's initial starting point and the convergence to the unique stationary distribution is colloquially known as the burn-in period. This is discussed further in subsection 4.2.3. Once the chain reaches the stationary distribution, all points sampled after that point will look like samples from that distribution.

1021      Further details of the theories underpinning MCMC techniques are discussed  
1022    in [132] but can be summarised by the requirement that the chain satisfies the three  
1023    ‘regularity conditions’:

- 1024    • Irreducibility: From every position in the parameter space  $\vec{x}$ , there must exist a  
1025    non-zero probability for every other position in the parameter space to be reached.
- 1026    • Recurrence: Once the chain arrives at the stationary distribution, every step fol-  
1027    lowing from that position must be samples from the same stationary distribution.
- 1028    • Aperiodicity: The chain must not repeat the same sequence of steps at any point  
1029    throughout the sampling period.

1030      The output of the chain after burn-in (ie. the sampled points after the chain  
1031    has reached the stationary distribution) can be used to approximate the posterior  
1032    distribution and model parameters  $\vec{\theta}$ . To achieve the requirement that the unique  
1033    stationary distribution found by the chain be the posterior distribution, one can use  
1034    the Metropolis-Hastings algorithm. This guides the stochastic process depending on  
1035    the likelihood of the current proposed step compared to that of the previous step.  
1036    Implementation and other details of this technique are discussed in subsection 4.2.2.

### 1037 4.2.2 Metropolis-Hastings Algorithm

1038   As a requirement for MCMCs, the Markov chain implemented in this technique must  
1039   have a unique stationary distribution that is equivalent to the posterior distribution.  
1040   To ensure this requirement and that the regularity conditions are met, this analysis  
1041   utilises the Metropolis-Hastings (MH) algorithm [136,137]. For the  $i^{th}$  step in the chain,  
1042   the MH algorithm determines the position in the parameter space to which the chain  
1043   moves to based on the current step,  $\vec{x}_i$ , and the proposed step,  $\vec{y}_{i+1}$ . The proposed step  
1044   is randomly selected from some proposal function  $f(\vec{x}_{i+1} | \vec{x}_i)$ , which depends solely

1045 on the current step (ie. not the further history of the chain). The next step in the chain  
 1046  $\vec{x}_{i+1}$  can be either the current step or the proposed step determined by whether the  
 1047 proposed step is accepted or rejected. To decide if the proposed step is selected, the  
 1048 acceptance probability,  $\alpha(\vec{x}_i, \vec{y}_i)$ , is calculated as

$$\alpha(\vec{x}_i, \vec{y}_{i+1}) = \min \left( 1, \frac{P(\vec{y}_{i+1}|D)f(\vec{x}_i|\vec{y}_{i+1})}{P(\vec{x}_i|D)f(\vec{y}_{i+1}|\vec{x}_i)} \right). \quad (4.4)$$

1049 Where  $P(\vec{y}_{i+1}|D)$  is the posterior distribution as introduced in section 4.1. To  
 1050 simplify this calculation, the proposal function is required to be symmetric such that  
 1051  $f(\vec{x}_i|\vec{y}_{i+1}) = f(\vec{y}_{i+1}|\vec{x}_i)$ . In practice, a multi-variate Gaussian distribution is used to  
 1052 throw parameter proposals from. This reduces Equation 4.4 to

$$\alpha(\vec{x}_i, \vec{y}_{i+1}) = \min \left( 1, \frac{P(\vec{y}_{i+1}|D)}{P(\vec{x}_i|D)} \right). \quad (4.5)$$

1053 After calculating this quantity, a random number,  $\beta$ , is generated uniformly be-  
 1054 tween 0 and 1. If  $\beta \leq \alpha(\vec{x}_i, \vec{y}_{i+1})$ , the proposed step is accepted. Otherwise, the chain  
 1055 sets the next step equal to the current step and this procedure is repeated. This can be  
 1056 interpreted as if the posterior probability of the proposed step is greater than that of  
 1057 the current step, ( $P(\vec{y}_{i+1}|D) \geq P(\vec{x}_i|D)$ ), the proposed step will always be accepted.  
 1058 If the opposite is true, ( $P(\vec{y}_{i+1}|D) \leq P(\vec{x}_i|D)$ ), the proposed step will be accepted  
 1059 with probability  $P(\vec{x}_i|D)/P(\vec{y}_{i+1}|D)$ . This ensures that the Markov chain does not get  
 1060 trapped in any local minima in the potentially non-Gaussian posterior distribution.  
 1061 The outcome of this technique is that the density of steps taken in a discrete region is  
 1062 directly proportional to the probability density in that region.

### <sup>1063</sup> 4.2.3 MCMC Optimisation

<sup>1064</sup> As discussed in subsection 4.2.2, the proposal function invoked within the MH algo-  
<sup>1065</sup> rithm can take any form and the chain will still converge to the stationary distribution.  
<sup>1066</sup> At each set of proposed parameter values, a prediction of the same spectra has to be  
<sup>1067</sup> generated which requires significant computational resources. Therefore, the number  
<sup>1068</sup> of steps taken before the unique stationary distribution is found should be minimised  
<sup>1069</sup> as only steps after convergence add information to the oscillation analysis. Further-  
<sup>1070</sup> more, the chain should entirely cover the allowable parameter space to ensure that all  
<sup>1071</sup> values have been considered. Tuning the distance that the proposal function jumps  
<sup>1072</sup> between steps on a parameter-by-parameter basis can both minimise the length of the  
<sup>1073</sup> burn-in period and ensure that the correlation between step  $\vec{x}_i$  and  $\vec{x}_j$  is sufficiently  
<sup>1074</sup> small.

<sup>1075</sup> The effect of changing the width of the proposal function is highlighted in Figure 4.3.  
<sup>1076</sup> Three scenarios, each with the same underlying stationary distribution (A Gaussian of  
<sup>1077</sup> width 1.0 and mean 0.), are presented. The only difference between the three scenarios  
<sup>1078</sup> is the width of the proposal function, colloquially known as the ‘step size  $\sigma$ ’. Each  
<sup>1079</sup> scenario starts at an initial parameter value of 10.0 which would be considered an  
<sup>1080</sup> extreme variation. For the case where  $\sigma = 0.1$ , it is clear to see that the chain takes  
<sup>1081</sup> a long time to reach the expected region of the parameter. This indicates that this  
<sup>1082</sup> chain would have a large burn-in period and does not converge to the stationary  
<sup>1083</sup> distribution until step  $\sim 500$ . Furthermore, whilst the chain does move towards the  
<sup>1084</sup> expected region, each step is significantly correlated with the previous. Considering  
<sup>1085</sup> the case where  $\sigma = 5.0$ , the chain approaches the expected parameter region almost  
<sup>1086</sup> instantly meaning that the burn-in period is not significant. However, there are clearly  
<sup>1087</sup> large regions of steps where the chain does not move. This is likely due to the chain  
<sup>1088</sup> proposing steps in the tails of the distribution which have a low probability of being

1089 accepted. Consequently, this chain would take a significant number of steps to fully  
 1090 span the allowable parameter region. For the final scenario, where  $\sigma = 0.5$ , you can see  
 1091 a relatively small burn-in period of approximately 100 steps. Once the chain reaches  
 1092 the stationary distribution, it moves throughout the expected region of parameter  
 1093 values many times, sufficiently sampling the full parameter region. This example is a  
 1094 single parameter varying across a continuous distribution and does not fully reflect  
 1095 the difficulties in the many-hundred multi-variate parameter distribution used within  
 1096 this analysis. However, it does give a conceptual idea of the importance of selecting  
 1097 the proposal function and associated step size.

1098 As discussed, step size tuning directly correlates to the average step acceptance  
 1099 rate. If the step size is too small, many steps will be accepted but the chain moves  
 1100 slowly. If the opposite is true, many steps will be rejected as the chain proposes steps  
 1101 in the tails of the distribution. Discussion in [138] suggests that the ‘ideal’ acceptance  
 1102 rate of a high dimension MCMC chain should be approximately  $\sim 25\%$ . An “ideal”  
 1103 step size [138] of

$$\sigma = \frac{2.4}{N_p}, \quad (4.6)$$

1104 where  $N_p$  is the number of parameters included in the MCMC fit. However, the  
 1105 complex correlations between systematics mean that some parameters have to be hand  
 1106 tuned and many efforts have been taken to select a set of parameter-by-parameter step  
 1107 sizes to approximately reach the ideal acceptance rate.

1108 Figure 4.3 highlights the likelihood as calculated by the fit in [DB: Link to AsimovA](#)  
 1109 **Sensitivity Section** as a function of the number of steps in each chain. In practice,  
 1110 many independent MCMC chains are run simultaneously to parallelise the task of

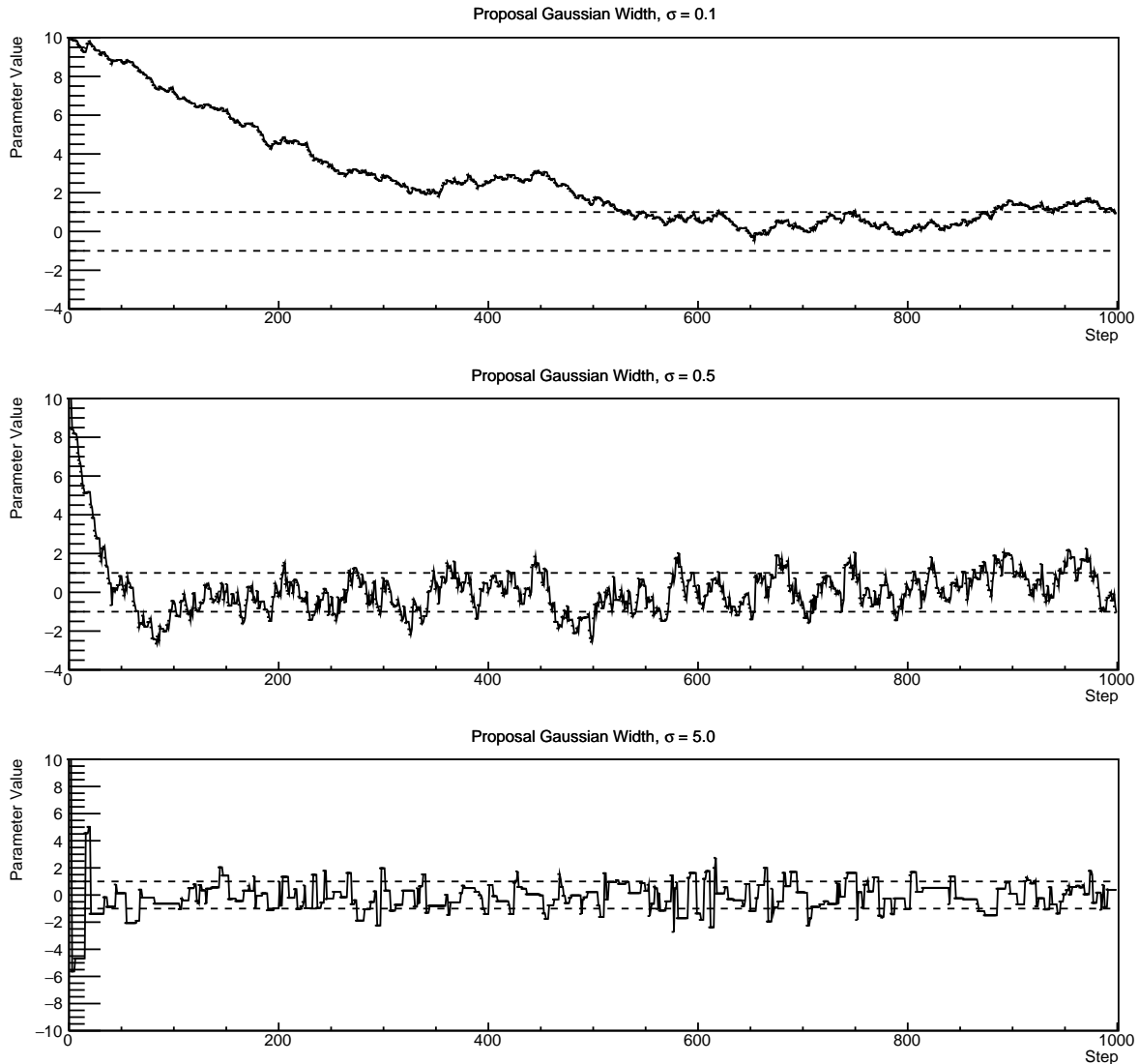


**Figure 4.3:** Three MCMC chains, each with a stationary distribution equal to a Gaussian centered at 0 and width 1 (As indicated by the black dotted lines). All of the chains use a Gaussian proposal function but have different widths (or ‘step size  $\sigma$ ’). The top panel has  $\sigma = 0.1$ , middle panel has  $\sigma = 0.5$  and the bottom panel has  $\sigma = 5.0$ .

1111 performing the fit. This figure overlays the distribution found in each chain. As seen,  
 1112 the likelihood decreases from its initial value and converges towards a stationary  
 1113 distribution after  $\sim 1 \times 10^5$  steps.

1114 Multiple configurations of this analysis have been performed throughout this thesis  
 1115 where different samples or systematics have been used. For all of these configurations,  
 1116 it was found that a burnin period of  $1 \times 10^5$  was sufficient in all cases.

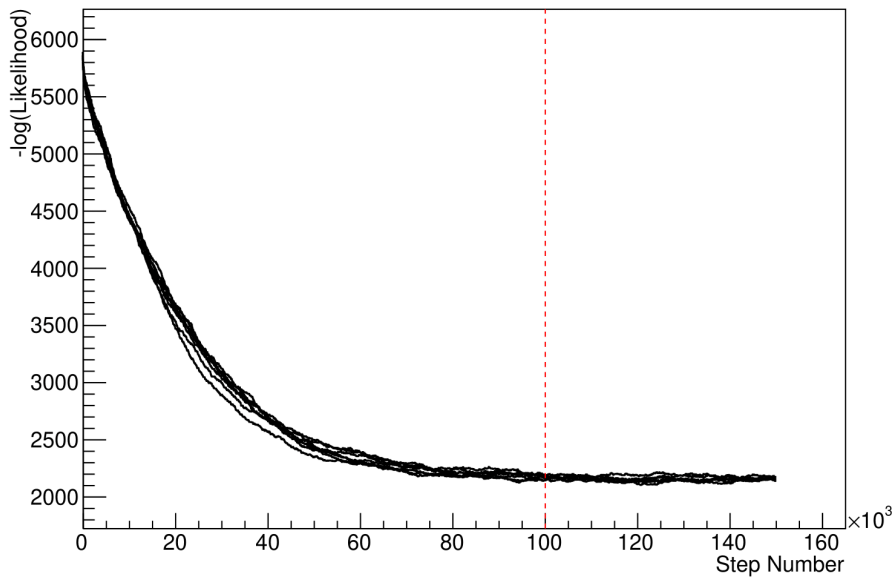


**Figure 4.4:** The log-likelihood from the fit detailed in DB: [Link to AsimovA Sensitivity Section](#) as a function of the number of steps accumulated in each fit. Many independent MCMC chains were run in parallel and overlaid on this plot. The red line indicates the  $1 \times 10^5$  step burn-in period after which the log-likelihood becomes stable.

## 1117 4.3 Understanding the MCMC Results

1118 The previous sections have described how to generate the posterior probability distri-  
1119 bution using Bayesian MCMC techniques. However, this analysis focuses on oscillation  
1120 parameter determination. The posterior distribution output from the chain is a high  
1121 dimension object, with as many dimensions as there are parameters included in the os-  
1122 cillation analysis. However, this multi-dimensional object is difficult to conceptualize  
1123 so parameter estimations are often presented in one or two-dimensional projections  
1124 of this probability distribution. To do this, we invoke the marginalisation technique  
1125 highlighted in subsection 4.3.1.

### <sup>1126</sup> 4.3.1 Marginalisation

<sup>1127</sup> The output of the MCMC chain is a highly dimensional probability distribution  
<sup>1128</sup> which is very difficult to interpret. From the standpoint of an oscillation analysis  
<sup>1129</sup> experiment, the one or two-dimensional ‘projections’ of the oscillation parameters of  
<sup>1130</sup> interest are most relevant. Despite this, the best fit values and uncertainties on the  
<sup>1131</sup> oscillation parameters of interest should correctly encapsulate the correlations to the  
<sup>1132</sup> other systematic uncertainties (colloquially called ‘nuisance’ parameters). For this joint  
<sup>1133</sup> beam and atmospheric analysis, the oscillation parameters of interest are  $\sin^2(\theta_{23})$ ,  
<sup>1134</sup>  $\sin^2(\theta_{13})$ ,  $\Delta m_{23}^2$ , and  $\delta_{CP}$ . All other parameters (Including the oscillation parameter  
<sup>1135</sup> this fit is insensitive to) are deemed nuisance parameters. To generate these projections,  
<sup>1136</sup> we rely upon integrating the posterior distribution over all nuisance parameters. This  
<sup>1137</sup> is called marginalisation. A simple example of this technique is to imagine the scenario  
<sup>1138</sup> where two coins are flipped. To determine the probability that the first coin returned  
<sup>1139</sup> a ‘head’, the exact result of the second coin flip is disregarded and simply integrated  
<sup>1140</sup> over. For the parameters of interest,  $\vec{\theta}_i$ , we can calculate the marginalised posterior by  
<sup>1141</sup> integrating over the nuisance parameters,  $\vec{\theta}_n$ . In this case, Equation 4.2 becomes

$$P(\vec{\theta}_i|D) = \frac{\int P(D|\vec{\theta}_i, \vec{\theta}_n)P(\vec{\theta}_i, \vec{\theta}_n)d\vec{\theta}_n}{\int P(D|\vec{\theta})P(\vec{\theta})d\vec{\theta}} \quad (4.7)$$

<sup>1142</sup> Where  $P(\vec{\theta}_i, \vec{\theta}_n)$  encodes the prior knowledge about the uncertainty and correlations  
<sup>1143</sup> between the parameters of interest and the nuisance parameters. In practice, this  
<sup>1144</sup> is simply taking the one or two-dimensional projection of the multi-dimensional  
<sup>1145</sup> probability distribution.

Whilst in principle an easy solution to a complex problem, correlations between the interesting and nuisance parameters can bias the marginalised results. A similar effect is found when the parameters being marginalised over have non-Gaussian probability distributions. For example, Figure 4.5 highlights the marginalisation bias in the probability distribution found for a parameter when requiring a correlated parameter to have a positive parameter value. Due to the complex nature of this oscillation parameter fit presented in this thesis, there are correlations occurring between the oscillation parameters of interest and the other nuisance parameters included in the fit.

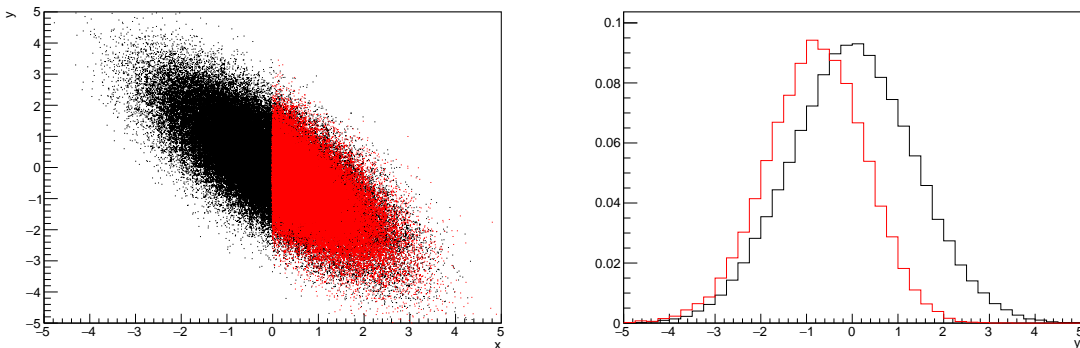


**Figure 4.5:** Left: The two dimensional probability distribution for two correlated parameters  $x$  and  $y$ . The red distribution shows the two dimensional probability distribution when  $0 \leq x \leq 5$ . Right: The marginalised probability distribution for the  $y$  parameter found when requiring the  $x$  to be bound between  $-5 \leq x \leq 5$  and  $0 \leq x \leq 5$  for the black and red distribution, respectively.

### 4.3.2 Parameter Estimation and Credible Intervals

The purpose of this analysis is to determine the best fit values for the oscillation parameters that the beam and atmospheric samples are sensitive to:  $\sin^2(\theta_{23})$ ,  $\sin^2(\theta_{13})$ ,  $\Delta m_{23}^2$ , and  $\delta_{CP}$ . Typically, the results presented take the form of one or two-dimension marginalised probability distributions for the appearance ( $\sin^2(\theta_{13})$  and  $\delta_{CP}$ ) and disappearance ( $\sin^2(\theta_{23})$  and  $\Delta m_{23}^2$ ) parameters. The posterior probability density

<sub>1161</sub> taken from the output MCMC chain is binned in these parameters. The parameter  
<sub>1162</sub> best-fit point is then taken to be the value that has the highest posterior probability.  
<sub>1163</sub> This is performed in both one and two-dimensional projections.

<sub>1164</sub> However, the single best-fit point in a given parameter is not of much use on its  
<sub>1165</sub> own. We would also like to determine the uncertainty, or credible interval, on that  
<sub>1166</sub> best-fit point. The definition of the  $1\sigma$  credible interval is that we have 68% belief that  
<sub>1167</sub> the parameter is within those bounds. For a more generalised definition, the credible  
<sub>1168</sub> interval is the region,  $R$ , of the posterior distribution that contains a specific fraction of  
<sub>1169</sub> the total probability, such that

$$\int_R P(\theta|D)d\theta = \alpha \quad (4.8)$$

<sub>1170</sub> Where  $\theta$  is the parameter on which we calculate the credible interval. This technique  
<sub>1171</sub> then calculates the  $\alpha \times 100\%$  credible interval.

<sub>1172</sub> In practice, this analysis uses the highest posterior density (HPD) credible intervals  
<sub>1173</sub> which are calculated through the following method. First, the probability distribution  
<sub>1174</sub> is area-normalised such that it has an integrated area equal to 1.0. The bins of proba-  
<sub>1175</sub> bility are then summed from the highest to lowest until the sum exceeds the  $1\sigma$  level  
<sub>1176</sub> (0.68 in this example). This process is repeated for a range of credible intervals, notably  
<sub>1177</sub> the  $1\sigma$ ,  $2\sigma$  and  $3\sigma$  along with other levels where the critical values for each level can  
<sub>1178</sub> be found in [139]. This process can be repeated for the two-dimensional probability  
<sub>1179</sub> distributions by creating two-dimensional contours of credible intervals rather than a  
<sub>1180</sub> one-dimensional result.

---

### <sup>1181</sup> 4.3.3 Bayesian Model Comparisons

<sup>1182</sup> Due to the matter resonance, this analysis has some sensitivity to the mass hierarchy  
<sup>1183</sup> of neutrino states (whether  $\Delta m_{23}^2$  is positive or negative) and the octant of  $\sin^2(\theta_{23})$   
<sup>1184</sup> . The Bayesian approach utilised within this analysis gives an intuitive method of  
<sup>1185</sup> model comparison by determining which hypothesis is most favourable. Taking the  
<sup>1186</sup> ratio of Equation 4.3 for the two hypotheses of normal hierarchy,  $NH$ , and inverted  
<sup>1187</sup> hierarchy,  $IH$ , gives

$$\frac{P(\vec{\theta}_{NH}|D)}{P(\vec{\theta}_{IH}|D)} = \frac{P(D|\vec{\theta}_{NH})}{P(D|\vec{\theta}_{IH})} \times \frac{P(\vec{\theta}_{NH})}{P(\vec{\theta}_{IH})}. \quad (4.9)$$

<sup>1188</sup> The middle term defines the Bayes factor which is a data-driven interpretation of  
<sup>1189</sup> how strong the data prefers one hierarchy to the other. For this analysis, equal priors  
<sup>1190</sup> on both mass hierarchy hypotheses are chosen ( $P(\vec{\theta}_{NH}) = P(\vec{\theta}_{IH}) = 0.5$ ). In practice,  
<sup>1191</sup> the MCMC chain proposes a value of  $|\Delta m_{23}^2|$  and then applies a 50% probability  
<sup>1192</sup> that the value is sign flipped. Consequently, the Bayes factor can be calculated from  
<sup>1193</sup> the ratio of the probability density in either hypothesis. This equates to counting the  
<sup>1194</sup> number of steps taken in the normal and inverted hierarchies and taking the ratio. The  
<sup>1195</sup> same approach can be taken to compare the upper octant (UO) compared to the lower  
<sup>1196</sup> octant (LO) hypothesis of  $\sin^2(\theta_{23})$ .

<sup>1197</sup> Whilst the value of the Bayes factor should always be shown, the Jeffreys scale [140]  
<sup>1198</sup> (highlighted in Table 4.1) gives an indication of the strength of preference for one model  
<sup>1199</sup> compared to the other. Other interpretations of the strength of preference of a model  
<sup>1200</sup> exist, e.g. the Kass and Raferty Scale [141].

$\log_{10}(B_{AB})$	$B_{AB}$	Strength of Preference
< 0.0	< 1	No preference for hypothesis A (Supports hypothesis B)
0.0 – 0.5	1.0 – 3.16	Preference for hypothesis A is weak
0.5 – 1.0	3.16 – 10.0	Preference for hypothesis A is substantial
1.0 – 1.5	10.0 – 31.6	Preference for hypothesis A is strong
1.5 – 2.0	31.6 – 100.0	Preference for hypothesis A is very strong
> 2.0	> 100.0	Decisive preference for hypothesis A

**Table 4.1:** Jeffreys scale for strength of preference for two models  $A$  and  $B$  as a function of the calculated Bayes factor ( $B_{AB} = B(A/B)$ ) between the two models [140]. The original scale is given in terms of  $\log_{10}(B(A/B))$  but converted to linear scale for easy comparison throughout this thesis.

#### 1201 4.3.4 Comparison of MCMC Output to Expectation

1202 To ensure the fit is performing well, a best-fit spectra is produced using the posterior  
 1203 probability distribution and compared with the data, allowing easy by-eye compar-  
 1204 isons to be made. A simple method of doing this is to perform a comparison in the  
 1205 fitting parameters (For instance, the reconstructed neutrino energy and lepton direc-  
 1206 tion for T2K far detector beam samples) of the spectra generated by the MCMC chain to  
 1207 ‘data’. This ‘data’ could be true data or some variation of Monte Carlo prediction. This  
 1208 allows easy comparison of the MCMC probability distribution to the data. To perform  
 1209 this,  $N$  steps from the post burn-in MCMC chain are randomly selected (Where for all  
 1210 plots of this style in this thesis,  $N = 3000$ ). From these, the Monte Carlo prediction at  
 1211 each step is generated by reweighting the model parameters to the values specified at  
 1212 that step. Due to the probability density being directly correlated with the density of  
 1213 steps in a certain region, parameter values close to the best fit value are most likely to  
 1214 be selected.

1215 In practice, for each bin of the fitting parameters has a probability distribution  
 1216 of event rates, with one entry per sampled MCMC step. This distribution is binned  
 1217 where the bin with the highest probability is selected as the mean and an error on

1218 the width of this probability distribution is calculated using the approach highlighted  
1219 in subsection 4.3.2. Consequently, the best fit distribution in the fit parameter is not  
1220 necessarily that which would be attained by reweighting the Monte Carlo prediction  
1221 to the most probable parameter values.

1222 A similar study can be performed to illustrate the freedom of the model parameter  
1223 space prior to the fit. This can be done by throwing parameter values from the prior  
1224 uncertainty of each parameter. This becomes troublesome for parameters with no  
1225 prior uncertainty as the range is technically infinite. Where applicable solutions to  
1226 remove these have been addressed.

<sub>1227</sub> **Chapter 5**

<sub>1228</sub> **Simulation, Reconstruction, and Event  
Reduction**

<sub>1230</sub> As a crucial part of the oscillation analysis, an accurate prediction of the expected  
<sub>1231</sub> neutrino spectrum at the far detector is required. This includes modeling the flux  
<sub>1232</sub> generation, neutrino interactions, and detector effects. All of the simulation packages  
<sub>1233</sub> required to do this are briefly described in section 5.1. The reconstruction of neutrino  
<sub>1234</sub> events inside the far detector, including the `fitQun` algorithm, is documented in  
<sub>1235</sub> section 5.2. This also includes data quality checks of the SK-V data which the author  
<sub>1236</sub> performed for the T2K oscillation analysis presented at Neutrino 2020 [80]. Finally,  
<sub>1237</sub> section 5.3 describes the steps taken in the SK detector to trigger on events of interest  
<sub>1238</sub> whilst removing the comparatively large rate of cosmic ray muon events.

<sub>1239</sub> **5.1 Simulation**

<sub>1240</sub> In order to generate a Monte Carlo prediction of the expected event rate at the far  
<sub>1241</sub> detector, all the processes in the beam and atmospheric flux, neutrino interaction, and  
<sub>1242</sub> detector need to be modeled. Each of these parts is individually modeled and each of  
<sub>1243</sub> them is detailed below.

<sub>1244</sub> The beamline simulation consists of three distinct parts: the initial hadron inter-  
<sub>1245</sub> action modeled by FLUKA [142], the target station geometry and particle tracking

performed by JNUBEAM, [143, 144] and any hadronic re-interactions simulated by GCALOR [145]. The primary hadronic interactions are  $O(10)\text{GeV}$ , where FLUKA matches external cross-section data better than GCALOR [146]. However, FLUKA is not very adaptable so a small simulation is built to model the interactions in the target and the output is then passed to JNUBEAM and GCALOR for propagation. The hadronic interactions are tuned to data from the NA61/SHINE [147–149] and HARP [150] experiments. The tuning is done by reweighting the FLUKA and GCALOR predictions to match the external data multiplicity and cross-section measurements, based on final state particle kinematics [146]. The culmination of this simulation package generates the predicted flux for neutrino and antineutrino beam modes which are illustrated in Figure 3.7.

The atmospheric neutrino flux predictions are simulated by the HKKM model [43, 45]. The primary cosmic ray flux is tuned to AMS [151] and BESS [152] data assuming the US-standard atmosphere '76 [153] density profile and includes geomagnetic field effects. The primary cosmic rays interact to generate pions and muons. The interaction of these secondary particles to generate neutrinos is handled by DPMJET-III [154] for energies above 32GeV and JAM [45, 155] for energies below that value **DB: Question for Giles: Why different generators for above/below 32GeV?**. These hadronic interactions are tuned to BESS and L3 data [156, 157] using the same methodology as the tuning of the beamline simulation. The energy and cosine zenith predictions of  $\nu_e, \bar{\nu}_e, \nu_\mu, \bar{\nu}_\mu$  flux are given in Figure 2.3 and Figure 2.5, respectively. The flux is approximately symmetrical and peaked around the horizon ( $\cos(\theta_Z) = 0.0$ ). This is because horizontally-going pions and kaons can travel further than their vertically-going counterparts resulting in a larger probability of decaying to neutrinos. The symmetry is broken in low-energy neutrinos due to geomagnetic effects, which modify the track of the primary cosmic rays. Updates to the HKKM model are currently ongoing [158].

Once a flux prediction has been made for all three detectors, NEUT 5.4.0 [159, 160] models the interactions of the neutrinos in the detectors. For the purposes of this analysis, quasi-elastic (QE), meson exchange (MEC), single meson production (PROD), coherent pion production (COH), and deep inelastic scattering (DIS) interactions are simulated. These interaction categories can be further broken down by whether they were propagated via a  $W^\pm$  boson in Charged Current (CC) interactions or via a  $Z^0$  boson in Neutral Current (NC) interactions. CC interactions have a charged lepton in the final state, which can be flavour-tagged in reconstruction to determine the flavour of the neutrino. In contrast, NC interactions have a neutrino in the final state so no flavour information can be determined from the observables left in the detector after an interaction. This is the reason why NC events are assumed to not oscillate within this analysis. Both CC and NC interactions are modeled for all the above interaction categories, other than MEC interactions which are only modeled for CC events. The SK detector is only sensitive to charged particles, so all charged current interactions are simulated whilst only neutral current processes that produce charged mesons (NCDIS, NCCOH, and NCProd) are modeled. NC MEC interactions can only produce charged particles through secondary re-interactions which is a low cross-section process.

As illustrated in Figure 5.1, CC QE interactions dominate the low-energy cross-section of neutrino interactions. The NEUT implementation adopts the Llewellyn Smith [161] model for neutrino-nucleus interactions, where the nuclear ground state of any bound nucleons (neutrino-oxygen interactions) is approximated by a spectral-function [162] model that simulates the effects of Fermi momentum and Pauli blocking. The cross-section of QE interactions are controlled by vector and axial-vector form factors parameterised by the BBBA05 [163] model and a dipole form factor with  $M_A^{QE} = 1.21\text{GeV}$  fit to external data [164], respectively. NEUT implements the Valencia [165] model to simulate MEC events, where two nucleons and two holes in the nuclear target are produced (Often called 2p2h interactions).

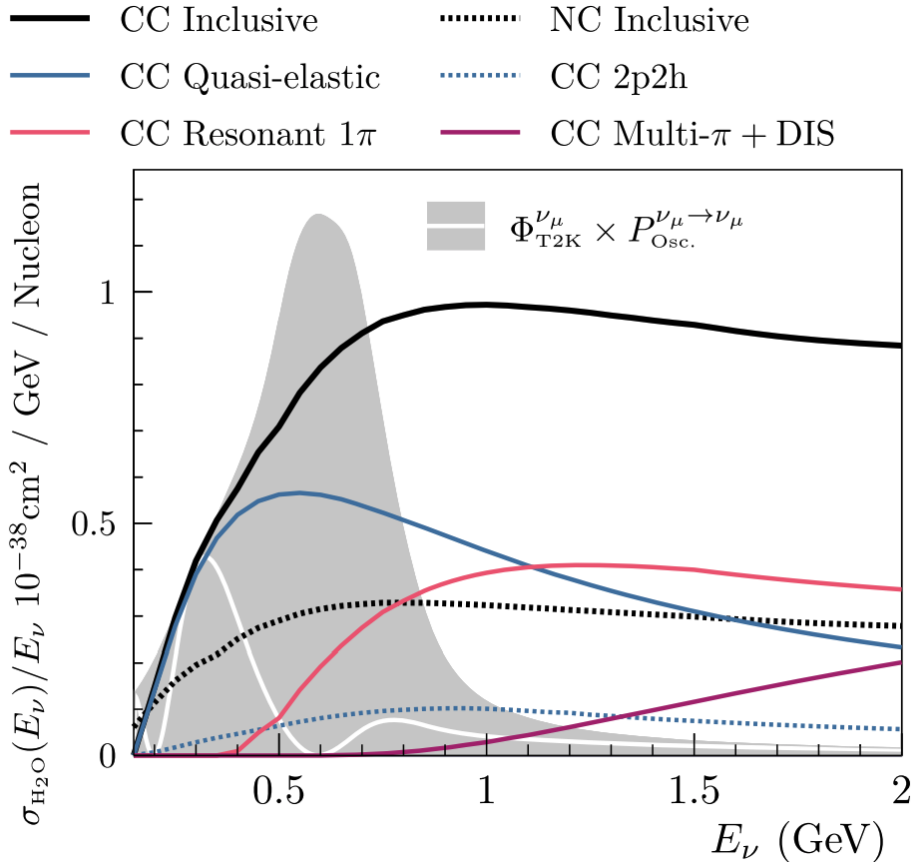


**Figure 5.1:** The NEUT prediction of the  $\nu_\mu$ -H<sub>2</sub>O cross-section overlaid on the T2K  $\nu_\mu$  flux. The charged current (black, solid) and neutral current (black, dashed) inclusive, charged current quasi-elastic (blue, solid), charged current 2p2h (blue, dashed), charged current single pion production (pink), and charged current multi- $\pi$  and DIS (Purple) cross-sections are illustrated. Figure taken from [159].

1299 For neutrinos of energy  $O(1)\text{GeV}$ , PROD interactions become dominant. These  
 1300 predominantly produce charged and neutral pions although  $\gamma$ , kaon, and  $\eta$  production  
 1301 is also considered. To simulate these interactions, the Berger-Sehgal [166] model is  
 1302 implemented within NEUT. It simulates the excitation of a nucleon from a neutrino  
 1303 interaction, production of an intermediate baryon, and the consequential decay to a  
 1304 single meson or  $\gamma$ . Pions can also be produced through COH interactions, which occur  
 1305 when the incoming neutrino interacts with the entire oxygen nuclei target leaving a  
 1306 single pion outside of the nucleus. NEUT utilises the Berger-Sehgal [167] model to  
 1307 simulate these COH interactions.

1308 DIS and multi- $\pi$  producing interactions become the most dominant for energies  
1309  $> O(5)\text{GeV}$ . PYTHIA [168] is used to simulate any interaction with invariant mass,  
1310  $W > 2\text{GeV}/c^2$ , which produces at least one meson. For any interaction which produces  
1311 at least two mesons but has  $W < 2\text{GeV}/c^2$ , the Bronner model is invoked [169].  
1312 Both of these models use Parton distribution functions based on the Bodek-Yang  
1313 model [170–172].

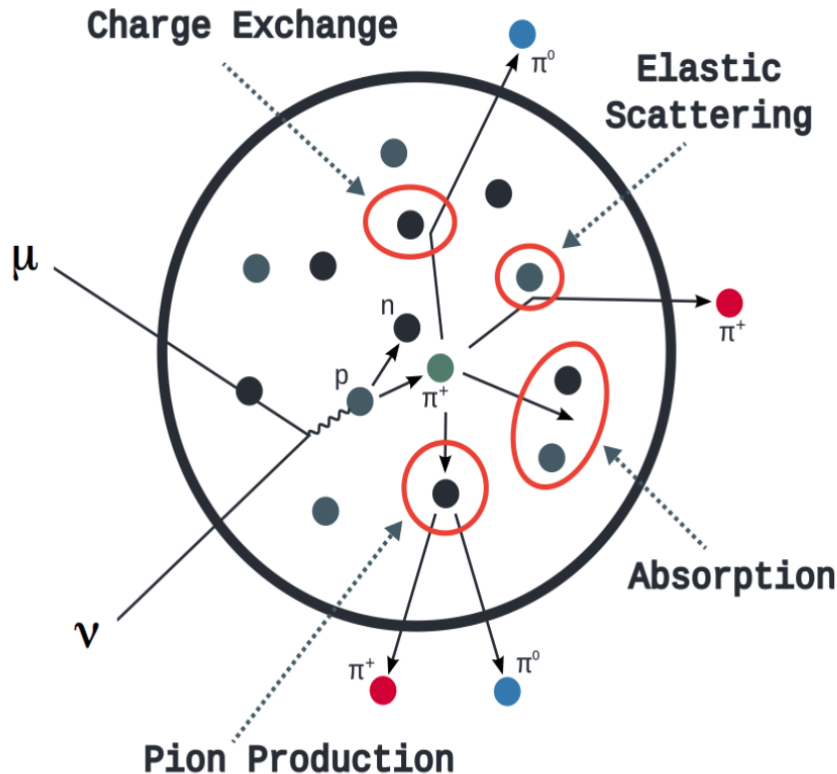


**Figure 5.2:** Illustration of the various processes which a pion can undergo before exiting the nucleus. Taken from [173].

1314 Any pion which is produced within the nucleus can re-interact through final state  
1315 interactions before it exits, as illustrated by the scattering, absorption, production, and  
1316 exchange interactions in Figure 5.2. These re-interactions alter the observable particles  
1317 within the detector. For instance, if the charged pion from a CC PROD interaction is  
1318 absorbed, the observables would mimic a CC QE interaction. To simulate these effects,

1319 NEUT uses a semi-classical intranuclear cascade model [159]. This cascade functions by  
1320 stepping the pion through the nucleus in fixed-length steps equivalent to  $dx = R_N/100$ ,  
1321 where  $R_N$  is the radius of the nucleus. At each step, the simulation allows the pion  
1322 to interact through scattering, charged exchange, absorption, or production with an  
1323 interaction-dependent probability calculated from a fit to external data [174]. This  
1324 cascade continues until the pion is absorbed or exits the nucleus.

1325 Once the final state particle kinematics have been determined from NEUT, they  
1326 are passed into the detector simulation. The near detectors, ND280 and INGRID, are  
1327 simulated using a GEANT4 package [118,175] to simulate the detector geometry, particle  
1328 tracking, and energy deposition. The response of the detectors is simulated using  
1329 the elecSim package [118]. The far detector simulation is based upon the original  
1330 Kamiokande experiment software which uses the GEANT3-based SKDETSIM [118,176]  
1331 package. This controls the interactions of particles in the water as well as Cherenkov  
1332 light production. The water quality and PMT calibration measurements detailed in  
1333 subsection 3.1.2 are also used within this simulation to make accurate predictions of  
1334 the detector response.

## 1335 5.2 Event Reconstruction at SK

1336 Any above Cherenkov threshold event which occurs in SK will be recorded by the  
1337 PMT array, where each PMT records the time and accumulated charge. This recorded  
1338 information is shown in event displays similar to those illustrated in Figure 5.3. To  
1339 be useful for physics analyses, this series of PMT hit information needs to be recon-  
1340 structed to determine the particle's identity and kinematics (or track parameters):  
1341 four-vertex, direction, and momenta. This is because the charge and timing distribu-  
1342 tion of photons generated by a particular particle in an event is dependent upon its

1343 initial kinematics. The concept of distinguishing electron and muon events is from the  
 1344 “fuzziness” of the ring. Muons are heavier and less affected by scattering or showering  
 1345 meaning they typically produce “crisp” rings. Electrons are more likely to interact  
 1346 via electromagnetic showering or scattering which results in larger variations of their  
 1347 direction from the initial direction. Consequently, electrons typically produce “fuzzier”  
 1348 rings compared to muons.

1349 For the purposes of this analysis, the `fiTQun` reconstruction algorithm is utilised.  
 1350 Its core function is to compare a prediction of the accumulated charge and timing  
 1351 distribution from each PMT, generated for a particular particle identity and track  
 1352 parameters, to that observed in the neutrino event. It determines the preferred values  
 1353 by minimising a likelihood function which includes information from PMTs which  
 1354 were hit and those that were not hit. The `fiTQun` algorithm improves upon the APFit  
 1355 reconstruction algorithm which has been used for many previous SK analyses. APFit  
 1356 fits the vertex from timing information and then fits the momentum and direction  
 1357 of the particle from PMT hits within a 43 deg Cherenkov cone (which assumes an  
 1358 ultra-relativistic particle). It then fits the particle identity once the track parameters  
 1359 have been fit. Conversely, `fiTQun` performs a simultaneous fit of particle kinematics  
 1360 and identity, improving both the accuracy of the fit parameters and the rejection of  
 1361 neutral current  $\pi^0$  events [177,178]. The `fiTQun` algorithm is based on the key concepts  
 1362 of the MiniBooNE reconstruction algorithm [179] and is described in [180] which is  
 1363 summarised below.

1364 An event in SK can consist of multiple particles. For example, a charge current  
 1365 muon neutrino interaction can generate two particles that have the potential of gen-  
 1366 erating Cherenkov photons: the primary muon, and the secondary decay-electron  
 1367 from the muon. To ensure both subevents are reconstructed separately, each event is  
 1368 divided into time clusters which are called “subevents”. The number of subevents is

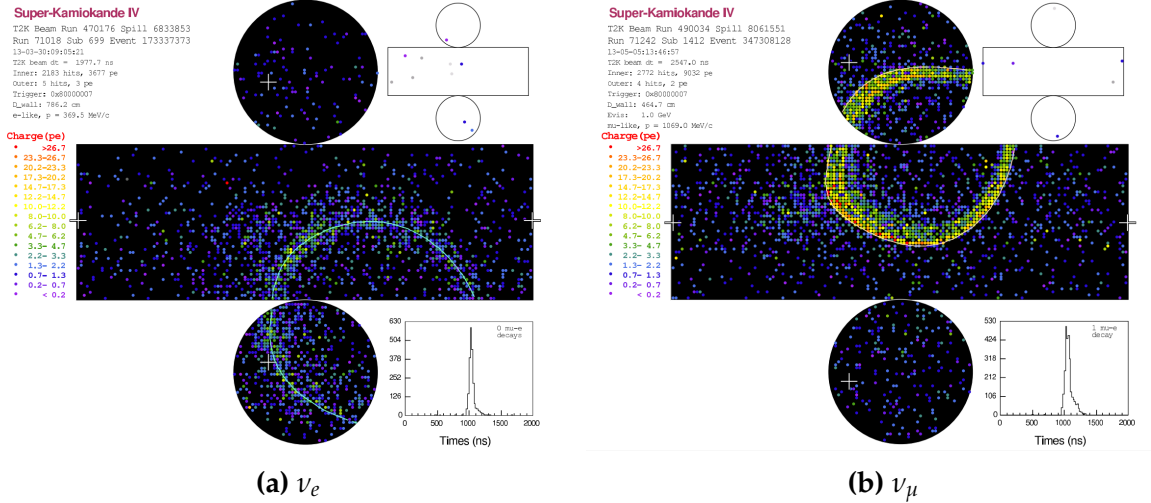


**Figure 5.3:** Event displays from Super Kamiokande illustrating the “crisp” ring from a muon and the typically “fuzzy” electron ring. Each pixel represents a PMT and the color scheme denotes the accumulated charge deposited on that PMT. Figures taken from [181].

1369 equal to the number of decay electrons minus one (the primary event). To find all the  
 1370 subevents in an event, a vertex goodness metric is calculated for some vertex position  
 1371  $\vec{x}$  and time  $t$ ,

$$G(\vec{x}, t) = \sum_i^{\text{hit PMTs}} \exp \left( -\frac{1}{2} \left( \frac{T_{Res}^i(\vec{x}, t)}{\sigma} \right)^2 \right) \quad (5.1)$$

1372 where

$$T_{Res}^i(\vec{x}, t) = t^i - t - |R_{PMT}^i - \vec{x}| / c_n \quad (5.2)$$

1373 is the residual hit time. It is the difference in time between the PMT hit time,  $t^i$ ,  
 1374 of the  $i^{th}$  PMT and the expected time of the PMT hit if the photon was emitted at  
 1375 the start of the vertex.  $R_{PMT}^i$  is the position of the  $i^{th}$  PMT,  $c_n$  is the speed of light in

water and  $\sigma = 4\text{ns}$  which is comparable to the time resolution of the PMT. When the proposed fit values of time and vertex are close to the true values,  $T_{Res}^i(\vec{x}, t)$  tends to zero resulting in subevents appearing as spikes in the goodness metric. The proposed fit vertex and time are grid-scanned, and the values which maximise the goodness metric are selected as the “pre-fit vertex”. Whilst this predicts a vertex for use in the clustering algorithm, the final vertex is fit using the higher-precision maximum likelihood method described below.

Once the pre-fit vertex has been determined, the goodness metric is scanned as a function of  $t$  to determine the number of subevents. A peak-finding algorithm is then used on the goodness metric, requiring the goodness metric to exceed some threshold and drop below a reduced threshold before any subsequent additional peaks are considered. The thresholds are set such that the rate of false peak finding is minimised while still attaining good data to Monte Carlo agreement. To improve performance, the pre-fit vertex for each delayed subevent is re-calculated after PMT hits from the previous subevent are masked. This improves the decay-electron tagging performance. Once all subevents have been determined, the time window around each subevent is then defined by the earliest and latest time which satisfies  $-180 < T_{Res}^i < 800\text{ns}$ . The subevents and associated time windows are then used as seeds for further reconstruction.

For a given subevent, the `fiTQun` algorithm constructs a likelihood based on the accumulated charge  $q_i$  and time information  $t_i$  from the  $i^{th}$  PMT,

$$L(\Gamma, \vec{\theta}) = \prod_j^{\text{unhit}} P_j(\text{unhit}|\Gamma, \vec{\theta}) \prod_i^{\text{hit}} \{1 - P_i(\text{unhit}|\Gamma, \vec{\theta})\} f_q(q_i|\Gamma, \vec{\theta}) f_t(t_i|\Gamma, \vec{\theta}), \quad (5.3)$$

1397 where  $\vec{\theta}$  defines the track parameters; vertex position, direction vector and mo-  
 1398 ments, and  $\Gamma$  represents the particle hypothesis.  $P_i(\text{unhit}|\Gamma, \vec{\theta})$  defines the probability  
 1399 of the  $i^{\text{th}}$  tube to not register a hit given the track parameters and particle hypothesis.  
 1400 The charge likelihood,  $f_q(q_i|\Gamma, \vec{\theta})$ , and time likelihood,  $f_t(t_i|\Gamma, \vec{\theta})$ , represent the prob-  
 1401 ability density function of observing charge  $q_i$  and time  $t_i$  on the  $i^{\text{th}}$  PMT given the  
 1402 specified track parameters and particle hypothesis.

1403 As the generation and propagation of the optical photons are independent of the  
 1404 PMT and electronics response, it is natural to split the calculation into two. Firstly,  
 1405 the expected number of photoelectrons (or predicted charge),  $\mu_i = \mu_i(\vec{\theta}, \Gamma)$ , at the  $i^{\text{th}}$   
 1406 PMT is calculated. This value is then substituted into the likelihood function. This  
 1407 allows the charge likelihood density  $f_q(q_i|\mu_i)$  and unhit probability  $P_i(\text{unhit}|\mu_i)$  to be  
 1408 expressed via quantities that are only dependent on the response of the PMT.

1409 The predicted charge is calculated based on contributions from both the direct  
 1410 light and the scattered light. The direct light contribution is determined based on the  
 1411 integration of the Cherenkov photon profile along the track. PMT angular acceptance,  
 1412 water quality, and calibration measurements discussed in subsection 3.1.2 are included  
 1413 to accurately predict the charge probability density at each PMT. The scattered light  
 1414 is calculated in a similar way, although it includes a scattering function that depends  
 1415 on the vertex of the particle and the position of the PMT. The charge likelihood is  
 1416 calculated by comparing the prediction to the observed charge in the PMT.

1417 The time likelihood is approximated to depend on the vertex  $\vec{x}$ , direction  $\vec{d}$ , and  
 1418 time  $t$  of the track parameters as well as the particle hypothesis. The expected time  
 1419 for PMT hits is calculated by assuming unscattered photons being emitted from the  
 1420 midpoint of the track,  $S_{\text{mid}}$ ,

$$t_{exp}^i = t + S_{mid}/c + |R_{PMT}^i - \vec{x} - S_{mid}\vec{d}|/c_n, \quad (5.4)$$

where  $c$  is the speed of light in a vacuum. The time likelihood is then expressed in terms of the residual difference between the PMT hit time and the expected hit time,  $t_{Res}^i = t^i - t_{exp}^i$ . The particle hypothesis and momentum also affect the Cherenkov photon distribution. These parameters modify the shape of the time likelihood density since in reality not all photons are emitted at the midpoint of the track. As with the charge likelihood, the contributions from both the direct and scattered light to the time likelihood density are calculated separately, which are both calculated from particle gun studies.

The track parameters and particle identity which maximise  $L(\Gamma, \vec{\theta})$  are defined as the best-fit parameters. In practice MINUIT [182] is used to minimise the value of  $-\ln L(\Gamma, \vec{\theta})$ . The `fitQun` algorithm considers an electron-like, muon-like, and charged pion-like hypothesis for events with a single final state particle, denoted “single-ring events”. The particle’s identity is determined by taking the ratio of the likelihood of each of the hypotheses. For instance, electrons and muons are distinguished by considering the value of  $\ln(L(e, \vec{\theta}_e)/L(\mu, \vec{\theta}_\mu))$  in comparison to the reconstructed momentum of the electron hypothesis [180]. This distance from this criteria is termed the PID parameter and is illustrated in Figure 5.4.

### DB: Mentiton Pi0 rejection and mu/pip separation cuts

The `fitQun` algorithm also considers a  $\pi^0$  hypothesis. To do this, it performs a fit looking for two standard electron-hypothesis tracks which point to the same four-vertex. This assumes the electron tracks are generated from photon-conversion so the electron tracks actually appear offset from the proposed  $\pi^0$  vertex. For these fits, the

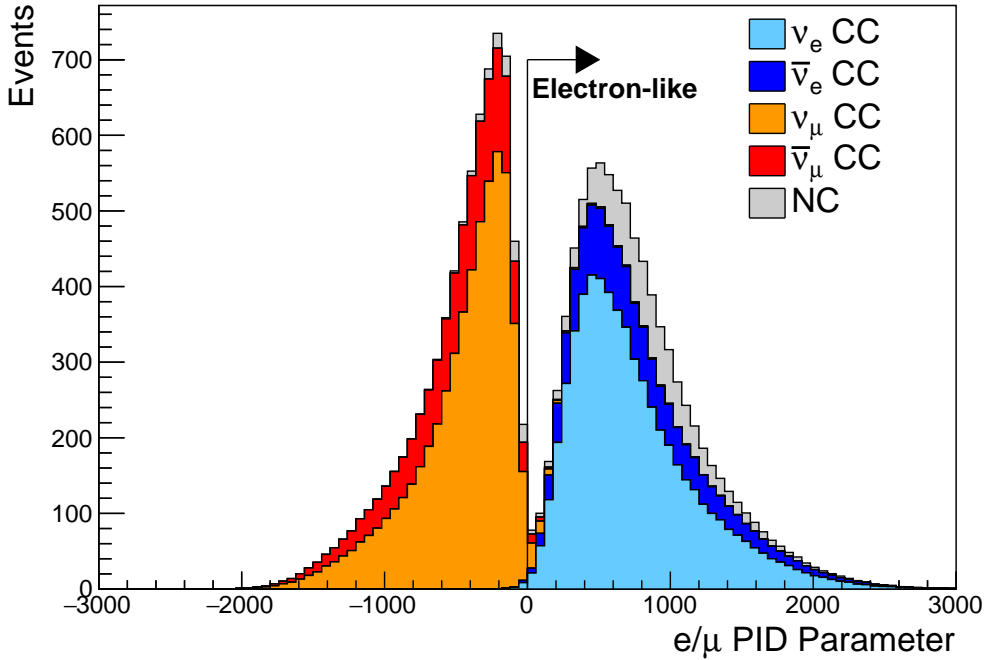


**Figure 5.4:** The electron/muon PID separation parameter for all sub-GeV single-ring events in SK-IV. The charged current (CC) component is broken down in four flavours of neutrino ( $\nu_\mu$ ,  $\bar{\nu}_\mu$ ,  $\nu_e$  and  $\bar{\nu}_e$ ). Events with positive values of the parameter are determined to be electron-like.

<sup>1443</sup> conversion length, direction, and momenta of each photon are also considered as track  
<sup>1444</sup> parameters which are then fit in the same methodology as the standard single-ring  
<sup>1445</sup> hypotheses.

<sup>1446</sup> Whilst low energy events are predominately single-ring events, higher energy  
<sup>1447</sup> neutrino events can generate final states with multiple particles which generate  
<sup>1448</sup> Cherenkov photons. These “multi-ring” hypotheses are also considered in the `fitQun`  
<sup>1449</sup> algorithm. When calculating the charge likelihood density, the predicted charge  
<sup>1450</sup> associated with each ring is calculated separately and then merged to calculate the  
<sup>1451</sup> total accumulated charge on each PMT. Similarly, the time likelihood for the multi-ring  
<sup>1452</sup> hypothesis is calculated assuming each ring is independent. Each track is time-ordered  
<sup>1453</sup> based on the time of flight from the center of the track to the PMT and the direct light  
<sup>1454</sup> from any ring incident on the PMT is assumed to arrive before any scattered light. To

reduce computational resources, the multi-ring fits only consider electron-like and charged pion-like rings as the pion fit can be used as a proxy for a muon fit due to their similar mass.

Multi-ring fits proceed by proposing another ring to the previous fit and then fitting the parameters in the method described above. Typically, multi-ring fits have the largest likelihood because of the additional degrees of freedom introduced. Consequently, the additional ring is only added if the ratio of likelihoods passes a criterion, which is determined by Monte Carlo studies.

As an example of how the reconstruction depends on the detector conditions, the author of this thesis assessed the quality of event reconstruction for SK-V data. The detector systematics invoked within the T2K-only oscillation analysis are determined using data to Monte Carlo comparisons using the SK-IV data [183]. Due to tank-open maintenance occurring between SK-IV and SK-V, the dark rate of each PMT was observed to increase in SK-V due to light exposure for a significant time during the repairs. This increase can be seen in Figure 5.5. Run-10 of the T2K experiment was conducted in the SK-V period, so the consistency of SK-IV and SK-V data needs to be studied to determine whether the SK-IV-defined systematics can be applied to the run-10 data. This comparison study was performed using the stopping muon data set for both the SK-IV and SK-V periods. This data sample is used due to the high rate of interactions ( $O(200)$  events per hour) as well as having similar energies to muons from CCQE  $\nu_\mu$  interactions from beam interactions. The rate of cosmic muons does depend on the solar activity cycle [184] but has been neglected in this comparison study. This is because the shape of the distributions is most important for the purposes of being compared to the detector systematics. The SK-IV and SK-V data samples consist of 2398.42 and 626.719 hours of data which equates to 686k and 192k events respectively.

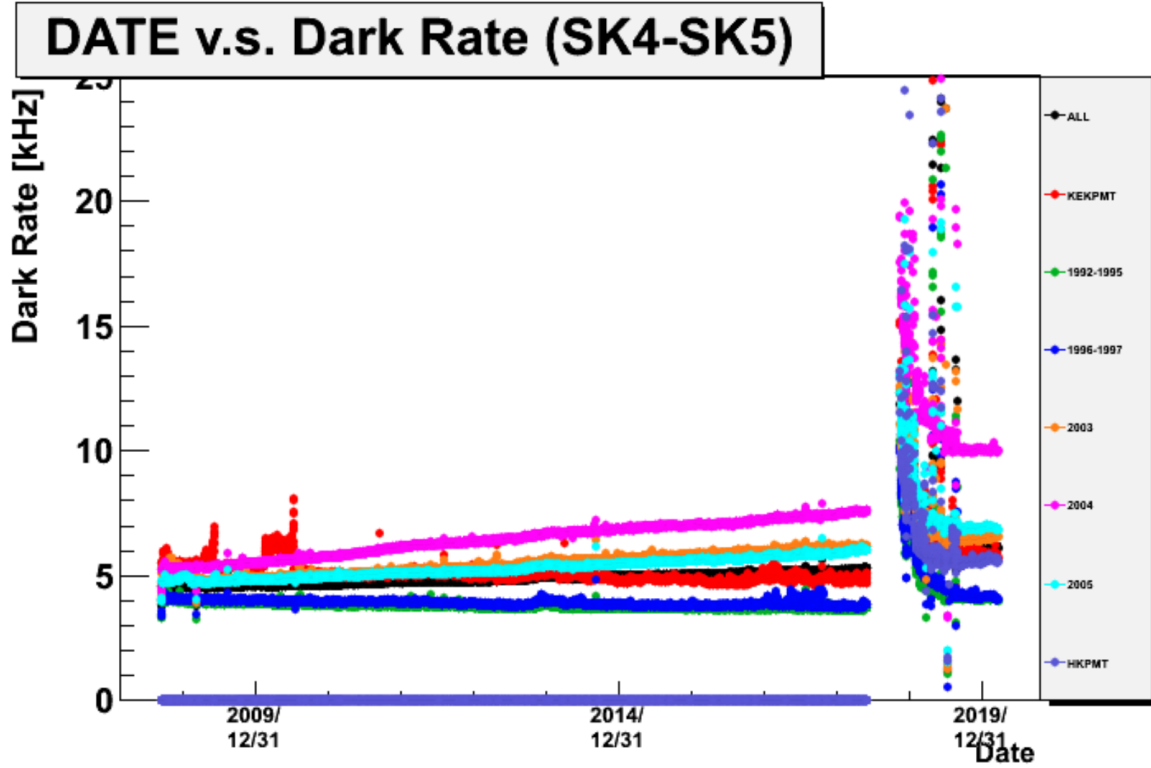


**Figure 5.5:** The variation of the measured dark rate as a function of date, broken down by PMT type. The SK-IV and SK-V periods span September 2008 to May 2018 and January 2019 to July 2020, respectively. The break in measurement in 2018 corresponds to the period of tank repair and refurbishment. Figure adapted from [183].

The predicted charge calculated in the `fitQun` charge likelihood prediction includes a contribution from the photoelectron emission due to dark noise. Therefore, the increase in the SK-V dark rate needs to be accounted for. In practice, the average dark rate in each SK period is calculated and used as an input in the reconstruction. This is calculated by averaging the dark rate per run for each period separately, using the calibration measurements detailed in subsection 3.1.2. The average dark rate from SK-IV and SK-V were found to be 4.57kHz and 6.30kHz, respectively. The associated charge with the muon and decay electron subevents are illustrated in Figure 5.6. The photoelectron emission from dark noise will be more noticeable for events that have lower energy. This is because this contribution becomes more comparable to the number of photoelectrons emitted from incident photons in low-energy events. This

1491 behaviour is observed in the data, where the charge deposited by the muon subevent  
 1492 is mostly unaffected by the increase in dark rate, whilst the charge associated with the  
 1493 decay-electron is clearly affected.

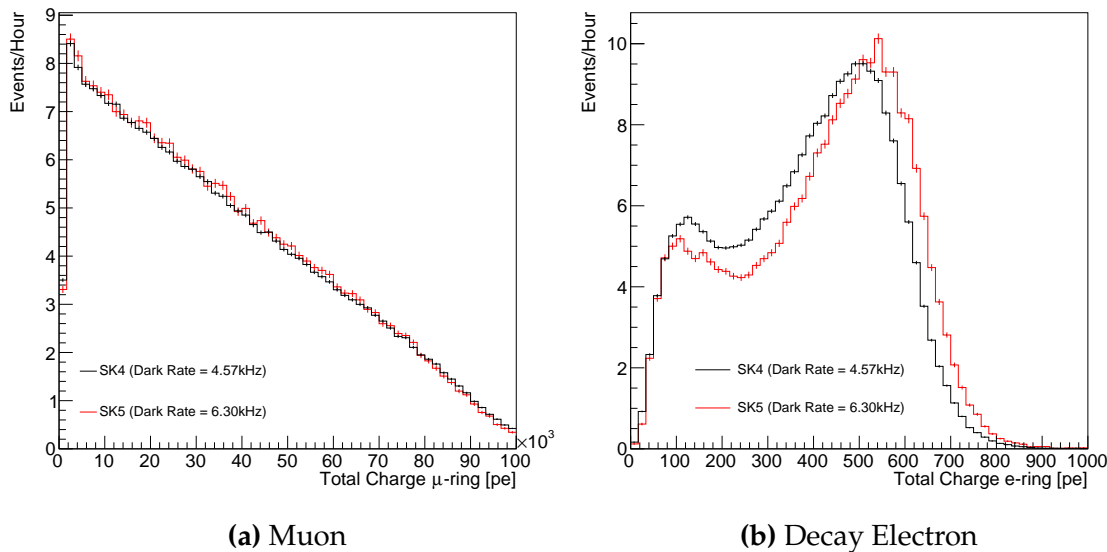


**Figure 5.6:** Comparison of the measured raw charge deposited per event from the stopping muon data samples between SK-IV (Blue) and SK-V (Red), split by the primary muon subevent and the associated decay electron subevent.

1494 The energy scale systematic for the SK-IV period was determined to be 2.1% [185].  
 1495 It is defined to be equal to the difference between data and Monte Carlo prediction  
 1496 in the stopping muon data sample. To determine the consistency of the SK-IV and  
 1497 SK-V with respect to the energy scale systematic, the muon momentum distribution is  
 1498 compared between the two SK periods. As the total number of Cherenkov photons  
 1499 is integrated across the track length, the reconstructed momentum divided by track  
 1500 length (or range) is compared between SK-IV and SK-V as illustrated in Figure 5.7.

1501 The consistency between these distributions has been computed in two ways.  
 1502 Firstly, a Gaussian is fit to each distribution separately. The mean of which is found to  
 1503 be  $(2.272 \pm 0.003)\text{MeV/cm}$  and  $(2.267 \pm 0.006)\text{MeV/cm}$  for SK-IV and SK-V respec-  
 1504 tively. The ratio of these is equal to  $1.002 \pm 0.003$ . The mean of the Gaussian fits are

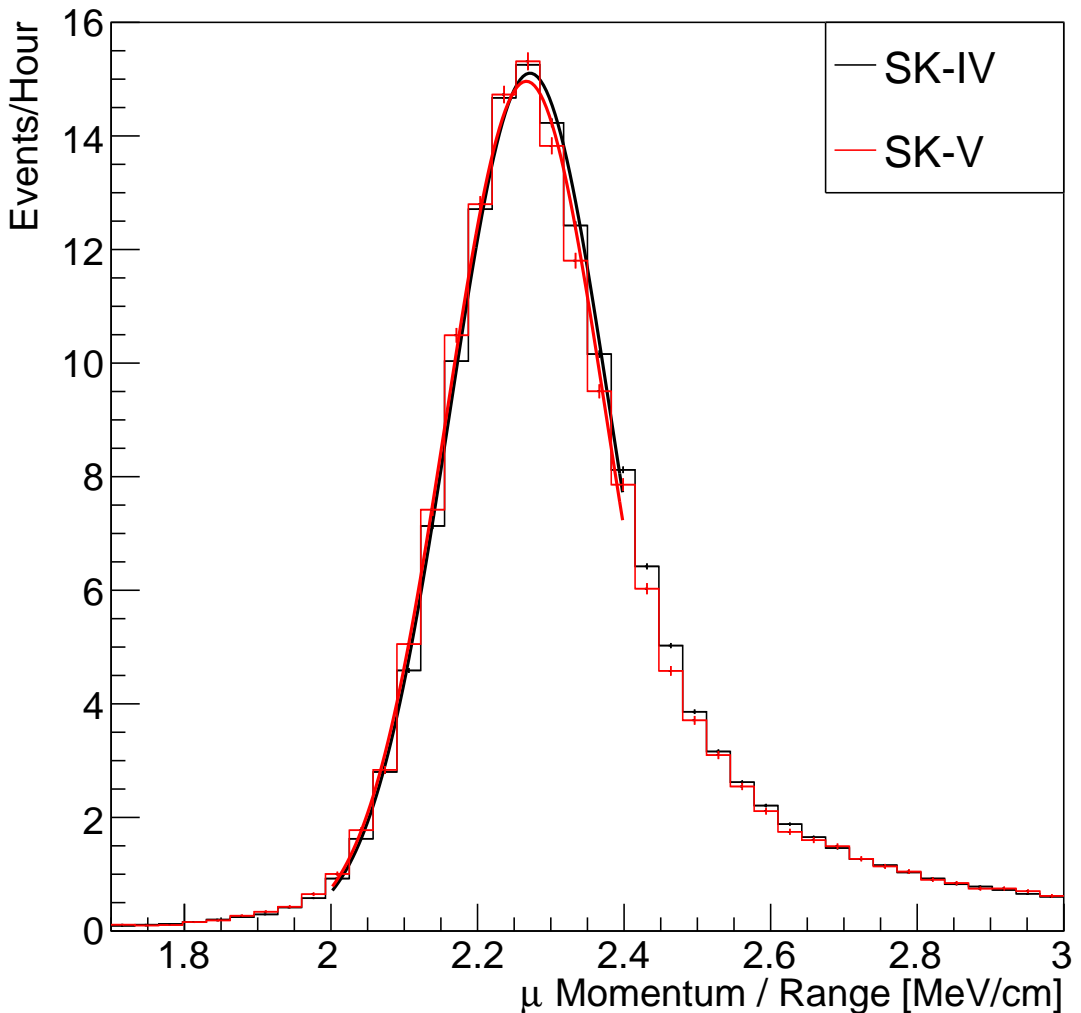


**Figure 5.7:** The distribution of the reconstructed momentum from the muon ring divided by the distance between the reconstructed muon and decay electron vertices as found in the stopping muon data sets of SK-IV (Black) and SK-IV (Red). Only events with one tagged decay electron are considered. A Gaussian fit is considered in the range [2.0, 2.4] MeV/cm and illustrated as the solid curve.

consistent with the expected stopping power of a minimum ionising muon for a target material (water) with  $Z/A \sim 0.5$  [186]. The second consistency check is performed by introducing a nuisance parameter,  $\alpha$ , which modifies the SK-V distribution. The value of  $\alpha$  which minimises the  $\chi^2$  value between the SK-IV and SK-V is determined by scanning across a range of values. This is repeated by applying the nuisance parameter as both a multiplicative factor and an additive shift. The  $\chi^2$  distributions for different

<sub>1511</sub> values of  $\alpha$  is illustrated in Figure 5.8. The values which minimise the  $\chi^2$  are found to  
<sub>1512</sub> be 0.0052 and 1.0024 for the additive and multiplicative implementations, respectively.  
<sub>1513</sub> No evidence of shifts larger than the 2.1% uncertainty on the energy scale systematic  
<sub>1514</sub> has been found in the reconstructed momentum distribution of SK-IV and SK-V.

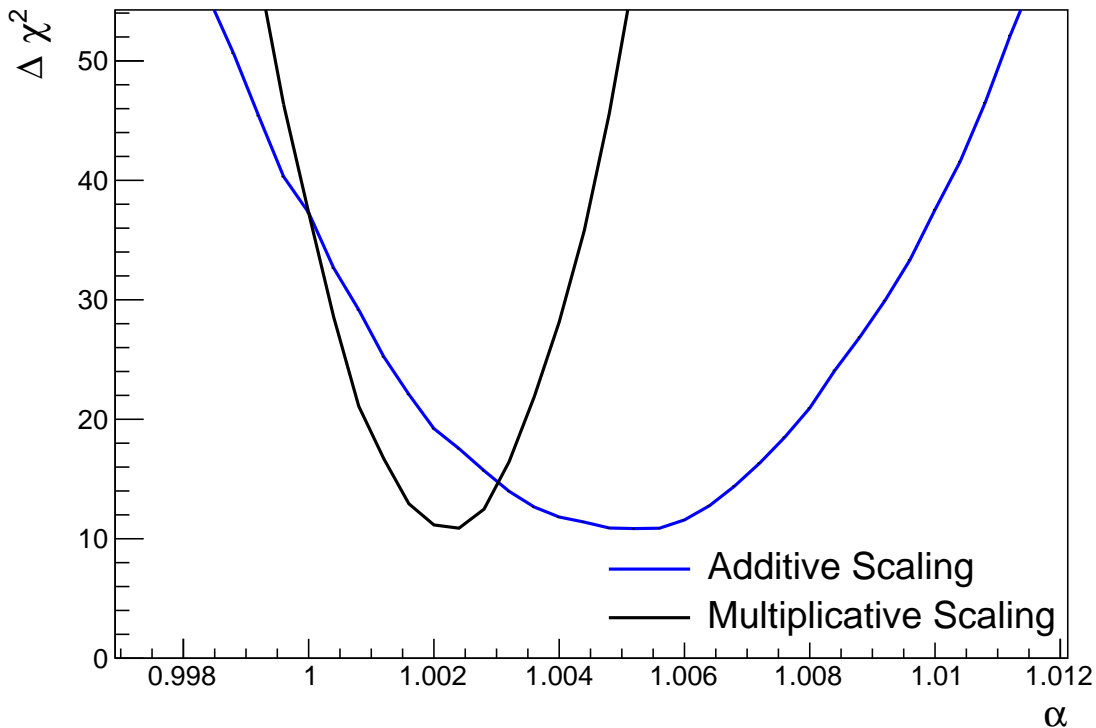


**Figure 5.8:** The  $\chi^2$  difference between the SK-IV and SK-V reconstructed muon momentum divided by range when the SK-V is modified by the scaling parameter  $\alpha$ . Both additive (Blue) and multiplicative (Black) scaling factors have been considered. In practice, the additive scaling factor actually uses the value of  $(\alpha - 1.0)$  but is illustrated like this so the results can be shown on the same axis range.

### <sub>1515</sub> 5.3 Event Reduction at SK

<sub>1516</sub> Atmospheric neutrino events observed in the SK detector are categorised into three  
<sub>1517</sub> different types of samples: fully contained (FC), partially contained (PC) and up-  
<sub>1518</sub> going muon ( $\text{Up-}\mu$ ), using PMT hit signatures in the inner and outer detector (ID

and OD, respectively). To identify FC neutrino events, it is required that the neutrino interacts inside the fiducial volume of the ID such that no significant OD activity is observed. For this analysis, an event is defined to be in the fiducial volume providing the event vertex is at least 0.5m away from the ID walls. PC events have the same ID requirements but can have a larger signal present inside the OD. Typically these events are higher energy muon interactions that penetrate the ID walls. The Up- $\mu$  sample contains events where muons are created from neutrino interactions in the OD water or rock below the tank. They then propagate upwards through the detector. The reason downward-going muons generated from neutrino interactions above the tank are neglected is due to the difficulty in separating their signature from the cosmic muon shower background. The sample categories are visually depicted in Figure 5.9.

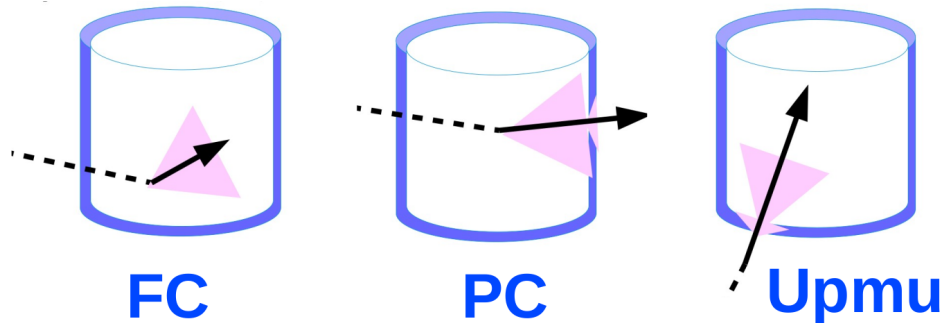


**Figure 5.9:** A depiction of the topology patterns for fully-contained (FC), partially-contained (PC) and up-going muon (Up- $\mu$ ) samples included in this analysis.

Based on the event characteristics, as defined by the `fitQun` event reconstruction software, the FC events are categorised by

- **Visible Energy:** equal to the sum of the reconstructed kinetic energy above the Cerenkov threshold for all rings present in the event. The purpose is to separate events into sub-GeV and multi-GeV categories.
- **Number of observed Cerenkov rings.** The purpose is to separate single-ring and multi-ring events, where single-ring events predominantly consist of quasi-elastic

interactions and multi-ring events are typically resonant pion production or deep inelastic scattering events.

- **Particle identification parameter of the most energetic ring:** A value determined from the maximum likelihood value based on `fitQun`'s electron, muon, or pion hypothesis. The purpose is to separate electron-like and muon-like events.
- **Number of decay electrons:** The purpose is to separate quasi-elastic events (which have one decay electron emitted from the muon decay) and resonant pion production events (which have two decay electrons emitted from the muon and pion).

The PC and Up- $\mu$  categories are broken down into “through-going” and “stopping” samples depending on whether the muon left the detector. This is because the stopping events deposit the entire energy of the interaction into the detector, resulting in better reconstruction. The energy of events that exit the detector has to be estimated which introduces much larger systematic uncertainties. Through-going Up- $\mu$  samples are further broken down by whether any hadronic showering was observed in the event which typically indicates DIS interactions. The expected neutrino energy for the different categories is given in Figure 5.10. FC sub-GeV and multi-GeV events peak around 0.7GeV and 3GeV respectively, with slightly different peak energies for  $\nu_x \rightarrow \nu_e$  and  $\nu_x \rightarrow \nu_\mu$  oscillation channels. PC and Up- $\mu$  are almost entirely comprised of  $\nu_x \rightarrow \nu_\mu$  events and peak around 7GeV and 100GeV, respectively.

In normal data-taking operations, the SK detector observes many background events alongside the beam and atmospheric neutrino signal events of physics interest. Cosmic ray muons and flasher events, which are the spontaneous discharge of a given PMT, contribute the largest amount of background events in the energy range relevant to any analysis searching for neutrino events. Lower energy analyses like DSNB searches are also subject to radioactive backgrounds [187]. Therefore the data recorded

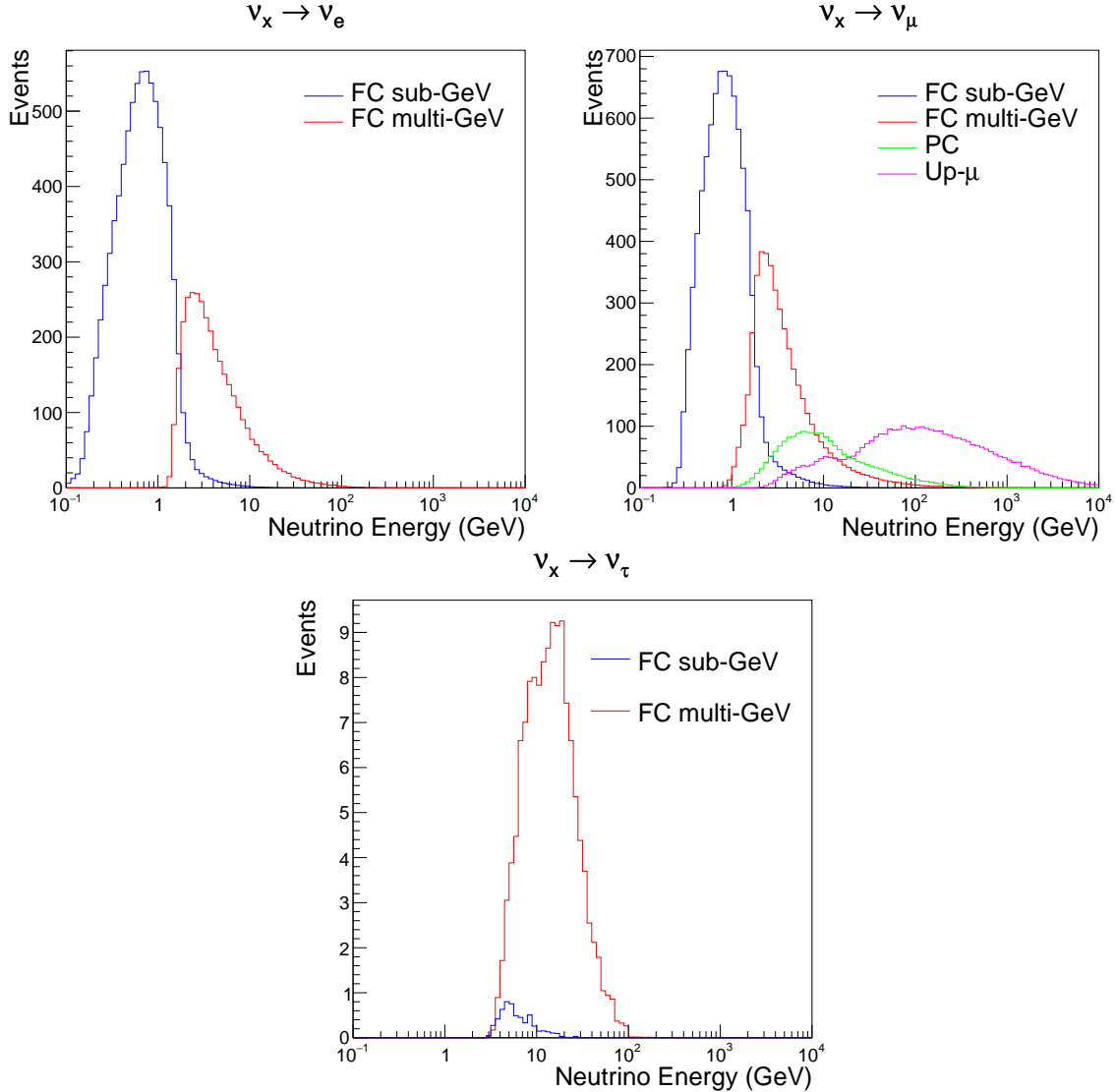


**Figure 5.10:** The predicted neutrino flux of the fully contained (FC) sub-GeV and multi-GeV, partially contained (PC), and upward-going muon (Up- $\mu$ ) events. The prediction is broken down by the  $\nu_x \rightarrow \nu_e$  prediction (top left),  $\nu_x \rightarrow \nu_\mu$  prediction (top right) and  $\nu_x \rightarrow \nu_\tau$  prediction (bottom). All systematic dials are set to their nominal values and the Asimov A oscillation parameters are assumed.

is reduced with the aim of removing these background events. The reduction process

is detailed in [47, 89] and briefly summarised below.

The first two steps in the FC reconstruction remove the majority of cosmic ray

muons by requiring a significant amount of ID activity compared to that measured in

the OD. Events that pass this cut are typically very high momentum muons or events

that leave very little activity in the OD. Consequently, a third reduction step is then

1569 applied to select cosmic-ray muons that pass the initial reduction step. A purpose-built  
 1570 cosmic muon fitter is used to determine the entrance (or exit) position of the muon and  
 1571 a cut is applied to OD activity contained within 8m of this position. Flasher events are  
 1572 removed in the fourth reduction step which is based on the close proximity of PMT  
 1573 hits surrounding the PMT producing the flash. Events that pass all these reduction  
 1574 steps are reconstructed with the APFit algorithm. The fifth step of the reduction uses  
 1575 information from the more precise fitter to repeat the previous two steps with tighter  
 1576 cuts. Muons below the Cherenkov threshold can not generate optical photons in the  
 1577 ID but the associated decay electron can due to its lower mass. These are the types of  
 1578 events targeted in the fifth reduction step. The final cuts require the event vertex to be  
 1579 within the fiducial volume (0.5m from the wall although the nominal distance is 2.0m),  
 1580 visible energy  $E_{vis} > 30\text{MeV}$  and fewer than 16 hits within the higher energy OD  
 1581 cluster. The culmination of the fully contained reduction results in 8.09 events/day in  
 1582 the nominal fiducial volume [188]. The uncertainty in the reconstruction is calculated  
 1583 by comparing Monte Carlo prediction to data. The largest discrepancy is found to be  
 1584 1.3% in the fourth reduction step.

1585 The PC and Up- $\mu$  events are processed through their own reduction processes  
 1586 detailed in [47]. Both of these samples are reconstructed with the APFit algorithm  
 1587 rather than `fiTQun`. This is because the efficiency of reconstructing events that leave  
 1588 the detector has not been sufficiently studied for reliable systematic uncertainties. The  
 1589 PC and Up- $\mu$  samples attain events at approximately 0.66 and 1.44 events/day.

1590 Events due to beam neutrinos undergo the same reduction steps as FC events and  
 1591 are then subject to further cuts [189]. The GPS system which links the timing between  
 1592 the beam facility and SK needs to be operating correctly and there should be no activity  
 1593 within the detector in the previous  $100\mu\text{s}$  before the trigger. The events then need to  
 1594 triggered between  $-2\mu\text{s}$  and  $10\mu\text{s}$  of the expected spill timing.

1595 Due to the lower energy beam neutrinos, the T2K samples are not dependent  
 1596 upon the visible energy neutrino as the range of neutrino energies are smaller than  
 1597 that found in atmospheric neutrinos. Furthermore, the 2020 T2K-only oscillation  
 1598 analysis only considers events which contain a single ring. Similar to atmospheric  
 1599 event selection, the number of decay electrons is used as a proxy for distinguishing  
 1600 CCQE and CCRES events. The expected neutrino energy, broken down by number of  
 1601 decay electrons, is given in Figure 5.11.

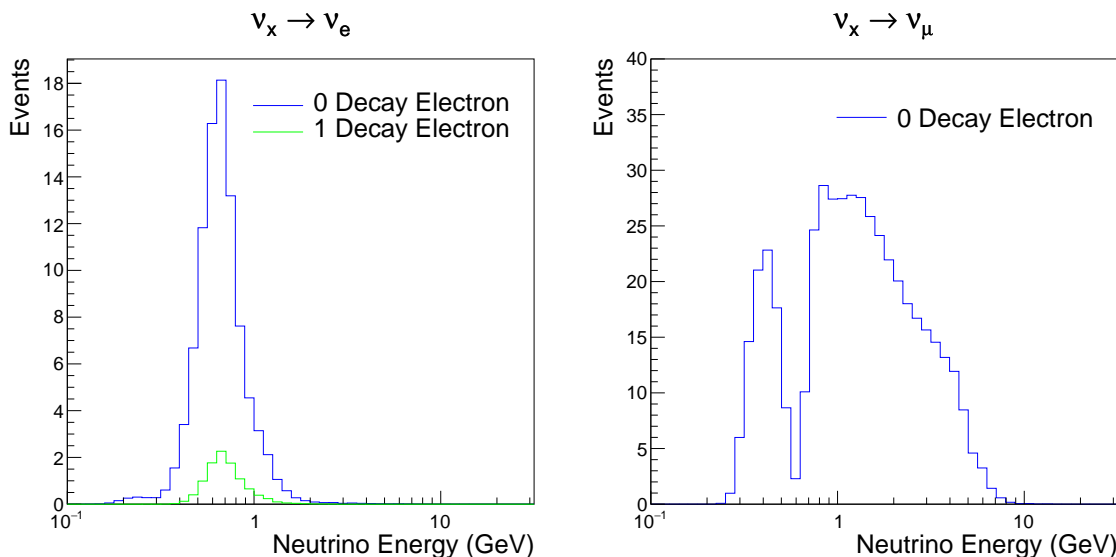


**Figure 5.11:** The predicted neutrino flux of the beam neutrinos, illustrated as a function of neutrino energy. The predictions are broken down by the number of decay electrons associated with the particular events. All systematic dials are set to their nominal values and the Asimov A oscillation parameters are assumed.

1602 **Chapter 6**

1603 **Sample Selections and Systematics**

1604 **6.1 Sample Selection**

1605 **6.1.1 Atmospheric Samples**

1606 The atmospheric event selection follows the official SK analysis presented in [89] and is  
1607 documented below. The Monte Carlo prediction used within this analysis corresponds  
1608 to 500 years worth of neutrino events, which is weighted down to match the SK-IV  
1609 livetime of 3244.4 days.

1610 The fully contained (FC), partially contained (PC) and upward going muon events  
1611 ( $\text{up-}\mu$ ) which pass the reduction cuts discussed in section 5.3 are further broken down  
1612 into different samples based on reconstruction information. This section details the  
1613 samples used within the oscillation analysis, alongside the chosen binning and final  
1614 spectra used within the fit.

1615 In general, the FC events are first separated by the visible energy deposited within  
1616 the detector. This is calculated as the sum of the reconstructed kinetic energy above the  
1617 Cerenkov threshold for all rings present in the event. Events are separated by whether  
1618 they were above or below  $E_{vis} = 1.33\text{GeV}$ . This separates “subGeV” and “multiGeV”  
1619 events. Typically, lower energy events consist of charge current quasi-elastic (CCQE)  
1620 interactions which are simpler to reconstruct resulting in smaller systematic uncertain-  
1621 ties. Events are further separated by the number of rings associated with the event due

1622 to a similar reasoning. As the oscillation probability is dependent upon the flavour of  
 1623 neutrino, electron and muon events are separated using a similar likelihood method  
 1624 to that discussed in section 5.2. To reduce computational resources required for the  
 1625 reconstruction, only electron and pion hypothesis are considered so this separation  
 1626 cuts depends on the ratio of the electron to pion likelihoods. Finally, the number of  
 1627 decay electrons is also used to classify events. As charged current resonant pion prod-  
 1628 iction (CCRES) generates a final-state pion which decays to an electron, electron-like  
 1629 events with one decay electron or muon-like events with two decay electrons must  
 1630 have contained a pion in the final state. Consequently, the number of decay electrons  
 1631 is used to target CCQE and CCRES interaction modes. FC subGeV events are then  
 1632 separated into the samples listed in Table 6.1.

Index	Sample
0	SubGeV-elikely-0dcy Single ring $e$ -like events with zero decay electrons
1	SubGeV-elikely-1dcy Single ring $e$ -like events with one or more decay electrons
2	SubGeV-mulike-0dcy Single ring $\mu$ -like events with zero decay electrons
3	SubGeV-mulike-1dcy Single ring $\mu$ -like events with one decay electrons
4	SubGeV-mulike-2dcy Single ring $\mu$ -like events with two or more decay electrons
5	SubGeV-pi0like Two $e$ -like ring events with zero decay electrons and reconstructed $\pi^0$ mass $85 \leq m_{\pi^0} < 215\text{MeV}$

**Table 6.1:** The fully contained subGeV samples used within this oscillation analysis. Both the sample name and description are given.

1633 In addition to the cuts discussed above, multiGeV samples also have additional cuts  
 1634 to separate samples which target neutrino and antineutrino separation. As discussed  
 1635 in section 7.1, the matter resonance only occurs for neutrinos in normal hierarchy and

<sub>1636</sub> antineutrinos in inverse mass hierarchy so having flavour-enriched samples aides in  
<sub>1637</sub> the determination of the mass hierarchy. For a CCRES interaction,

$$\begin{aligned}
 \bar{\nu}_e + N &\rightarrow e^+ + N' + \pi^-, \\
 \nu_e + N &\rightarrow e^- + N' + \pi^+ \\
 &\quad \downarrow \mu^+ + \nu_\mu \\
 &\quad \downarrow e^+ + \nu_e + \bar{\nu}_\mu.
 \end{aligned} \tag{6.1}$$

<sub>1638</sub> Where the  $\pi^-$  emitted from a  $\bar{\nu}_e$  interaction is more likely to be absorbed within  
<sub>1639</sub> the oxygen nucleus [190] compared to the  $\pi^+$  from  $\nu_e$  interactions. Consequently, the  
<sub>1640</sub> number of tagged decay electrons associated with an event gives an indication of  
<sub>1641</sub> whether the interaction was due to a neutrino or antineutrino: zero for  $\bar{\nu}_e$  events, and  
<sub>1642</sub> one or more for  $\nu_e$  events. The ability to separate neutrino from antineutrino events is  
<sub>1643</sub> illustrated in Table 6.3, where the MultiGeV-*e*-like-nue has 78% purity enhancement  
<sub>1644</sub> of neutrino events with only 7% antineutrino background in that sample.

<sub>1645</sub> This relatively simple discriminator works reasonably well for single-ring events.  
<sub>1646</sub> However, this is not the case for multi-ring events. A multi-GeV multi-ring separation  
<sub>1647</sub> (MME) likelihood cut which specifically targets multiGeV multiRing electron-like  
<sub>1648</sub> events was introduced in [191, 192]. Four observables are used within this likelihood  
<sub>1649</sub> cut: number of decay electrons, maximum distance between the vertex of the neutrino  
<sub>1650</sub> and the decay electrons, the energy deposited by the leading energy ring, and the  
<sub>1651</sub> reconstructed particle identification of that highest energy ring. The last three variables  
<sub>1652</sub> are selected based on typical event kinematics comparing  $CC\nu_e$  events to the  $CC\nu_\mu$   
<sub>1653</sub> and NC backgrounds. Typically, more energy is carried by the hadronic system in  
<sub>1654</sub> these background interactions and the distance cut targets the decay of muons from  
<sub>1655</sub>  $CC\nu_\mu$ , which tend to travel further than the pions from  $CC\nu_e$  interactions.

Index	Sample
0	MultiGeV- <i>e</i> like-nue Single ring <i>e</i> -like events with zero decay electrons
1	MultiGeV- <i>e</i> like-nuebar Single ring <i>e</i> -like events with one or more decay electrons
2	MultiGeV- <i>μ</i> like Single ring <i>μ</i> -like events
3	MultiRing- <i>e</i> like-nue Two or more ring events with leading energy <i>e</i> -like ring and passed both MME and $\nu/\bar{\nu}$ separation likelihood cuts
4	MultiRing- <i>e</i> like-nuebar Two or more ring events with leading energy <i>e</i> -like ring and passed MME and failed $\nu/\bar{\nu}$ separation likelihood cuts
5	MultiRing- <i>μ</i> like Two or more ring events with leading energy <i>μ</i> -like ring and only requires $E_{vis} > 0.6\text{GeV}$
6	MultiRing-Other1 Two or more ring events with leading energy <i>e</i> -like ring and failed the MME likelihood cut

**Table 6.2:** The fully contained multiGeV samples used within this oscillation analysis. Both the sample name and description are given.

1656      Neutrino and antineutrino events are then separated by a second likelihood method  
 1657      ( $\nu/\bar{\nu}$  separation) detailed in [52]. This uses the number of decay electrons, the number  
 1658      of reconstructed rings and the event’s transverse momentum. As discussed above,  
 1659      positively charged pions from neutrino interactions are less likely to be absorbed. For  
 1660      this high energy sample, the majority of those pions will be above the Cherenkov  
 1661      threshold which results in more number of rings compared to an antineutrino interac-  
 1662      tion. The angular distribution also tends to be more forward peaked in antineutrino  
 1663      interactons. The FC multiGeV sample definitions are detailed in Table 6.2.

1664      The PC and up- $\mu$  events are split by the amount of energy deposited within the  
 1665      outer detector, into “stopping” and “through-going” samples. If an event leaves the

detector, the energy it takes with it has to be estimated which increases the systematic uncertainty compared to events entirely contained within the inner detector. The through-going up- $\mu$  are further separated by the presence of any electromagenetic showering in the event, as the assumption of non-showering muon does not give reliable reconstruction for these types of events [47]. In total, 13 FC, 2 PC, and 3 up- $\mu$  atmospheric samples are included within this analysis.

Sample	$CC\nu_e$	$CC\bar{\nu}_e$	$CC(\nu_\mu + \bar{\nu}_\mu)$	$CC(\nu_\tau + \bar{\nu}_\tau)$	NC
SubGeV-elike-0dcy	72.17	23.3	0.724	0.033	3.77
SubGeV-elike-1dcy	86.81	1.773	7.002	0.062	4.351
SubGeV-mulike-0dcy	1.003	0.380	90.07	0.036	8.511
SubGeV-mulike-1dcy	0.023	0.	98.46	0.029	1.484
SubGeV-mulike-2dcy	0.012	0.	99.25	0.030	0.711
SubGeV-pi0like	6.923	2.368	0.928	0.011	89.77
MultiGeV-elike-nue	78.18	7.041	3.439	1.886	9.451
MultiGeV-elike-nuebar	56.68	37.81	0.174	0.614	4.718
MultiGeV-mulike	0.024	0.005	99.67	0.245	0.058
MultiRing-elike-nue	59.32	12.39	4.906	3.385	20
MultiRing-elike-nuebar	52.39	31.03	1.854	1.585	13.14
MultiRing-mulike	0.673	0.080	97.33	0.342	1.578
MultiRingOther-1	27.98	2.366	34.93	4.946	29.78
PCStop	8.216	3.118	84.45	0.	4.214
PCThrus	0.564	0.207	98.65	0.	0.576
UpStop-mu	0.829	0.370	98.51	0.	0.289
UpThruNonShower-mu	0.206	0.073	99.62	0.	0.103
UpThruShower-mu	0.128	0.054	99.69	0.	0.132

**Table 6.3:** The purity of each atmospheric sample used within this analysis, broken down by charged current (CC) and neutral current (NC) interactions and which neutrino flavour interacted within the detector. The pre-fit dial values and Asimov A oscillation parameter sets are assumed. Electron neutrino and antineutrino events are separated to illustrate the ability of the separation likelihood cuts used within the sample selections.

The atmospheric samples are binned in reconstructed lepton momentum and direction, as given by Table 6.4. The distribution of the reconstructed lepton momentum

Sample	$\cos(\theta_Z)$ Bins	Momentum Bin Edges ( $\log_{10}(P)$ MeV)
SubGeV- <i>e</i> like-0dcy	10	2.0, 2.4, 2.6, 2.8, 3.0, 3.2
SubGeV- <i>e</i> like-1dcy	1	2.0, 2.4, 2.6, 2.8, 3.0, 3.2
SubGeV- <i>m</i> ulike-0dcy	10	2.0, 2.4, 2.6, 2.8, 3.0, 3.2
SubGeV- <i>m</i> ulike-1dcy	10	2.0, 2.4, 2.6, 2.8, 3.0, 3.2
SubGeV- <i>m</i> ulike-2dcy	1	2.0, 2.4, 2.6, 2.8, 3.0, 3.2
SubGeV- <i>p</i> i0like	1	2.0, 2.2, 2.4, 2.6, 2.8, 3.2
MultiGeV- <i>e</i> like-nue	10	3.0, 3.4, 3.7, 4.0, 5.0
MultiGeV- <i>e</i> like-nuebar	10	3.0, 3.4, 3.7, 4.0, 5.0
MultiGeV- <i>m</i> ulike	10	3.0, 3.4, 5.0
MultiRing- <i>e</i> like-nue	10	3.0, 3.4, 3.7, 5.0
MultiRing- <i>e</i> like-nuebar	10	3.0, 3.4, 3.7, 5.0
MultiRing- <i>m</i> ulike	10	2.0, 3.124, 3.4, 3.7, 5.0
MultiRing- <i>O</i> ther1	10	3.0, 3.4, 3.7, 4.0, 5.0
PC-Stop	10	2.0, 3.4, 5.0
PC-Through	10	2.0, 3.124, 3.4, 3.7, 5.0
Upmu-Stop	10	3.2, 3.4, 3.7, 8.0
Upmu-Through-Showering	10	2.0, 8.0
Upmu-Through-NonShowering	10	2.0, 8.0

**Table 6.4:** The reconstructed cosine zenith and lepton momentum binning assigned to the atmospheric samples. The “ $\cos(\theta_Z)$  Bins” column illustrates the number of bins uniformly distributed over the  $-1.0 \leq \cos(\theta_Z) \leq 1.0$  region for fully and partially contained samples and  $-1.0 \leq \cos(\theta_Z) \leq 0.0$  region for up- $\mu$  samples.

<sup>1674</sup> (for samples which only have one bin reconstructed zenith angle) and reconstructed  
<sup>1675</sup> direction for each atmospheric sample used within this analysis is illustrated in Fig-  
<sup>1676</sup> ure 6.1.

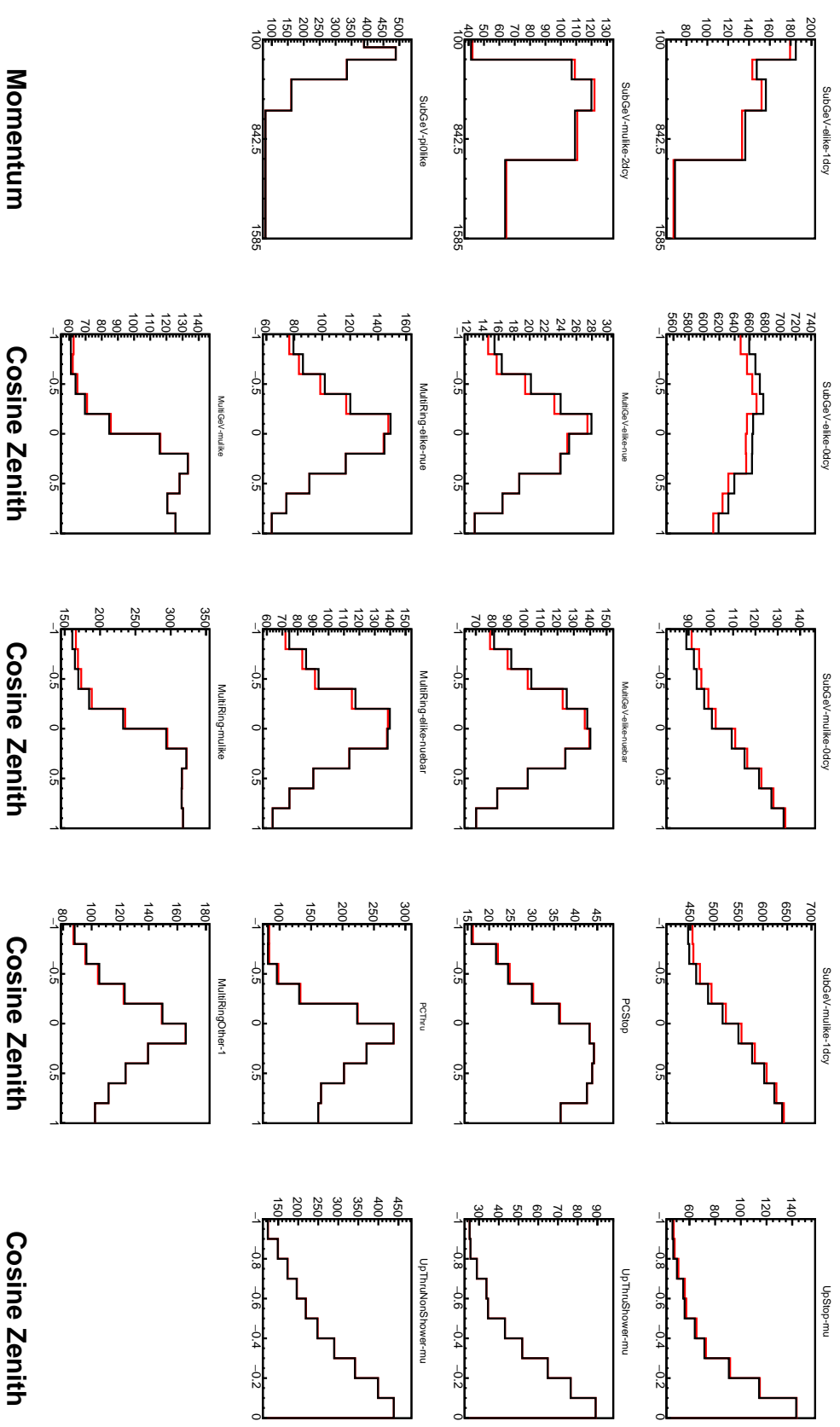


**Figure 6.1:** Comparison of the SK-IV atmospheric samples between predictions made with the Asimov A (Black) and Asimov B (Red) oscillation parameter sets, given in Table 2.2. The subGeV samples CCRES and  $\pi^0$ -like samples are given in their reconstructed lepton momentum. All other samples are presented in their reconstructed zenith angle projection.

### **6.1.2 Near Detector Beam Samples**

The near detector sample selections are documented in detail within [193] and summarised below. Samples are selected based upon the particular Fine Grained Detector (FGD) (see subsection 3.2.2) the neutrino interacted within as well as the operating mode of the beam. For stronger constraints on cross-section model parameters, wrong-sign neutrino samples are also considered when the beam is operating in RHC (antineutrino) mode. Samples from the wrong-sign component of the FHC beam mode are not included as they are statistically insignificant compared to those already listed.

Before being assigned a sample, all events have to undergo CC-inclusive cuts, as defined in TN212.

- Event Timing: The DAQ must be operational and the event must occur within the expected time window
- TPC Requirement: The track path must intercept one or more TPCs
- Fiducial volume: The event must originate from within a fiducial volume
- Upstream Background: Remove reconstruction failures occurring from muons which originate upstream of the FGDs by requiring no high-momentum tracks within 150mm of the candidate vertex. Additionally, events which occur within the downstream FGD are vetoed if a secondary track starts within the upstream FGD
- Broken track removal: All candidates where the muon candidate is broken in two tracks are removed
- Muon PID: Measurements of  $dE/dx$  in a TPC are used to distinguish muon-like events using a likelihood cut

<sub>1700</sub> In addition to these cuts, the RHC neutrino events also have to undergo the following cuts to aide in the separation of neutrino and antineutrino TN246:

- <sub>1702</sub> • TPC Requirement: The track path must intercept TPC2
- <sub>1703</sub> • Positive Track: The highest momentum track must be positive
- <sub>1704</sub> • TPC1 Veto: Remove any events originating upstream of TPC1

<sub>1705</sub> Once all CC-inclusive events have been determined, they are further segregated  
<sub>1706</sub> into sub-samples which target the constraints on interaction modes most relevant at  
<sub>1707</sub> the far detector. These are CC0 $\pi$ , CC1 $\pi$  and CCOther, which target CCQE, CCRES  
<sub>1708</sub> and other CC background interactions. They are defined with the following cuts:

- <sub>1709</sub> •  $\nu_\mu$ CC0 $\pi$  Selection:
- <sub>1710</sub> •  $\nu_\mu$ CC1 $\pi$  Selection:
- <sub>1711</sub> •  $\nu_\mu$ CCOther Selection:

### <sub>1712</sub> 6.1.3 Far Detector Beam Samples

<sub>1713</sub> The beam neutrino events which occur at the SK detector, which pass the reduction  
<sub>1714</sub> cuts detailed in section 5.3, are separated depending on the whether the beam was  
<sub>1715</sub> operating in neutrino or antineutrino mode. The events are then segregated into three  
<sub>1716</sub> separate samples: electron-like (1Re), muon-like (1R $\mu$ ) and CC1 $\pi^+$ -like which are  
<sub>1717</sub> observed as electron-like events with an associated decay electron. As discussed in  
<sub>1718</sub> subsection 6.1.1, positively charged pions from emitted from neutrino interactions are  
<sub>1719</sub> less likely to be absorbed by oxygen nuclei thus are more likely to produce events  
<sub>1720</sub> which are observed with an associated decay electron. Consequently, the CC1 $\pi^+$ -like  
<sub>1721</sub> sample is only selected when the beam is operating in FHC-neutrino mode. Therefore,  
<sub>1722</sub> five beam samples measured at SK are used within this analysis. As the T2K oscillation

1723 analysis has evolved over the years and the selections changed, the sample names  
1724 are suffixed with 2020 to indicate they are the samples used within the 2020 T2K  
1725 oscillation analysis.

1726 The fiducial volume definition for beam samples is slightly different from that used  
1727 within the atmospheric samples. It uses both the distance to the closest wall (`dWall`)  
1728 and the distance to the wall along the particles trajectory (`toWall`). This allows events  
1729 that originate close to the wall but are facing into the tank to be included within the  
1730 analysis, which would have otherwise been removed. The exact cut values for both  
1731 `dWall` and `toWall` are different for each of the three types of sample and optimised  
1732 based on T2K sensitivity to  $\delta_{CP}$  [194, 195].

1733 **1Re event selection** For an event to be classified as a 1Re-like, the event must follow:

- 1734 • Fully-contained and within  $dWall > 80\text{cm}$  and  $toWall > 170\text{cm}$
- 1735 • Total of one ring which is reconstructed as electron-like with reconstructed mo-
- 1736      mentum  $P_e > 100\text{MeV}$
- 1737 • Zero decay electrons are associated with the event
- 1738 • Passes  $\pi^0$  rejection cut discussed in section 5.2

1739 The zero decay electron cut specifically targets CCQE interactions and the  $\pi^0$   
1740 rejection cut it designed to remove neutral current  $\pi^0$  background events as they can  
1741 be easily reconstructed as 1Re events without this cut.

1742 **CC1 $\pi^+$  event selection** This event selection is very similar to that of the 1Re sample.  
1743 The only difference is that the `dWall` and `toWall` criteria are shifted to  $> 50\text{cm}$  and  
1744  $> 270\text{cm}$ , respectively. Furthermore, exactly one decay electron is required from the  
1745  $\pi^+$  decay.

<sup>1746</sup> **1R $\mu$  event selection** A 1Re-like event is determined by the following cuts:

- <sup>1747</sup> • Fully-contained and within  $d_{Wall} > 50\text{cm}$  and  $t_{Wall} > 250\text{cm}$
- <sup>1748</sup> • Total of one ring which is reconstructed as muon-like with reconstructed momentum  $P_\mu > 200\text{MeV}$
- <sup>1749</sup> • Fewer than two decay electrons are associated with the event
- <sup>1750</sup> • Passes  $\pi^+$  rejection cut discussed in section 5.2

<sup>1752</sup> As pions and muons have similar masses, the Cherenkov rings they generate have  
<sup>1753</sup> similar opening angles. Consequently, to select muons, the events have to pass the  $\pi^+$   
<sup>1754</sup> rejection cut which is specifically optimised to separate the two types of events.

<sup>1755</sup> All of these samples are binned in reconstructed neutrino energy. This is possible as  
<sup>1756</sup> the direction from the source is known extremely well, unlike atmospheric neutrinos.  
<sup>1757</sup> This value is calculated for the 1Re and 1R $\mu$  samples assuming CCQE interactions,

$$E_\nu^{rec} = \frac{(M_N - V_{nuc})E_l - m_l^2/2 + M_N V_{nuc} - V_{nuc}^2/2 + (M_P^2 + M_N^2)/2}{M_N - V_{nuc} - E_l + P_l \cos(\theta_{beam})} \quad (6.2)$$

<sup>1758</sup> Where  $M_N$ ,  $M_P$  and  $m_l$  are the masses of the neutron, proton and outgoing lepton,  
<sup>1759</sup> respectively.  $V_{nuc} = 27\text{MeV}$  is the binding energy of the oxygen nuclei,  $\theta_{beam}$  is the  
<sup>1760</sup> angle between the beam and the direction of the outgoing lepton, and  $E_l$  and  $P_l$  are  
<sup>1761</sup> the energy and momentum of that outgoing lepton.

<sup>1762</sup> The reconstructed neutrino energy of the CC1 $\pi^+$  events is modified to include the  
<sup>1763</sup> delta resonance resonantly produced within the interaction,

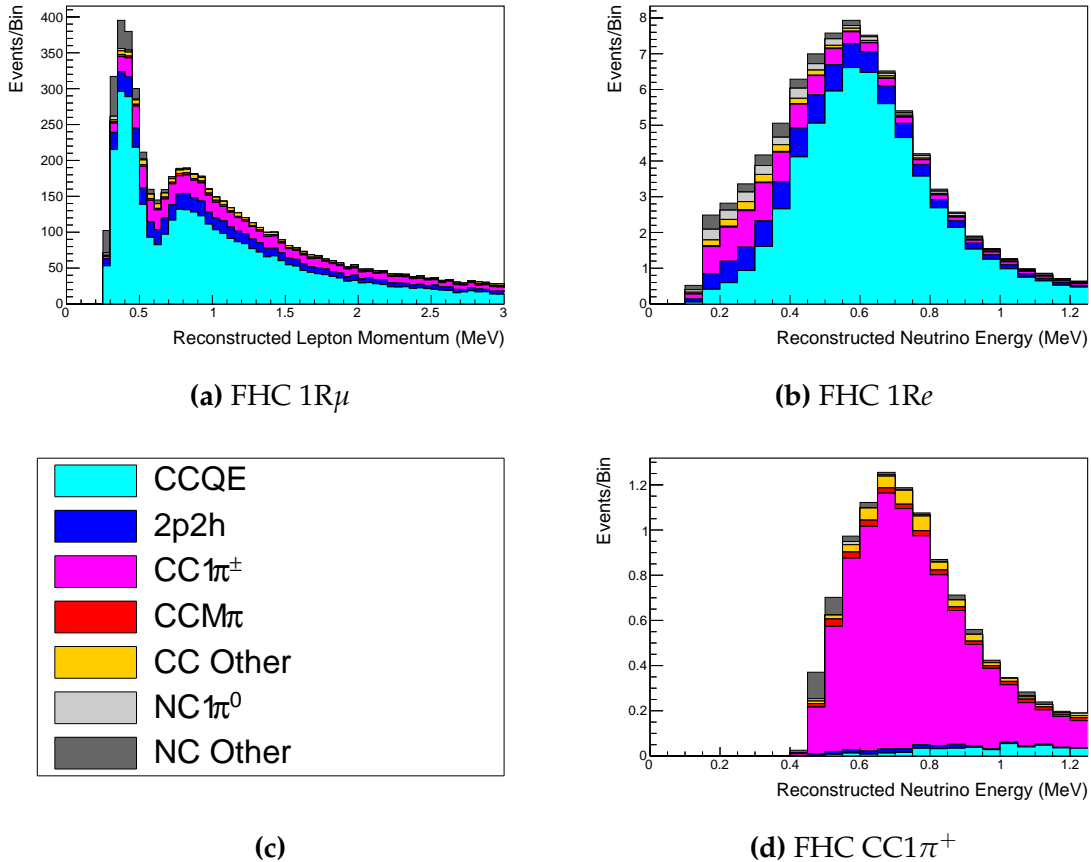


**Figure 6.2:** The reconstructed neutrino energy, as defined by Equation 6.2 and Equation 6.3, for the 1R $\mu$ , 1Re and CC1 $\pi^+$  samples. The generated dial values and Asimov A oscillation parameter sets are assumed. These samples are the FHC mode samples. For ease of viewing, the 1R $\mu$  sample only shows the  $0. \leq E_\nu^{rec} < 3.0\text{GeV}$  but the binning extends out to 30.0GeV.

$$E_\nu^{rec} = \frac{2M_N E_l + M_{\Delta^{++}}^2 - M_N^2 - m_l^2}{2(M_N - E_l + P_l \cos(\theta_{beam}))} \quad (6.3)$$

1764 Where  $M_{\Delta^{++}}$  is the mass of the delta baryon. Binding energy effects are not  
 1765 considered due to the two body process with the delta baryon is assumed.

1766 The reconstructed neutrino energy for the FHC samples is illustrated in Figure 6.2.  
 1767 This is the binning used within the analysis. As expected, the 1R $\mu$  and 1Re are  
 1768 heavily dominated by CCQE interactions, with smaller contributions from 2p2h

meson exchange and resonant pion production interactions. The CC1 $\pi^+$  sample predominantly consists of charged current resonant pion production interactions. The 1Re and CC1 $\pi^+$  samples are also binned by angle between the neutrino beam and the reconstructed lepton momentum. This is to aide in charged current and neutral current separation as indicated in Figure 6.3. This is because the neutral current backgrounds are predominantly due to  $\pi^0$ -decays, where the opening angle of the two gammas alongside the different final state kinematics produces a slightly broader angular distribution compared to the final state particles originating from charged current  $\nu_e$  interactions.

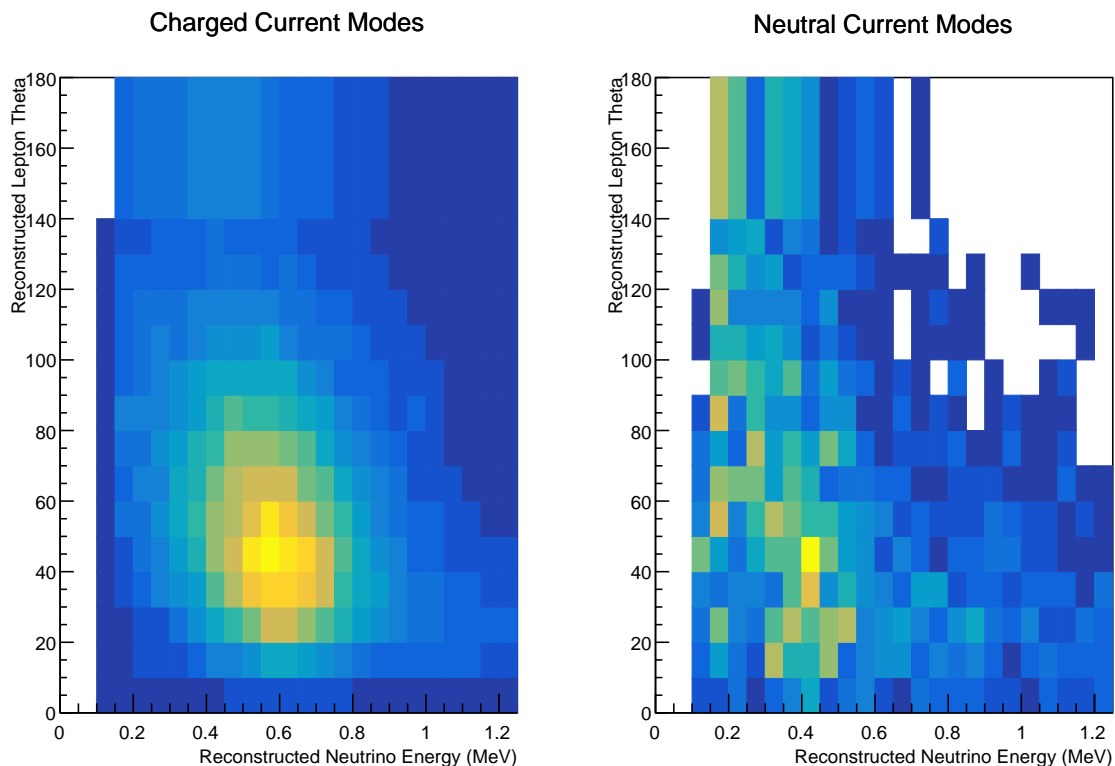


**Figure 6.3:** The distribution of the angle between the neutrino beam direction and the reconstructed final state lepton, for the FHC neutrino mode beam one ring electron sample. The distribution is broken down by neutrino interaction mode into charged current (left) and neutral current (right) components. The pre-fit systematic dial values and Asimov A oscillation parameter sets are assumed.

## <sup>1778</sup> 6.2 Systematic Uncertainties

<sup>1779</sup> The systematics for this uncertainty are split into the groups, or blocks, depending  
<sup>1780</sup> on their purpose. They consist of flux uncertainties, neutrino-matter interaction  
<sup>1781</sup> systematics and detector efficiencies. There are also uncertainties on the oscillation  
<sup>1782</sup> parameters which this analysis will not be sensitive to,  $\Delta m_{12}^2$  and  $\sin^2(\theta_{12})$ . As  
<sup>1783</sup> described in chapter 4, each model parameter used within this analysis requires a  
<sup>1784</sup> prior uncertainty. This is provided via separate covariance matrices for each block.  
<sup>1785</sup> The covariance matrices can include prior correlations between parameters within a  
<sup>1786</sup> single block, but the separate treatment means prior uncertainties can not be included  
<sup>1787</sup> for parameters in different groups. Alternatively, some parameters have no reasonably  
<sup>1788</sup> motivated uncertainties. These parameters are assigned flat priors which do not  
<sup>1789</sup> change the likelihood penalty. The flux, neutrino interaction and detector modelling  
<sup>1790</sup> has already been discussed in section 5.1. The uncertainties invoked within these  
<sup>1791</sup> models are described below.

### <sup>1792</sup> 6.2.1 Beam Flux

<sup>1793</sup> The neutrino beam flux systematics are based upon our uncertainty in the modelling of  
<sup>1794</sup> the components of the beam. This includes: the hadron production model and their re-  
<sup>1795</sup> interactions, the shape, intensity and alignment of the beam with respect to the target,  
<sup>1796</sup> and the uniformity of the magnetic field produced by the horn, alongside other effects.  
<sup>1797</sup> The uncertainty, as a function of neutrino energy, is illustrated in Figure 6.4 which  
<sup>1798</sup> includes the total uncertainty as well as the individual components. The uncertainty  
<sup>1799</sup> for events below, and much higher than, the peak neutrino energy is dominated by  
<sup>1800</sup> hadron production and re-interaction systematics. The beam profile and alignment of  
<sup>1801</sup> the proton beam dominates the systematic uncertainty for events with  $E_\nu \sim 1\text{GeV}$ .

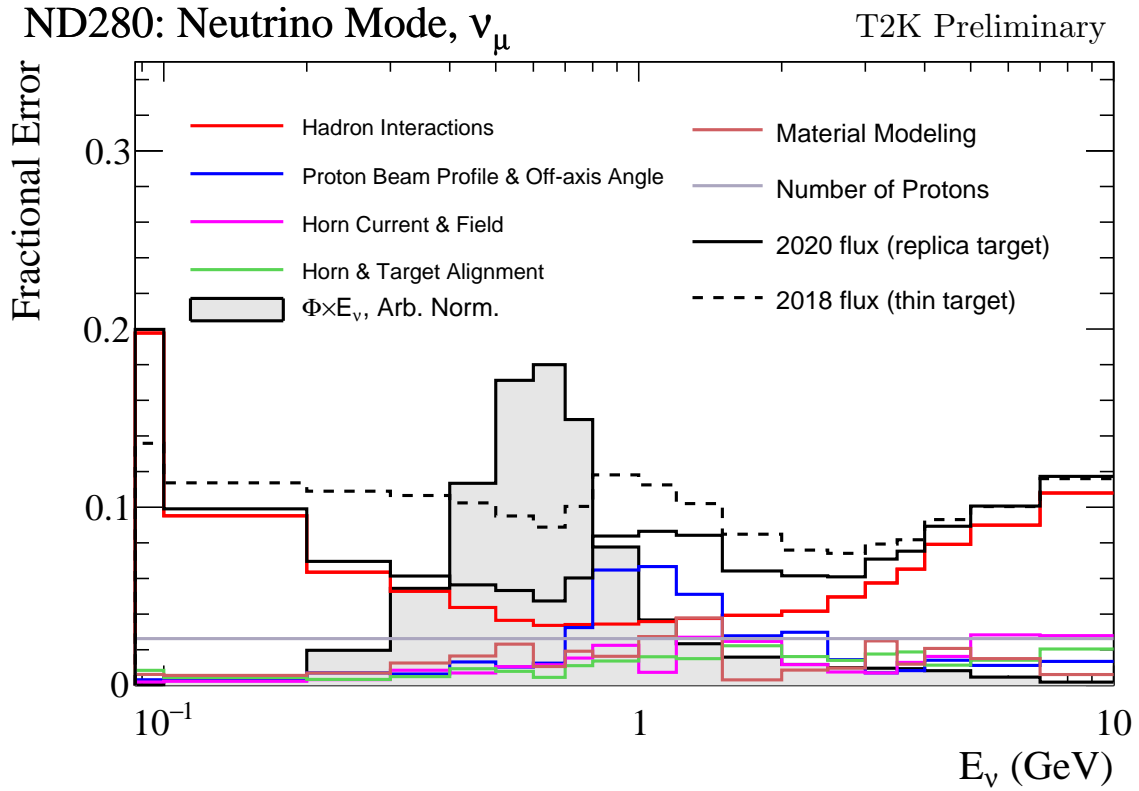


**Figure 6.4:** The total uncertainty evaluated on the near detector  $\nu_\mu$  flux prediction constrained by the replica-target data, illustrated as a function of neutrino energy. The solid(dashed) line indicates the uncertainty used within this analysis(the T2K 2018 analysis). The solid histogram indicates the neutrino flux as a function of energy. Figure taken from [196].

1802        The beam flux uncertainties are described by one hundred parameters. They are  
 1803        split between both ND280 and SK detectors and binned by neutrino flavour:  $\nu_\mu$ ,  $\bar{\nu}_\mu$ ,  $\nu_e$   
 1804        and  $\bar{\nu}_e$ . The response is then broken down as a function of neutrino energy. The bin  
 1805        density in the neutrino energy is the same for the FHC- $\nu_\mu$  and RHC- $\bar{\nu}_\mu$ , and narrows  
 1806        for neutrino energies close to the oscillation maxima of  $E_\nu = 0.6\text{GeV}$ . This binning is  
 1807        specified in Table 6.5. All of these systematic uncertainties are applied as normalisation  
 1808        parameters with Gaussian priors centered at 1.0 and error specified from a covariance  
 1809        matrix provided by the T2K beam group.

Neutrino Flavour	Sign	Neutrino Energy Bin Edges (GeV)
$\mu$	Right	0., 0.4, 0.5, 0.6, 0.7, 1., 1.5, 2.5, 3.5, 5., 7., 30.
$\mu$	Wrong	0., 0.7, 1., 1.5, 2.5, 30.
$e$	Right	0., 0.5, 0.7, 0.8, 1.5, 2.5, 4., 30.
$e$	Wrong	0., 2.5, 30.

**Table 6.5:** The neutrino energy binning for the different neutrino flavours. “Right” sign indicates neutrinos in the FHC beam and antineutrinos in the RHC beam mode. “Wrong” sign indicates antineutrinos in the FHC beam and neutrinos in the RHC beam mode. The binning of the detector response is identical for the FHC and RHC modes as well as at ND280 and SK.

### 1810 6.2.2 Atmospheric Flux

1811 The atmospheric neutrino flux is modelled by the HKKM model, however 16 system-  
 1812 atic uncertainties are applied to control the normalisation of each neutrino flavour,  
 1813 energy and direction. All of the parameters are given Gaussian priors centered at 0  
 1814 and width 1.. They are summarised below:

- 1815 • **Absolute Normalisation:** The overall normalisation of each neutrino flavour is  
 1816 controlled by two independent systematic uncertainties, for  $E_\nu < 1\text{GeV}$  and  $E_\nu >$   
 1817  $1\text{GeV}$ , respectively. This is driven mostly by hadronic interaction uncertainties for  
 1818 the production of pions and kaons [43]. The strength of the response is dependent  
 1819 upon the neutrino energy.
- 1820 • **Relative Normalisation:** Uncertainties on the ratio of  $(\nu_\mu + \bar{\nu}_\mu) / (\nu_e + \bar{\nu}_e)$  are  
 1821 controlled by the difference between the HKKM model [43], FLUKA [46] and  
 1822 Bartol models [42]. Three independent parameters are applied in the energy  
 1823 ranges:  $E_\nu < 1\text{GeV}$ ,  $1\text{GeV} < E_\nu < 10\text{GeV}$ , and  $E_\nu > 10\text{GeV}$ .
- 1824 •  **$\nu/\bar{\nu}$  Normalisation:** The uncertainties in the  $\pi^+/\pi^-$  (and kaon equivalent) pro-  
 1825 duce uncertainties in the flux of  $\nu/\bar{\nu}$ . The response is applied in the same way as  
 1826 the relative normalisation parameters.

1827 • **Up/Down and Vertical/Horizontal Ratio:** Similar to the above two systematics,  
1828 the difference between the HKKM, FLUKA and Bartol model predictions, as a  
1829 function of  $\cos(\theta_Z)$ , is used to control the normalisation of events as a function of  
1830 zenith angle.

1831 •  **$K/\pi$  Ratio:** Higher energy neutrinos ( $E_\nu < 10\text{GeV}$ ) become dependent upon  
1832 kaon decay as the dominant source of neutrinos. Measurements of the ratio of  
1833  $K/\pi$  [197] are used to control the systematic uncertainty of the expected ratio of  
1834 pion and kaon production.

1835 • **Solar Activity:** As the 11-year solar cycle can affect the Earth's magnetic field, the  
1836 flux of primary cosmic rays is modulated across the same period. The uncertainty  
1837 is calculated by taking a  $\pm 1$  year variation, equating to a 10% uncertainty for the  
1838 SK-IV period.

1839 • **Atmospheric Density:** The height of the interaction of the primary cosmic rays is  
1840 dependent upon the atmospheric density. The HKKM assumes the US standard  
1841 1976 [153] profile. This systematic controls the uncertainty in that model.

1842 Updates to the HKKM and Bartol models are underway to use a similar tuning  
1843 technique to that used in the beam flux predictions. After those updates, it may be  
1844 possible to include correlations in the hadron production uncertainty systematics for  
1845 beam and atmospheric flux predictions.

### 1846 6.2.3 Neutrino Interaction

1847 The neutrino interactions which occur within all the detectors are modelled by NEUT.  
1848 The two independent oscillation analyses, T2K beam only and the SK atmospheric  
1849 only, have developed separate interaction models. The T2K-only analysis uses the  
1850 systematics model defined in [198] and the SK-only analysis uses the uncertainties

1851 detailed in [52]. To leverage the most sensitivity out of this joint beam and atmospheric  
1852 analysis, a correlated interaction model has been defined. Where applicable, these  
1853 correlations allow the systematic uncertainties applied to the atmospheric samples to  
1854 be constrained by measurements of the near detector in the beam experiment leading  
1855 to stronger sensitivity to oscillation parameters as compared to an uncorrelated model.  
1856 An in-depth discussion of the reasoning and validity of enforcing correlations is  
1857 documented in [199] and briefly summarised below.

1858 The low energy T2K systematic model has a more sophisticated treatment of CCQE,  
1859 CCMEC and CCRES uncertainties which is due to the purpose made cross-section  
1860 measurements made by the near detector. Furthermore, extensive testing of this model  
1861 has been performed by the working group responsible for this model [198]. However,  
1862 it is not designed for the high energy atmospheric events illustrated in Figure 5.10.  
1863 Therefore the high energy systematic model from the SK-only analysis is implemented  
1864 for the relevant multiGeV samples. The CCQE systematic parameters invoked within  
1865 the SK high energy model are actually contained within T2K's CCQE model. Conse-  
1866 quently, the more sophisticated CCQE and CCMEC T2K model parameters have been  
1867 incorporated into the high energy model but are uncorrelated from the low energy  
1868 counterparts. This results in a more complete model but without any constraint from  
1869 the near detector measurements.

1870 The high energy systematic model includes parameters developed from compar-  
1871 isons of Nieves and Rein-Seghal models which affect CCRES interactions, comparisons  
1872 of the GRV98 and CKMT models which control DIS interactions, and hadron multipli-  
1873 city measurements which modulate the normalisation of  $CCN\pi$  events. The uncertainty  
1874 of the  $\nu_\tau$  cross-section is particularly large and is controlled by a 25% normalisation  
1875 uncertainty. These parameters are applied via normalisation or shape parameters. The  
1876 former linearly scales the weight of all effected Monte-Carlo events, whereas the latter

1877 can increase or decrease a particular events weight depending on its neutrino energy  
1878 and mode of interaction. The response of the shape parameters are defined by third  
1879 order polynominal splines which return a weight for a particular neutrino energy. In  
1880 total, 17 normalisation and 15 shape parameters are included in the more sophisticated  
1881 high energy model.

1882 Figure 6.5 indicates the predicted neutrino energy distibution for both beam and  
1883 subGeV atmospheric samples, and Figure 6.6 illustrates the fractional contribution  
1884 of the different interaction modes per sample. There is clearly significant overlap in  
1885 neutrino energy between the subGeV atmospheric and beam samples, allowing similar  
1886 kinematics in the final state particles. Comparing beam samples with zero decay  
1887 electrons and atmospheric electron-like(muon-like) samples with zero(zero or one)  
1888 decay electrons, there is a very similar contribution of CCQE, CC 2p2h and CC1 $\pi^\pm$   
1889 interactions. The samples which target CC1 $\pi^\pm$  interactions, FHC 1Re1de beam sample  
1890 and atmospheric electron-like(muon-like) samples with one(two) decay electrons, also  
1891 consist of very similar mode interactions. As a consequence of the similarity in energy  
1892 and mode contributions, correlating the systematic model between the beam and  
1893 subGeV atmospheric samples ensures that this analysis attains the largest sensitivity  
1894 to oscillation parameters while still ensuring neutrino interaction systematics are  
1895 correctly accounted for. Due to its sophisticated CCQE model, the T2K systematic  
1896 model was chosen as the basis of the correlated model.

1897 The T2K uncertainty model is applied in a similar methodology to the SK model  
1898 parameters. It consists of 19 shape parameters applied via third order polynominal  
1899 splines and 24 normalisation parameters. Four additional parameters, which model  
1900 the uncertainty in the binning energy, are applied in a way to shift the momentum  
1901 of lepton emitted from a nucleus. The majority of these parameters are assigned a  
1902 Gaussian prior uncertainty. Those that have no theoretical reasoning, or those which

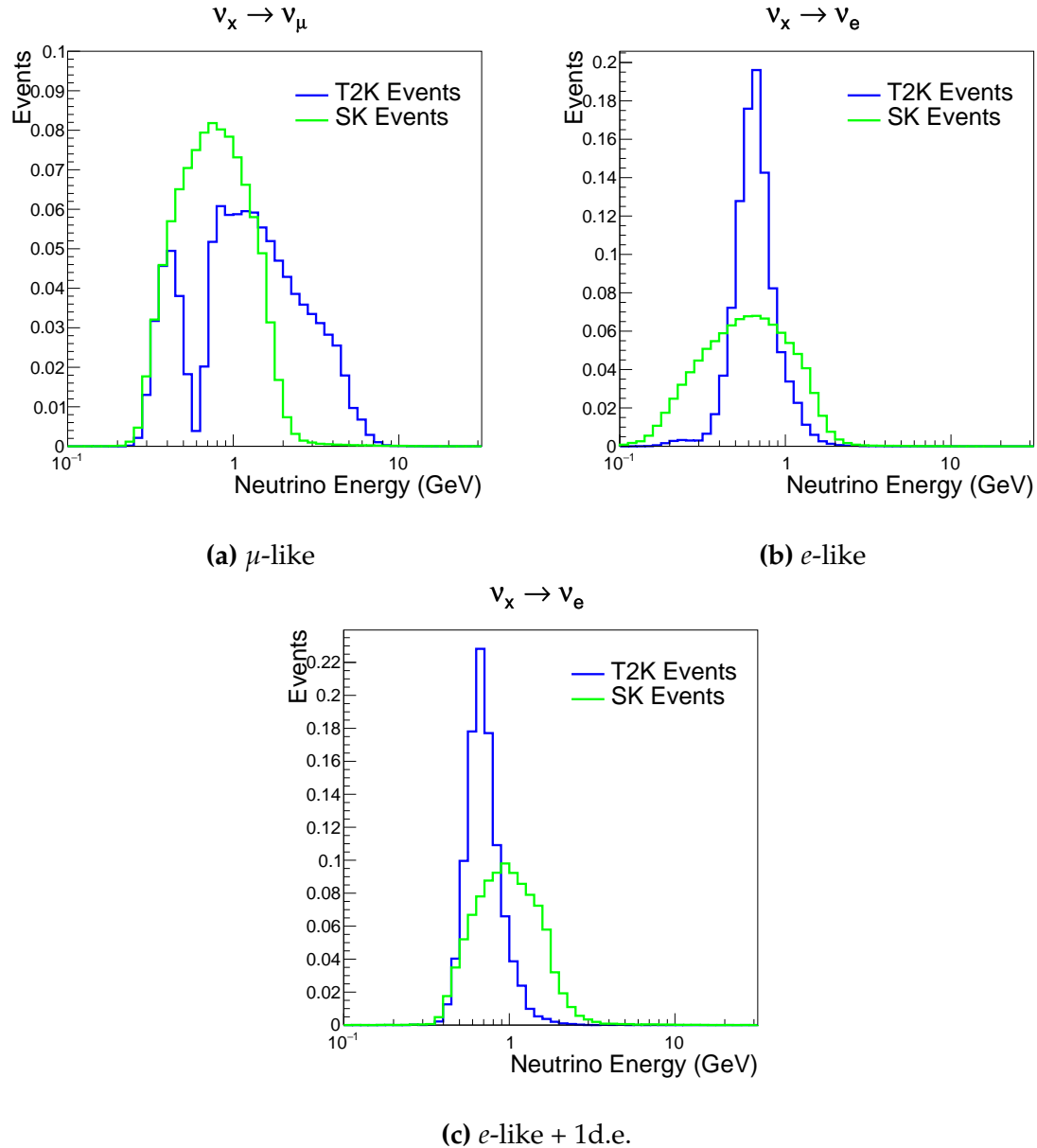


**Figure 6.5:** The prediction neutrino energy distribution for subGeV atmospheric and beam samples, given for muon-like samples FHC+RHC 1R $\mu$  beam samples compared to the subGeV  $\mu$ -like 0+1 decay electrons (d.e.) atmospheric samples, electron-like 0d.e. samples FHC+RHC 1Re beam samples compared to the subGeV  $e$ -like 1d.e. sample, and electron-like 1d.e. sample FHC1Re1de beam sample compared to the subGeV  $e$ -like 1d.e. atmospheric sample.

<sup>1903</sup> have not been fit to external data, are assigned a flat prior which does not affect the  
<sup>1904</sup> penalty term. The CCQE model parameters were tuned to MiniBooNE [200] and  
<sup>1905</sup> MINER $\nu$ A [201] measurements and CCRES model parameters are tuned to ANL and  
<sup>1906</sup> BNL experiments [202].

	CC QE	CC 2p2h	CC $1\pi^\pm$	CC $M\pi$	CC Other	NC $\pi^0$	NC $1\pi^\pm$	NC $M\pi$	NC Coh.	NC Other
FHC 1R+1d.e. e-like	<b>0.04</b>	<b>0.02</b>	<b>0.83</b>	<b>0.03</b>	<b>0.04</b>	<b>0.01</b>	<b>0.01</b>	<b>0.01</b>	<b>0.00</b>	<b>0.01</b>
RHC 1R e-like	<b>0.62</b>	<b>0.12</b>	<b>0.11</b>	<b>0.01</b>	<b>0.02</b>	<b>0.06</b>	<b>0.01</b>	<b>0.01</b>	<b>0.01</b>	<b>0.04</b>
FHC 1R e-like	<b>0.68</b>	<b>0.12</b>	<b>0.10</b>	<b>0.00</b>	<b>0.02</b>	<b>0.04</b>	<b>0.01</b>	<b>0.00</b>	<b>0.00</b>	<b>0.02</b>
RHC 1R $\mu$ -like	<b>0.62</b>	<b>0.13</b>	<b>0.17</b>	<b>0.02</b>	<b>0.03</b>	<b>0.00</b>	<b>0.02</b>	<b>0.00</b>	<b>0.00</b>	<b>0.00</b>
FHC 1R $\mu$ -like	<b>0.62</b>	<b>0.12</b>	<b>0.16</b>	<b>0.02</b>	<b>0.03</b>	<b>0.00</b>	<b>0.03</b>	<b>0.00</b>	<b>0.00</b>	<b>0.00</b>
S.G. $\pi^0$ -like	<b>0.05</b>	<b>0.01</b>	<b>0.02</b>	<b>0.00</b>	<b>0.01</b>	<b>0.68</b>	<b>0.06</b>	<b>0.07</b>	<b>0.06</b>	<b>0.04</b>
S.G. $\mu$ -like 2de	<b>0.04</b>	<b>0.01</b>	<b>0.80</b>	<b>0.10</b>	<b>0.04</b>	<b>0.00</b>	<b>0.00</b>	<b>0.00</b>	<b>0.00</b>	<b>0.00</b>
S.G. $\mu$ -like 1de	<b>0.72</b>	<b>0.11</b>	<b>0.12</b>	<b>0.01</b>	<b>0.02</b>	<b>0.00</b>	<b>0.01</b>	<b>0.00</b>	<b>0.00</b>	<b>0.00</b>
S.G. $\mu$ -like 0de	<b>0.68</b>	<b>0.11</b>	<b>0.10</b>	<b>0.01</b>	<b>0.02</b>	<b>0.01</b>	<b>0.05</b>	<b>0.01</b>	<b>0.00</b>	<b>0.02</b>
S.G. e-like 1de	<b>0.05</b>	<b>0.01</b>	<b>0.75</b>	<b>0.10</b>	<b>0.05</b>	<b>0.00</b>	<b>0.01</b>	<b>0.02</b>	<b>0.00</b>	<b>0.01</b>
S.G. e-like 0de	<b>0.73</b>	<b>0.11</b>	<b>0.10</b>	<b>0.01</b>	<b>0.02</b>	<b>0.02</b>	<b>0.00</b>	<b>0.00</b>	<b>0.00</b>	<b>0.00</b>

**Figure 6.6:** The interaction mode contribution of each sample given as a fraction of the total event rate in that sample. All systematic dials are set to their nominal values and the Asimov A oscillation parameters are assumed. The Charged Current (CC) modes are broken into quasi-elastic (QE), meson exchange (2p2h), resonant charged pion production ( $1\pi^\pm$ ), multi-pion production ( $M\pi$ ), and other interaction category. Neutral Current (NC) interaction modes are given in interaction mode categories:  $\pi^0$  production, resonant charged pion production, multi-pion production and other.

1907 There are three particular tunes of the T2K low energy cross section model typically  
 1908 considered. Firstly, the “generated” tune which is the set of dial values at which the  
 1909 Monte Carlo was generated with. Secondly, the set of dial values which are taken  
 1910 from external data measurements and used as inputs. These are the “pre-fit” dial  
 1911 values. The reason these two sets of dial values are different is because the external  
 1912 data measurements are continually updated but it is very computational intensive  
 1913 to regenerate a Monte Carlo prediction after each update. Consequently the pre-fit  
 1914 and generated dial values differ. The final tune is the “post-fit” or “post-BANFF”  
 1915 dial values. These are the values taken from a fit to the beam near detector data.  
 1916 This fit is performed by two independent fitting frameworks, MaCh3 and BANFF, which

ensures reliable measurements. The output of each fitter is converted into a covariance matrix to describe the error and correlations between all the cross section parameters. This is then propagated to the far-detector oscillation analysis group for use in the P-Theta fitting framework. As MaCh3 can perform a near detector fit, it is included within the simultaneous fit of far-detector beam and atmospheric oscillation analysis. This is because this technique does not require any assumption of Gaussian posterior distributions which is required in the covariance matrix methodology.

On top of the combination of the SK and T2K interaction models, several other parameters have been specifically developed for the joint oscillation analysis. As the majority of the atmospheric samples'  $\delta_{CP}$  sensitivity comes from the normalisation of subGeV electron-like events, additional dial which models an alternative Continous Random Phase Approximation (CRPA) nuclear ground state has been implemented [199]. As the near detector can not sufficiently constrain the model, this dial approximates the event weights if a CRPA model had been assumed rather than a spectral function. This dial only effects  $\nu_e$  and  $\bar{\nu}_e$  and is applied as a shape parameter.

Further additions to the model have been included due to the the subGeV  $\pi^0$  atmospheric sample. This particulary targets charged current and neutral current  $\pi^0$  producing interactions to constrain the systematic uncertainties. However, there is no analogous sample in the T2K beam-only analysis so no significant effort has been placed into building a sufficient uncertainty model. Therefore, an uncertainty which effects neutral current resonant  $\pi^0$  production is incorporated in this analysis. Comparisons of NEUT's NC resonant pion production predictions have been made to MiniBooNE [203] data and a consistent 16% to 21% underprediction is observed. Consequently, a conservative 30% normalisation is invoked.

Events which originate from above the detector and travel downward are very insensitive to oscillation parameters and act similar to the near detector within an

1943 accelerator experiment (Details are illustrated in chapter 7). Consequently, the applica-  
 1944 tion of the T2K low energy cross section and the effect of the near detector constraint  
 1945 on the atmospheric samples can be studied through these events, without biasing  
 1946 the results from oscillation effects. The downward going predictives are illustrated  
 1947 in Figure 6.7. For samples which target CCQE interactions (electron-like with 0 de-  
 1948 cay electrons and muon-like with 0 or 1 decay electrons), the application of the near  
 1949 detector constraint is well within statistical fluctuation of the down-going data and  
 1950 no significant tension is observed between the data and the Monte Carlo prediction  
 1951 with the T2K near detector constraint. This is not the case for samples with target  
 1952 CCRES interactions (electron-like with 1 decay electron and muon-like with 2 deca-  
 1953 electrons). The electron-like data is consistent with the constrained prediction at higher  
 1954 reconstructed momenta but diverges at lower momentum, whereas the muon-like  
 1955 sample is under-predicted throughout the range of momenta. To combat this disagree-  
 1956 ment, an additional cross section systematic dial, specifically designed to inflate the  
 1957 low pion momentum systematics was developed in [199]. This is a shape parameter  
 1958 implemented with through a splined response.

## 1959 6.2.4 Near Detector

1960 The systematics applied due to uncertainties arising from the response of the near  
 1961 detector is contained within 574 normalisation parameters binned in momentum and  
 1962 angle,  $P_\mu \text{ ad } \cos(\theta_\mu)$ , of the final-state muon. These are applied via a covariance  
 1963 matrix with each parameter been assigned a Gaussian prior from that covariance  
 1964 matrix. These normalisation parameters are built from underlying systematics, e.g.  
 1965 pion secondary interaction systematics, which are randomly thrown and the variation  
 1966 in each  $P_\mu \times \cos(\theta_\mu)$  bin is determined. This is performed 2000 times and a covariance  
 1967 matrix response is created. This allows significant correlations between FGD1 and

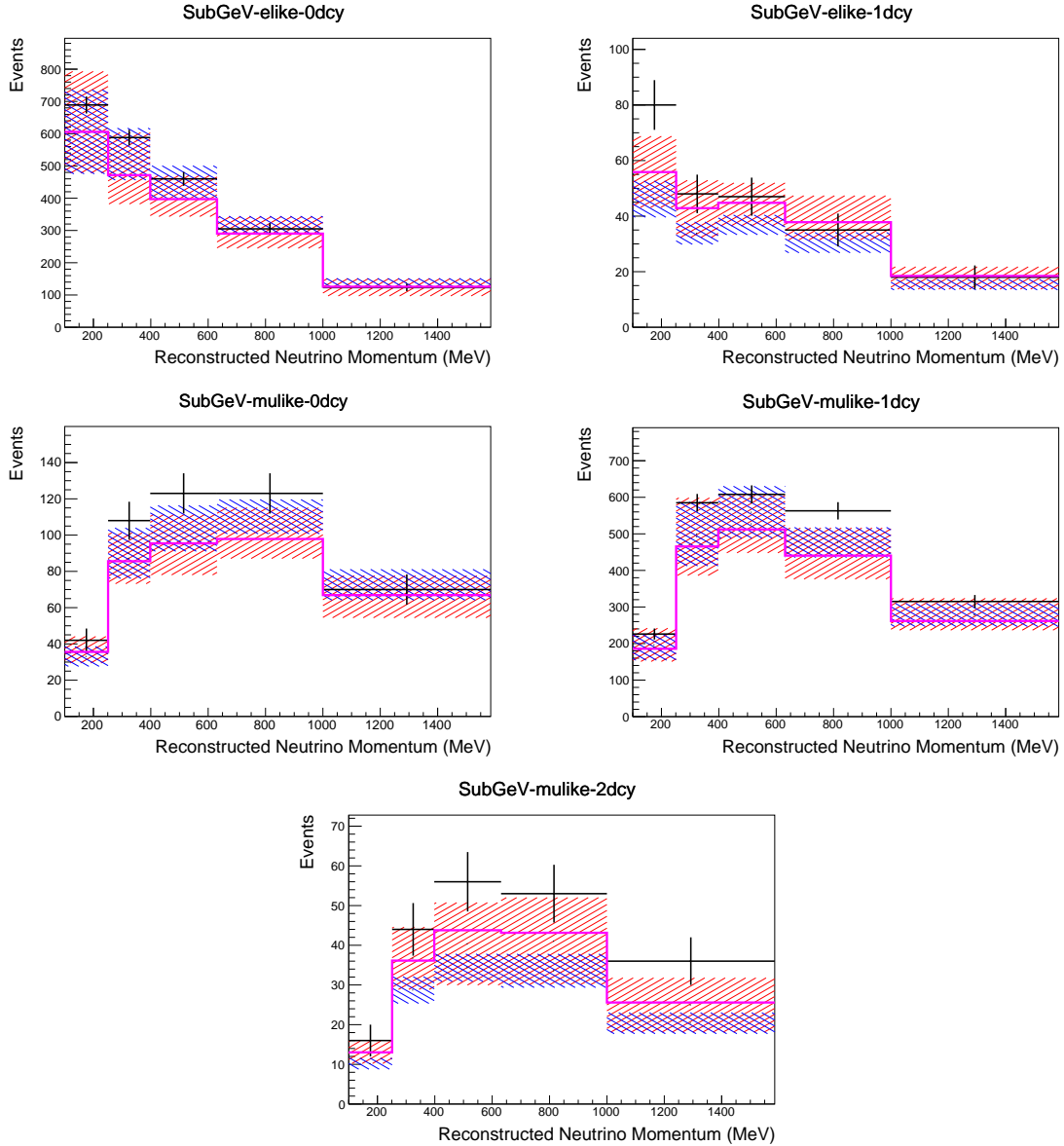


**Figure 6.7:** Down-going atmospheric subGeV single-ring samples comparing the mean and error of the pre-fit and post-fit Monte Carlo predictions in red and blue, respectively. The magneta histogram illustrates the Monte Carlo prediction using the generated dial values. The black points illustrates the down-going data with statistical errors given. The mean and errors of the Monte Carlo predictions are calculated by the techniques documented in subsection 4.3.4. The cross-section and atmospheric flux parameters are either thrown from their pre-fit uncertainties (denoted pre-fit band), or the cross section dial values are randomly sampled from a MCMC chain whilst the atmospheric flux parameters are thrown from their pre-fit distributions (denoted post-fit band).

1968 FGD2 samples, as well as adjacent bins. Statistical uncertainties are accounted for by  
 1969 including fluctuations of each event's weight from a Poission distribution.

1970 Similar to the cross section systematics, MaCh3 and BANFF are used to constrain  
1971 the uncertainty of these systematics through independent validations. Each fitter  
1972 generates a post-fit covariance matrix which is compared and passed to the far-detector  
1973 oscillation analysis working group. However, as the analysis presented within this  
1974 thesis uses the MaCh3 framework, a joint oscillation analysis fit of all three sets of  
1975 samples is performed. From the T2K-only perspective, this joint analysis including  
1976 atmospheric samples allows additional constraints on the systematic uncertainties  
1977 where correlations have been invoked.

### 1978 6.2.5 Far Detector

1979 Two configurations of the far detector systematic model implementation have been  
1980 considered. Firstly, the far detector systematic uncertainties for beam and atmo-  
1981 spheric samples are taken from their respective analysis inputs, denoted “official  
1982 inputs” analysis. Consequently, no correlations are assumed between the beam and  
1983 atmospheric samples. The generation of the beam- and atmospheric- specific inputs  
1984 are documented in subsubsection 6.2.5.1 and subsubsection 6.2.5.2 for the beam and  
1985 atmospheric samples, respectively. Secondly, a correlated detector model has been  
1986 considered. Here, the distribution of parameters used for applying event cuts (e.g.  
1987 electron-muon separation) are modified within the fit, following similar methodology  
1988 to the beam far detector systematics model implementation. However, it has been  
1989 designed to ensure that the atmospheric data is not double-counted, which would be  
1990 the case for the official inputs analysis. This alternative implementation is detailed in  
1991 subsubsection 6.2.5.3.

---

### 1992 6.2.5.1 Beam Samples

1993 There are 45 systematics which describe the response of the far detector, specifically for  
 1994 beam sample neutrino events. 44 of these parameters are normalisation parameters and  
 1995 are split by the interaction mode, true neutrino flavour, reconstructed neutrino energy  
 1996 and sample which they effect. The final parameter is the energy scale uncertainty. It is  
 1997 applied as a multiplicative factor to the reconstructed neutrino energy. The value of  
 1998 the systematic is taken from Monte Carlo to data differences illustrated in [185]. The  
 1999 normalisation parameters are assigned a Gaussian error centrelised at 1.0 and error  
 2000 taken from a covariance matrix. A detailed breakdown of the following procedure is  
 2001 found in [194]. To build the covariance matrix, first a fit is performed to atmospheric  
 2002 data which has been selected using beam sample selection cuts. The variable which  
 2003 defines each cut,  $L$  (e.g. the electron-muon pid parameter) is assigned a smear,  $\alpha$ , and  
 2004 shift,  $\beta$  parameter such that,

$$L_j^i \rightarrow \bar{L}_j^i = \alpha_j^i L + \beta_j^i \quad (6.4)$$

2005 Where  $L_j^i$  ( $\bar{L}_j^i$ ) correspond to nominal(varied) pid cut parameters given in Table 6.6.  
 2006 The shift and smear parameters are binned by final-state topology,  $j$ , where the binning  
 2007 is given in Table 6.7. This approach is used to allow the cut parameter distributions to  
 2008 be modified within the fit which allows better data to Monte Carlo agreement.

2009 Beyond the uncertainty on the pid cut criteria, the mis-modelling of  $\pi^0$  events is also  
 2010 considered. If one of the two rings from a  $\pi^0$  event is missed, this will be reconstructed  
 2011 as a  $CC\nu_e$  event. This is one of the largest systematics hindering the electron neutrino  
 2012 appearance analyses. Consequently, a systematic has been introduced to constrain  
 2013 the mis-modelling of  $\pi^0$  events in SK. To evaluate this systematic uncertainty, a set of

Cut Variable	Parameter Name
0	<code>fitQun e/μ PID</code>
1	<code>fitQun e/π<sup>0</sup> PID</code>
2	<code>fitQun μ/π PID</code>
3	<code>fitQun Ring-Counting Parameter</code>

**Table 6.6:** List of cut variables which are included within the shift/smear fit documented in [194].

Category	Description
1e	Only one electron above Cerenkov threshold in the final state
1μ	Only one muon above Cerenkov threshold in the final state
1e+other	One electron and one or more other charged particles above Cerenkov threshold in the final state
1μ+other	One muon and one or more other charged particles above Cerenkov threshold in the final state
1π <sup>0</sup>	Only one π <sup>0</sup> in the final state
1π <sup>±</sup> or 1p	Only one hadron (typically charged pion or proton) in the final state
Other	Any other final state

**Table 6.7:** Reconstructed event topology categories on which the SK detector systematics [194] are based.

“hybrid- $\pi^0$  samples is constructed. These events are built by overlaying one electron-like ring from the SK atmospheric neutrino samples or decay electron ring from a stopping cosmic ray muon with one simulated photon ring. Both rings are chosen so that momenta and opening angle follow the decay kinematics of NC  $\pi^0$  events from the T2K-MC. Hybrid- $\pi^0$  Monte Carlo samples with both rings from the SK Monte Carlo are produced to compare with the hybrid- $\pi^0$  data samples and the difference in the fraction of events that pass the  $\nu_e$  selection criteria is used to assign the systematic error. In order to investigate any data to Monte Carlo differences which may originate from either the higher energy ring or lower energy ring, two samples are built; a sample in which the electron constitutes the higher energy ring from the  $\pi^0$  decay called the primary sample, and another one in which it constitutes the lower energy

2025 ring called the secondary sample. The standard T2K  $\nu_e$  `fiTQun` event selection criteria  
2026 are used to select events.

2027 Final contributions to the covariance matrix are determined by supplementary  
2028 uncertainties attained by comparing stopping muon data to Monte Carlo prediction,  
2029 as first introduced in section 5.2. The efficiency of tagging decay electrons is estimated  
2030 by the stopping muon data/Monte Carlo differences by comparing the number of  
2031 one decay electron events to the number of events with one or less decay electrons.  
2032 The rate at which fake decay electrons are reconstructed by `fiTQun` is estimated in a  
2033 similar way with the only difference being the ratio compares the number of two decay  
2034 electron events to the number of events with one or two reconstructed decay electrons.  
2035 The two sources of systematics are added in quadrature weighted by the number of  
2036 events with one true decay electron yielding a 0.2% systematic uncertainty. The muon  
2037 mis-identification rate is estimated by comparing the number of electron-like events  
2038 which have one decay electron to the total number of events with one decay electron.  
2039 This systematic is estimated as a 30% effect in the rate of muon mis-identification.  
2040 A fiducial volume systematic of  $\pm 2.5\text{cm}$  which corresponds to a 0.5% shift in the  
2041 normalisation of events. Additional normalisation uncertainties based on neutrino  
2042 flavour and interaction mode are also defined in [183, 204, 205].

2043 This covariance matrix is then added in quadrature with two other covariance matri-  
2044 ces. These are matrices which describe the uncertainties due to secondary interactions  
2045 which modify the final state kinematics and the photo-nucleon interactions. These  
2046 are generated by studying the effect of each samples event rates when considering  
2047 variations of the underlying parameters.

**2048 6.2.5.2 Atmospheric Samples**

2049 The systematic parameters which control the detector systematics are split into two  
2050 sub-groups. Those which are related to particle identification and ring counting  
2051 systematics and those which are related to calibration measurements.

2052 The particle identification systematics consist of five parameters. The ring sepa-  
2053 ration systematic enforces an anti-correlated response between the single-ring and  
2054 multi-ring samples. This is implemented as a fractional increase/decrease in the over-  
2055 all normalisation of each sample, depending on the distance to the nearest wall from  
2056 an event's vertex. The coefficients of the normalisation is estimated prior to the fit and  
2057 depends on the atmospheric sample. The single-ring and multi-ring PID systematics  
2058 encode the detector's ability to separate electron-like and muon-like events and are  
2059 implemented in an identical way as the ring separation systematic.

2060 The multi-ring electron-like separation systematics encode the ability of the detector  
2061 to separate neutrino from anti-neutrino events. As an important systematic in the mass  
2062 hierarchy determination, this systematic controls the relative normalisation's of the  $\nu_e$   
2063 and  $\bar{\nu}_e$  enriched samples. A two-stage approach is implemented in the event selection  
2064 and a systematic is implemented for both stages. The first stage in the event selection  
2065 is to confirm that the most energetic ring, which is required to be electron-like, is from  
2066 the neutrino interaction rather than a pion decay from any hadronic system present  
2067 in the event. The second stage of separation uses a likelihood-based cut to separate  
2068  $\nu_e/\bar{\nu}_e$  events. This takes the typical properties of  $\nu_e$  scattering events into account;  
2069 e.g. less forward-going, with larger energy fractions in the hadronic system. These  
2070 parameters are implemented via normalisation parameters which vary the event rate  
2071 of each multi-ring sample, whilst ensuring the total event rate is conserved.

2072 There are 22 systematics related to calibration measurements, including effects  
2073 from backgrounds, reduction and showering effects. They are documented in [89] and  
2074 briefly summarised in Table 6.8. They are applied via normalisation parameters, with  
2075 the separation systematics required the conservation of event rate across all samples.

**Table 6.8:** Sources of systematic errors specified within the grouped into the “calibration” systematics model.

Index	Description
0	Partially contained reduction
1	Fully contained reduction
2	Separation of fully contained and partially contained events
3	Separation of stopping and through-going partially contained events in top of detector
4	Separation of stopping and through-going partially contained events in barrel of detector
5	Separation of stopping and through-going partially contained events in bottom of detector
6	Background due to cosmic rays
7	Background due to flasher events
8	Vertex systematic moving events into and out of fiducial volume
9	Upward going muon event reduction
10	Separation of stopping and through-going in upward going muon events
11	Energy systematic in upward going muon events
12	Reconstruction of path length of upward going muon events
13	Separation of showering and non-showering upward going muon events
14	Background of stopping upward going muon events
15	Background of non-showering through-going upward going muon events
16	Background of showering through-going upward going muon events
17	Efficiency of tagging two rings from $\pi^0$ decay
18	Efficiency of decay electron tagging
19	Background from down going cosmic muons
20	Asymmetry of energy deposition in tank
21	Energy scale deposition

**2076 6.2.5.3 Correlated Detector Model**

2077 A complete uncertainty model of the SK detector would be able to determine the  
2078 systematic shift on the sample spectra for a variation of the underlying parameters, e.g.  
2079 PMT angular acceptance. However, this is particularly resource intensive, requiring  
2080 Monte Carlo predictions to be made for each plausible variation. Consequently an  
2081 effective parameter model has been utilised for a correlated detector model. This  
2082 follows from the T2K-only model implementation documented in subsubsection 6.2.5.1.  
2083 The T2K-only implementation can not be used for atmospheric sample systematics  
2084 because it is built upon on a fit to atmospheric data. Consequently, an implementation  
2085 where the cut distributions (given in Table 6.6) from both beam and atmospheric  
2086 samples are fit, whilst simultaneously fitting for oscillation parameters. The fit to the  
2087 cut variables performs a shape-only fit to ensure that no double-counting occurs.

2088 The correlated detector model utilises the same smear and shift parameters doc-  
2089 umented in subsubsection 6.2.5.1, split by final state topology. This splitting is done  
2090 because the detector will respond differently for events which have one or multiple  
2091 rings. For example, the detector will be able to distinguish single-ring events better  
2092 than two overlapping ring events, resulting in smaller systematic uncertainty for one  
2093 ring events compared to two ring events. Furthermore, the shift and smear param-  
2094 eters are split by visible energy deposited within the tank has been included, with  
2095 binning specified in Table 6.9. This is because atmospheric events are categorised by  
2096 subGeV and multiGeV events based on visible energy, so this splitting is required  
2097 when correlating the systematic model for beam and atmospheric events. Alongside  
2098 the technical requirement, higher energy events will be better reconstructed due to  
2099 fractionally less noise within the detector. Consequently, this analysis correlates the  
2100 detector systematics between the far-detector beam and subGeV atmospheric samples

2101 due to their similar energies and interaction types. As a result of the inclusion of visible  
2102 energy binning, Equation 6.4 becomes

$$L_{jk}^i \rightarrow \bar{L}_{jk}^i = \alpha_{jk}^i L + \beta_{jk}^i, \quad (6.5)$$

2103 where  $k$  is the visible energy bin. The multi-GeV, multi-ring, PC and Up- $\mu$  samples  
2104 will be subject to the ATMPD particle identification systematics implementation as  
2105 described in subsubsection 6.2.5.2 rather than using this correlated detector model.  
2106 The calibration systematics also described in the aforementioned chapter still apply to  
2107 all atmospheric samples.

Index	Range (MeV)
0	$30 \geq x > 300$
1	$300 \geq x > 700$
2	$700 \geq x > 1330$
3	$1330 \geq x$

**Table 6.9:** Reconstructed event topology categories on which the SK detector systematics are based

2108 The implementation of this systematic model takes the events reconstructed values  
2109 of the cut parameters, modifies them by the particular shift and smear parameter for  
2110 that event, and then re-applies event selection. This invokes event migration, which is  
2111 a new feature incorporated into the MaCh3 framework which is only achievable due  
2112 to the event-by-event reweighting scheme.

2113 Particular care has to be taken when varying the ring counting parameter. This is  
2114 because the number of rings is a finite value (one-ring, two-rings, etc.) which can not be  
2115 continuously varied. Consequently a ring counting parameter,  $RC_i$ , is calculated for the  
2116  $i^{th}$  event, following the definition in [206]. The likelihood from all considered one-ring

2117 (1R) and two-ring (2R) fits are compared to determine the preferred hypothesis. This  
2118 is done by searching for the minimum log likelihoods,  $\log(L_{1R})$  and  $\log(L_{2R})$ . The  
2119 difference is computed as  $\Delta_{LLH} = \log(L_{1R}) - \log(L_{2R})$ . The ring counting parameter  
2120 is then defined as,

$$RC_i = \text{sgn}(\Delta_{LLH} - C_{Thres}) \times \sqrt{|\Delta_{LLH} - C_{Thres}|}, \quad (6.6)$$

2121 where  $C_{Thres} = 150.0 - 0.6 \times P_{2R}$ , and  $P_{2R}$  is the momentum of the preferred two-  
2122 ring hypothesis, and  $\text{sgn}(x) = x/|x|$ . The co-efficients used within the definition  
2123 of  $C_{Thres}$  are calculated based Monte Carlo studies. This ring counting parameter  
2124 corresponds to an intermediate likelihood value used within the `fitQun` algorithm to  
2125 decide the number of rings associated with a particular event. However, fake-ring  
2126 merging algorithms are applied after this likelihood value is used to determine the  
2127 number of rings associated with an event. Consequently, this ring counting parameter  
2128 does not always exactly correspond to the number of reconstructed rings. This can be  
2129 seen in Figure 6.8.

2130 As the `fitQun` algorithm does not provide a likelihood value after the fake-ring  
2131 algorithms have been applied, the ring counting parameter distribution is connected  
2132 to the final number of reconstructed rings through “maps”. These are two dimen-  
2133 sional distributions linking the ring counting parameter and the final number of  
2134 reconstructed rings. An example is illustrated in Figure 6.9. In principle, the `fitQun`  
2135 reconstruction algorithm should be re-ran after the variation in the ring counting  
2136 parameter. However, this is not computationally viable. Therefore the “maps” are  
2137 used as a reweighting template.

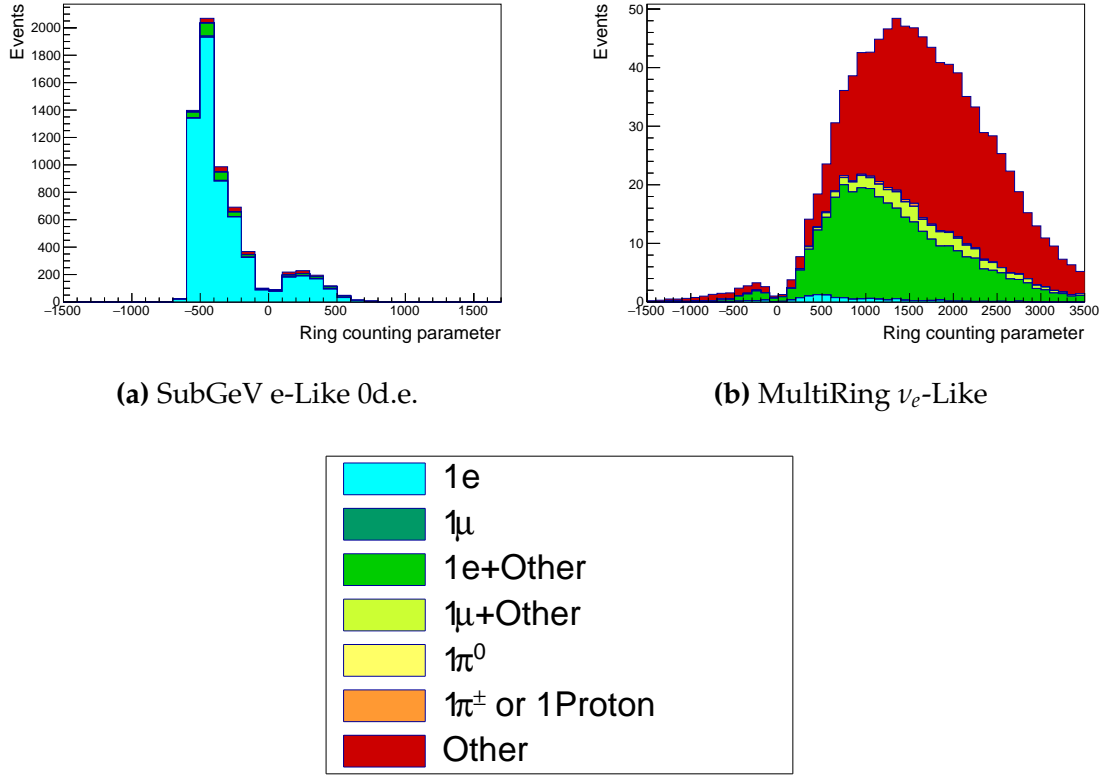


**Figure 6.8:** The ring counting parameter, as defined in Equation 6.6, for the subGeV electron-like zero decay electron and multi-ring  $\nu_e$ -like samples.

The maps are split by final state topology and true neutrino flavour and all fitQun -  
 reconstructed Monte Carlo events are used to fill them. To ensure conservation of event  
 rate, the maps are normalised such that the total event rate across all number of recon-  
 structed rings is equal to one. Prior to the fit, an event's nominal weight is calculated as  
 $W(N_{Rings}^i, L_{jk}^i)$ , where  $N_{Rings}^i$  is the reconstructed number of rings for the  $i^{th}$  event and  
 $W(x, y)$  is the bin content in the associated map for  $x$  number of rings and ring count-  
 ing parameter  $L$ . Then during the fit, the value of  $R = W(N_{Rings}^i, \bar{L}_{jk}^i) / W(N_{Rings}^i, L_{jk}^i)$   
 is calculated as the ring-counting weight for the  $i^{th}$  event. This is the only cut variable  
 which uses a reweighting scheme rather than event migration.

The  $\pi^0$  systematics introduced in subsection 6.2.4 were expected to be applied  
 via a covariance matrix. As this alternative technique performs a simultaneous fit  
 between detector distributions and oscillation parameters, the implementation of the

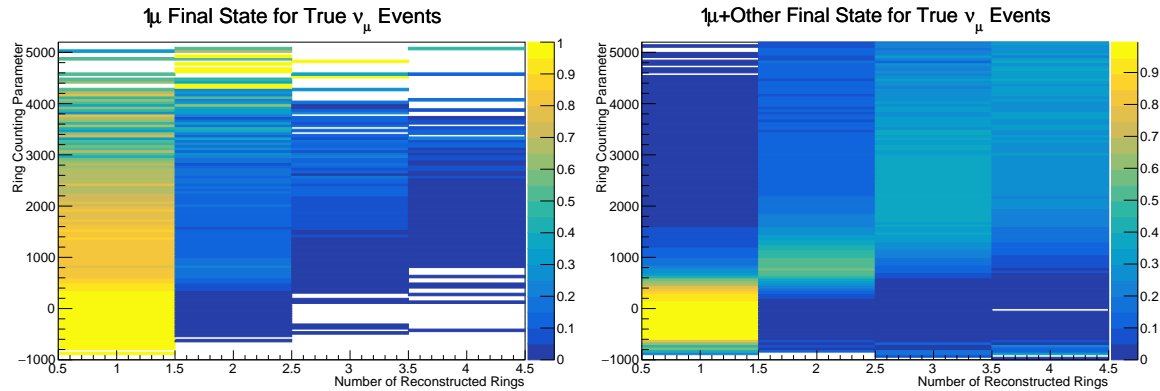


**Figure 6.9:** The ring counting parameter, defined in Equation 6.6, as a function of the number of reconstructed rings as found by the `fitQun` algorithm. Left: true  $\nu_\mu$  events with only one muon above Cherenkov threshold in the final state. Right: true  $\nu_\mu$  events with one muon and at least one other charged particle above Cherenkov threshold in the final state.

2150  $\pi^0$  systematics has been modified. In practice, the inputs from the hybrid  $\pi^0$  sample  
 2151 is included via the use of “ $\chi^2$  maps”, which are two dimensional histograms in  $\alpha$   
 2152 and  $\beta$  parameters over some range. Illustrative examples of the  $\chi^2$  maps are given  
 2153 in Figure 6.10. Due to their nature, the shift and smear parameter are typically very  
 2154 correlated.

2155 The maps are filled through the  $\chi^2$  comparison of the hybrid  $\pi^0$  Monte Carlo and  
 2156 data in the particle identification parameters documented in Table 6.6. The Monte  
 2157 Carlo distribution is modified with the  $\alpha$  and  $\beta$  scaling, whilst cross-section and flux  
 2158 nuisance parameters are thrown from there prior uncertainties, and the  $\chi^2$  between  
 2159 the scaled Monte Carlo and data is calculated and the relevant point in the  $\chi^2$  map is  
 2160 filled. Then in the fit, the likelihood penalty term is found for the particular particle  
 2161 identification parameter by using the value of the relevant  $\chi^2$  map for the  $\alpha$  and  $\beta$   
 2162 parameter at that step in the MCMC fit. For this fit, only  $1\pi^0$  final state topology shift  
 2163 and smear parameters use the hybrid  $\pi^0$   $\chi^2$  prior uncertainty.

2164 Similarly, the supplementary systematics which are added into the covariance from  
 2165 stopping muon and decay electron studies need to be included. A new framework  
 2166 [207] was built in tandem with the T2K-SK working group [183] so the additional

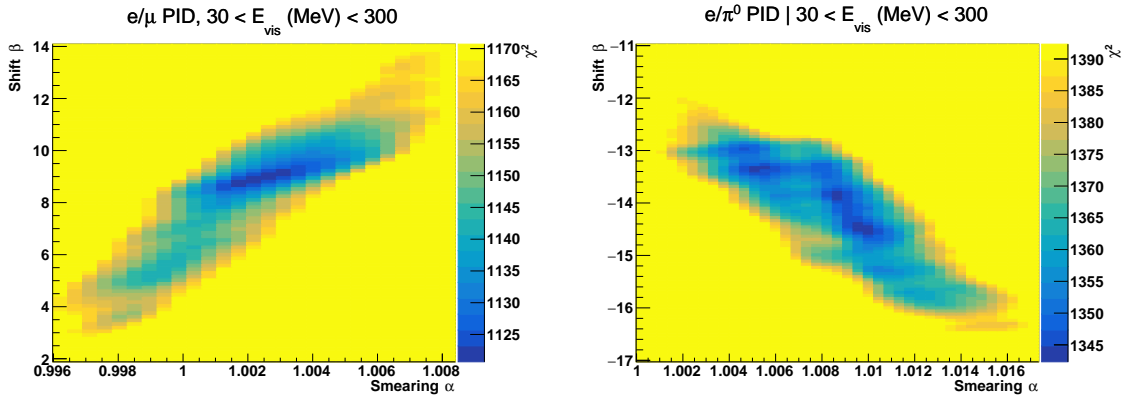


**Figure 6.10:** The  $\chi^2$  between the hybrid- $\pi^0$  Monte Carlo and data samples, as a function of smear ( $\alpha$ ) and shift ( $\beta$ ) parameters, for events which have  $1\pi^0$  final state topology. Left: Electron-muon separation PID parameter for events with  $30 \geq E_{vis}(\text{MeV}) < 300$ . Right: Electron- $\pi^0$  separation PID parameter for events with  $30 \geq E_{vis}(\text{MeV}) < 300$ .

parameters can be incorporated in the MaCh3 framework. These are applied as normalisation parameters, depending on the particular interaction mode, number of tagged decay electrons and whether the primary particle generated Cherenkov light. They are assigned Gaussian uncertainties with widths described by a covariance matrix.

Finally, the secondary interaction and photo-nuclear effects need to be accounted for in this detector model. In the T2K-only analysis, a covariance matrix was built to describe the response of the samples to variations of these parameters which was then added in quadrature to the detector covariance matrix. However, this technique can not be applied in the correlated detector model. Consequently, a binned response of each of the secondary interaction systematic parameters and the photo-nuclear response was generated and included through splined shape parameters, similar to the application of shape parameters in the cross-section model (see subsection 6.2.3).

There are a total of 224  $\alpha_{jk}^i$  and  $\beta_{jk}^i$  parameters, of which 32 have prior constraints from the hybrid  $\pi^0$  samples.

One final complexity of this correlated detector model is that the two sets of samples, beam and subGeV atmospheric, use slightly different parameters to distinguish electron and muon like events. The beam-only events use the  $\log(L_e/L_\mu)$  whereas the atmospheric samples use  $\log(L_e/L_\pi)$ , where  $L_X$  is the likelihood for hypothesis X. This is because the beam-only fits use single-ring fitQun fitting techniques, whereas multi-ring fits are applied to the atmospheric samples where only the electron and pion hypothesis are considered. As discussed in section 5.2, the pion hypothesis is a very good approximation of the muon hypothesis due to their similar mass. The correlation between the two likelihood ratios is illustrated in Figure 6.11. A very strong correlation is clearly shown. Consequently, using the same shift and smear parameters correlated between beam and subGeV atmospheric is a good approximation.

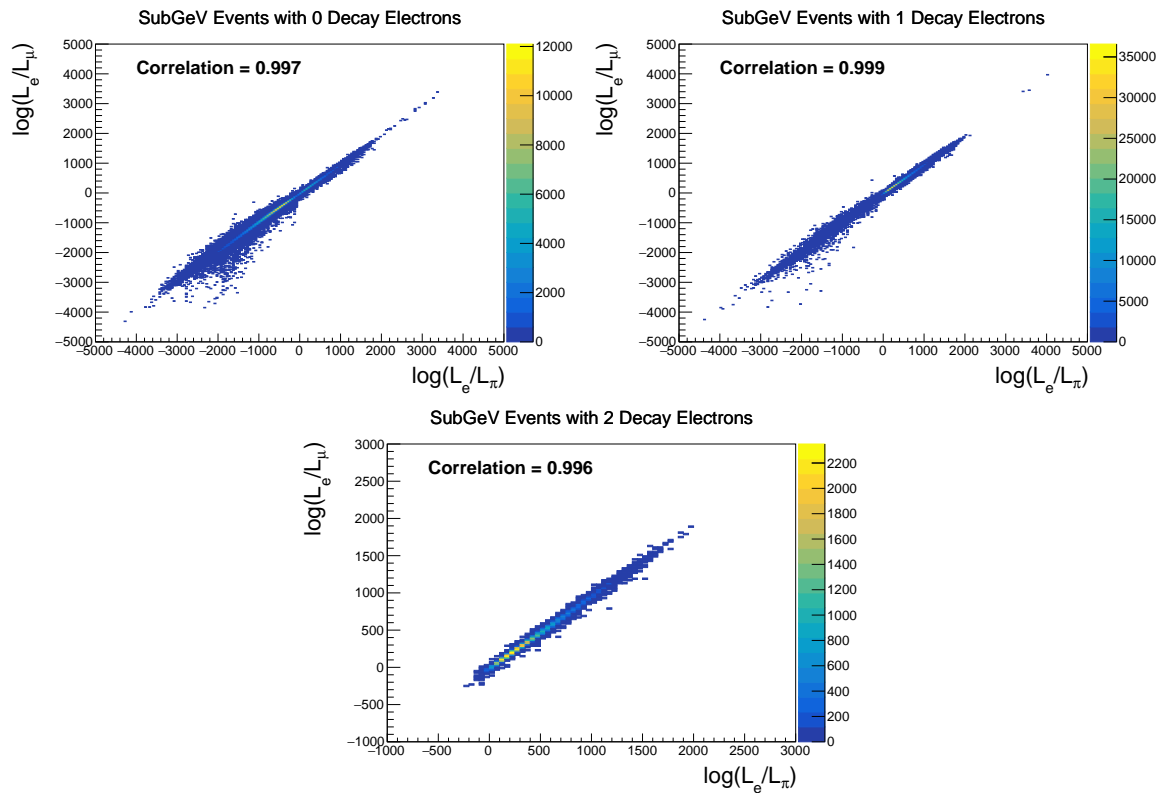


**Figure 6.11:** The distribution of  $\log(L_e/L_\mu)$  compared to  $\log(L_e/L_\pi)$  for subGeV events with zero (top left), one (top right) or two (bottom) decay electrons. The correlation in the distribution is calculated as 0.997, 0.999 and 0.996, respectively.

<sub>2193</sub> **Chapter 7**

<sub>2194</sub> **Oscillation Probability Calculation**

<sub>2195</sub> It is important to understand how and where the sensitivity to the oscillation pa-  
<sub>2196</sub> rameters comes from for both atmospheric and beam samples. An overview of how  
<sub>2197</sub> these samples observe changes in  $\delta_{CP}$ ,  $\Delta m_{23}^2$ , and  $\sin^2(\theta_{23})$  is given in section 7.1. It  
<sub>2198</sub> also explains the additional complexities involved when performing an atmospheric  
<sub>2199</sub> neutrino analysis as compared to a beam-only analysis.

<sub>2200</sub> Without additional techniques, atmospheric sub-GeV upward-going neutrinos  
<sub>2201</sub> ( $E_\nu < 1.33\text{GeV}, \cos(\theta_Z) < 0.$ ) can artificially inflate the sensitivity to  $\delta_{CP}$  due to the  
<sub>2202</sub> quickly varying oscillation probability in this region. Therefore, a “sub-sampling”  
<sub>2203</sub> approach has been developed to reduce these biases ensuring accurate and reliable  
<sub>2204</sub> sensitivity measurements. This technique ensures that small-scale unresolvable fea-  
<sub>2205</sub> tures of the oscillation probability have been averaged over whilst the large-scale  
<sub>2206</sub> features in the oscillation probability are unaffected. The documentation and valida-  
<sub>2207</sub> tion of this technique are found in section 7.2. The oscillation probability calculation is  
<sub>2208</sub> computationally intensive due to the large number of matrix multiplications needed.  
<sub>2209</sub> Consequently, the CUDAProb3 implementation choice made within the fitting frame-  
<sub>2210</sub> work, as detailed in section 7.3, ensures that the analysis can be done in a timely  
<sub>2211</sub> manner.

<sub>2212</sub> Whilst the beam neutrinos are assumed to propagate through a constant density  
<sub>2213</sub> slab of material, the density variations through the Earth result in more complex  
<sub>2214</sub> oscillation patterns. Furthermore, the uncertainty in the electron density can modify  
<sub>2215</sub> the oscillation probability for the denser core layers of the Earth. The model of the

2216 Earth used within this analysis is detailed in section 7.4. This includes information  
2217 about the official SK-only methodology as well as improvements that can be made  
2218 to remove some of the approximations made in that analysis. Another complexity of  
2219 atmospheric neutrinos oscillation studies is that the height of production in the atmo-  
2220 sphere is not known on an event-by-event basis. An analytical averaging technique  
2221 that approximates the uncertainty of the oscillation probability has been followed,  
2222 with the author of this thesis being responsible for the implementation and validation.  
2223 This implementation of an external technique is illustrated in section 7.5.

## 2224 7.1 Overview

2225 DB: Should this be moved into an earlier chapter? The selections chapter references  
2226 the matter resonance which has not yet been explained at that point

2227 The analysis presented within this thesis focuses on the determination of oscillation  
2228 parameters from atmospheric and beam neutrinos. Whilst subject to the same oscil-  
2229 lation formalism, the way in which the two samples have sensitivity to the different  
2230 oscillation parameters differs quite significantly.

2231 Atmospheric neutrinos have a varying baseline, or “path length”,  $L$ , such that  
2232 the distance each neutrino travels before interacting is dependent upon the zenith  
2233 angle,  $\theta_Z$ . As primary cosmic rays can interact anywhere between the Earth’s surface  
2234 and  $\sim 50\text{km}$  above that, the height,  $h$ , in the atmosphere at which the neutrino was  
2235 generated also affects the path length,

$$L = \sqrt{(R_E + h)^2 - R_E^2 (1 - \cos^2(\theta_Z))} - R_E \cos(\theta_Z). \quad (7.1)$$

2236 Where  $R_E = 6,371\text{km}$  is the Earth's radius. Consequently, the oscillation probabil-  
2237 ity is dependent upon two parameters,  $\cos(\theta_Z)$  and  $E_\nu$ .

2238 The oscillation probability used within this analysis is based on [21]. The neutrino  
2239 wavefunction in the vacuum Hamiltonian evolves in each layer of constant matter  
2240 density via

$$i \frac{d\psi_j(t)}{dt} = \frac{m_j^2}{2E_\nu} \psi_j(t) - \sum_k \sqrt{2} G_F N_e U_{ej} U_{ke}^\dagger \psi_k(t), \quad (7.2)$$

2241 where  $m_j^2$  is the square of the  $j^{th}$  vacuum eigenstate mass,  $E_\nu$  is the neutrino  
2242 energy,  $G_F$  is Fermi's constant,  $N_e$  is the electron number density and  $U$  is the PMNS  
2243 matrix. The transformation  $N_e \rightarrow -N_e$  and  $\delta_{CP} \rightarrow -\delta_{CP}$  is applied for antineutrino  
2244 propagation. Thus, a model of the Earth's density is required for atmospheric neutrino  
2245 propagation. Following the official SK-only methodology [208], this analysis uses the  
2246 Preliminary Reference Earth Model (PREM) [209]. This model provides piecewise cubic  
2247 polynomials as a function of the Earth's radius which results in the density profile  
2248 illustrated in Figure 7.1. As discussed, the propagator requires layers of constant  
2249 density. The SK methodology approximates the PREM model by using four layers of  
2250 constant density [208]. The details of these layers are detailed in Table 7.1.

Layer	Outer Radius [km]	Density [ $\text{g}/\text{cm}^3$ ]	Chemical composition (Z/A)
Inner Core	1220	13	$0.468 \pm 0.029$
Outer Core	3480	11.3	$0.468 \pm 0.029$
Lower Mantle	5701	5.0	0.496
Transition Zone	6371	3.3	0.496

**Table 7.1:** Description of the four layers of the Earth invoked within the constant density approximation of the PREM model [209].

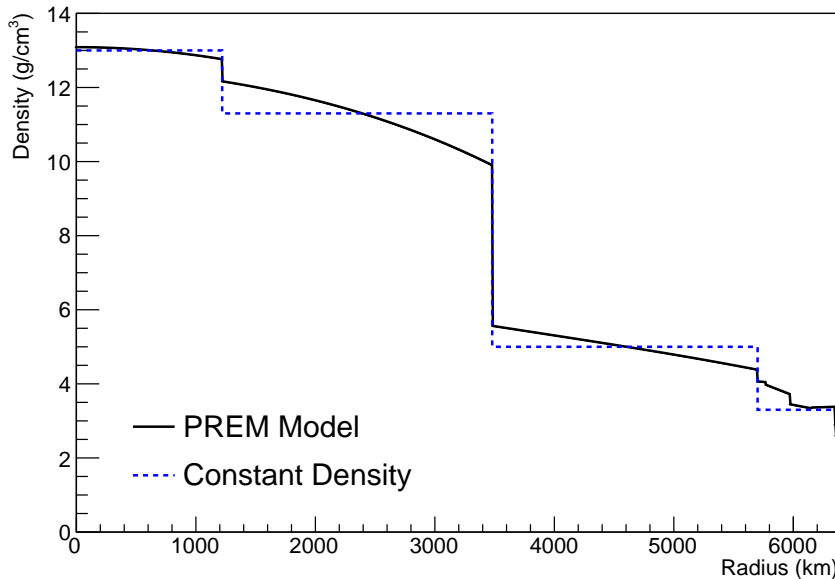


**Figure 7.1:** The density of the Earth given as a function of the radius, as given by the PREM model (Black), and the constant density four-layer approximation (Blue), as used in the official SK-only analysis.

2251     The atmospheric neutrino oscillation probabilities can be presented as two dimen-  
 2252     sional “oscillograms” as illustrated in Figure 7.2. The distinct discontinuities, as a  
 2253     function of  $\cos(\theta_Z)$ , are due to the discrete change in density invoked within the PREM  
 2254     model.

2255     Atmospheric neutrinos do have sensitivity to  $\delta_{CP}$  through a normalisation term.  
 2256     Figure 7.3 illustrates the difference in oscillation probability between CP-conserving  
 2257     ( $\delta_{CP} = 0$ ) and a CP-violating ( $\delta_{CP} = -1.601$ ) value taken from Asimov A oscillation  
 2258     parameter set (Table 2.2). The result is a complicated oscillation pattern in the appear-  
 2259     ance probability for sub-GeV upgoing neutrinos. The detector does not have sufficient  
 2260     resolution to resolve these individual patterns so the sensitivity to  $\delta_{CP}$  for atmospheric  
 2261     neutrinos comes via the overall normalisation of these events.

2262     The presence of matter means that the effect  $\delta_{CP}$  has on the oscillation probability  
 2263     is not equal between neutrinos and antineutrinos, which would be expected when  
 2264     propagating through a vacuum. This is further extenuated by the fact that SK can

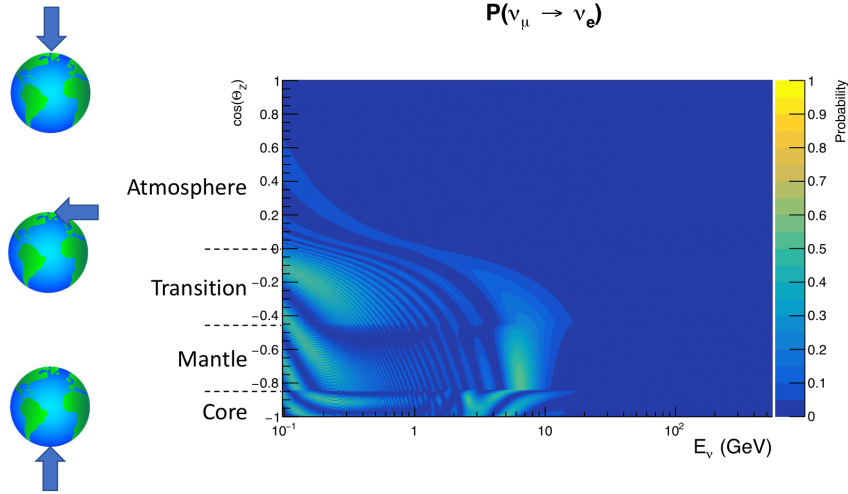


**Figure 7.2:** An “oscillogram” that depicts the  $P(\nu_\mu \rightarrow \nu_e)$  oscillation probability as a function of neutrino energy and cosine of the zenith angle. The zenith angle is defined such that  $\cos(\theta_Z) = 1.0$  represents neutrinos that travel from directly above the detector. The four-layer constant density PREM model approximation is used and Asimov A oscillation parameters are assumed (Table 2.2).

not distinguish neutrinos and antineutrinos well and that the cross-section neutrino interaction is larger than that for antineutrinos. Finally, sample selections (discussed in subsection 6.1.1) targeting different neutrino interaction modes result in an imbalance in the percentage of neutrinos to anti-neutrinos. This is because negatively charged pions from antineutrino interactions are more likely to be captured by a nucleus compared to a positively charged pion. All of these effects lead to a difference in the number of neutrinos detected compared to antineutrinos. This changes how the  $\delta_{CP}$  normalisation term is observed, resulting in a very complex sensitivity to  $\delta_{CP}$ .

Atmospheric neutrinos are subject to matter effects as they travel through the dense matter in the Earth. The vacuum and matter oscillation probabilities for  $P(\nu_e \rightarrow \nu_e)$  and  $P(\bar{\nu}_e \rightarrow \bar{\nu}_e)$  are presented in Figure 7.4, where the PREM model has been assumed. The oscillation probability for both neutrinos and antineutrinos is affected in the presence of matter. However, the resonance effects around  $O(5)\text{GeV}$  only occur for neutrinos in normal mass hierarchy and antineutrinos in inverse mass hierarchy. The

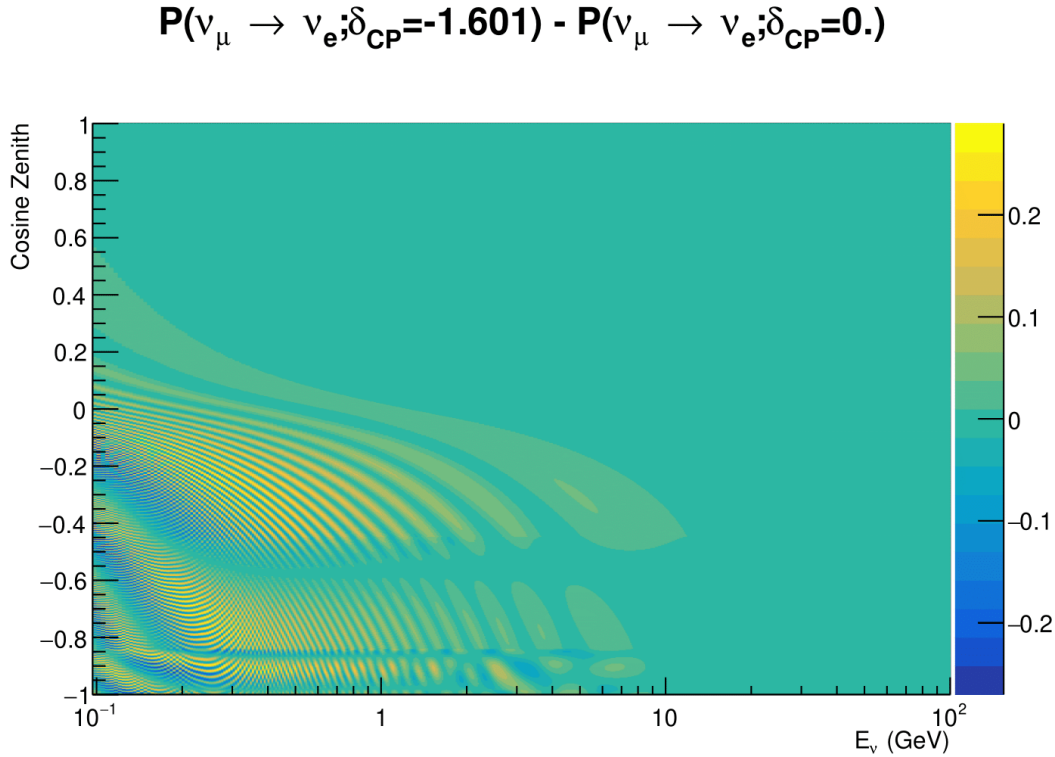


**Figure 7.3:** The effect of  $\delta_{CP}$  for atmospheric neutrinos given in terms of the neutrino energy and zenith angle. This oscillogram compares the  $P(\nu_\mu \rightarrow \nu_e)$  oscillation probability for a CP conserving ( $\delta_{CP} = 0.0$ ) and a CP violating ( $\delta_{CP} = -1.601$ ) value taken from the Asimov A parameter set. The other oscillation parameters assume the Asimov A oscillation parameter set given in Table 2.2.

exact position and amplitude of the resonance depend on  $\sin^2(\theta_{23})$  meaning that the atmospheric neutrinos have sensitivity to  $\sin^2(\theta_{23})$ .

As the T2K beam flux is centered at the first oscillation maximum ( $E_\nu = 0.6\text{GeV}$ ), the sensitivity to  $\delta_{CP}$  is predominantly observed as a change in the event-rate of e-like samples in  $\nu/\bar{\nu}$  modes. Figure 7.5 illustrates the  $P(\nu_\mu \rightarrow \nu_e)$  oscillation probability for a range of  $\delta_{CP}$  values. A circular modulation of the first oscillation peak (in both magnitude and position) is observed when varying throughout the allowable values of  $\delta_{CP}$ . The CP-conserving values of  $\delta_{CP} = 0, \pi$  have a lower(higher) oscillation maximum than the CP-violating values of  $\delta_{CP} = -\pi/2(\delta_{CP} = \pi/2)$ . A sub-dominant

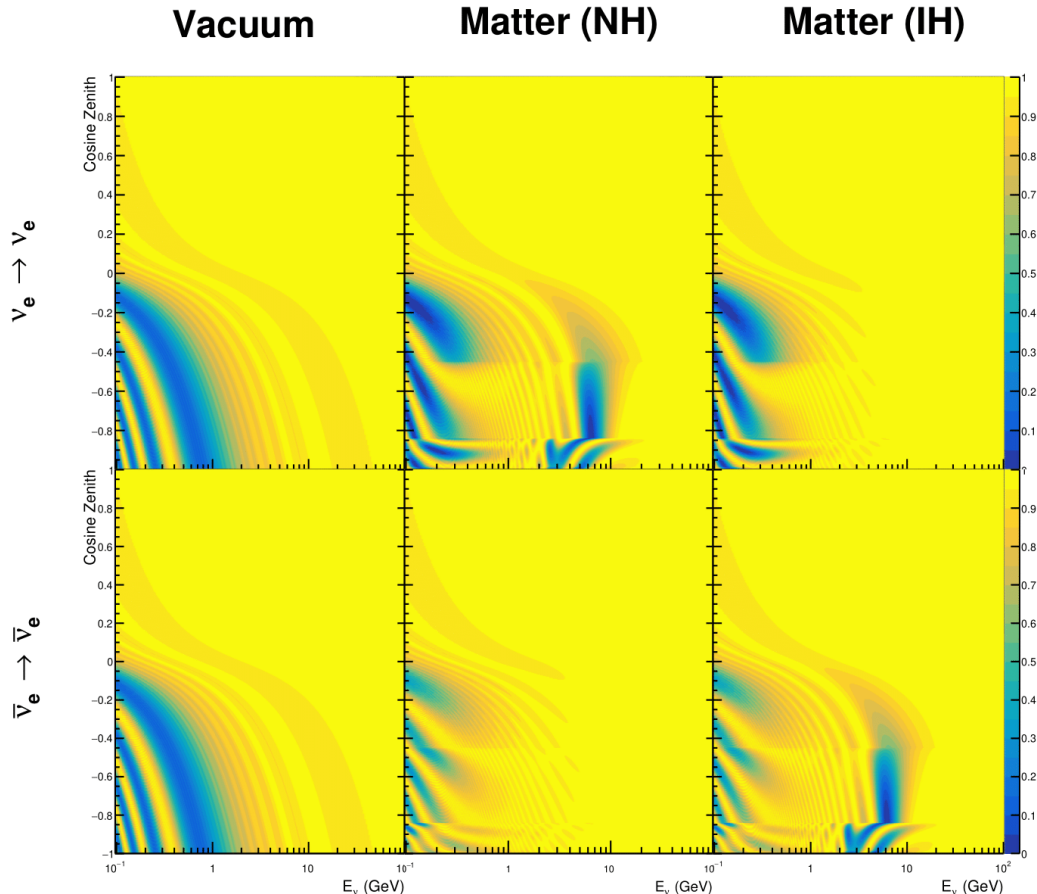


**Figure 7.4:** An illustration of the matter-induced effects on the oscillation probability, given as a function of neutrino energy and zenith angle. The top row of panels gives the  $P(\nu_e \rightarrow \nu_e)$  oscillation probability and the bottom row illustrates the  $P(\bar{\nu}_e \rightarrow \bar{\nu}_e)$  oscillation probability. The left column highlights the oscillation probability in a vacuum, whereas the middle and right column represents the oscillation probabilities when the four-layer fixed density PREM model is assumed. All oscillation probabilities assume the “Asimov A” set given in Table 2.2, but importantly, the right column sets an inverted mass hierarchy. The “matter resonance” effects at  $E_\nu \sim 5\text{GeV}$  can be seen in the  $P(\nu_e \rightarrow \nu_e)$  for normal mass hierarchy and  $P(\bar{\nu}_e \rightarrow \bar{\nu}_e)$  for inverted hierarchy.

shift in the energy of the oscillation peak is also present to aid in separating the two

CP-conserving values of  $\delta_{CP}$ .

T2K’s sensitivity to the  $\sin^2(\theta_{23})$  and  $\Delta m_{23}^2$  is observed as a shape-based variation

of the muon-like samples, as illustrated in Figure 7.5. The value of  $\Delta m_{32}^2$  laterally shifts

the position of the oscillation dip (around  $E_\nu \sim 0.6\text{GeV}$ ) in the  $P(\nu_\mu \rightarrow \nu_\mu)$  oscillation

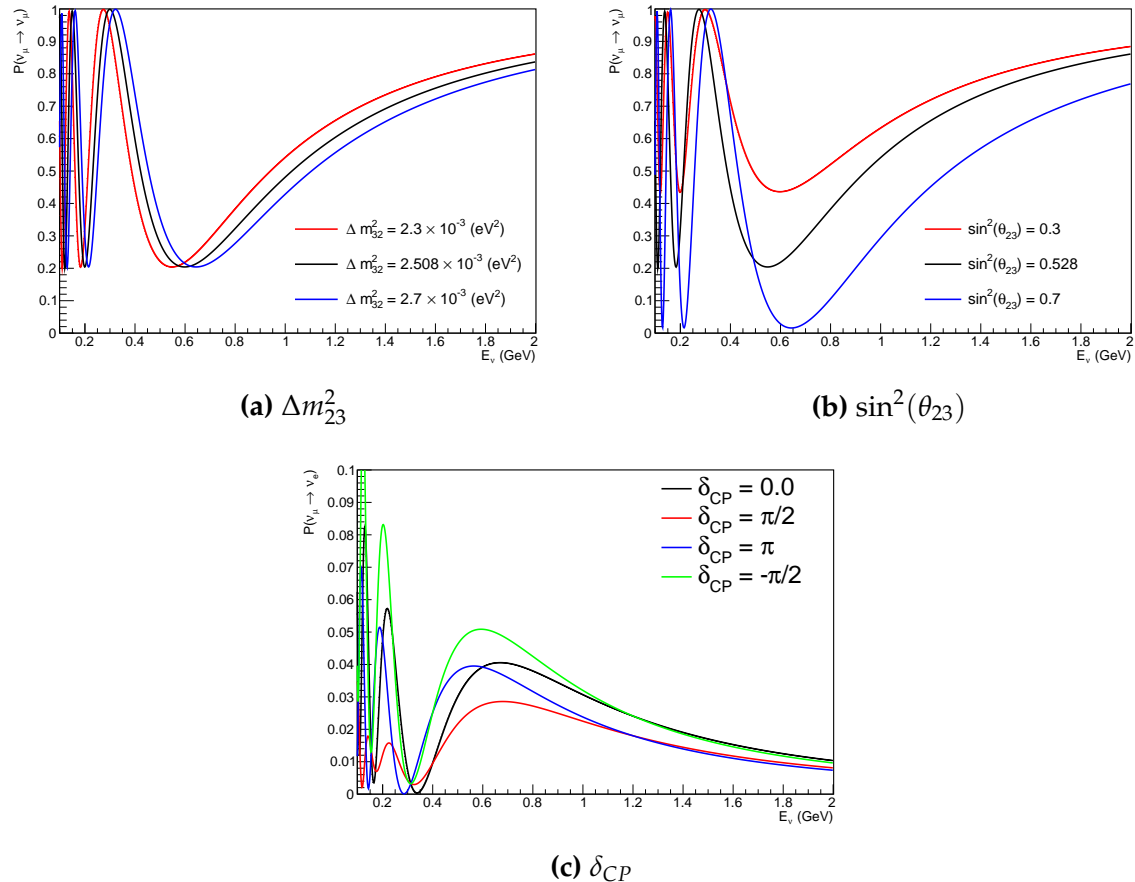


**Figure 7.5:** The oscillation probability for beam neutrino events given as a function of neutrino energy. All oscillation parameters assume the “Asimov A” set given in Table 2.2 unless otherwise stated. Each panel represents a change in one of the oscillation parameters whilst keeping the remaining parameters fixed.

probability. A variation of  $\sin^2(\theta_{23})$  is predominantly observed as a vertical shift of the oscillation dip with second-order horizontal shifts being due to matter effects. The beam neutrinos have limited sensitivity to matter effects due to the relatively shorter baseline as well as the Earth’s mantle being a relatively low-density material (as compared to the Earth’s core). For some values of  $\delta_{CP}$ , the degeneracy in the number of e-like events allows the mass hierarchy to be resolved. This leads to a  $\delta_{CP}$ -dependent mass hierarchy sensitivity which can be seen in Figure 7.6.

Whilst all oscillation channels should be included for completeness, the computational resources required to run a fit are limited and any reasonable approximations

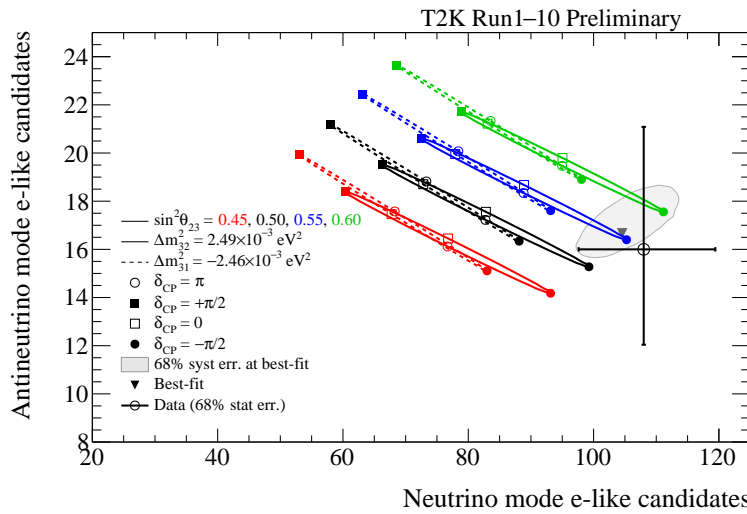


**Figure 7.6:** The number of electron-like events in the FHC and RHC operating mode of the beam, as a function of the oscillation probabilities. Both normal hierarchy (Solid) and inverse hierarchy (Dashed) values of  $\Delta m_{23}^2$  are given.

which reduce the number of oscillation probability calculations that need to be made should be applied. The  $\nu_e \rightarrow \nu_{e,\mu,\tau}$  (and antineutrino equivalent) oscillations can be ignored for beam neutrinos as the  $\nu_e/\bar{\nu}_e$  fluxes are approximately two orders of magnitude smaller than the corresponding  $\nu_\mu/\bar{\nu}_\mu$  flux. Furthermore, as the peak neutrino energy of the beam is well below the threshold for charged current tau production ( $E_\nu = 3.5 \text{ GeV}$  [51], only a small proportion of the neutrinos produced in the beam have the required energy. For the few neutrinos that have sufficient energy, the oscillation probability is very small due to the short baseline. Whilst these approximations can be made for the beam neutrinos, the atmospheric flux of  $\nu_e$  is of the same order of magnitude as the  $\nu_\mu$  flux and the energy distribution of atmospheric neutrinos extends well above the tau production threshold.

## <sup>2313</sup> 7.2 Treatment of Fast Oscillations

<sup>2314</sup> As shown in Figure 7.7, atmospheric neutrino oscillations have a significantly more  
<sup>2315</sup> complex structure for upgoing neutrinos with energy below 1GeV. This is because the  
<sup>2316</sup>  $L/E$  dependence of the oscillation probability in this region induces rapid variations  
<sup>2317</sup> for small changes in  $L$  or  $E$ . As discussed in section 7.1, this is also the region in which  
<sup>2318</sup> atmospheric neutrinos have sensitivity to  $\delta_{CP}$ . In practice, the direction of the neutrino  
<sup>2319</sup> is inferred from the direction of the final state particles traveling in the detector, which  
<sup>2320</sup> can be poor for low-energy neutrino interactions. This creates a distinct difference  
<sup>2321</sup> from the beam neutrinos where the position of the source is very precisely known.

<sup>2322</sup> As a consequence of the unresolvable structure, an average oscillation probability  
<sup>2323</sup> is observed in the subGeV upgoing region. This creates a computational problem; A  
<sup>2324</sup> significantly large amount of Monte Carlo statistics would be required to accurately  
<sup>2325</sup> predict the number of events if Monte Carlo averaging was the only technique used.  
<sup>2326</sup> This section describes the ‘sub-sampling’ approach developed for this analysis and  
<sup>2327</sup> compares it to the methodology used within the SK-only analysis.

<sup>2328</sup> The official SK-only analysis uses the osc3++ oscillation parameter fitter [208].  
<sup>2329</sup> To perform the fast oscillation averaging, it uses a ‘nearest-neighbour’ technique.  
<sup>2330</sup> For a given neutrino event, the nearest twenty neighbours in reconstructed lepton  
<sup>2331</sup> momentum and zenith angle are found and a distribution of their neutrino energies is  
<sup>2332</sup> built. The RMS,  $\sigma$ , of this distribution is then used to compute an average oscillation  
<sup>2333</sup> probability for the given neutrino Monte Carlo event.

<sup>2334</sup> For the  $i^{th}$  event, the oscillation weight is calculated as

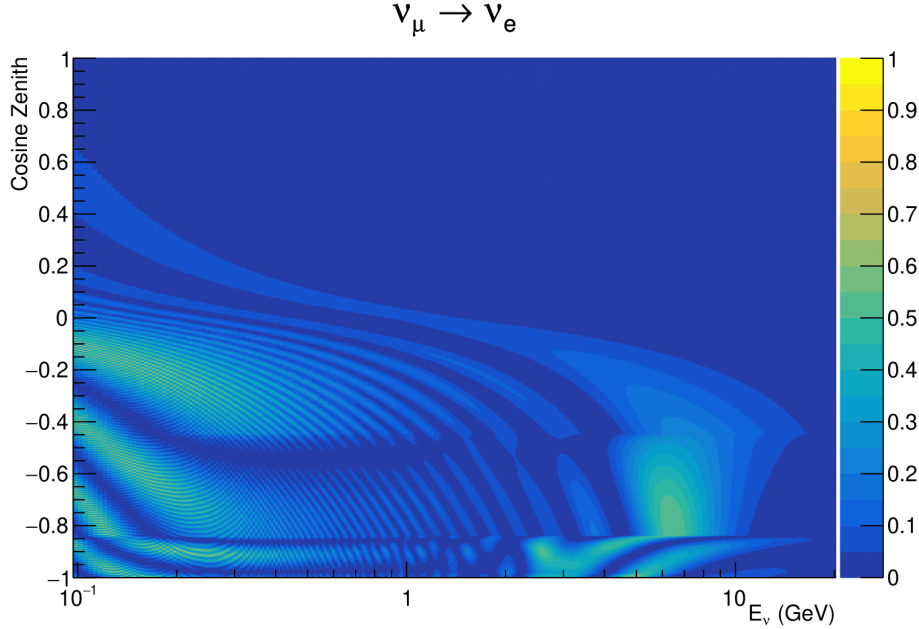


**Figure 7.7:** The oscillation probability  $P(\nu_\mu \rightarrow \nu_e)$ , given as a function of neutrino energy and zenith angle, which highlights an example of the “fast” oscillations in the sub-GeV upgoing region.

$$W_i = \frac{1}{5}P(E_i, \bar{L}_i) + \frac{1}{5} \sum_{\beta=-1,-0.5,0.5,1} P(E_i + \beta\sigma_i, L_\beta), \quad (7.3)$$

where  $P(E, L)$  is the oscillation probability calculation for neutrino energy  $E$  and path length  $L$  and the two path lengths,  $\bar{L}_i$  and  $L_\beta$  are discussed below. All of the oscillation probability calculations are performed with a fixed zenith angle such that the same density profile is used.

The uncertainty in the production height is controlled by using an “average” production height,  $\bar{L}_i$ , which represents the average path length computed using twenty production heights taken from the Honda flux model’s prediction [45]. For a given event, the production heights are sampled in steps of 5% of their cumulative distribution function.  $L_\beta$  values are similarly calculated but instead use different combinations of four production heights,

$$\begin{aligned}
 L_{-1.0} &= \frac{1}{4}L(45, 50, 55, 60), \\
 L_{-0.5} &= \frac{1}{4}L(35, 40, 65, 70), \\
 L_{+0.5} &= \frac{1}{4}L(25, 30, 75, 68), \\
 L_{+1.0} &= \frac{1}{4}L(15, 20, 85, 89).
 \end{aligned} \tag{7.4}$$

2345 This averaging technique works because of the inference between the zenith angle  
 2346 and the reconstructed direction of final state particles in the detector. For low-energy  
 2347 neutrinos, where the resolution of the true neutrino direction is poor,  $\sigma_i$  will be large,  
 2348 resulting in significant averaging effects. Contrary to this, the inferred direction of  
 2349 high-energy neutrinos will be much closer to the true value, meaning that  $\sigma_i$  will be  
 2350 smaller, culminating in small averaging effects.

2351 In practice, this technique is performed before the fit in order to deal with the  
 2352 computational cost. This is possible as the Osc3++ framework uses binned oscillation  
 2353 parameters rather than continuous so the oscillation parameters used in the fit are  
 2354 known prior to run-time. The framework used in this analysis uses continuous  
 2355 oscillation parameters, and due to the MCMC fitting technique, there is no way to  
 2356 know which oscillation parameter values will be selected *a priori*. Therefore, the  
 2357 oscillation parameter calculation has to be performed at run-time. Computing five  
 2358 oscillation probabilities per event would require far too many computational resources  
 2359 to be viable. Therefore SK technique can not be used within this analysis. However,  
 2360 the concept of the averaging technique can be taken from it.

2361 To perform a similar averaging as the SK analysis, a sub-sampling approach using  
 2362 binned oscillograms has been devised. The technique can be explained by considering  
 2363 a “fine” and “coarse” oscillogram. The fine oscillograms are used to define the array of

2364  $\cos(\theta_Z)$  and  $E_\nu$  used in the oscillation engine. The coarse oscillograms cover the same  
2365 phase-space but have fewer bins, where the value of a particular coarse bin is taken  
2366 as the linear average (flat prior in  $E_\nu$  and  $\cos(\theta_Z)$ ) of all fine bins which falls into it.  
2367 The coarse oscillogram is then used for determining the oscillation weight for a given  
2368 event. The binning which is used to calculate the oscillation probabilities, known as  
2369 the ‘fine’ binning, has  $N \times N$  subdivisions per coarse bin. Figure 7.8 illustrates the  
2370  $N = 2$  example where the assigned value to a coarse bin is the average of the four fine  
2371 bins which fall in that coarse bin. Whilst the coarse bin edges do not have to be linear  
2372 on either axis, the sub-division of the fine bins is linear over the range of a coarse bin.

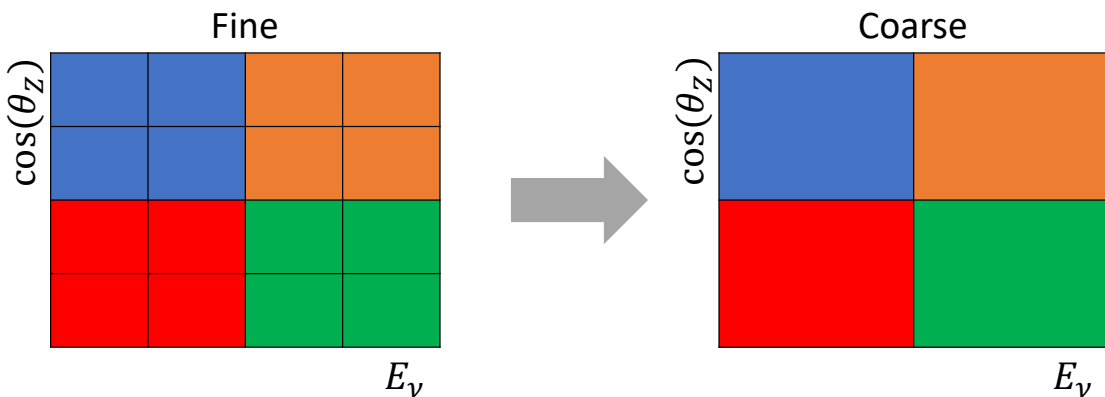


**Figure 7.8:** Illustration of the averaging procedure for  $N = 2$ . The oscillation probabilities calculated on the finer left binning are averaged to obtain the oscillation probabilities in the coarser right binning. These averaged oscillation probabilities with the coarser binning are then applied to each event during the fit.

2373 The coarse binning is defined with  $67 \times 52$  bins in true neutrino energy  $\times$  cosine  
2374 zenith. It is picked to be identical to that provided in [210]. In general, the binning is  
2375 logarithmically spaced in neutrino energy but has some hand-picked bin edges. Firstly,  
2376 the bin density around the matter resonance is smoothly increased around the matter  
2377 resonance region. This is to avoid smearing this region which can be well sampled by  
2378 the Monte Carlo. Secondly, bin edges are selected to hit  $0.4, 0.6, 1, 10, 30, 50, 100\text{GeV}$ .  
2379 This is to ensure that the Coulomb correction systematic and the atmospheric flux  
2380 systematics definitions in neutrino energy can be hit. The cosine zenith binning is

2381 approximately linearly spaced across the allowable range but the values of layer  
 2382 transitions are hit precisely:  $-0.8376$  (core-mantle) and  $-0.4464$  (mantle/transition  
 2383 zone). Bins are spread further apart for downgoing events as this is a region unaffected  
 2384 by the fast oscillation wavelengths and reduces the total number of calculations  
 2385 required to perform the calculation.

2386 The choice of  $N$  is justified based on two studies. Firstly, the variation of event rates  
 2387 of each sample is studied as a function of  $N$ . For a given set of oscillation parameters  
 2388 thrown from the PDG prior constraints (detailed in Table 2.1), the oscillation probabili-  
 2389 ties are calculated using a given value of  $N$ . Each sample is re-weighted and the event  
 2390 rate is stored. The value of  $N$  is scanned from 1, which corresponds to no averaging, to  
 2391 24, which corresponds to the largest computationally viable subdivision binning. The  
 2392 event rate of each sample at large  $N$  is expected to converge to a stationary value due  
 2393 to the fine binning fully sampling the small-scale structure. Figure 7.9 illustrates this  
 2394 behaviour for the SubGeV\_elike\_0dcy sample for 30 different throws of the oscillation  
 2395 parameters.

2396 Denoting the event rate for one sample for a given throw  $t$  at each  $N$  by  $\lambda_t^N$ , the  
 2397 average over all considered  $N$  values ( $\bar{\lambda}_t = \frac{1}{24} \sum_{N=1}^{24} \lambda_t^N$ ) is computed. The variance in  
 2398 the event rate at each  $N$  is then calculated as

$$\text{Var}[\lambda^N] = \frac{1}{N_{\text{throws}}} \sum_{t=1}^{N_{\text{throws}}} (\lambda_t^N - \bar{\lambda}_t)^2 - \left[ \frac{1}{N_{\text{throws}}} \sum_{t=1}^{N_{\text{throws}}} (\lambda_t^N - \bar{\lambda}_t) \right]^2. \quad (7.5)$$

2399 The aim of the study is to find the lowest value of  $N$  such that this variance is  
 2400 below 0.001. This is the typical threshold used by T2K fitters to validate systematic  
 2401 implementation so has been set as the same criteria. The results of this study for  
 2402 each atmospheric sample used within this thesis are illustrated in Figure 7.10 for

### SubGeV-elike-0dcy

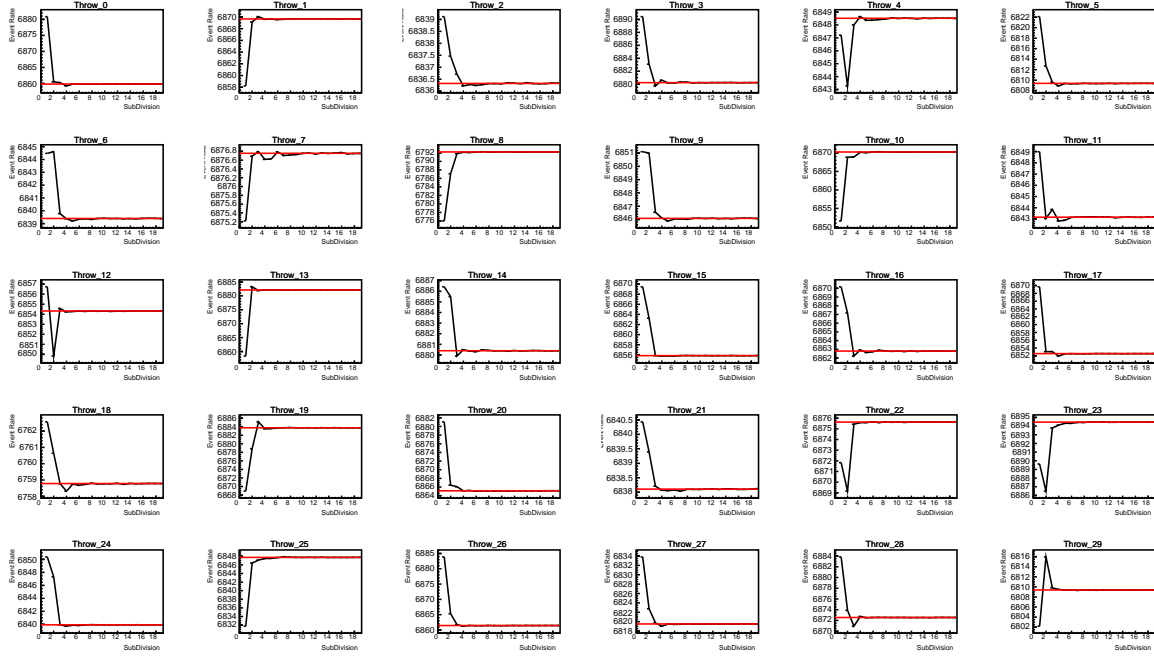


**Figure 7.9:** Event rate of the SubGeV\_elike\_0dcy sample as a function of the number of subdivisions per coarse bin. Each subplot represents the event rate of the sample at a different oscillation parameter set thrown from the PDG priors detailed in Table 2.1. The red line in each subplot represents the mean of the event rate over the different values of sub-divisions for that particular oscillation parameter throw.

2403 2000 throws of the oscillation parameters. As can be seen, the variance is below  
 2404 the threshold at  $N = 10$ , and is driven primarily by the SubGeV\_mulike\_1dcy and  
 2405 SubGeV\_elike\_0dcy samples.

2406 The second study to determine the value of  $N$  is as follows. The likelihood for each  
 2407 sample is computed against an Asimov data set created with Asimov A oscillation  
 2408 parameters (Table 2.2). Following Equation 7.5, the variance of the log-likelihood over  
 2409 all considered  $N$  is computed. The results are shown in Figure 7.11.

2410 A choice of  $N = 10$  sub-divisions per coarse bin has a variance in both event rate  
 2411 and log-likelihood residuals less than the required threshold of 0.001. The largest  
 2412 value of the likelihood variance is of order  $10^{-7}$ , corresponding to an error on the log-

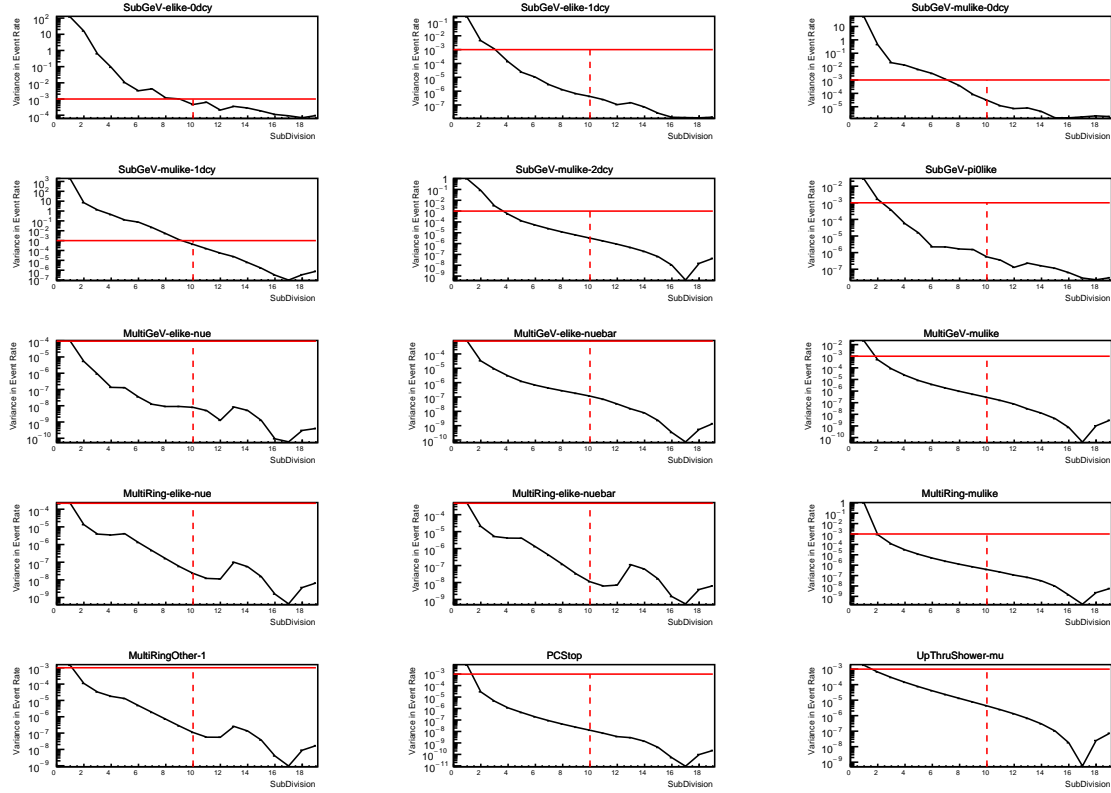


**Figure 7.10:** Variance of event rate for each atmospheric sample as a function of the number of sub-divisions per coarse bin. The solid red line indicates the 0.1% threshold and the dashed red line indicates the variance at a sub-division  $N = 10$ .

likelihood of about  $3 \times 10^{-4}$  which is small enough to be negligible for the oscillation analysis.

Figure 7.12 illustrates the effect of the smearing using  $N = 10$ . The fast oscillations in the sub-GeV upgoing region have been replaced with a normalisation effect whilst the large matter resonance structure remains.

### 7.3 Calculation Engine

As previously discussed in section 7.2, the calculation of oscillation probabilities is performed at run-time due to utilising continuous oscillation parameters. Consequently, the time per calculation is crucial for fit performance. The initial fitting framework

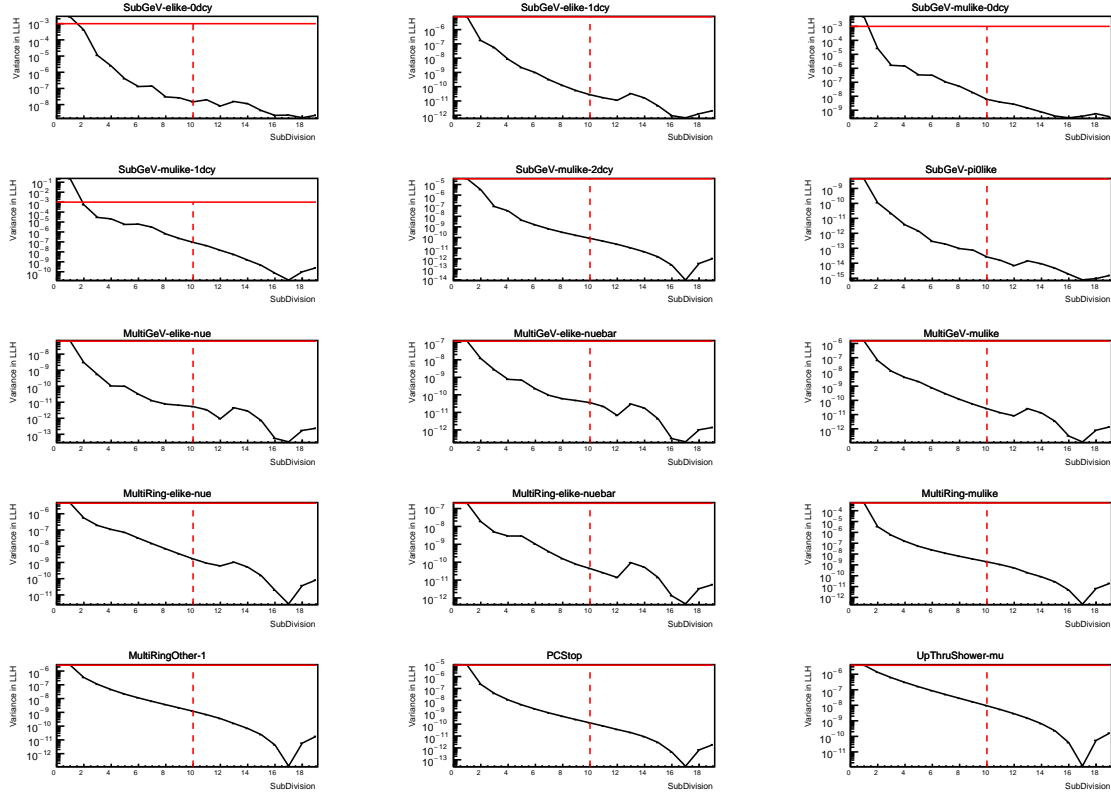


**Figure 7.11:** Variance of sample likelihood, when compared to ‘Asimov data’ set at Asimov A, for each atmospheric sample as a function of the number of sub-divisions per coarse bin. The solid red line indicates the 0.1% threshold and the dashed red line is a graphical indication of the variance at a sub-division  $N = 10$ .

used for this analysis was developed with ProbGPU [211]. This is a GPU-only implementation of the prob3 engine [212]. It is primarily designed for neutrino propagation in a beam experiment (single layer of constant density) with the atmospheric propagation code not being used prior to the analysis in this thesis.

Another engine, CUDAProb3 [213], has been implemented within the fitting framework used in this analysis. It has been specifically optimised for atmospheric neutrino oscillation calculation so does not contain the code to replace the beam oscillation calculation. The engine utilises object-orientated techniques as compared to the functional implementation of ProbGPU. This allows the energy and cosine zenith arrays to be kept on GPU memory, rather than having to load these arrays onto GPU memory for each calculation. General memory interfacing is one of the slowest tasks which

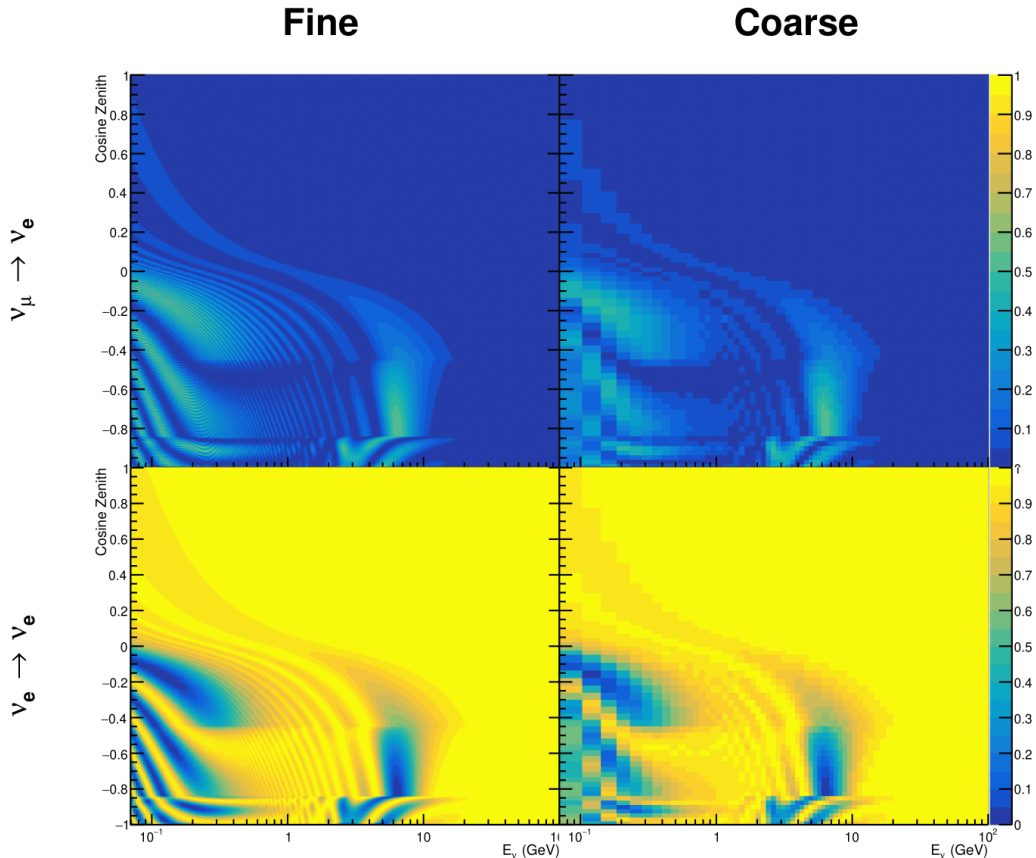


**Figure 7.12:** The oscillation probability,  $P(\nu_\mu \rightarrow \nu_e)$  (top row) and  $P(\nu_e \rightarrow \nu_e)$  (bottom row), given as a function of neutrino energy and zenith angle. The left column gives the “fine” binning used to calculate the oscillation probabilities and the right column illustrates the “coarse” binning used to reweight the Monte Carlo events. The fine binning choice is given with  $N = 10$ , which was determined to be below the threshold from Figure 7.10 and Figure 7.11.

2433    GPUs can do, so being able to eliminate this significantly reduces the time required  
 2434    for calculation. This can be seen in Figure 7.13, where the GPU implementation of  
 2435    CUDAProb3 is approximately three times faster than the ProbGPU engine.

2436       Another significant advantage of CUDAProb3 is that it contains a CPU multithreaded  
 2437    implementation which is not possible with the ProbGPU or prob3 engines. This elimi-  
 2438    nates the requirement for GPU resources when submitting jobs to batch systems. As  
 2439    illustrated in Figure 7.13, the calculation speed depends on the number of available

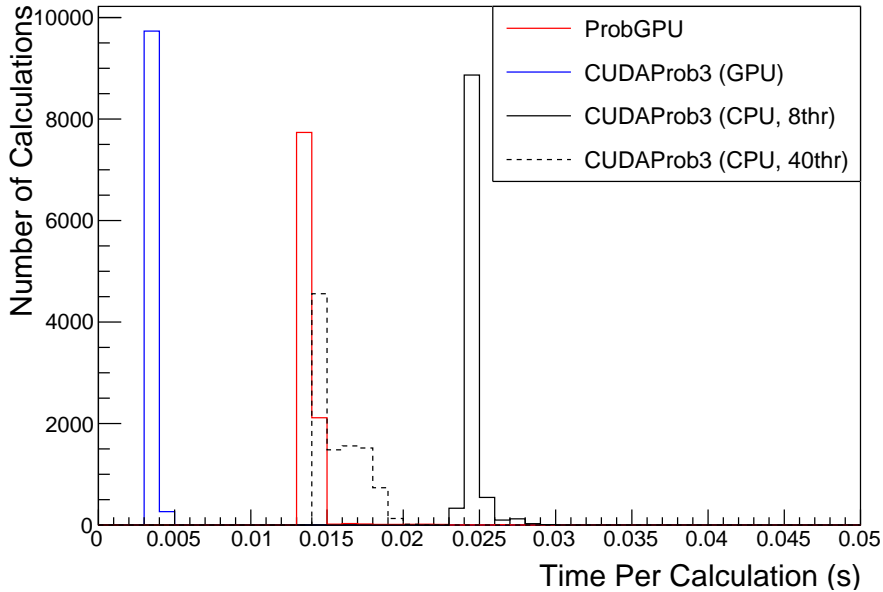


**Figure 7.13:** The calculation time taken to both calculate the oscillation probabilities and fill the “coarse” oscillograms, following the technique given in section 7.2, for the CUDAProb3 and ProbGPU (Red) calculation engines. CUDAProb3 has both a GPU (Blue) and CPU (Black) implementation, where the CPU implementation is multithreaded. Therefore, 8-threads (solid) and 40-threads (dashed) configurations have been tested. Prob3, which is a CPU single-thread implementation has a mean step time of 1.142s.

2440 threads. Using 8 threads (which is typical of the batch systems being used) is ap-  
 2441 proximately twice as slow as the ProbGPU engine implementation, but would allow  
 2442 the fitting framework to be run on many more resources. This fact is utilised for any  
 2443 SK-only fits but GPU resources are required for any fits which include beam samples  
 2444 due to the ProbGPU requirement. Based on the benefits shown by the implementa-  
 2445 tion in this section, efforts are being placed into including linear propagation for beam  
 2446 neutrino propagation into the engine [214].

## 2447 7.4 Matter Density Profile

2448 For an experiment observing atmospheric neutrinos propagating through the Earth, a  
 2449 model of the Earth’s density profile is required. The model used within this analysis is

the Preliminary Reference Earth Model (PREM) [209], as illustrated in Figure 7.1. As discussed in section 7.1, the propagator used within the calculation engine requires constant density layers. To follow the official SK-only analysis [208], the average density of each layer has been taken from the PREM model. Table 7.1 documents the density and radii of the layers used within this approximation. The density measurements provided in the PREM model are provided in terms of mass density, whereas neutrino oscillations are sensitive to the electron number density. This value can be computed as the product of the chemical composition, or the  $Z/A$  value, and the mass density of each layer. Currently, the only way to calculate the chemical composition value for layers close to the Earth’s core is through neutrino oscillations.

The chemical composition of the upper layers of the Earth’s Mantle and the Transition zone is well known due to it being predominantly pyrolite which has a chemical composition value of 0.496 [215]. The components of the Earth’s core region are less well known. Consequently, the chemical composition dial for the core layers is set to a value of 0.468, as calculated in [216]. This value is assigned a Gaussian error with a standard deviation equivalent to the difference in chemical composition in core and mantle layers. Figure 7.14 illustrates the effect of moving from the  $Z/A = 0.5$  method which is used in the official SK-only analysis [208] to these more precise values.

The beam oscillation probability in this thesis uses a baseline of 295km, density  $2.6\text{g/cm}^3$ , and chemical composition 0.5 as is done by the official T2K-only analysis [217].

Whilst the propagator requires a fixed density layer model of the Earth, the density only has to be fixed for a specific  $E_\nu \times \cos(\theta_Z)$  bin in a given layer. As the density is a function of radius, which is a function of the direction in which a neutrino propagates, a better approximation of the PREM model can be made if a  $\cos(\theta_Z)$ -specific density is calculated.

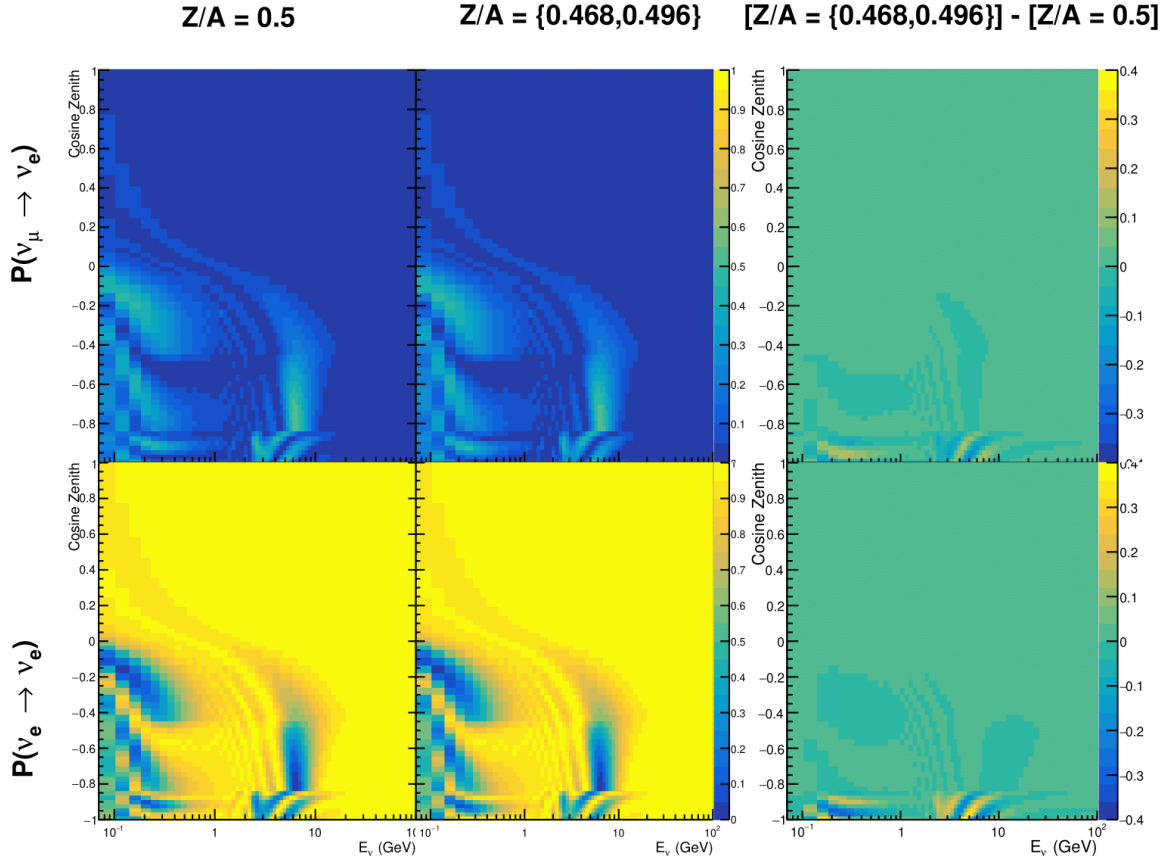


**Figure 7.14:** The oscillation probability,  $P(\nu_\mu \rightarrow \nu_e)$  (top row) and  $P(\nu_e \rightarrow \nu_e)$  (bottom row), given as a function of neutrino energy and zenith angle. The left column gives probabilities where the constant  $Z/A = 0.5$  approximation which is used in the official SK-only analysis. The middle column gives the probabilities where  $Z/A = [0.468, 0.498]$  values are used, as given in Table 7.1. The right column illustrates the difference in oscillation probability between the two different techniques.

<sup>2476</sup> To achieve this, the average density,  $\langle \rho \rangle_i$ , in the  $i^{th}$  layer, is calculated as the density,  
<sup>2477</sup>  $\rho(t)$ , integrated over the track a given  $\cos(\theta_Z)$ ,

$$\langle \rho \rangle_i = \frac{1}{t_{i+1} - t_i} \int_{t_i}^{t_{i+1}} \rho(t) dt \quad (7.6)$$

2478 where  $t_i$  are the intersection points between each layer and  $t$  is the path length of  
2479 the trajectory across the layer.

2480 The oscillation probability calculation speed is approximately linear in the number  
2481 of layers invoked within the Earth model. Therefore a four-layer model is still utilized  
2482 with the only difference to the official SK-only analysis being that the four-layer model  
2483 used for each value of  $\cos(\theta_Z)$  is different. Following the method outlined in [218],  
2484 a four-layer piecewise quadratic polynomial is fit to the PREM model for the four  
2485 layers defined in Table 7.1. This fit was not performed by the author of the thesis  
2486 and is documented in [210]. The coefficients of the quadratic fit to each layer are  
2487 given in Table 7.2 with the final distribution illustrated in Figure 7.15. The quadratic  
2488 approximation is clearly much closer to the PREM model as compared to the constant  
2489 density approximation.

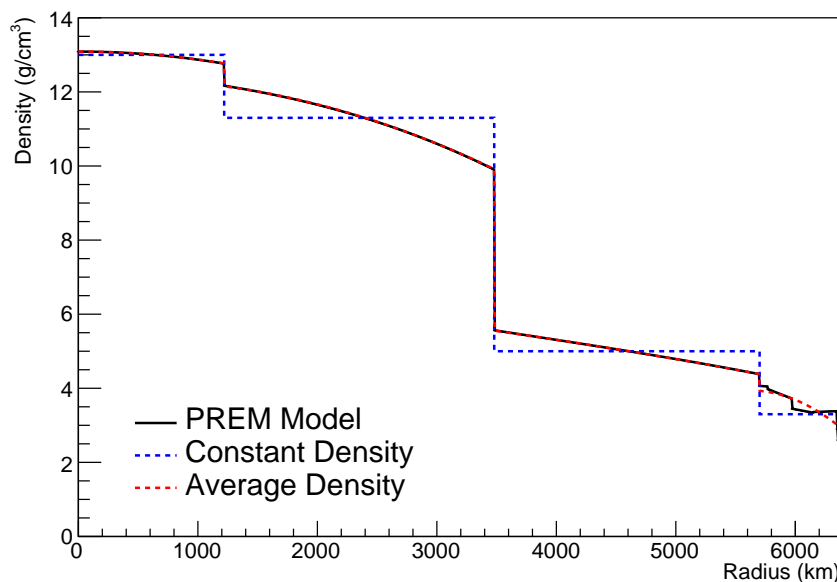


**Figure 7.15:** The density of the Earth given as a function of the radius, as given by the PREM model (Black), the constant density four-layer approximation (Blue), as used in the official SK-only analysis, and the quadratic approximation of the PREM model (Red).

Layer	Outer Radius [km]	Density [g/cm <sup>3</sup> ]
Inner Core	1220	$13.09 - 8.84x^2$
Outer Core	3480	$12.31 + 1.09x - 10.02x^2$
Lower Mantle	5701	$6.78 - 1.56x - 1.25x^2$
Transition Zone	6371	$-50.42 + 123.33x - 69.95x^2$

**Table 7.2:** The quadratic polynomial fits to the PREM model for four assumed layers of the PREM model. The fit to calculate the coefficients is given in [210], where  $x = R/R_{Earth}$ .

The effect of using the quadratic density per  $\cos(\theta_Z)$  model is highlighted in Figure 7.16. The slight discontinuity in the oscillation probability around  $\cos(\theta_Z) \sim -0.45$  in the fixed density model, which is due to the transition to mantle layer boundary, has been reduced. This is expected as the difference in the density across this boundary is significantly smaller in the quadratic density model as compared to the constant density model. Whilst the difference in density across the other layer transitions is reduced, there is still a significant difference. This means the discontinuities in the oscillation probabilities remain but are significantly reduced. However, as the quadratic density approximation matches the PREM model well in this region, these discontinuities are due to the Earth model rather than an artifact of the oscillation calculation.

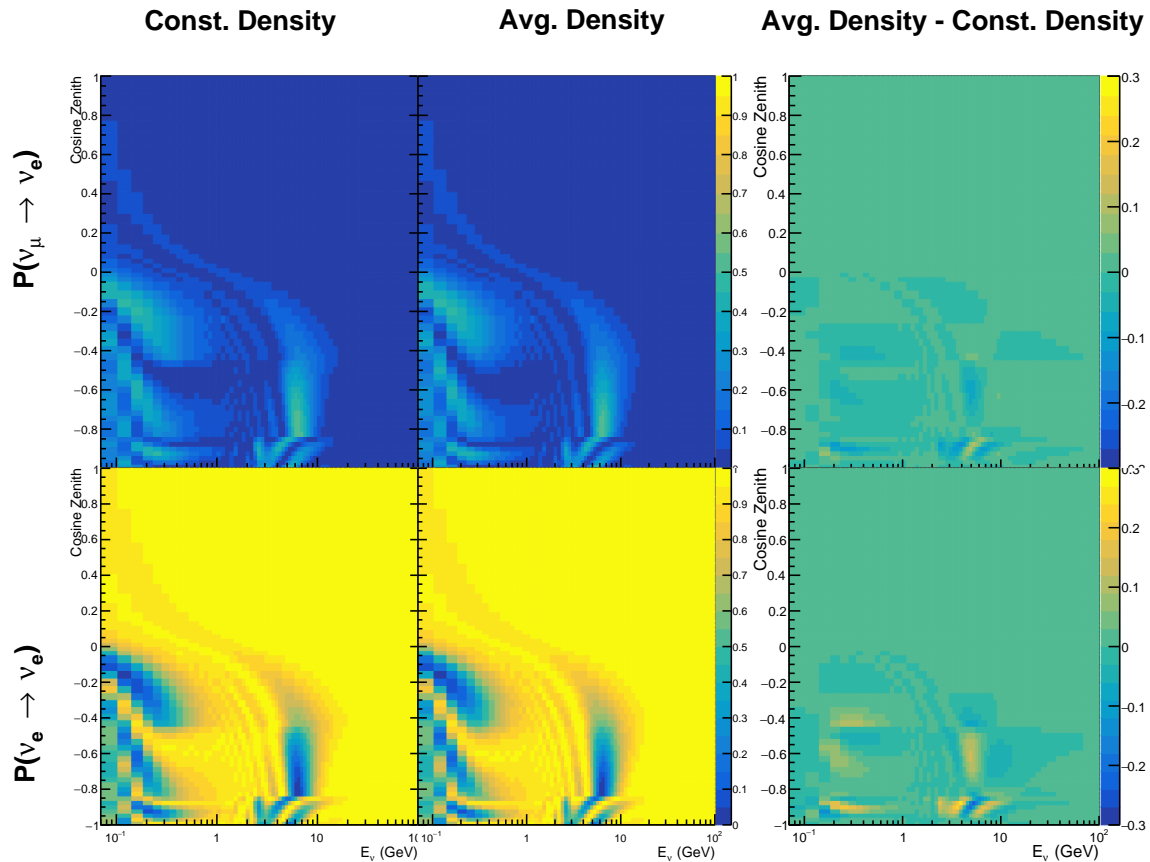


**Figure 7.16:** The oscillation probability,  $P(\nu_\mu \rightarrow \nu_e)$  (top row) and  $P(\nu_e \rightarrow \nu_\mu)$  (bottom row), given as a function of neutrino energy and zenith angle. The left column gives probabilities where the four-layer constant density approximation is used. The middle column gives the probabilities where the density is integrated over the trajectory, using the quadratic PREM approximation, for each  $\cos(\theta_Z)$  is used. The right column illustrates the difference in oscillation probability between the two different techniques.

## 2501 7.5 Production Height Averaging

2502 As discussed in section 7.1, the height at which the cosmic ray flux interacts in the  
2503 atmosphere is not known on an event-by-event basis. The production height can vary  
2504 from the Earth’s surface to  $\sim 50\text{km}$  above that. The SK-only analysis methodology  
2505 (described in section 7.2) for including the uncertainty on the production height is  
2506 to include variations from the Honda model when pre-calculating the oscillation  
2507 probabilities prior to the fit. This technique is not possible for this analysis which  
2508 uses continuous oscillation parameters that can not be known prior to the fit. Conse-  
2509 quently, an analytical averaging technique was developed in [210]. The author of this  
2510 thesis was not responsible for the derivation of the technique but has performed the  
2511 implementation and validation of the technique for this analysis alone.

2512 Using the 20 production heights per Monte Carlo neutrino event, provided as 5%  
2513 percentiles from the Honda flux model, a production height distribution  $p_j(h|E_\nu, \cos \theta_Z)$   
2514 is built for each neutrino flavour  $j = \nu_e, \bar{\nu}_e, \nu_\mu, \bar{\nu}_\mu$ . In practice, a histogram is filled with  
2515 20 evenly spaced bins in production height  $h$  between 0 and 50km. The neutrino energy  
2516 and cosine zenith binning of the histogram is the same as that provided in section 7.2.  
2517 The average production height,  $\bar{h} = \int dh \frac{1}{4} \sum_j p_j(h|E_\nu, \cos(\theta_Z))$ , is calculated. The  
2518 production height binning of this histogram is then translated into  $\delta t(h) = t(\bar{h}) - t(h)$ ,  
2519 where  $t(h)$  is the distance travelled along the trajectory.

2520 For the  $i^{\text{th}}$  traversed layer, the transition amplitude,  $D_i(t_{i+1}, t_i)$ , is computed. The  
2521 time-ordered product of these is then used as the overall transition amplitude via

$$A(t_{n+1}, t_0) = D_n(t_{n+1}, t_n) \dots D_1(t_2, t_1) D_0(t_1, t_0), \quad (7.7)$$

2522 where,

$$\begin{aligned} D_n(t_{n+1}, t_n) &= \exp[-iH_n(t_{n+1} - t_n)] \\ &= \sum_{k=1}^3 C_k \exp[ia_k(t_{n+1} - t_n)] \end{aligned} \quad (7.8)$$

2523 is expressed as a diagonalised time-dependent solution to the Schrodinger equation.  
2524 The  $0^{th}$  layer is the propagation through the atmosphere and is the only term that  
2525 depends on the production height. Using the substitution  $t_0 = t(\bar{h}) - \delta t(h)$ , it can be  
2526 shown that

$$D_0(t_1, t_0) = D_0(t_1, \bar{h})D_0(\delta t). \quad (7.9)$$

2527 Thus Equation 7.7 becomes

$$\begin{aligned} A(t_{n+1}, t_0) &= D_n(t_{n+1}, t_n) \dots D_1(t_2, t_1)D_0(t_1, \bar{h})D(\delta t) \\ &= A(t_{n+1}, \bar{h}) \sum_{k=1}^3 C_k \exp[ia_k \delta t], \\ &= \sum_{k=1}^3 B_k \exp[ia_k \delta t]. \end{aligned} \quad (7.10)$$

2528 The oscillation probability averaged over production height is then calculated as

$$\begin{aligned}
 \bar{P}(\nu_j \rightarrow \nu_i) &= \int d(\delta t) p_j(\delta t | E_\nu, \cos \theta_Z) P(\nu_j \rightarrow \nu_i) \\
 &= \int d(\delta t) p_j(\delta t | E_\nu, \cos \theta_Z) A(t_{n+1}, t_0) A^*(t_{n+1}, t_0) \\
 &= \sum_{km} (B_k)_{ij} (B_m)_{ij}^* \int d(\delta t) p_j(\delta t | E_\nu, \cos \theta_Z) \exp[i(a_k - a_m)\delta t]
 \end{aligned} \tag{7.11}$$

2529 In practice, implementation in CUDAProb3 [213] is relatively straightforward as  
 2530 the majority of these terms are already calculated in the standard oscillation calculation.  
 2531 Figure 7.17 illustrates the results of the production height averaging. As expected,  
 2532 the main effect is observed in the low-energy downward-going and horizontal-going  
 2533 events. Upward-going events have to travel the radius of the Earth,  $R_E = 6371\text{km}$ ,  
 2534 where the production height uncertainty is a small fraction of the total path length.

2535

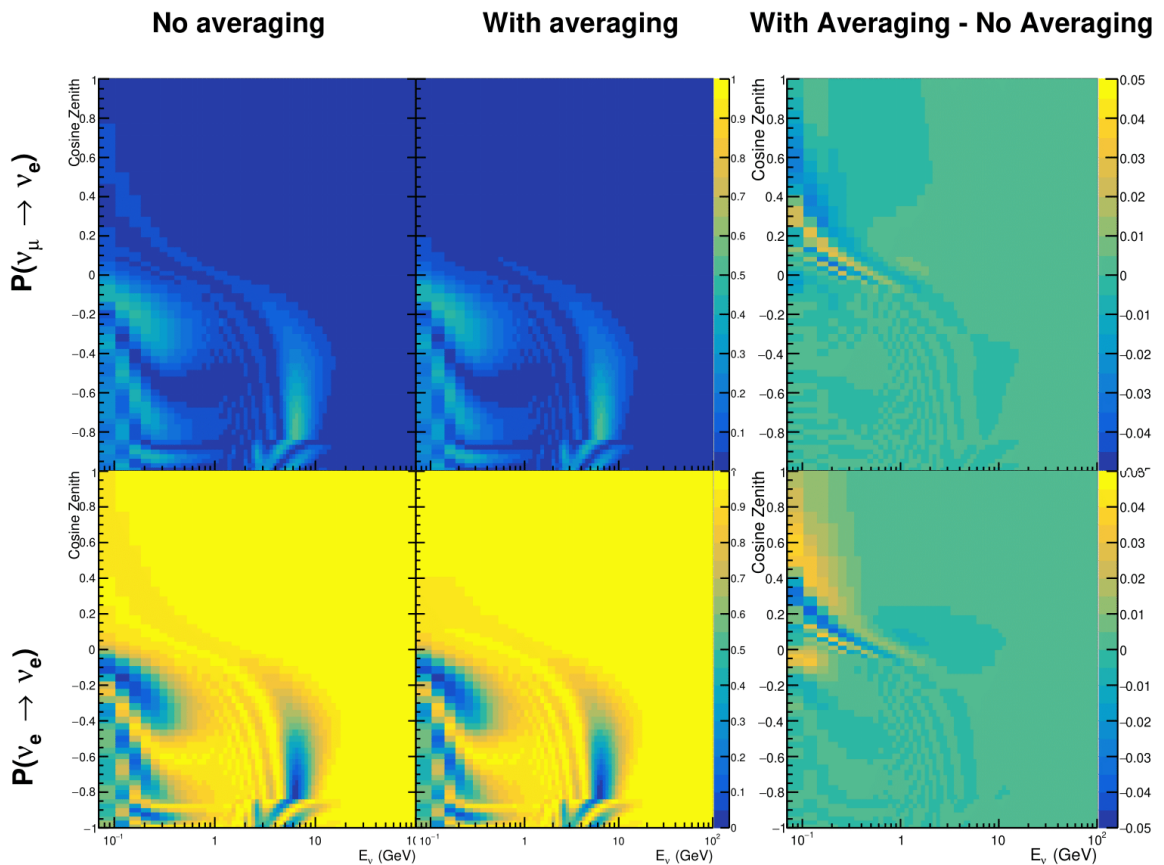


**Figure 7.17:** The oscillation probability,  $P(\nu_\mu \rightarrow \nu_e)$  (top row) and  $P(\nu_e \rightarrow \nu_\mu)$  (bottom row), given as a function of neutrino energy and zenith angle. The left column gives probabilities where a fixed production height of 25km is used. The middle column gives the probabilities where the production height is analytically averaged. The right column illustrates the difference in oscillation probability between the two different techniques.

2536

# Bibliography

- 2537 [1] J. Chadwick, Verhandl. Dtsc. Phys. Ges. **16**, 383 (1914).
- 2538 [2] C. D. Ellis and W. A. Wooster, Proc. R. Soc. Lond. A Math. Phys. Sci. **117**, 109  
2539 (1927).
- 2540 [3] W. Pauli, Phys. Today **31N9**, 27 (1978).
- 2541 [4] E. Fermi, Z. Phys. **88**, 161 (1934).
- 2542 [5] F. Reines and C. L. Cowan, Phys. Rev. **92**, 830 (1953).
- 2543 [6] C. L. Cowan, F. Reines, F. B. Harrison, H. W. Kruse, and A. D. McGuire, Science  
2544 **124**, 103 (1956), <http://science.sciencemag.org/content/124/3212/103.full.pdf>.
- 2545 [7] G. Danby *et al.*, Phys. Rev. Lett. **9**, 36 (1962).
- 2546 [8] K. Kodama *et al.*, Physics Letters B **504**, 218 (2001).
- 2547 [9] LSND, A. Aguilar-Arevalo *et al.*, Phys. Rev. **D64**, 112007 (2001), hep-ex/0104049.
- 2548 [10] MiniBooNE Collaboration, A. A. Aguilar-Arevalo *et al.*, Phys. Rev. Lett. **110**,  
2549 161801 (2013).
- 2550 [11] Planck Collaboration *et al.*, aap **641** (2020).
- 2551 [12] The ALEPH Collaboration, The Delphi Collaboration, The L3 Collaboration, The  
2552 SLD Collaboration, The LEP Electroweak Working Group, The SLD Electroweak  
2553 and Heavy Flavour Groups, J. A. Bagger *et al.*, Physics Reports **427**, 257 (2006).
- 2554 [13] B. Pontecorvo, Sov. Phys. JETP **26**, 984 (1968), [Zh. Eksp. Teor. Fiz. 53, 1717 (1967)].
- 2555 [14] B. Pontecorvo, Sov. Phys. JETP **7**, 172 (1958), [Zh. Eksp. Teor. Fiz. 34, 247 (1957)].
- 2556 [15] M. Kobayashi and T. Maskawa, Progress of Theoretical Physics **49**, 652 (1973).
- 2557 [16] N. Cabibbo, Phys. Rev. Lett. **10**, 531 (1963).
- 2558 [17] A. M. and, Journal of Physics: Conference Series **587**, 012030 (2015).
- 2559 [18] A. Y. Smirnov, (2003).
- 2560 [19] S. Mikheyev and A. Smirnov, Soviet Journal of Nuclear Physics **42**, 913 (1985).

- 2561 [20] L. Wolfenstein, Phys. Rev. D **17**, 2369 (1978).
- 2562 [21] V. D. Barger, K. Whisnant, S. Pakvasa, and R. J. N. Phillips, Phys. Rev. D **22**, 2718  
2563 (1980).
- 2564 [22] The Super-Kamiokande Collaboration, Y. Ashie *et al.*, Phys. Rev. Lett. **93**, 101801  
2565 (2004).
- 2566 [23] SNO Collaboration, Q. R. Ahmad *et al.*, Phys. Rev. Lett. **89**, 011301 (2002).
- 2567 [24] 2015 Nobel prize in Physics as listed by Nobelprize.org, [https://www.](https://www.nobelprize.org/nobel_prizes/physics/laureates/2015/)  
2568 [nobelprize.org/nobel\\_prizes/physics/laureates/2015/](https://www.nobelprize.org/nobel_prizes/physics/laureates/2015/), Accessed: 22-06-  
2569 2022.
- 2570 [25] J. A. Formaggio and G. P. Zeller, Rev. Mod. Phys. **84**, 1307 (2012), 1305.7513.
- 2571 [26] A. Bellerive, Int. J. Mod. Phys. A **19**, 1167 (2004).
- 2572 [27] R. Davis, D. S. Harmer, and K. C. Hoffman, Phys. Rev. Lett. **20**, 1205 (1968).
- 2573 [28] N. Vinyoles *et al.*, Astrophys. J. **835**, 202 (2017).
- 2574 [29] V. Gribov and B. Pontecorvo, Phys. Lett. B **28**, 493 (1969).
- 2575 [30] K. S. Hirata *et al.*, Phys. Rev. Lett. **63**, 16 (1989).
- 2576 [31] W. Hampel *et al.*, Phys. Lett. B **447**, 127 (1999).
- 2577 [32] SAGE Collaboration, J. N. Abdurashitov *et al.*, Phys. Rev. C **60**, 055801 (1999).
- 2578 [33] Q. R. Ahmad *et al.*, Phys. Rev. Lett. **89** (2002).
- 2579 [34] Borexino Collaboration, Nature **562**, 505 (2018).
- 2580 [35] B. Aharmim *et al.*, Astrophys. J. **653**, 1545 (2006).
- 2581 [36] M. Agostini *et al.*, (2020).
- 2582 [37] S. Andringa *et al.*, Adv. High Energy Phys. **2016**, 1 (2016).
- 2583 [38] J. F. Beacom *et al.*, Chin. phys. C **41**, 023002 (2017).
- 2584 [39] F. An *et al.*, J. Phys. G Nucl. Part. Phys. **43**, 030401 (2016).
- 2585 [40] J. Aalbers *et al.*, (2020), 2006.03114.
- 2586 [41] T. K. Gaisser and M. Honda, (2002).

- 2587 [42] G. D. Barr, T. K. Gaisser, P. Lipari, S. Robbins, and T. Stanev, Physical Review D  
2588 **70** (2004).
- 2589 [43] M. Honda, T. Kajita, K. Kasahara, S. Midorikawa, and T. Sanuki, Physical Review  
2590 D **75** (2007).
- 2591 [44] M. Honda, T. Kajita, K. Kasahara, and S. Midorikawa, Phys. Rev. D **70**, 043008  
2592 (2004).
- 2593 [45] M. Honda, T. Kajita, K. Kasahara, and S. Midorikawa, Phys. Rev. D **83**, 123001  
2594 (2011).
- 2595 [46] A. Fasso, A. Ferrari, P. R. Sala, and J. Ranft, (2001).
- 2596 [47] Y. Ashie *et al.*, Physical Review D **71** (2005).
- 2597 [48] F. Reines *et al.*, Phys. Rev. Lett. **15**, 429 (1965).
- 2598 [49] D. Casper *et al.*, Phys. Rev. Lett. **66**, 2561 (1991).
- 2599 [50] K. S. Hirata *et al.*, Phys. Lett. B **280**, 146 (1992).
- 2600 [51] Z. Li *et al.*, Physical Review D **98** (2018).
- 2601 [52] Kamiokande Collaboration *et al.*, (2017).
- 2602 [53] T2K Collaboration, Nature **580**, 339 (2020).
- 2603 [54] M. A. Acero *et al.*, Phys. Rev. Lett. **123**, 151803 (2019).
- 2604 [55] M. G. Aartsen *et al.*, Phys. Rev. Lett. **120** (2018).
- 2605 [56] P. Adamson *et al.*, Phys. Rev. Lett. **112** (2014).
- 2606 [57] M. S. Athar *et al.*, Progress in Particle and Nuclear Physics **124**, 103947 (2022).
- 2607 [58] G. Danby *et al.*, Phys. Rev. Lett. **9**, 36 (1962).
- 2608 [59] K. Abe *et al.*, Physical Review D **87** (2013).
- 2609 [60] MINOS Collaboration, D. G. Michael *et al.*, Phys. Rev. Lett. **97**, 191801 (2006).
- 2610 [61] G. Danby *et al.*, Phys. Rev. Lett. **9**, 36 (1962).
- 2611 [62] NOvA Collaboration, M. A. Acero *et al.*, Phys. Rev. Lett. **123**, 151803 (2019).
- 2612 [63] B. Abi, R. Acciarri, M. A. Acero, and G. e. a. Adamov, Eur. Phys. J. C Part. Fields

- 2613       **80** (2020).
- 2614 [64] Hyper-Kamiokande Proto-Collaboration *et al.*, Prog. Theor. Exp. Phys. **2015**,  
2615       53C02 (2015).
- 2616 [65] C. Blanco, D. Hooper, and P. Machado, Physical Review D **101** (2020).
- 2617 [66] MicroBooNE Collaboration *et al.*, Search for an Excess of Electron Neutrino  
2618       Interactions in MicroBooNE Using Multiple Final State Topologies, 2021.
- 2619 [67] KARMEN Collaboration, B. Armbruster *et al.*, Phys. Rev. D **65**, 112001 (2002).
- 2620 [68] S.-B. Kim, T. Lasserre, and Y. Wang, Adv. High Energy Phys. **2013**, 1 (2013).
- 2621 [69] M. Sajjad Athar *et al.*, Prog. Part. Nucl. Phys. **124**, 103947 (2022), 2111.07586.
- 2622 [70] K. Abe *et al.*, Nucl. Instrum. Methods Phys. Res. A **1027**, 166248 (2022).
- 2623 [71] F. P. An *et al.*, Phys. Rev. Lett. **108**, 171803 (2012).
- 2624 [72] RENO Collaboration, J. K. Ahn *et al.*, Phys. Rev. Lett. **108**, 191802 (2012).
- 2625 [73] Double Chooz Collaboration, Y. Abe *et al.*, Phys. Rev. Lett. **108**, 131801 (2012).
- 2626 [74] J. Collaboration *et al.*, TAO Conceptual Design Report: A Precision Measurement  
2627       of the Reactor Antineutrino Spectrum with Sub-percent Energy Resolution, 2020,  
2628       2005.08745.
- 2629 [75] for the RENO Collaboration, New results from RENO and the 5 MeV excess,  
2630       AIP Publishing LLC, 2015.
- 2631 [76] Y. Abe *et al.*, Journal of High Energy Physics **2014** (2014).
- 2632 [77] Daya Bay Collaboration, D. Adey *et al.*, Phys. Rev. Lett. **123**, 111801 (2019).
- 2633 [78] M. P. Decowski, Nucl. Phys. B. **908**, 52 (2016).
- 2634 [79] The KamLAND Collaboration, A. Gando *et al.*, Phys. Rev. D **83**, 052002 (2011).
- 2635 [80] P. Dunne, Latest Neutrino oscillation results from T2K, 2020.
- 2636 [81] M. Tanabashi *et al.*, Phys. Rev. D. **98** (2018).
- 2637 [82] Particle Data Group, R. L. Workman and Others, PTEP **2022**, 083C01 (2022).
- 2638 [83] T2K Collaboration, K. Abe *et al.*, Phys. Rev. Lett. **112**, 181801 (2014).

- 2639 [84] Y. Fukuda *et al.*, Phys. Rev. Lett. **81**, 1562 (1998).
- 2640 [85] Linyan Wan, (2022).
- 2641 [86] K. Abe *et al.*, Nuclear Instruments and Methods in Physics Research Section  
2642 A: Accelerators, Spectrometers, Detectors and Associated Equipment **737**, 253  
2643 (2014).
- 2644 [87] S. Fukuda *et al.*, Nucl. Instrum. Methods Phys. Res. A **501**, 418 (2003).
- 2645 [88] Y. Itow *et al.*, (2001).
- 2646 [89] M. Jiang *et al.*, Prog. Theor. Exp. Phys. **2019** (2019).
- 2647 [90] S. Fukuda *et al.*, Nuclear Instruments and Methods in Physics Research Section  
2648 A: Accelerators, Spectrometers, Detectors and Associated Equipment **501**, 418  
2649 (2003), <http://www.sciencedirect.com/science/article/pii/S016890020300425X>.
- 2650 [91] Y. Nakano *et al.*, Nucl. Instrum. Methods Phys. Res. A **977**, 164297 (2020).
- 2651 [92] Hamamatsu, Hamamatsu Photonics Photomultiplier Tubes Handbook.
- 2652 [93] K. Abe *et al.*, Nucl. Instrum. Methods Phys. Res. A **1027**, 166248 (2022).
- 2653 [94] J. F. Beacom and M. R. Vagins, Phys. Rev. Lett. **93**, 171101 (2004).
- 2654 [95] L. Marti *et al.*, Nucl. Instrum. Methods Phys. Res. A **959**, 163549 (2020).
- 2655 [96] L. Marti *et al.*, (2019).
- 2656 [97] M. Vagins, Solar/DSNB Neutrino\_SK-Gd, 2022.
- 2657 [98] J. Focht, PhD thesis, Massachusetts Institute of Technology, 2004.
- 2658 [99] T. Tanimori *et al.*, IEEE Transactions on Nuclear Science **36**, 497 (1989).
- 2659 [100] Super-Kamiokande Collaboration, J. Hosaka *et al.*, Phys. Rev. D **73**, 112001  
2660 (2006).
- 2661 [101] H. Nishino *et al.*, Nucl. Instrum. Methods Phys. Res. A **610**, 710 (2009).
- 2662 [102] S. Yamada *et al.*, IEEE Transactions on Nuclear Science **57**, 428 (2010).
- 2663 [103] S. Yamada, Y. Hayato, Y. Obayashi, and M. Shiozawa, New online system  
2664 without hardware trigger for the Super-Kamiokande experiment, in *2007 IEEE Nuclear Science Symposium Conference Record*, IEEE, 2007.
- 2665

- 2666 [104] G. Carminati, Phys. Procedia **61**, 666 (2015).
- 2667 [105] P. A. Čerenkov, Phys. Rev. **52**, 378 (1937).
- 2668 [106] I. Frank and I. Tamm, Coherent visible radiation of fast electrons passing  
2669 through matter, in *Selected Papers*, pp. 29–35, Springer Berlin Heidelberg, Berlin,  
2670 Heidelberg, 1991.
- 2671 [107] The T2K Collaboration, KEK Proposal (2001),  
2672 <http://neutrino.kek.jp/jhfnu/loi/loi.v2.030528.pdf>.
- 2673 [108] Y. Itow *et al.*, (2001), hep-ex/0106019.
- 2674 [109] The K2K Collaboration and S. H. Ahn, (2001), hep-ex/0103001.
- 2675 [110] The T2K Collaboration, KEK Proposal (2006), [http://j-parc.jp/researcher/Hadron/en/pac\\_0606/pdf/p11-Nishikawa.pdf](http://j-parc.jp/researcher/Hadron/en/pac_0606/pdf/p11-Nishikawa.pdf).
- 2677 [111] C. Bronner, Accelerator Neutrino I\_Recent results from T2K, 2022.
- 2678 [112] T2K Collaboration, K. Abe *et al.*, Phys. Rev. Lett. **112**, 061802 (2014),  
2679 <https://link.aps.org/doi/10.1103/PhysRevLett.112.061802>.
- 2680 [113] NINJA Collaboration, T. Fukuda *et al.*, Proposal for precise measurement of  
2681 neutrino-water cross-section in NINJA physics run, Proposal for J-PARC and  
2682 KEK, 2017.
- 2683 [114] T. Ovsiannikova *et al.*, Physics of Particles and Nuclei **48**, 1014 (2017),  
2684 <https://doi.org/10.1134/S1063779617060478>.
- 2685 [115] M. Antonova *et al.*, Journal of Instrumentation **12**, C07028 (2017),  
2686 <http://stacks.iop.org/1748-0221/12/i=07/a=C07028>.
- 2687 [116] The T2K Collaboration, K. Abe *et al.*, Phys. Rev. D **102**, 012007 (2020).
- 2688 [117] K. Abe *et al.*, Progress of Theoretical and Experimental Physics **2021** (2021).
- 2689 [118] The T2K Collaboration, K. Abe *et al.*, Nuclear Instruments  
2690 and Methods in Physics Research Section A: Accelerators, Spectrometers,  
2691 Detectors and Associated Equipment **659**, 106 (2011),  
2692 <http://www.sciencedirect.com/science/article/pii/S0168900211011910>.
- 2693 [119] K. Matsuoka *et al.*, Nuclear Instruments and Methods in Physics Research Section  
2694 A: Accelerators, Spectrometers, Detectors and Associated Equipment **624**, 591

- 2695 (2010), <http://www.sciencedirect.com/science/article/pii/S016890021002098X>.
- 2696 [120] K. Abe *et al.*, Phys. Rev. D. **103** (2021).
- 2697 [121] T. Vladisavljevic, *Predicting the T2K neutrino flux and measuring oscillation parameters* Springer theses, 1 ed. (Springer Nature, Cham, Switzerland, 2020).
- 2699 [122] D. Beavis, A. Carroll, and I. Chiang, (1995).
- 2700 [123] P.-A. Amaudruz *et al.*, Nuclear Instruments and Methods in Physics Research  
2701 Section A: Accelerators, Spectrometers, Detectors and Associated Equipment  
2702 **696**, 1 (2012).
- 2703 [124] N. Abgrall *et al.*, Nuclear Instruments and Methods in Physics Research Section  
2704 A: Accelerators, Spectrometers, Detectors and Associated Equipment **637**, 25  
2705 (2011).
- 2706 [125] S. Assylbekov *et al.*, Nuclear Instruments and Methods in Physics Research  
2707 Section A: Accelerators, Spectrometers, Detectors and Associated Equipment  
2708 **686**, 48 (2012).
- 2709 [126] D. Allan *et al.*, Journal of Instrumentation **8**, P10019 (2013).
- 2710 [127] F. Vannucci, Advances in High Energy Physics **2014**, 1 (2014).
- 2711 [128] UA1 magnet sets off for a second new life, 2022.
- 2712 [129] S. Aoki *et al.*, Nuclear Instruments and Methods in Physics Research Section  
2713 A: Accelerators, Spectrometers, Detectors and Associated Equipment **698**, 135  
2714 (2013).
- 2715 [130] K. Suzuki *et al.*, Progress of Theoretical and Experimental Physics **2015**, 53C01  
2716 (2015).
- 2717 [131] S. Brooks, A. Gelman, G. L. Jones, and X.-L. Meng, *Handbook of Markov Chain  
Monte Carlo* (CRC Press, 2011).
- 2719 [132] W. R. Gilks, S. Richardson, and D. J. Spiegelhalter, *Markov Chain Monte Carlo in  
Practice* (Chapman & Hall/CRC Interdisciplinary Statistics, 1995).
- 2721 [133] C. Wret, *Minimising systematic uncertainties in the T2K experiment using near-  
detector and external data*, PhD thesis, Imperial College London, 2018.
- 2723 [134] K. E. Duffy, *Measurement of the Neutrino Oscillation Parameters  $\sin^2 \theta_{23}$ ,  $\Delta m_{32}^2$ ,*

- <sup>2724</sup>  $\sin^2 \theta_{13}$ , and  $\delta_{CP}$  in Neutrino and Antineutrino Oscillation at T2K, PhD thesis, Oriel  
<sup>2725</sup> College, University of Oxford, 2016.
- <sup>2726</sup> [135] T. Bayes, Rev. Phil. Trans. Roy. Soc. Lond. **53**, 370 (1764).
- <sup>2727</sup> [136] N. Metropolis, A. W. Rosenbluth, M. N. Rosenbluth, A. H. Teller, and E. Teller,  
<sup>2728</sup> Journal of Chemical Physics **21** (1970).
- <sup>2729</sup> [137] W. K. Hastings, Biometrika **57** (1970).
- <sup>2730</sup> [138] J. Dunkley, M. Bucher, P. G. Ferreira, K. Moodley, and C. Skordis, Mon. Not. R.  
<sup>2731</sup> Astron. Soc. **356**, 925 (2005).
- <sup>2732</sup> [139] Particle Data Group *et al.*, Prog. Theor. Exp. Phys. **2020** (2020).
- <sup>2733</sup> [140] H. Jeffreys, *The Theory of Probability* Oxford Classic Texts in the Physical Sciences  
<sup>2734</sup> (, 1939).
- <sup>2735</sup> [141] R. E. Kass and A. E. Raftery, J. Am. Stat. Assoc. **90**, 773 (1995).
- <sup>2736</sup> [142] T. Böhlen *et al.*, Nuclear Data Sheets **120**, 211 (2014),  
<sup>2737</sup> <http://www.sciencedirect.com/science/article/pii/S0090375214005018>.
- <sup>2738</sup> [143] R. Brun *et al.*, GEANT: Detector Description and Simulation Tool; Oct 1994 CERN  
<sup>2739</sup> Program Library (CERN, Geneva, 1993), <http://cds.cern.ch/record/1082634>,  
<sup>2740</sup> Long Writeup W5013.
- <sup>2741</sup> [144] T2K Collaboration, K. Abe *et al.*, Phys. Rev. D **87**, 012001 (2013).
- <sup>2742</sup> [145] C. Zeitnitz and T. Gabriel, Nuclear Instruments and Methods in  
<sup>2743</sup> Physics Research Section A: Accelerators, Spectrometers,  
<sup>2744</sup> Detectors and Associated Equipment **349**, 106 (1994),  
<sup>2745</sup> <http://www.sciencedirect.com/science/article/pii/0168900294906130>.
- <sup>2746</sup> [146] A. Fiorentini *et al.*, T2K Technical Note **217** (2017).
- <sup>2747</sup> [147] N. Abgrall *et al.*, Physical Review C **84** (2011).
- <sup>2748</sup> [148] N. Abgrall *et al.*, Physical Review C **85** (2012).
- <sup>2749</sup> [149] N. Abgrall *et al.*, Nuclear Instruments and Methods in Physics Research Section  
<sup>2750</sup> A: Accelerators, Spectrometers, Detectors and Associated Equipment **701**, 99  
<sup>2751</sup> (2013), <http://www.sciencedirect.com/science/article/pii/S016890021201234X>.

- 2752 [150] HARP Collaboration, M. Apollonio *et al.*, Phys. Rev. C **80**, 035208 (2009),  
2753 <https://link.aps.org/doi/10.1103/PhysRevC.80.035208>.
- 2754 [151] B. Blau *et al.*, Nuclear Physics B - Proceedings Supplements **113**, 125 (2002).
- 2755 [152] S. Haino *et al.*, Physics Letters B **594**, 35 (2004).
- 2756 [153] NASA, U.S. Standard Atmosphere, 1976, 1976.
- 2757 [154] S. Roesler, R. Engel, and J. Ranft, The Monte Carlo Event Generator DPMJET-III,  
2758 in *Advanced Monte Carlo for Radiation Physics, Particle Transport Simulation and*  
2759 *Applications*, pp. 1033–1038, Springer Berlin Heidelberg, 2001.
- 2760 [155] K. Niita *et al.*, Radiation Measurements **41**, 1080 (2006).
- 2761 [156] T. Sanuki *et al.*, Physics Letters B **541**, 234 (2002).
- 2762 [157] P. Achard *et al.*, Physics Letters B **598**, 15 (2004).
- 2763 [158] K. Sato, Atmospheric Neutrino\_Reviews on neutrino fluxes (low E atm nu),  
2764 2022.
- 2765 [159] Y. Hayato and L. Pickering, The European Physical Journal Special Topics **230**,  
2766 4469 (2021).
- 2767 [160] Y. Hayato, Acta Physica Polonica B **40** (2009).
- 2768 [161] C. L. Smith, Physics Reports **3**, 261 (1972),  
2769 <http://www.sciencedirect.com/science/article/pii/0370157372900105>.
- 2770 [162] O. Benhar, A. Fabrocini, and S. Fantoni, Nuclear Physics A **497**, 423 (1989).
- 2771 [163] R. Bradford, A. Bodek, H. Budd, and J. Arrington, Nuclear Physics B - Proceedings Supplements **159**, 127 (2006),  
2772 <http://www.sciencedirect.com/science/article/pii/S0920563206005184>,  
2773 Proceedings of the 4th International Workshop on Neutrino-Nucleus Interac-  
2774 tions in the Few-GeV Region.
- 2775
- 2776 [164] A. A. Aguilar-Arevalo *et al.*, Physical Review D **81** (2010).
- 2777 [165] R. Gran, J. Nieves, F. Sanchez, and M. J. V. Vacas, Phys. Rev. D **88**, 113007 (2013),  
2778 <https://link.aps.org/doi/10.1103/PhysRevD.88.113007>.
- 2779 [166] C. Berger and L. M. Sehgal, Phys. Rev. D **76**, 113004 (2007).

- 2780 [167] C. Berger and L. M. Sehgal, Phys. Rev. D **79**, 053003 (2009),  
2781 <https://link.aps.org/doi/10.1103/PhysRevD.79.053003>.
- 2782 [168] T. Sjöstrand, Computer Physics Communications **82**, 74 (1994).
- 2783 [169] C. Bronner and M. Hartz, Tuning of the Charged Hadrons Multiplicities for Deep  
2784 Inelastic Interactions in NEUT, in *Proceedings of the 10th International Workshop on*  
2785 *Neutrino-Nucleus Interactions in Few-GeV Region (NuInt15)*, Journal of the Physical  
2786 Society of Japan, 2016.
- 2787 [170] M. Glück, E. Reya, and A. Vogt, The European Physical Journal C **5**, 461 (1998).
- 2788 [171] A. Bodek and U.-k. Yang, Axial and Vector Structure Functions for Electron- and  
2789 Neutrino- Nucleon Scattering Cross Sections at all  $Q^2$  using Effective Leading  
2790 order Parton Distribution Functions, 2010.
- 2791 [172] A. Bodek and U.-K. Yang, (2010).
- 2792 [173] S. Gollapinni, (2016).
- 2793 [174] E. S. P. Guerra *et al.*, Phys. Rev. D **99**, 052007 (2019).
- 2794 [175] GEANT4, S. Agostinelli *et al.*, Nucl. Instrum. Meth. **A506**, 250 (2003).
- 2795 [176] R. Brun, F. Bruyant, M. Maire, A. C. McPherson, and P. Zanarini, (1987).
- 2796 [177] K. Abe *et al.*, Physical Review Letters **121** (2018).
- 2797 [178] K. Abe *et al.*, Physical Review D **91** (2015).
- 2798 [179] R. Patterson *et al.*, Nuclear Instruments and Methods in Physics Research Section  
2799 A: Accelerators, Spectrometers, Detectors and Associated Equipment **608**, 206  
2800 (2009).
- 2801 [180] e. a. S. Berkman, T2K Technical Note **146** (2013).
- 2802 [181] e. a. A. Himmel, T2K Technical Note **219** (2015).
- 2803 [182] F. a. James, (1998), CERN Program Library Long Writeups.
- 2804 [183] e. a. D. Barrow, T2K Technical Note **326** (2020).
- 2805 [184] A. Maghrabi, A. Aldosari, and M. Almutairi, Advances in Space Research **68**,  
2806 2941 (2021).

- 2807 [185] Super-Kamiokande Collaboration, K. Abe *et al.*, Phys. Rev. D **97**, 072001 (2018),  
2808 <https://link.aps.org/doi/10.1103/PhysRevD.97.072001>.
- 2809 [186] Particle Data Group, J. Beringer *et al.*, Phys. Rev. D **86**, 010001 (2012).
- 2810 [187] Y. N. and, Journal of Physics: Conference Series **888**, 012191 (2017).
- 2811 [188] M. Jiang, *Study of the neutrino mass hierarchy with the atmospheric neutrino data*  
2812 *collected in Super-Kamiokande IV*, PhD thesis, Kyoto University, 2019.
- 2813 [189] S. N. K. Iyogi and Y. Obayashi., T2K Technical Note **027** (2011).
- 2814 [190] LeeKaPik, *Study of the neutrino mass hierarchy with the atmospheric neutrino data*  
2815 *observed in Super-Kamiokande*, PhD thesis, Tokyo University, 2012.
- 2816 [191] The Super-Kamiokande Collaboration, R. Wendell *et al.*, Phys. Rev. D **81**, 092004  
2817 (2010).
- 2818 [192] Super-Kamiokande Collaboration, J. Hosaka *et al.*, Phys. Rev. D **74**, 032002  
2819 (2006).
- 2820 [193] L. M. et al, T2K Technical Note **395** (2020).
- 2821 [194] J. Misset, T2K Technical Note **318** (2017).
- 2822 [195] X. Li and M. Wilking, T2K Technical Note **319** (2017).
- 2823 [196] e. a. Tomislav Vladisavljevic, T2K Technical Note **354** (2020).
- 2824 [197] G. Ambrosini *et al.*, Phys. Lett. B **420**, 225 (1998).
- 2825 [198] e. a. Edward Atkin, T2K Technical Note **344** (2019).
- 2826 [199] e. a. D. Barrow, T2K Technical Note **422** (2022).
- 2827 [200] MiniBooNE Collaboration, A. A. Aguilar-Arevalo *et al.*, Phys. Rev. D **81**, 092005  
2828 (2010), <https://link.aps.org/doi/10.1103/PhysRevD.81.092005>.
- 2829 [201] MINERvA Collaboration, L. Fields *et al.*, Phys. Rev. Lett. **111**, 022501 (2013),  
2830 <https://link.aps.org/doi/10.1103/PhysRevLett.111.022501>.
- 2831 [202] C. Wilkinson, P. Rodrigues, S. Cartwright, L. Thompson,  
2832 and K. McFarland, Phys. Rev. D **90**, 112017 (2014),  
2833 <https://link.aps.org/doi/10.1103/PhysRevD.90.112017>.

- 2834 [203] The MiniBooNE Collaboration, A. A. Aguilar-Arevalo *et al.*, Phys. Rev. D **81**,  
2835 013005 (2010), <https://link.aps.org/doi/10.1103/PhysRevD.81.013005>.
- 2836 [204] P. de Perio and J. Imber, T2K Technical Note **186** (2014).
- 2837 [205] P. de Perio and J. Imber, T2K Technical Note **107** (2012).
- 2838 [206] S. Tobayama, *An Analysis of the Oscillation of Atmospheric Neutrinos*, PhD thesis,  
2839 British Columbia U., 2016.
- 2840 [207] C. V. Daniel Barrow, T2K-SK Detector Matrix Uncertainties - MaCh3 In-  
2841 tegration, <https://git.t2k.org/t2k-sk/t2ksk-detcovmat/-/tree/feature/MaCh3Integration>, Accessed: 22-06-2022.
- 2843 [208] R. Wendell, *Three Flavor Oscillation Analysis of Atmospheric Neutrinos in Super-*  
2844 *Kamiokande*, PhD thesis, University of North Carolina, 2008.
- 2845 [209] A. M. Dziewonski and D. L. Anderson, Phys. Earth Planet. Inter. **25**, 297 (1981).
- 2846 [210] e. a. D. Barrow, T2K Technical Note **425** (2022).
- 2847 [211] R. G. Calland, A. C. Kaboth, and D. Payne, **9**, P04016 (2014).
- 2848 [212] R. Wendell, <http://www.phy.duke.edu/raw22/public/Prob3++/>.
- 2849 [213] F. Kallenborn, C. Hundt, S. Böser, and B. Schmidt, Computer Physics Communi-  
2850 cations **234**, 235 (2019).
- 2851 [214] L. Warsame, MaCh3 Analysis Progress.
- 2852 [215] S. Bourret, J. A. B. Coelho, and V. V. E. and, Journal of Physics: Conference Series  
2853 **888**, 012114 (2017).
- 2854 [216] C. Rott, A. Taketa, and D. Bose, Scientific Reports **5** (2015).
- 2855 [217] K. Hagiwara, N. Okamura, and K. ichi Senda, Journal of High Energy Physics  
2856 **2011** (2011).
- 2857 [218] D. Typinski, Earth Gravity, <http://www.typnet.net/Essays/EarthGravGraphics/EarthGrav.pdf>, Accessed: 24-06-2022.

<sup>2859</sup> **List of Figures**

2860	2.1	The cross-section of neutrinos from various natural and man-made sources as a function of neutrino energy. Taken from [25] . . . . .	10
2861			
2862	2.2	The solar neutrino flux as a function of neutrino energy for various fusion reactions and decay chains as predicted by the Standard Solar Model. Taken from [26]. . . . .	11
2863			
2864			
2865	2.3	Left panel: The atmospheric neutrino flux for different neutrino flavours as a function of neutrino energy as predicted by the 2007 Honda model (“This work”) [43], the 2004 Honda model (“HKKM04”) [44], the Bartol model [42] and the FLUKA model [46]. Right panel: The ratio of the muon to electron neutrino flux as predicted by all the quoted models. Both figures taken from [43]. . . . .	14
2866			
2867			
2868			
2869			
2870			
2871	2.4	A diagram illustrating the definition of zenith angle as used in the Super Kamiokande experiment [47]. . . . .	14
2872			
2873	2.5	Prediction of $\nu_e, \bar{\nu}_e, \nu_\mu, \bar{\nu}_\mu$ fluxes as a function of zenith angle as calculated by the HKKM model [45]. The left, middle and right panels represent three values of neutrino energy, 0.32GeV, 1.0GeV and 3.2GeV respectively. Predictions for other models including Bartol [42], Honda [43] and FLUKA [46] are given in [47]. . . . .	15
2874			
2875			
2876			
2877			
2878	2.6	Constraints on the atmospheric oscillation parameters, $\sin^2(\theta_{23})$ and $\Delta m_{23}^2$ , from atmospheric and long baseline experiments: SK [52], T2K [53], NO $\nu$ A [54], IceCube [55] and MINOS [56]. Figure taken from [57].	16
2879			
2880			
2881	2.7	Reactor electron antineutrino fluxes for $^{235}\text{U}$ (Black), $^{238}\text{U}$ (Green), $^{239}\text{Pu}$ (Purple), and $^{241}\text{Pu}$ (Orange) isotopes. The inverse $\beta$ -decay cross-section (Blue) and corresponding measurable neutrino spectrum (Red) are also given. Top panel: Schematic of Inverse $\beta$ -decay interaction including the eventual capture of the emitted neutron. This capture emits a $\gamma$ -ray which provides a second signal of the event. Taken from [69]. . . . .	19
2882			
2883			
2884			
2885			
2886			
2887	3.1	A schematic diagram of the Super-Kamiokande Detector. Taken from [88].	25

2888	3.2	The location of “standard PMTs” (red) inside the SK detector. Taken from [86]. . . . .	29
2889			
2890	3.3	Schematic view of the data flow through the data acquisition and online system. Taken from [102]. . . . .	32
2891			
2892	3.4	The cross-section view of the Tokai to Kamioka experiment illustrating the beam generation facility at J-PARC, the near detector situated at a baseline of 280m and the Super Kamiokande far detector situated 295km from the beam target. . . . .	35
2893			
2894			
2895			
2896	3.5	The near detector suite for the T2K experiment showing the ND280 and INGRID detectors. The distance between the detectors and the beam target is 280m. . . . .	36
2897			
2898			
2899	3.6	Top panel: Bird’s eye view of the most relevant part of primary and secondary beamline used within the T2K experiment. The primary beamline is the main-ring proton synchrotron, kicker magnet, and graphite target. The secondary beamline consists of the three focusing horns, decay volume, and beam dump. Figure taken from [118]. Bottom panel: The side-view of the secondary beamline including the focusing horns, beam dump and neutrino detectors. Figure taken from [119]. . . . .	38
2900			
2901			
2902			
2903			
2904			
2905			
2906	3.7	The Monte Carlo prediction of the energy spectrum for each flavour of neutrino ( $\nu_e$ , $\bar{\nu}_e$ , $\nu_\mu$ and $\bar{\nu}_\mu$ ) in the neutrino dominated beam FHC mode (Left) and antineutrino dominated beam RHC mode (Right) expected at SK. Taken from [120]. . . . .	39
2907			
2908			
2909			
2910	3.8	Top panel: T2K muon neutrino disappearance probability as a function of neutrino energy. Middle panel: T2K electron neutrino appearance probability as a function of neutrino energy. Bottom panel: The neutrino flux distribution for three different off-axis angles (Arbitrary units) as a function of neutrino energy. . . . .	41
2911			
2912			
2913			
2914			
2915	3.9	The components of the ND280 detector. The neutrino beam travels from left to right. Taken from [118]. . . . .	42
2916			
2917	3.10	Comparison of data to Monte Carlo prediction of integrated deposited energy as a function of track length for particles that stopped in FGD1. Taken from [123]. . . . .	44
2918			
2919			

---

2920	3.11 Schematic design of a Time Projection Chamber detector. Taken from [124].	45
2921	3.12 The distribution of energy loss as a function of reconstructed momentum for charged particles passing through the TPC, comparing data to Monte Carlo prediction. Taken from [124].	45
2922		
2923		
2924	3.13 A schematic of the P0D side-view. Taken from [125].	47
2925	3.14 Left panel: The Interactive Neutrino GRID on-axis Detector. 14 modules are arranged in a cross-shape configuration, with the center modules being directly aligned with the on-axis beam. Right panel: The layout of a single module of the INGRID detector. Both figures are recreated from [118].	49
2926		
2927		
2928		
2929		
2930	4.1 Example of using Monte Carlo techniques to find the area under the blue line. The gradient and intercept of the line are 0.4 and 1.0 respectively. The area found to be under the curve using one thousand samples is 29.9 units.	54
2931		
2932		
2933		
2934	4.2 The area under a line of gradient 0.4 and intercept 1.0 for the range $0 \leq x \leq 10$ as calculated using Monte Carlo techniques as a function of the number of samples used in each repetition. The analytical solution to the area is 30 units as given by the red line.	54
2935		
2936		
2937		
2938	4.3 Three MCMC chains, each with a stationary distribution equal to a Gaussian centered at 0 and width 1 (As indicated by the black dotted lines). All of the chains use a Gaussian proposal function but have different widths (or 'step size $\sigma$ '). The top panel has $\sigma = 0.1$ , middle panel has $\sigma = 0.5$ and the bottom panel has $\sigma = 5.0$ .	60
2939		
2940		
2941		
2942		
2943	4.4 The log-likelihood from the fit detailed in <a href="#">DB: Link to AsimovA Sensitivity Section</a> as a function of the number of steps accumulated in each fit. Many independent MCMC chains were run in parallel and overlaid on this plot. The red line indicates the $1 \times 10^5$ step burn-in period after which the log-likelihood becomes stable.	61
2944		
2945		
2946		
2947		

2948	4.5	Left: The two dimensional probability distribution for two correlated parameters $x$ and $y$ . The red distribution shows the two dimensional probability distribution when $0 \leq x \leq 5$ . Right: The marginalised probability distribution for the $y$ parameter found when requiring the $x$ to be bound between $-5 \leq x \leq 5$ and $0 \leq x \leq 5$ for the black and red distribution, respectively. . . . .	63
2954	5.1	The NEUT prediction of the $\nu_\mu$ -H <sub>2</sub> O cross-section overlaid on the T2K $\nu_\mu$ flux. The charged current (black, solid) and neutral current (black, dashed) inclusive, charged current quasi-elastic (blue, solid), charged current 2p2h (blue, dashed), charged current single pion production (pink), and charged current multi- $\pi$ and DIS (Purple) cross-sections are illustrated. Figure taken from [159]. . . . .	71
2960	5.2	Illustration of the various processes which a pion can undergo before exiting the nucleus. Taken from [173]. . . . .	72
2962	5.3	Event displays from Super Kamiokande illustrating the “crisp” ring from a muon and the typically “fuzzier” electron ring. Each pixel represents a PMT and the color scheme denotes the accumulated charge deposited on that PMT. Figures taken from [181]. . . . .	75
2966	5.4	The electron/muon PID separation parameter for all sub-GeV single-ring events in SK-IV. The charged current (CC) component is broken down in four flavours of neutrino ( $\nu_\mu$ , $\bar{\nu}_\mu$ , $\nu_e$ and $\bar{\nu}_e$ ). Events with positive values of the parameter are determined to be electron-like. . .	79
2970	5.5	The variation of the measured dark rate as a function of date, broken down by PMT type. The SK-IV and SK-V periods span September 2008 to May 2018 and January 2019 to July 2020, respectively. The break in measurement in 2018 corresponds to the period of tank repair and refurbishment. Figure adapted from [183]. . . . .	81
2975	5.6	Comparison of the measured raw charge deposited per event from the stopping muon data samples between SK-IV (Blue) and SK-V (Red), split by the primary muon subevent and the associated decay electron subevent. . . . .	82

2979	5.7	The distribution of the reconstructed momentum from the muon ring divided by the distance between the reconstructed muon and decay electron vertices as found in the stopping muon data sets of SK-IV (Black) and SK-IV (Red). Only events with one tagged decay electron are considered. A Gaussian fit is considered in the range [2.0, 2.4] MeV/cm and illustrated as the solid curve. . . . .	83
2985	5.8	The $\chi^2$ difference between the SK-IV and SK-V reconstructed muon momentum divided by range when the SK-V is modified by the scaling parameter $\alpha$ . Both additive (Blue) and multiplicative (Black) scaling factors have been considered. In practice, the additive scaling factor actually uses the value of $(\alpha - 1.0)$ but is illustrated like this so the results can be shown on the same axis range. . . . .	84
2991	5.9	A depiction of the topology patterns for fully-contained (FC), partially-contained (PC) and up-going muon (Up- $\mu$ ) samples included in this analysis. . . . .	85
2994	5.10	The predicted neutrino flux of the fully contained (FC) sub-GeV and multi-GeV, partially contained (PC), and upward-going muon (Up- $\mu$ ) events. The prediction is broken down by the $\nu_x \rightarrow \nu_e$ prediction (top left), $\nu_x \rightarrow \nu_\mu$ prediction (top right) and $\nu_x \rightarrow \nu_\tau$ prediction (bottom). All systematic dials are set to their nominal values and the Asimov A oscillation parameters are assumed. . . . .	87
3000	5.11	The predicted neutrino flux of the beam neutrinos, illustrated as a function of neutrino energy. The predictions are broken down by the number of decay electrons associated with the particular events. All systematic dials are set to their nominal values and the Asimov A oscillation parameters are assumed. . . . .	89
3005	6.1	Comaprison of the SK-IV atmospheric samples between predictions made with the Asimov A (Black) and Asimov B (Red) oscillation parameter sets, given in Table 2.2. The subGeV samples CCRES and $\pi^0$ -like samples are given in their reconstructed lepton momentum. All other samples are presented in their reconstructed zenith angle projection. . . . .	96

3010      6.2	The reconstructed neutrino energy, as defined by Equation 6.2 and 3011      Equation 6.3, for the $1R\mu$ , $1Re$ and $CC1\pi^+$ samples. The generated dial 3012      values and Asimov A oscillation parameter sets are assumed. These 3013      samples are the FHC mode samples. For ease of viewing, the $1R\mu$ 3014      sample only shows the $0. \leq E_\nu^{rec} < 3.0\text{GeV}$ but the binning extends out 3015      to $30.0\text{GeV}$ . . . . .	101
3016      6.3	The distribution of the angle between the neutrino beam direction and 3017      the reconstructed final state lepton, for the FHC neutrino mode beam 3018      one ring electron sample. The distribution is broken down by neutrino 3019      interaction mode into charged current (left) and neutral current (right) 3020      components. The pre-fit systematic dial values and Asimov A oscillation 3021      parameter sets are assumed. . . . .	102
3022      6.4	The total uncertainty evaluated on the near detector $\nu_\mu$ flux prediction 3023      constrained by the replica-target data, illustrated as a function 3024      of neutrino energy. The solid(dashed) line indicates the uncertainty 3025      used within this analysis(the T2K 2018 analysis). The solid histogram 3026      indicates the neutrino flux as a function of energy. Figure taken from [196].104	
3027      6.5	The prediction neutrino energy distribution for subGeV atmospheric 3028      and beam samples, given for muon-like samples FHC+RHC $1R\mu$ beam 3029      samples compared to the subGeV $\mu$ -like 0+1 decay electrons (d.e.) at- 3030      mospheric samples, electron-like 0d.e. samples FHC+RHC $1Re$ beam 3031      samples compared to the subGeV $e$ -like 1d.e. sample, and electron-like 3032      1d.e. sample FHC1Re1de beam sample compared to the subGeV $e$ -like 3033      1d.e. atmospheric sample. . . . .	109
3034      6.6	The interaction mode contribution of each sample given as a fraction 3035      of the total event rate in that sample. All systematic dials are set to 3036      their nominal values and the Asimov A oscillation parameters are as- 3037      sumed. The Charged Current (CC) modes are broken into quasi-elastic 3038      (QE), meson exchange (2p2h), resonant charged pion production ( $1\pi^\pm$ ), 3039      multi-pion production ( $M\pi$ ), and other interaction category. Neutral 3040      Current (NC) interaction modes are given in interaction mode cate- 3041      gories: $\pi^0$ production, resonant charged pion production, multi-pion 3042      production and other. . . . .	110

3043	6.7 Down-going atmospheric subGeV single-ring samples comparing the 3044 mean and error of the pre-fit and post-fit Monte Carlo predictions in 3045 red and blue, respectively. The magenta histogram illustrates the Monte 3046 Carlo prediction using the generated dial values. The black points illus- 3047 trates the down-going data with statistical errors given. The mean and 3048 errors of the Monte Carlo predictions are calculated by the techniques 3049 documented in subsection 4.3.4. The cross-section and atmospheric flux 3050 parameters are either thrown from their pre-fit uncertainties (denoted 3051 pre-fit band), or the cross section dial values are randomly sampled 3052 from a MCMC chain whilst the atmospheric flux parameters are thrown 3053 from their pre-fit distributions (denoted post-fit band). . . . .	113
3054	6.8 The ring counting parameter, as defined in Equation 6.6, for the subGeV 3055 electron-like zero decay electron and multi-ring $\nu_e$ -like samples. . . . .	123
3056	6.9 The ring counting parameter, defined in Equation 6.6, as a function of 3057 the number of reconstructed rings as found by the <code>fitQun</code> algorithm. 3058 Left: true $\nu_\mu$ events with only one muon above Cherenkov threshold in 3059 the final state. Right: true $\nu_\mu$ events with one muon and at least one 3060 other charged particle above Cherenkov threshold in the final state. . .	124
3061	6.10 The $\chi^2$ between the hybrid- $\pi^0$ Monte Carlo and data samples, as a 3062 function of smear ( $\alpha$ ) and shift ( $\beta$ ) parameters, for events which have 3063 $1\pi^0$ final state topology. Left: Electron-muon separation PID parameter 3064 for events with $30 \geq E_{vis}(\text{MeV}) < 300$ . Right: Electron- $\pi^0$ separation 3065 PID parameter for events with $30 \geq E_{vis}(\text{MeV}) < 300$ . . . . .	125
3066	6.11 The distribution of $\log(L_e/L_\mu)$ compared to $\log(L_e/L_\pi)$ for subGeV 3067 events with zero (top left), one (top right) or two (bottom) decay elec- 3068 trons. The correlation in the distribution is calculated as 0.997, 0.999 3069 and 0.996, respectively. . . . .	126
3070	7.1 The density of the Earth given as a function of the radius, as given by the 3071 PREM model (Black), and the constant density four-layer approximation 3072 (Blue), as used in the official SK-only analysis. . . . .	130

3073	7.2 An “oscillogram” that depicts the $P(\nu_\mu \rightarrow \nu_e)$ oscillation probability as 3074 a function of neutrino energy and cosine of the zenith angle. The zenith 3075 angle is defined such that $\cos(\theta_Z) = 1.0$ represents neutrinos that travel 3076 from directly above the detector. The four-layer constant density PREM 3077 model approximation is used and Asimov A oscillation parameters are 3078 assumed (Table 2.2). . . . .	131
3079	7.3 The effect of $\delta_{CP}$ for atmospheric neutrinos given in terms of the 3080 neutrino energy and zenith angle. This oscillogram compares the 3081 $P(\nu_\mu \rightarrow \nu_e)$ oscillation probability for a CP conserving ( $\delta_{CP} = 0.0$ ) 3082 and a CP violating ( $\delta_{CP} = -1.601$ ) value taken from the Asimov A 3083 parameter set. The other oscillation parameters assume the Asimov A 3084 oscillation parameter set given in Table 2.2. . . . .	132
3085	7.4 An illustration of the matter-induced effects on the oscillation probabil- 3086 ity, given as a function of neutrino energy and zenith angle. The top row 3087 of panels gives the $P(\nu_e \rightarrow \nu_e)$ oscillation probability and the bottom 3088 row illustrates the $P(\bar{\nu}_e \rightarrow \bar{\nu}_e)$ oscillation probability. The left column 3089 highlights the oscillation probability in a vacuum, whereas the middle 3090 and right column represents the oscillation probabilities when the four- 3091 layer fixed density PREM model is assumed. All oscillation probabilities 3092 assume the “Asimov A” set given in Table 2.2, but importantly, the right 3093 column sets an inverted mass hierarchy. The “matter resonance” effects 3094 at $E_\nu \sim 5\text{GeV}$ can be seen in the $P(\nu_e \rightarrow \nu_e)$ for normal mass hierarchy 3095 and $P(\bar{\nu}_e \rightarrow \bar{\nu}_e)$ for inverted hierarchy. . . . .	133
3096	7.5 The oscillation probability for beam neutrino events given as a function 3097 of neutrino energy. All oscillation parameters assume the “Asimov A” 3098 set given in Table 2.2 unless otherwise stated. Each panel represents a 3099 change in one of the oscillation parameters whilst keeping the remaining 3100 parameters fixed. . . . .	134
3101	7.6 The number of electron-like events in the FHC and RHC operating 3102 mode of the beam, as a function of the oscillation probabilities. Both 3103 normal hierarchy (Solid)) and inverse hierarchy (Dashed) values of 3104 $\Delta m_{23}^2$ are given. . . . .	135

3105	7.7	The oscillation probability $P(\nu_\mu \rightarrow \nu_e)$ , given as a function of neutrino energy and zenith angle, which highlights an example of the “fast” oscillations in the sub-GeV upgoing region. . . . .	137
3108	7.8	Illustration of the averaging procedure for $N = 2$ . The oscillation probabilities calculated on the finer left binning are averaged to obtain the oscillation probabilities in the coarser right binning. These averaged oscillation probabilities with the coarser binning are then applied to each event during the fit. . . . .	139
3113	7.9	Event rate of the SubGeV_elike_0dcy sample as a function of the number of sub-divisions per coarse bin. Each subplot represents the event rate of the sample at a different oscillation parameter set thrown from the PDG priors detailed in Table 2.1. The red line in each subplot represents the mean of the event rate over the different values of sub-divisions for that particular oscillation parameter throw. . . . .	141
3119	7.10	Variance of event rate for each atmospheric sample as a function of the number of sub-divisions per coarse bin. The solid red line indicates the 0.1% threshold and the dashed red line indicates the variance at a sub-division $N = 10$ . . . . .	142
3123	7.11	Variance of sample likelihood, when compared to ‘Asimov data’ set at Asimov A, for each atmospheric sample as a function of the number of sub-divisions per coarse bin. The solid red line indicates the 0.1% threshold and the dashed red line is a graphical indication of the variance at a sub-division $N = 10$ . . . . .	143
3128	7.12	The oscillation probability, $P(\nu_\mu \rightarrow \nu_e)$ (top row) and $P(\nu_e \rightarrow \nu_e)$ (bottom row), given as a function of neutrino energy and zenith angle. The left column gives the “fine” binning used to calculate the oscillation probabilities and the right column illustrates the “coarse” binning used to reweight the Monte Carlo events. The fine binning choice is given with $N = 10$ , which was determined to be below the threshold from Figure 7.10 and Figure 7.11. . . . .	144

3135	7.13 The calculation time taken to both calculate the oscillation probabilities 3136 and fill the “coarse” oscilloscopes, following the technique given in 3137 section 7.2, for the CUDAProb3 and ProbGPU (Red) calculation engines. 3138 CUDAProb3 has both a GPU (Blue) and CPU (Black) implementation, 3139 where the CPU implementation is multithreaded. Therefore, 8-threads 3140 (solid) and 40-threads (dashed) configurations have been tested. Prob3, 3141 which is a CPU single-thread implementation has a mean step time of 3142 1.142s. . . . .	145
3143	7.14 The oscillation probability, $P(\nu_\mu \rightarrow \nu_e)$ (top row) and $P(\nu_e \rightarrow \nu_e)$ (bot- 3144 tom row), given as a function of neutrino energy and zenith angle. The 3145 left column gives probabilities where the constant $Z/A = 0.5$ approx- 3146 imation which is used in the official SK-only analysis. The middle 3147 column gives the probabilities where $Z/A = [0.468, 0.498]$ values are 3148 used, as given in Table 7.1. The right column illustrates the difference 3149 in oscillation probability between the two different techniques. . . . .	147
3150	7.15 The density of the Earth given as a function of the radius, as given by 3151 the PREM model (Black), the constant density four-layer approxima- 3152 tion (Blue), as used in the official SK-only analysis, and the quadratic 3153 approximation of the PREM model (Red). . . . .	148
3154	7.16 The oscillation probability, $P(\nu_\mu \rightarrow \nu_e)$ (top row) and $P(\nu_e \rightarrow \nu_e)$ (bot- 3155 tom row), given as a function of neutrino energy and zenith angle. The 3156 left column gives probabilities where the four-layer constant density ap- 3157 proximation is used. The middle column gives the probabilities where 3158 the density is integrated over the trajectory, using the quadratic PREM 3159 approximation, for each $\cos(\theta_Z)$ is used. The right column illustrates the 3160 difference in oscillation probability between the two different techniques.	150
3161	7.17 The oscillation probability, $P(\nu_\mu \rightarrow \nu_e)$ (top row) and $P(\nu_e \rightarrow \nu_e)$ (bot- 3162 tom row), given as a function of neutrino energy and zenith angle. The 3163 left column gives probabilities where a fixed production height of 25km 3164 is used. The middle column gives the probabilities where the produc- 3165 tion height is analytically averaged. The right column illustrates the 3166 difference in oscillation probability between the two different techniques.	154

# 3167 List of Tables

<small>3168</small>	2.1	The 2018 Particle Data Group constraints of the oscillation parameters taken from [81]. The value of $\Delta m_{23}^2$ is given for both normal hierarchy (N.H.) and inverted hierarchy (I.H.) and $\sin^2(\theta_{23})$ is broken down by whether its value is below (Q1) or above (Q2) 0.5. . . . .	<small>3169</small> 21
<small>3170</small>			
<small>3171</small>			
<small>3172</small>	2.2	Reference values of the neutrino oscillation parameters for two different oscillation parameter sets. . . . .	<small>3173</small> 22
<small>3174</small>			
<small>3175</small>			
<small>3176</small>	3.1	The various SK periods and respective live-time. The SK-VI live-time is calculated until 1 <sup>st</sup> April 2022. SK-VII started during the writing of this thesis. . . . .	24
<small>3177</small>			
<small>3178</small>			
<small>3179</small>			
<small>3180</small>	3.2	The trigger thresholds and extended time windows saved around an event which were utilised throughout the SK-IV period. The exact thresholds can change and the values listed here represent the thresholds at the start and end of the SK-IV period. . . . .	33
<small>3181</small>			
<small>3182</small>			
<small>3183</small>	3.3	The threshold momentum and energy for a particle to generate Cherenkov light in ultrapure water, as calculated in Equation 3.2 in ultrapure water which has refractive index $n = 1.33$ . . . . .	34
<small>3184</small>			
<small>3185</small>			
<small>3186</small>			
<small>3187</small>	4.1	Jeffreys scale for strength of preference for two models $A$ and $B$ as a function of the calculated Bayes factor ( $B_{AB} = B(A/B)$ ) between the two models [140]. The original scale is given in terms of $\log_{10}(B(A/B))$ but converted to linear scale for easy comparison throughout this thesis.	66
<small>3188</small>			
<small>3189</small>	6.1	The fully contained subGeV samples used within this oscillation analysis. Both the sample name and description are given. . . . .	91
<small>3190</small>			
<small>3191</small>	6.2	The fully contained multiGeV samples used within this oscillation analysis. Both the sample name and description are given. . . . .	93

3192      6.3	The purity of each atmospheric sample used within this analysis, broken 3193      down by charged current (CC) and neutral current (NC) interactions 3194      and which neutrino flavour interacted within the detector. The pre- 3195      fit dial values and Asimov A oscillation parameter sets are assumed. 3196      Electron neutrino and antineutrino events are separated to illustrate the 3197      ability of the separation likelihood cuts used within the sample selections. . . . .	94
3198      6.4	The reconstructed cosine zenith and lepton momentum binning as- 3199      signed to the atmospheric samples. The “cos( $\theta_Z$ ) Bins” column illus- 3200      trates the number of bins uniformly distributed over the $-1.0 \leq$ 3201 $\cos(\theta_Z) \leq 1.0$ region for fully and partially contained samples and 3202 $-1.0 \leq \cos(\theta_Z) \leq 0.0$ region for up- $\mu$ samples. . . . .	95
3203      6.5	The neutrino energy binning for the different neutrino flavours. “Right” 3204      sign indicates neutrinos in the FHC beam and antineutrinos in the RHC 3205      beam mode. “Wrong” sign indicates antineutrinos in the FHC beam 3206      and neutrinos in the RHC beam mode. The binning of the detector 3207      response is identical for the FHC and RHC modes as well as at ND280 3208      and SK. . . . .	105
3209      6.6	List of cut variables which are included within the shift/smear fit docu- 3210      mented in [194]. . . . .	116
3211      6.7	Reconstructed event topology categories on which the SK detector 3212      systematics [194] are based. . . . .	116
3213      6.8	Sources of systematic errors specified within the grouped into the “cali- 3214      bration” systematics model. . . . .	119
3215      6.9	Reconstructed event topology categories on which the SK detector 3216      systematics are based . . . . .	121
3217      7.1	Description of the four layers of the Earth invoked within the constant 3218      density approximation of the PREM model [209]. . . . .	129
3219      7.2	The quadratic polynomial fits to the PREM model for four assumed 3220      layers of the PREM model. The fit to calculate the coefficients is given 3221      in [210], where $x = R/R_{Earth}$ . . . . .	149